

Effect of natural fracture on hydraulic fracture propagation in poroelastic formation: fully coupled numerical model to investigate the interaction between induced and natural fracture

Author:

Rahman, Mohammad Mustafizur

Publication Date:

2010

DOI:

<https://doi.org/10.26190/unsworks/23812>

License:

<https://creativecommons.org/licenses/by-nc-nd/3.0/au/>

Link to license to see what you are allowed to do with this resource.

Downloaded from <http://hdl.handle.net/1959.4/51215> in <https://unsworks.unsw.edu.au> on 2024-05-03

**EFFECT OF NATURAL FRACTURE ON HYDRAULIC
FRACTURE PROPAGATION IN POROELASTIC
FORMATION: FULLY COUPLED NUMERICAL MODEL TO
INVESTIGATE THE INTERACTION BETWEEN INDUCED
AND NATURAL FRACTURE**

By

Mohammad Mustafizur Rahman

Supervisor: Professor Sheik S. Rahman

Dissertation

Submitted to The University of New South Wales in partial fulfilment of
the requirements for the Degree of Doctor of Philosophy

In

Petroleum Engineering

School of Petroleum Engineering

The University of New South Wales

Sydney, NSW, AUSTRALIA

September 2010

Thesis/Dissertation Sheet

ORIGINALITY STATEMENT

‘I hereby declare that this submission is my own work and to the best of my knowledge it contains no materials previously published or written by another person, or substantial proportions of material which have been accepted for the award of any other degree or diploma at UNSW or any other educational institution, except where due acknowledgement is made in the thesis. Any contribution made to the research by others, with whom I have worked at UNSW or elsewhere, is explicitly acknowledged in the thesis. I also declare that the intellectual content of this thesis is the product of my own work, except to the extent that assistance from others in the project's design and conception or in style, presentation and linguistic expression is acknowledged.’

Signed

Date

ACKNOWLEDGEMENTS

I want to express my deepest gratitude to my adviser Prof. Sheik S Rahman for his consistent support and guidance throughout my PhD studies. The lessons learned from him will be an invaluable asset in my career. It would have been impossible to complete this work without his helpful supervision.

I would also like to thank Dr. Mohammad Ali Aghighi for his timely advice and directions in completing the project. I received valuable input from him when I was stuck with my research problem. Furthermore, I would like to extend my sincere appreciation to my all colleague for their continuous support. I also would like to express my gratefulness for financial support from the Faculty of Engineering of The University of New South Wales.

I would like to thank Nino Zajackowski for paying immediate attention to my computer and software related needs. His helpful attitude is deeply appreciated. I also want to thank my fellow graduate students in the petroleum engineering department, who have accompanied me in this long but exciting journey.

Finally, I want to thank my parents and my wonderful wife, Samiha for their endless support and patience over years of my study. I also want to thank my youngsters Adyan, Rayan and Zayan for allowing me the opportunity to work without interruption. Many friends, too numerous to mention here, were very helpful. Their companionship made my time at UNSW quite pleasant and smooth.

DEDICATION

I dedicate this thesis to my parents for their never ending love and support.

Abstract

This thesis deals with modeling of an induced hydraulic fracture and a natural fracture in a poroelastic medium and study their interaction. A finite element based numerical model is developed for this purpose. The model integrates a wellbore, an induced hydraulic fracture, a natural fracture and a reservoir in a fully coupled manner and simulates the interaction between induced hydraulic fracture and a natural fracture. A half reservoir model is used to take advantage of symmetry. In order to have control over the entire grid and element numbering, an innovative mesh generator was developed as part of this study. Fracture propagation is modeled based on KGD fracture mechanics.

The numerical studies have shown that a natural fracture has a profound effect on the induced fracture propagation. It has been observed that in most cases the induced fracture crosses the natural fracture at high angles of approach and high differential stress. The width of the induced fracture decreases as it propagates. Once the induced fracture crosses a natural fracture and it propagates further into the formation fracture width increases. At low angles of approach and low differential stress the induced fracture is more likely to be arrested (at least short time) and/or breaks out from the far end side of the natural fracture. Results also showed that in the case of high angle of approach the hydraulic fracture always crosses the natural fracture and the differential stress has no significant effect on the propagation of hydraulic fracture. It has been also observed that propagation of induced fracture is stopped by a large (>10m) natural fracture at high angle of approach. If the injection rate, however, is increased the induced fracture crosses the large natural fracture at high angle of approach. At low angle of approach the induced fracture deviates and propagates along natural fracture. Crossing of natural fracture and/or arrest by the natural fracture is controlled by shear strength of the natural fracture, natural fracture orientation and in-situ stress state of the reservoir.

From the results of this study it has been found that this model has a potential application in the design and optimization of hydraulic fracture treatments in naturally fractured reservoirs including tight gas reservoirs and enhanced geothermal systems. The model can also be used in the design of hydraulic stimulation of naturally fractured reservoirs based on shear dilation principle.

Publications

The following are publications are co-authored by the author of this thesis. They are based on the work of this study.

Published

M.M. Rahman, M.A. Aghighi, "Effect of Natural Fracture on Hydraulic Fracture Propagation in Naturally Fractured Reservoirs- A Finite Element Modelling", presented at the 72nd EAGE Conference & Exhibition, Spain, Barcelona, 14-17 June 2010.

M.M. Rahman, M.A. Aghighi, S.S. Rahman, "Effect of Natural Fracture on Hydraulic Fracture Propagation in Naturally Fractured Geothermal Reservoirs", World Geothermal Congress, Bali, Indonesia, 25-30 April 2010.

M.M. Rahman, M.A. Aghighi, S.S. Rahman, "A Fully Coupled Numerical Poroelastic Model to Investigate Interaction between Induced Hydraulic Fracture and Pre-existing Natural Fracture in a Naturally Fractured Reservoir: Potential Application in Tight Gas and Geothermal Reservoirs", SPE Annual Technical Conference and Exhibition, New Orleans, Louisiana, USA, 4-7 October 2009.

M.M. Rahman, M.A. Aghighi, S.S. Rahman, "Interaction between Induced Hydraulic Fracture and Pre-existing Natural Fracture in a Poroelastic Environment: Effect of Pore Pressure Change and the Orientation of Natural fractures", presented at the 2009 Asia Pacific Oil and Gas Conference and Exhibition, Jakarta, Indonesia, 4-6 Aug 2009.

M.M. Rahman, M.A. Aghighi, S. A. Ravoof, "Numerical Modeling of Fully Coupled Hydraulic Fracture Propagation in Naturally Fractured Poroelastic Reservoir", 71st EAGE Conference & Exhibition, Amsterdam, Netherlands, 8-11 June 2009.

Submitted for Publication

M.M. Rahman, M.A. Aghighi, S. S. Rahman," Hydraulic Fracture Propagation Trajectory in Presence of Natural Fracture in a Naturally Fractured Poroelastic Reservoir: Hydraulic Fracture Deviation and Crossing of Natural Fracture" the International Journal for Numerical and Analytical Methods in Geomechanics (in review).

M.M. Rahman, S.S. Rahman," A Fully Coupled Numerical Poroelastic Model to Investigate Interaction between Induced Hydraulic Fracture and Pre-existing Natural Fracture

in a Naturally Fractured Reservoir: Potential Application in Tight Gas and Geothermal Reservoirs”, International Journal of Rock Mechanics and Rock Engineering (in review).

Table of Contents

| | |
|--|------|
| ORIGINALITY STATEMENT | iii |
| ACKNOWLEDGEMENT | iv |
| DEDICATION | v |
| ABSTRACT | vi |
| PUBLICATION | vii |
| TABLE OF CONTENTS | viii |
| LIST OF TABLES | xi |
| LIST OF FIGURES | xi |
| CHAPTER 1: INTRODUCTION | |
| 1.1. Background knowledge | 1 |
| 1.2. Aims and significance | 2 |
| 1.3. Structure of the thesis | 3 |
| CHAPTER 2: MODELING OF FRACTURE PROPAGATION IN POROELASTIC FORMATION | |
| 2.1 Intact wellbore modelling | 5 |
| 2.2 Validation of intact wellbore model | 10 |
| 2.3 Modelling and validation of fracture propagation | 12 |
| 2.4 Summary | 21 |
| CHAPTER 3: MODELING OF HYDRAULIC FRACTURE PROPAGATION IN PRESENCE OF NATURAL FRACTURE | |
| 3.1 Modelling of fracture propagation in the presence of natural fracture (fracture arrest and/or deviation) | 67 |
| 3.2 Parametric study of hydraulic fracture propagation in presence of a natural fracture | 72 |
| 3.3 Analysis of the induced hydraulic fracture arrest by and/or breakout of natural | |

| | |
|--|------------|
| fracture. ----- | 77 |
| 3.4 Summary ----- | 81 |
| CHAPTER 4: CONCLUSION AND RECOMMENDATIONS | |
| 4.1 Summary of the completed work ----- | 110 |
| 4.2 Possible lines for future research ----- | 111 |
| NOMENCLATURE ----- | 112 |
| REFERENCES ----- | 114 |
| APPENDIX-2A: CHANGE IN BULK AND PORE VOLUME | |
| A.1 Total and bulk state variables ----- | 134 |
| A.2 Solid and bulk compressibility ----- | 135 |
| A.3 Total and effective stress ----- | 136 |
| A.4 Changes in bulk and pore volume ----- | 137 |
| APPENDIX-2B: DERIVATION OF PORO-ELASTIC GOVERNING EQUATIONS AND ANALYTICAL EQUATIONS | |
| 2.1 B Poroelastic Governing Equations ----- | 142 |
| 2.2 B Analytical equations to verify the numerical results for displacement, stress and pore pressure. ----- | 149 |
| 2.3 B Closed system of equations for KGD-C model. ----- | 151 |
| APPENDIX-2C: GENERAL IMPLEMENTATION OF FINITE ELEMENT METHOD (FEM) | |
| C.1 Model description ----- | 155 |
| C.2 Quarter model ----- | 155 |
| C.3 Four noded square element ----- | 156 |
| C.4 Eight noded square element ----- | 157 |
| C.5 General two dimensional transformation ----- | 158 |
| C.6 Four noded element transformation ----- | 159 |
| C.7 Eight noded element transformation ----- | 161 |

C.8 Half reservoir model and space discretization ----- 163

C.9 Super convergent patch recovery----- 165

APPENDIX-2D: IMPLEMENTATION OF FINITE ELEMENT METHOD (FEM) FOR GOVERNING EQUATIONS OF POROELASTICITY

D.1 Fully Coupled Poroelastic FEM Formulation----- 172

D.2 Rearrangement of element mass matrix to create a banded structure ---- 176

D.3 Rearrangement of element mass matrix for 4 and 8-noded pressure ----- 177

APPENDIX-2E: FLUID FLOW, ELASTIC AND POROELASTIC ANALYTICAL SOLUTIONS OF INTACT WELLBORE

E.1: Elastic deformation of a pressurized wellbore in a dry rock subjected to isotropic horizontal stress at finite outer boundary (Pressurized hollow cylinder)----- 181

E.2: Elastic deformation of a pressurized wellbore in an unstressed dry rock 182

E.3: Elastic deformation of an intact dry rock subjected to anisotropic in situ horizontal stress ----- 183

E.4: Elastic deformation of a pressurized wellbore in a dry rock subjected to isotropic in situ horizontal stress----- 184

E.5: Rearrangement Elastic deformation of a pressurized wellbore in a dry rock subjected to anisotropic in-situ horizontal stress (Kirsh's Problem)----- 185

E.6: Elastic deformation of a pressurized wellbore in a drained rock subjected to anisotropic in-situ horizontal stress (Kirsh's Problem)----- 186

E.7: Poroelastic behaviour of a pressurized wellbore (pw) in an unstressed rock containing fluid at zero pressure ----- 187

E.8: Poroelastic behaviour of a pressurized wellbore in an unstressed rock containing fluid at zero pressure ----- 189

E.9: Deformation of a wellbore with balanced pressure in a drained rock subjected to anisotropic horizontal stress ----- 190

E.10: Drained poroelastic response of a pressurized wellbore in a drained rock subjected to anisotropic horizontal stress ----- 191

List of Tables

| | |
|--|----|
| Table 2.1: Data used for verification of intact wellbore model. | 23 |
| Table 2.2: Parameter used for the study of hydraulic fracture propagation. | 23 |
| Table 2.3: Parameter used for the study of hydraulic fracture propagation model in poroelastic media. | 24 |
| Table 3.1: Parameter used for the study of fracture propagation and interaction..... | 83 |
| Table 3.2: Reservoir properties and wellbore data used for fracture interaction. | 83 |
| Table 3.3: Natural fracture data used for fracture interaction. | 84 |

List of Figures

| | |
|--|----|
| Fig. 2.1: Model geometry of pressurized Intact wellbore and reservoir. | 25 |
| Fig. 2.2: Pore pressure as a function of radius and time in poroelastic medium for $\sigma_H = 6000$ psi, $\sigma_h = 5000$ psi, $P_i = 4000$ psi, $P_w = 2000$ psi, $k_x = 1.0$ mD, $k_y = 1.0$ mD..... | 25 |
| Fig. 2.3(a): Pore pressure contour map after 1 min (Numerical results, $\sigma_H = 6000$ psi, $\sigma_h = 5000$ psi, $p_i = 4000$ psi, $p_w = 2000$ psi, $k_x = 1.0$ mD, $k_y = 1.0$ mD.) | 26 |
| Fig. 2.3(b): Pore pressure contour map after 1 min (Numerical results, $\sigma_H = 6000$ psi, $\sigma_h = 5000$ psi, $p_i = 4000$ psi, $p_w = 2000$ psi, $k_x = 1.0$ mD, $k_y = 1.0$ mD.) | 26 |
| Fig. 2.4(a): Pore pressure contour map after 1hr (Numerical results, $\sigma_H = 6000$ psi, $\sigma_h = 5000$ psi, $p_i = 4000$ psi, $p_w = 2000$ psi, $k_x = 1.0$ mD, $k_y = 1.0$ mD.) | 27 |
| Fig. 2.4(b): Pore pressure contour map after 1hr (Numerical results, $\sigma_H = 6000$ psi, $\sigma_h = 5000$ psi, $p_i = 4000$ psi, $p_w = 2000$ psi, $k_x = 1.0$ mD, $k_y = 1.0$ mD.) | 27 |
| Fig. 2.5(a): Pore pressure contour map after 1 day (Numerical results, $\sigma_H = 6000$ psi, $\sigma_h = 5000$ psi, $p_i = 4000$ psi, $P_w = 2000$ psi, $k_x = 1.0$ mD, $k_y = 1.0$ mD.) | 28 |
| Fig. 2.5(b): Pore pressure contour map after 1 day (Numerical results, $\sigma_H = 6000$ psi, $\sigma_h = 5000$ psi, $p_i = 4000$ psi, $p_w = 2000$ psi, $k_x = 1.0$ mD, $k_y = 1.0$ mD.) | 28 |
| Fig. 2.6(a): Pore pressure contour map after 1 month (Numerical results, $\sigma_H = 6000$ psi, $\sigma_h = 5000$ psi, $p_i = 4000$ psi, $p_w = 2000$ psi, $k_x = 1.0$ mD, $k_y = 1.0$ mD.) | 29 |

Fig. 2.6(b): Pore pressure contour map after 1 month (Numerical results, $\sigma_H = 6000$ psi, $\sigma_h = 5000$ psi, $p_i = 4000$ psi, $p_w = 2000$ psi, $k_x = 1.0$ mD, $k_y = 1.0$ mD.) 29

Fig. 2.7 (a): X-component of total stress (σ_x) as a function of time and radial position along X-axis for entire region (poroelastic reservoir, $\sigma_H = 6000$ psi, $\sigma_h = 5000$ psi, $p_i = 4000$ psi, $p_w = 2000$ psi, $k_x = 1.0$ mD, $k_y = 1.0$ mD.) 30

Fig. 2.7 (b): X-component of total stress (σ_x) as a function of time and radial position along X-axis for far field region (poroelastic reservoir, $\sigma_H = 6000$ psi, $\sigma_h = 5000$ psi, $p_i = 4000$ psi, $p_w = 2000$ psi, $k_x = 1.0$ mD, $k_y = 1.0$ mD.) 30

Fig.2.7 (c): X-component of total stress (σ_x) as a function of time and radial position along X-axis for near wellbore region (poroelastic reservoir, $\sigma_H = 6000$ psi, $\sigma_h = 5000$ psi, $p_i = 4000$ psi, $p_w = 2000$ psi, $k_x = 1.0$ mD, $k_y = 1.0$ mD.) 31

Fig. 2.8: Change in x-component of total stress ($\Delta\sigma_x$) as a function of time and radial position along X-axis (poroelastic reservoir, $\sigma_H = 6000$ psi, $\sigma_h = 5000$ psi, $p_i = 4000$ psi, $p_w = 2000$ psi, $k_x = 1.0$ mD, $k_y = 1.0$ mD.) 31

Fig. 2.9(a): X-component of effective stress (σ'_x) as a function of time and radial position along X-axis for entire region (poroelastic reservoir, $\sigma_H = 6000$ psi, $\sigma_h = 5000$ psi, $p_i = 4000$ psi, $p_w = 2000$ psi, $k_x = 1.0$ mD, $k_y = 1.0$ mD.) 32

Fig. 2.9(b): X-component of effective stress (σ'_x) as a function of time and radial position along X-axis for near wellbore region (poroelastic reservoir, $\sigma_H = 6000$ psi, $\sigma_h = 5000$ psi, $p_i = 4000$ psi, $p_w = 2000$ psi, $k_x = 1.0$ mD, $k_y = 1.0$ mD.) 32

Fig. 2.9(c): X-component of effective stress (σ'_x) as a function of time and radial position along X-axis for far field region (poroelastic reservoir, $\sigma_H = 6000$ psi, $\sigma_h = 5000$ psi, $p_i = 4000$ psi, $p_w = 2000$ psi, $k_x = 1.0$ mD, $k_y = 1.0$ mD.) 33

Fig. 2.10(a): X-component of total stress (σ_x) as a function of time and radial position along 45° for entire region (poroelastic reservoir, $\sigma_H = 6000$ psi, $\sigma_h = 5000$ psi, $p_i = 4000$ psi, $p_w = 2000$ psi, $k_x = 1.0$ mD, $k_y = 1.0$ mD.) 33

Fig. 2.10(b): X-component of total stress (σ_x) as a function of time and radial position along 45° for near wellbore region (poroelastic reservoir, $\sigma_H = 6000$ psi, $\sigma_h = 5000$ psi, $p_i = 4000$ psi, $p_w = 2000$ psi, $k_x = 1.0$ mD, $k_y = 1.0$ mD.) 34

Fig. 2.10(c): X-component of total stress (σ_x) as a function of time and radial position along

| | |
|---|----|
| 45° for far field region (poroelastic reservoir, $\sigma_H = 6000$ psi, $\sigma_h = 5000$ psi, $p_i = 4000$ psi, $p_w = 2000$ psi, $k_x = 1.0$ mD, $k_y = 1.0$ mD.) | 34 |
| Fig. 2.11: Change in x-component of total stress ($\Delta\sigma_x$) as a function of time and radial position along 45° (poroelastic reservoir, $\sigma_H = 6000$ psi, $\sigma_h = 5000$ psi, $p_i = 4000$ psi, $p_w = 2000$ psi, $k_x = 1.0$ mD, $k_y = 1.0$ mD.) | 35 |
| Fig. 2.12(a): X-component of effective stress (σ'_x) as a function of time and radial position along 45° for entire region (poroelastic reservoir, $\sigma_H = 6000$ psi, $\sigma_h = 5000$ psi, $p_i = 4000$ psi, $p_w = 2000$ psi, $k_x = 1.0$ mD, $k_y = 1.0$ mD.) | 35 |
| Fig. 2.12(b): X-component of effective stress (σ'_x) as a function of time and radial position along 45° for near wellbore region (poroelastic reservoir, $\sigma_H = 6000$ psi, $\sigma_h = 5000$ psi, $p_i = 4000$ psi, $p_w = 2000$ psi, $k_x = 1.0$ mD, $k_y = 1.0$ mD.) | 36 |
| Fig. 2.12(c): X-component of effective stress (σ'_x) as a function of time and radial position along 45° for far field region (poroelastic reservoir, $\sigma_H = 6000$ psi, $\sigma_h = 5000$ psi, $p_i = 4000$ psi, $p_w = 2000$ psi, $k_x = 1.0$ mD, $k_y = 1.0$ mD.) | 36 |
| Fig. 2.13(a): X-component of total stress (σ_x) as a function of time and radial position along y-axis (90°) for entire region (poroelastic reservoir, $\sigma_H = 6000$ psi, $\sigma_h = 5000$ psi, $p_i = 4000$ psi, $p_w = 2000$ psi, $k_x = 1.0$ mD, $k_y = 1.0$ mD.) | 37 |
| Fig. 2.13(b): X-component of total stress (σ_x) as a function of time and radial position along y-axis (90°) for near wellbore region (poroelastic reservoir, $\sigma_H = 6000$ psi, $\sigma_h = 5000$ psi, $p_i = 4000$ psi, $p_w = 2000$ psi, $k_x = 1.0$ mD, $k_y = 1.0$ mD.) | 37 |
| Fig. 2.13(c): X-component of total stress (σ_x) as a function of time and radial position along y-axis (90°) for far field region (poroelastic reservoir, $\sigma_H = 6000$ psi, $\sigma_h = 5000$ psi, $p_i = 4000$ psi, $p_w = 2000$ psi, $k_x = 1.0$ mD, $k_y = 1.0$ mD.) | 38 |
| Fig. 2.14: Change in x-component of total stress ($\Delta\sigma_x$) as a function of time and radial position along y-axis (poroelastic reservoir, $\sigma_H = 6000$ psi, $\sigma_h = 5000$ psi, $p_i = 4000$ psi, $p_w = 2000$ psi, $k_x = 1.0$ mD, $k_y = 1.0$ mD.) | 38 |
| Fig. 2.15(a): X-component of effective stress (σ'_x) as a function of time and radial position along y-axis (90°) for entire region (poroelastic reservoir, $\sigma_H = 6000$ psi, $\sigma_h = 5000$ psi, $p_i = 4000$ psi, $p_w = 2000$ psi, $k_x = 1.0$ mD, $k_y = 1.0$ mD.) | 39 |
| Fig. 2.15(b): X-component of effective stress (σ'_x) as a function of time and radial position | |

| | |
|--|----|
| along y-axis (90°) for near wellbore region (poroelastic reservoir, $\sigma_H = 6000$ psi, $\sigma_h = 5000$ psi, $p_i = 4000$ psi, $p_w = 2000$ psi, $k_x = 1.0$ mD, $k_y = 1.0$ mD.) | 39 |
| Fig. 2.15(c): X-component of effective stress (σ'_x) as a function of time and radial position along y-axis (90°) for far field region (poroelastic reservoir, $\sigma_H = 6000$ psi, $\sigma_h = 5000$ psi, $p_i = 4000$ psi, $p_w = 2000$ psi, $k_x = 1.0$ mD, $k_y = 1.0$ mD.) | 40 |
| Fig. 2.16(a): Y-component of total stress (σ_y) as a function of time and radial position along x-axis for entire region (poroelastic reservoir, $\sigma_H = 6000$ psi, $\sigma_h = 5000$ psi, $p_i = 4000$ psi, $p_w = 2000$ psi, $k_x = 1.0$ mD, $k_y = 1.0$ mD.) | 40 |
| Fig. 2.16(b): Y-component of total stress (σ_y) as a function of time and radial position along x-axis for near wellbore region (poroelastic reservoir, $\sigma_H = 6000$ psi, $\sigma_h = 5000$ psi, $p_i = 4000$ psi, $p_w = 2000$ psi, $k_x = 1.0$ mD, $k_y = 1.0$ mD.) | 41 |
| Fig. 2.16(c): Y-component of total stress (σ_y) as a function of time and radial position along x-axis for far field region (poroelastic reservoir, $\sigma_H = 6000$ psi, $\sigma_h = 5000$ psi, $p_i = 4000$ psi, $p_w = 2000$ psi, $k_x = 1.0$ mD, $k_y = 1.0$ mD.) | 41 |
| Fig. 2.17: Change in y-component of total stress ($\Delta\sigma_y$) as a function of time and radial position along y-axis (poroelastic reservoir, $\sigma_H = 6000$ psi, $\sigma_h = 5000$ psi, $p_i = 4000$ psi, $p_w = 2000$ psi, $k_x = 1.0$ mD, $k_y = 1.0$ mD.) | 42 |
| Fig. 2.18(a): Y-component of effective stress (σ'_y) as a function of time and radial position along X-axis for entire region (poroelastic reservoir, $\sigma_H = 6000$ psi, $\sigma_h = 5000$ psi, $p_i = 4000$ psi, $p_w = 2000$ psi, $k_x = 1.0$ mD, $k_y = 1.0$ mD.) | 42 |
| Fig. 2.18(b): Y-component of effective stress (σ'_y) as a function of time and radial position along X-axis for near wellbore region (poroelastic reservoir, $\sigma_H = 6000$ psi, $\sigma_h = 5000$ psi, $p_i = 4000$ psi, $p_w = 2000$ psi, $k_x = 1.0$ mD, $k_y = 1.0$ mD.) | 43 |
| Fig.2.18(c): Y-component of effective stress (σ'_y) as a function of time and radial position along X-axis for far field region (poroelastic reservoir, $\sigma_H = 6000$ psi, $\sigma_h = 5000$ psi, $p_i = 4000$ psi, $p_w = 2000$ psi, $k_x = 1.0$ mD, $k_y = 1.0$ mD.) | 43 |
| Fig. 2.19(a): Y-component of total stress (σ_y) as a function of time and radial position along 45° for entire region (poroelastic reservoir, $\sigma_H = 6000$ psi, $\sigma_h = 5000$ psi, $p_i = 4000$ psi, $p_w = 2000$ psi, $k_x = 1.0$ mD, $k_y = 1.0$ mD.) | 44 |
| Fig. 2.19(b): Y-component of total stress (σ_y) as a function of time and radial position along | |

| | |
|---|----|
| 45° for near wellbore region (poroelastic reservoir, $\sigma_H = 6000$ psi, $\sigma_h = 5000$ psi, $p_i = 4000$ psi, $p_w = 2000$ psi, $k_x = 1.0$ mD, $k_y = 1.0$ mD.) | 44 |
| Fig. 2.19(c): Y-component of total stress (σ_y) as a function of time and radial position along 45° for far field (poroelastic reservoir, $\sigma_H = 6000$ psi, $\sigma_h = 5000$ psi, $p_i = 4000$ psi, $p_w = 2000$ psi, $k_x = 1.0$ mD, $k_y = 1.0$ mD.) | 45 |
| Fig. 2.20: Change in y-component of total stress ($\Delta\sigma_y$) as a function of time and radial position along 45° (poroelastic reservoir, $\sigma_H = 6000$ psi, $\sigma_h = 5000$ psi, $P_i = 4000$ psi, $P_w = 2000$ psi, $k_x = 1.0$ mD, $k_y = 1.0$ mD.) | 45 |
| Fig. 2.21(a): Y-component of effective stress (σ'_y) as a function of time and radial position along 45° for entire region (poroelastic reservoir, $\sigma_H = 6000$ psi, $\sigma_h = 5000$ psi, $p_i = 4000$ psi, $p_w = 2000$ psi, $k_x = 1.0$ mD, $k_y = 1.0$ mD.) | 46 |
| Fig. 2.21(b): Y-component of effective stress (σ'_y) as a function of time and radial position along 45° for near wellbore region (poroelastic reservoir, $\sigma_H = 6000$ psi, $\sigma_h = 5000$ psi, $p_i = 4000$ psi, $p_w = 2000$ psi, $k_x = 1.0$ mD, $k_y = 1.0$ mD.) | 46 |
| Fig. 2.21(c): Y-component of effective stress (σ'_y) as a function of time and radial position along 45° for far field region (poroelastic reservoir, $\sigma_H = 6000$ psi, $\sigma_h = 5000$ psi, $p_i = 4000$ psi, $p_w = 2000$ psi, $k_x = 1.0$ mD, $k_y = 1.0$ mD.) | 47 |
| Fig. 2.22(a): Y-component of total stress (σ_y) as a function of time and radial position along y-axis (90°) for entire region (poroelastic reservoir, $\sigma_H = 6000$ psi, $\sigma_h = 5000$ psi, $p_i = 4000$ psi, $p_w = 2000$ psi, $k_x = 1.0$ mD, $k_y = 1.0$ mD.) | 47 |
| Fig. 2.22(b): Y-component of total stress (σ_y) as a function of time and radial position along y-axis (90°) for near wellbore region (poroelastic reservoir, $\sigma_H = 6000$ psi, $\sigma_h = 5000$ psi, $p_i = 4000$ psi, $p_w = 2000$ psi, $k_x = 1.0$ mD, $k_y = 1.0$ mD.) | 48 |
| Fig. 2.22(c): Y-component of total stress (σ_y) as a function of time and radial position along y-axis (90°) for far field region (poroelastic reservoir, $\sigma_H = 6000$ psi, $\sigma_h = 5000$ psi, $p_i = 4000$ psi, $p_w = 2000$ psi, $k_x = 1.0$ mD, $k_y = 1.0$ mD.) | 48 |
| Fig. 2.23: Change in y-component of total stress ($\Delta\sigma_y$) as a function of time and radial position along y-axis (poroelastic reservoir, $\sigma_H = 6000$ psi, $\sigma_h = 5000$ psi, $p_i = 4000$ psi, $p_w = 2000$ psi, $k_x = 1.0$ mD, $k_y = 1.0$ mD.) | 49 |
| Fig. 2.24(a): Y-component of effective stress (σ'_y) as a function of time and radial position | |

| | |
|--|----|
| along y-axis (90°) for entire region (poroelastic reservoir, $\sigma_H = 6000$ psi, $\sigma_h = 5000$ psi, $p_i = 4000$ psi, $p_w = 2000$ psi, $k_x = 1.0$ mD, $k_y = 1.0$ mD.) | 49 |
| Fig. 2.24(b): Y-component of effective stress (σ'_y) as a function of time and radial position along y-axis (90°) for near wellbore region (poroelastic reservoir, $\sigma_H = 6000$ psi, $\sigma_h = 5000$ psi, $p_i = 4000$ psi, $p_w = 2000$ psi, $k_x = 1.0$ mD, $k_y = 1.0$ mD.) | 50 |
| Fig. 2.24(c): Y-component of effective stress (σ'_y) as a function of time and radial position along y-axis (90°) for far field region (poroelastic reservoir, $\sigma_H = 6000$ psi, $\sigma_h = 5000$ psi, $p_i = 4000$ psi, $p_w = 2000$ psi, $k_x = 1.0$ mD, $k_y = 1.0$ mD.) | 50 |
| Fig. 2.25(a): Shear stress (σ_{xy}) as a function of time and radial position along 45° for entire region (poroelastic reservoir, $\sigma_H = 6000$ psi, $\sigma_h = 5000$ psi, $p_i = 4000$ psi, $p_w = 2000$ psi, $k_x = 1.0$ mD, $k_y = 1.0$ mD.) | 51 |
| Fig. 2.25(b): Shear stress (σ_{xy}) as a function of time and radial position along 45° for near wellbore region (poroelastic reservoir, $\sigma_H = 6000$ psi, $\sigma_h = 5000$ psi, $p_i = 4000$ psi, $p_w = 2000$ psi, $k_x = 1.0$ mD, $k_y = 1.0$ mD.) | 51 |
| Fig.2.25(c): Shear stress (σ_{xy}) as a function of time and radial position along 45° for far field region (poroelastic reservoir, $\sigma_H = 6000$ psi, $\sigma_h = 5000$ psi, $p_i = 4000$ psi, $p_w = 2000$ psi, $k_x = 1.0$ mD, $k_y = 1.0$ mD.) | 52 |
| Fig. 2.26: Change in shear stress (σ_{xy}) as a function of time and radial position along 45° (poroelastic reservoir, $\sigma_H = 6000$ psi, $\sigma_h = 5000$ psi, $p_i = 4000$ psi, $p_w = 2000$ psi, $k_x = 1.0$ mD, $k_y = 1.0$ mD.) | 52 |
| Fig. 2.27: Schematic illustration of three basic modes of fracture extension. | 53 |
| Fig. 2.28: Nodal arrangement of fracture tip element for calculation of critical width. | 53 |
| Fig. 2.29: Finite element mesh used for simulation. | 53 |
| Fig. 2.30: Algorithm of hydraulic fracture propagation model. | 54 |
| Fig. 2.31: Algorithm of fracture pressure profile calculation. | 55 |
| Fig. 2.32: Fracture profile for selected time steps (poroelastic reservoir, $\sigma_H=6000$ psi, $\sigma_h=5000$ psi, $p_i=4500$ psi, $\mu_f=1$ cp, $q=10$ bbl/min, $k=0.1$ mD, $K_{IC}=500$ psi.ft ^{0.5}) | 55 |
| Fig.2.33: Fracturing fluid pressure profile for selected time steps (poroelastic reservoir, $\sigma_H=6000$ psi, $\sigma_h=5000$ psi, $p_i=5000$ psi, $\mu_f=1$ cp, $q=10$ bbl/min, $k=0.1$ mD, $K_{IC}=500$ | |

| | |
|---|----|
| psi.ft ^{0.5}) | 56 |
| Fig. 2.34: Fracture half length vs., pumping time for the numerical poroelastic and elastic fracturing models as well as KGD-C model ($\sigma_H=6000$ psi, $\sigma_h=5000$ psi, $p_i=4500$ psi, $\mu_f=1$ cp, $q=10$ bbl/min, $K_{IC}=500$ psi.ft ^{0.5}) | 56 |
| Fig. 2.35: Fracture width vs. pumping time for the numerical poroelastic , elastic fracturing models and KGD-C model ($\sigma_H=6000$ psi, $\sigma_h=5000$ psi, $p_i=4500$ psi, $\mu_f=1$ cp, $q=10$ bbl/min, $K_{IC}=500$ psi.ft ^{0.5}) | 57 |
| Fig. 2.36: Fracture propagation pressure vs. pumping time for the numerical poroelastic, elastic fracturing models and KGD-C model ($\sigma_H=6000$ psi, $\sigma_h=5000$ psi, $p_i=4500$ psi, $\mu_f=1$ cp, $q=10$ bbl/min, $K_{IC}=500$ psi.ft ^{0.5}) | 57 |
| Fig. 2.37: Fracture half length vs. pumping time for two permeabilities of 0.1 mD and 5mD (poroelastic reservoir, $\sigma_H=6000$ psi, $\sigma_h=5000$ psi, $p_i=4500$ psi, $\mu_f=1$ cp, $q=10$ bbl/min, $K_{IC}=500$ psi.ft ^{0.5}) | 58 |
| Fig. 2.38: Fracture width vs. pumping time for two permeabilities of 0.1 mD and 5mD (poroelastic reservoir, $\sigma_H=6000$ psi, $\sigma_h=5000$ psi, $p_i=4500$ psi, $\mu_f=1$ cp, $q=10$ bbl/min, $K_{IC}=500$ psi.ft ^{0.5}) | 58 |
| Fig. 2.39: Fracture propagation pressure vs. pumping time for two permeabilities of 0.1 mD and 5mD (poroelastic reservoir, $\sigma_H=6000$ psi, $\sigma_h=5000$ psi, $p_i=4500$ psi, $\mu_f=1$ cp, $q=10$ bbl/min, $K_{IC}=500$ psi.ft ^{0.5}) | 59 |
| Fig. 2.40: Fracture propagation pressure vs. pumping time for two Biot's coefficient of 1.0 and 0.85 (poroelastic reservoir, $\sigma_H=6000$ psi, $\sigma_h=5000$ psi, $p_i=4500$ psi, $\mu_f=1$ cp, $q=10$ bbl/min, $K_{IC}=500$ psi.ft ^{0.5}) | 59 |
| Fig. 2.41: Fracture half length vs., pumping time for two pumping rate of 10 bbl/min and 20 bbl/min (poroelastic reservoir, $\sigma_H=6000$ psi, $\sigma_h=5000$ psi, $p_i=4500$ psi, $\mu_f=1$ cp, $k=0.1$ mD, $K_{IC}=500$ psi.ft ^{0.5}) | 60 |
| Fig. 2.42: Fracture width vs. pumping time for two pumping rate of 10 bbl/min and 20 bbl/min (poroelastic reservoir, $\sigma_H=6000$ psi, $\sigma_h=5000$ psi, $p_i=4500$ psi, $\mu_f=1$ cp, $k=0.1$ mD, $K_{IC}=500$ psi.ft ^{0.5}) | 60 |
| Fig. 2.43: Fracture propagation pressure vs. pumping time for two pumping rate of 10 bbl/min and 20 bbl/min (poroelastic reservoir, $\sigma_H=6000$ psi, $\sigma_h=5000$ psi, $p_i=4500$ psi, $\mu_f=1$ cp, $k=0.1$ mD, $K_{IC}=500$ psi.ft ^{0.5}) | 60 |

| | |
|--|----|
| psi, $\mu_f=1$ cp, $k=0.1$ mD, $K_{IC}=500$ psi.ft ^{0.5}) | 61 |
| Fig. 2.44: Fracture half length vs. pumping time for two fracture toughness of 500 psi.ft ^{0.5} and 1000 psi.ft ^{0.5} (poroelastic reservoir, $\sigma_H=6000$ psi, $\sigma_h=5000$ psi, $p_i=4500$ psi, $\mu_f=1$ cp, $k=0.1$ mD, $q=10$ bbl/min) | 61 |
| Fig. 2.45: Fracture width vs. pumping time for two fracture toughness of 500 psi.ft ^{0.5} and 1000 psi.ft ^{0.5} (poroelastic reservoir, $\sigma_H=6000$ psi, $\sigma_h=5000$ psi, $p_i=4500$ psi, $\mu_f=1$ cp, $k=0.1$ mD, $q=10$ bbl/min) | 62 |
| Fig. 2.46: Fracture propagation pressure vs. pumping time for two fracture toughness of 500 psi.ft ^{0.5} and 1000 psi.ft ^{0.5} (poroelastic reservoir, $\sigma_H=6000$ psi, $\sigma_h=5000$ psi, $p_i=4500$ psi, $\mu_f=1$ cp, $k=0.1$ mD, $q=10$ bbl/min) | 62 |
| Fig. 2.47: Fracture half length vs. pumping time for two fracturing fluid viscosities of 1cP and 100 cP (poroelastic reservoir, $\sigma_H=6000$ psi, $\sigma_h=5000$ psi, $p_i=4500$ psi, $\mu_f=1$ cp, $k=0.1$ mD, $q=10$ bbl/min, fracture toughness of 500 psi.ft ^{0.5}) | 63 |
| Fig. 2.48: Fracture width vs. pumping time for two fracturing fluid viscosities of 1cP and 100 cP (poroelastic reservoir, $\sigma_H=6000$ psi, $\sigma_h=5000$ psi, $p_i=4500$ psi, $\mu_f=1$ cp, $k=0.1$ mD, $q=10$ bbl/min, fracture toughness of 500 psi.ft ^{0.5}) | 63 |
| Fig. 2.49: Fracture propagation pressure vs. pumping time for two fracturing fluid viscosities of 1cP and 100 cP (poroelastic reservoir, $\sigma_H=6000$ psi, $\sigma_h=5000$ psi, $p_i=4500$ psi, $\mu_f=1$ cp, $k=0.1$ mD, $q=10$ bbl/min, fracture toughness of 500 psi.ft ^{0.5}) | 64 |
| | |
| Fig. 3.1: Schematic of Lammont and Jessen's model with existing fracture showing directions of loading (from Lammont and Jessen, 1943) | 85 |
| Fig. 3.2: Austin stone model with hairline fracture, angle of inclination 0°, angle of bearing 45° (from Lammont and Jessen, after Potluri, 2004) | 85 |
| Fig. 3.3: Austin stone model with 2-IN width fracture, angle of inclination 0°, angle of bearing 90° (from Lammont and Jessen, after Potluri, 2004) | 86 |
| Fig. 3.4: Austin stone model with 1/2-IN width fracture, angle of inclination 0°, angle of bearing 90° (from Lammont and Jessen, after Potluri, 2004) | 86 |
| Fig. 3.5: Schematic of Induced hydraulic fracture intersecting a pre-existing natural fracture. | 87 |

| | |
|--|----|
| Fig. 3.6: Quarter point singular element | 87 |
| Fig. 3.7: Nodal arrangement for computation of stress intensity factor using displacement correlation method. | 88 |
| Fig. 3.8(a): Schematic of finite element 2D mesh of the induced fracture, natural fracture and the reservoir system. (A total number of nodes=47123 and total number of elements=19444 are used for this study.) | 88 |
| Fig. 3.8 (b): Finite element 2D mesh of the induced fracture, natural fracture and the reservoir system showing near natural fracture region. (A total number of nodes=47123 and total number of elements=19444 are used for this study.) | 89 |
| Fig .3.9: Schematic of natural fracture showing different angular positions at the surface. .. | 89 |
| Fig .3.10: Fracture propagation/ extension algorithm using mixed mode fracture criteria. ... | 90 |
| Fig .3.11: Calculation of mixed mode fracture criteria. | 91 |
| Fig. 3.12: Identification of crack orientation. | 91 |
| Fig. 3.13: Fracture half length and propagation pressure vs. pumping time, natural fracture length 10 m, width 0.5 mm, angle of approach 90° and natural fracture position from well bore is 20 m, differential stress 1000 psi (poroelastic reservoir, $\sigma_H = 6000$ psi, $\sigma_h = 5000$ psi, $p_i = 4500$ psi, $\mu_f = 1$ cp, $k = 0.1$ mD, $q = 20$ bbl/min, fracture toughness = 500 psi.ft ^{0.5}) | 92 |
| Fig. 3.14: Fracture width and propagation pressure vs. pumping time, natural fracture length 10 m, width 0.5 mm, angle of approach 90°, natural fracture position from well bore is 20 m and differential stress 1000 psi (poroelastic reservoir, $\sigma_H = 6000$ psi, $\sigma_h = 5000$ psi, $p_i = 4500$ psi, $\mu_f = 1$ cp, $k = 0.1$ mD, $q = 20$ bbl/min, fracture toughness = 500 psi.ft ^{0.5}) | 92 |
| Fig. 3.15: Fracturing fluid pressure profile for selected time steps, natural fracture length 10 m, width 0.5 mm, angle of approach 90°, natural fracture position from well bore is 20 m and differential stress 1000 psi (poroelastic reservoir, $\sigma_H = 6000$ psi, $\sigma_h = 5000$ psi, $p_i = 4500$ psi, $\mu_f = 1$ cp, $k = 0.1$ mD, $q = 20$ bbl/min, fracture toughness = 500 psi.ft ^{0.5}) . | 93 |
| Fig. 3.16: Effective tangential stresses vs. angular position at the surfaces of the natural fracture for selected time steps, natural fracture length 10 m, width 0.5 mm, angle of approach 90°, natural fracture position from well bore is 20 m and differential stress | |

1000 psi (poroelastic reservoir, $\sigma_H = 6000$ psi, $\sigma_h = 5000$ psi, $p_i = 4500$ psi, $\mu_f = 1$ cp, $k = 0.1$ mD, $q = 20$ bbl/min, fracture toughness = 500 psi.ft^{0.5}) 93

Fig. 3.17: Fracture half length and propagation pressure vs. pumping time, natural fracture length 10 m, width 0.5 mm, angle of approach 60°, natural fracture position from well bore is 20 m and differential stress 1000 psi (poroelastic reservoir, $\sigma_H = 6000$ psi, $\sigma_h = 5000$ psi, $p_i = 4500$ psi, $\mu_f = 1$ cp, $k = 0.1$ mD, $q = 20$ bbl/min, fracture toughness = 500 psi.ft^{0.5}) 94

Fig. 3.18: Fracture width and propagation pressure vs. pumping time, natural fracture length 10 m, width 0.5 mm, angle of approach 60°, natural fracture position from well bore is 20 m and differential stress 1000 psi (poroelastic reservoir, $\sigma_H = 6000$ psi, $\sigma_h = 5000$ psi, $p_i = 4500$ psi, $\mu_f = 1$ cp, $k = 0.1$ mD, $q = 20$ bbl/min, fracture toughness = 500 psi.ft^{0.5}) 94

Fig. 3.19: Fracturing fluid pressure profile for selected time steps, natural fracture length 10 m, width 0.5 mm, angle of approach 60°, natural fracture position from well bore is 20 m and differential stress 1000 psi (poroelastic reservoir, $\sigma_H = 6000$ psi, $\sigma_h = 5000$ psi, $p_i = 4500$ psi, $\mu_f = 1$ cp, $k = 0.1$ mD, $q = 20$ bbl/min, fracture toughness = 500 psi.ft^{0.5}) . 95

Fig. 3.20: Effective tangential stresses vs. angular position at the surfaces of the natural fracture for selected time steps, natural fracture length 10 m, width 0.5 mm, angle of approach 60°, natural fracture position from well bore is 20 m and differential stress 1000 psi (poroelastic reservoir, $\sigma_H = 6000$ psi, $\sigma_h = 5000$ psi, $p_i = 4500$ psi, $\mu_f = 1$ cp, $k = 0.1$ mD, $q = 20$ bbl/min, fracture toughness = 500 psi.ft^{0.5}) 95

Fig. 3.21: Fracture half length and propagation pressure vs. pumping time, natural fracture length 10 m, width 0.5 mm, angle of approach 30° and natural fracture position from well bore is 20 m, differential stress 1000 psi (poroelastic reservoir, $\sigma_H = 6000$ psi, $\sigma_h = 5000$ psi, $p_i = 4500$ psi, $\mu_f = 1$ cp, $k = 0.1$ mD, $q = 20$ bbl/min, fracture toughness = 500 psi.ft^{0.5}) 96

Fig. 3.22: Fracture width and propagation pressure vs. pumping time, natural fracture length 10 m, width 0.5 mm, angle of approach 30°, natural fracture position from well bore is 20 m and differential stress 1000 psi (poroelastic reservoir, $\sigma_H = 6000$ psi, $\sigma_h = 5000$ psi, $p_i = 4500$ psi, $\mu_f = 1$ cp, $k = 0.1$ mD, $q = 20$ bbl/min, fracture toughness = 500 psi.ft^{0.5}) 96

- Fig. 3.23: Fracture half length vs. pumping time, natural fracture length 10 m, width 0.5 mm, angle of approach 60° and natural fracture position from well bore is 20 m (poroelastic reservoir, $\sigma_H = 6000$ psi, $\sigma_h = 5500$ psi, $p_i = 4500$ psi, $\mu_f = 1$ cp, $k = 0.1$ mD, $q = 20$ bbl/min, fracture toughness = $500 \text{ psi.ft}^{0.5}$) 97
- Fig. 3.24: Fracture width vs. pumping time, natural fracture length 10 m, width 0.5 mm, angle of approach 60° and natural fracture position from well bore is 20 m (poroelastic reservoir, $\sigma_H = 6000$ psi, $\sigma_h = 5500$ psi, $p_i = 4500$ psi, $\mu_f = 1$ cp, $k = 0.1$ mD, $q = 20$ bbl/min, fracture toughness = $500 \text{ psi.ft}^{0.6}$) 97
- Fig. 3.25: Fracturing fluid pressure profile for two differential stress of 500.0 psi and 1000.0 psi, natural fracture length 10 m, width 0.5 mm, angle of approach 60° and natural fracture position from well bore is 20 m (poroelastic reservoir, $\sigma_H = 6000$ psi, $\sigma_h = 5500 \sim 6000$ psi, $p_i = 4500$ psi, $\mu_f = 1$ cp, $k = 0.1$ mD, $q = 20$ bbl/min, fracture toughness = $500 \text{ psi.ft}^{0.5}$) 98
- Fig. 3.26: Fracture half length and propagation pressure vs. pumping time, natural fracture length 10 m, width 0.5 mm, angle of approach 30° and natural fracture position from well bore is 20 m, differential stress 500 psi (poroelastic reservoir, $\sigma_H = 6000$ psi, $\sigma_h = 5500$ psi, $p_i = 4500$ psi, $\mu_f = 1$ cp, $k = 0.1$ mD, $q = 20$ bbl/min, fracture toughness = $500 \text{ psi.ft}^{0.5}$) 98
- Fig. 3.27: Fracture width and propagation pressure vs. pumping time, natural fracture length 10 m, width 0.5 mm, angle of approach 30° , natural fracture position from well bore is 20 m and differential stress 500 psi (poroelastic reservoir, $\sigma_H = 6000$ psi, $\sigma_h = 5500$ psi, $p_i = 4500$ psi, $\mu_f = 1$ cp, $k = 0.1$ mD, $q = 20$ bbl/min, fracture toughness = $500 \text{ psi.ft}^{0.5}$) 99
- Fig. 3.28: Fracture half length and propagation pressure vs. pumping time, natural fracture length 20 m, width 0.5 mm, angle of approach 90° , natural fracture position from well bore is 20 m and differential stress 1000 psi (poroelastic reservoir, $\sigma_H = 6000$ psi, $\sigma_h = 5500$ psi, $p_i = 4500$ psi, $\mu_f = 1$ cp, $k = 0.1$ mD, $q = 20$ bbl/min, fracture toughness = $500 \text{ psi.ft}^{0.5}$) 99
- Fig. 3.29: Fracture width and propagation pressure vs. pumping time, natural fracture length 20 m, width 0.5 mm, angle of approach 90° , natural fracture position from well bore is 20 m and differential stress 1000 psi (poroelastic reservoir, $\sigma_H = 6000$ psi, $\sigma_h = 5500$

psi, $p_i = 4500$ psi, $\mu_f = 1$ cp, $k = 0.1$ mD, $q = 20$ bbl/min, fracture toughness of 500 psi.ft^{0.5}) 100

Fig. 3.30: Stress intensity factor at the fracture tip during pressurization after the induced fracture induced fracture propagation stops by the natural fracture for two differential stresses. Natural fracture length 20 m, width 0.5 mm, angle of approach 90°, natural fracture position from well bore is 20 m and differential stress 1000 psi (poroelastic reservoir, $\sigma_H = 6000$ psi, $\sigma_h = 5000\sim 5500$ psi, $p_i = 4500$ psi, $\mu_f = 1$ cp, $k = 0.1$ mD, $q = 20$ bbl/min, fracture toughness = 500 psi.ft^{0.5}) 100

Fig. 3.31: Effective tangential stresses vs. angular position at the surfaces of the natural fracture after the induced fracture propagation stops by the natural fracture, natural fracture length 20 m, width 0.5 mm, angle of approach 90°, natural fracture position from well bore is 20 m and differential stress 1000 psi (poroelastic reservoir, $\sigma_H = 6000$ psi, $\sigma_h = 5000$ psi, $p_i = 4500$ psi, $\mu_f = 1$ cp, $k = 0.1$ mD, $q = 20$ bbl/min, fracture toughness = 500 psi.ft^{0.5}) 101

Fig. 3.32: Propagating hydraulic fracture half length vs. nodal displacement along y axis of the induced fracture, angle of approach= 60°, natural fracture position from wellbore 20 m, length of natural fracture 20 m, width of natural fracture 0.5 mm, differential stress = 500 psi. (poroelastic reservoir, $\sigma_H = 6000$ psi, $\sigma_h = 5500$ psi, $p_i = 4500$ psi, $\mu_f = 1$ cp, $k = 0.1$ mD, $q = 20$ bbl/min, fracture toughness = 500 psi.ft^{0.5}). 101

Fig. 3.33: Propagating hydraulic fracture half length vs. nodal displacement along y axis of the induced fracture, angle of approach= 60°, natural fracture position from wellbore 20 m, length of natural fracture 20 m, width of natural fracture 0.5 mm, differential stress = 500 psi and 1000psi. (poroelastic reservoir, $\sigma_H = 6000$ psi, $\sigma_h = 5500\sim 5000$ psi, $p_i = 4500$ psi, $\mu_f = 1$ cp, $k = 0.1$ mD, $q = 20$ bbl/min, fracture toughness = 500 psi.ft^{0.5}). . 102

Fig. 3.34: Fracture half length and propagation pressure vs. pumping time, natural fracture length 20 m, width 0.5 mm, angle of approach 60°, natural fracture position from well bore is 20 m and differential stress 500 psi (poroelastic reservoir, $\sigma_H = 6000$ psi, $\sigma_h = 5500$ psi, $p_i = 4500$ psi, $\mu_f = 1$ cp, $k = 0.1$ mD, $q = 20$ bbl/min, fracture toughness = 500 psi.ft^{0.5}) 102

Fig. 3.35: Fracture half length and propagation pressure vs. pumping time, natural fracture length 20 m, width 0.5 mm, angle of approach 90°, natural fracture position from well

| | |
|---|-----|
| bore is 20 m and differential stress 1000 psi (poroelastic reservoir, $\sigma_H = 6000$ psi, $\sigma_h = 5000$ psi, $p_i = 4500$ psi, $\mu_f = 1$ cp, $k = 0.1$ mD, $q = 35$ bbl/min, fracture toughness = 500 psi.ft ^{0.5}) | 103 |
| Fig. 3.36 Fracture width and propagation pressure vs. pumping time, natural fracture length 20 m, width 0.5 mm, angle of approach 90°, natural fracture position from well bore is 20 m and differential stress 1000 psi (poroelastic reservoir, $\sigma_H = 6000$ psi, $\sigma_h = 5000$ psi, $p_i = 4500$ psi, $\mu_f = 1$ cp, $k = 0.1$ mD, $q = 35$ bbl/min, fracture toughness = 500 psi.ft ^{0.5}) | 103 |
| Fig. 3.37: Effective tangential stresses vs. angular position at the surfaces of the natural fracture after the induced fracture propagation stops by the natural fracture, natural fracture length 20 m, width 0.5 mm, angle of approach 90°, natural fracture position from well bore is 20 m and differential stress 1000 psi (poroelastic reservoir, $\sigma_H = 6000$ psi, $\sigma_h = 5000$ psi, $p_i = 4500$ psi, $\mu_f = 1$ cp, $k = 0.1$ mD, $q = 35$ bbl/min, fracture toughness = 500 psi.ft ^{0.5}) | 104 |
| Fig. 3.38: Schematic of initial condition of induced hydraulic and natural fracture intersection showing the angular positions at the natural fracture surface. | 104 |
| Fig. 3.39(a): Schematic of finite element mesh of the induced fracture, natural fracture and the reservoir system. | 105 |
| Fig. 3.39(b): Finite element 2D mesh of the induced fracture, natural fracture and the reservoir system showing a thin element near natural fracture region (angle of approach 90°). | 105 |
| Fig .3.40: Algorithm of the induced fracture arrest and/or breakout (BHP=bottom hole pressure, σ_t is the tangential stress around natural fracture and T_0 is the tensile strength of the natural fracture rock) | 106 |
| Fig. 3.41: Effective tangential stress vs. angular position at the surfaces of the natural fracture. Natural fracture length = 10 m, angle of approach = 90°, differential stress = 1000 psi, injection rate 20 bbl/min. | 107 |
| Fig. 3.42: Effective tangential stress vs. angular position at the surfaces of the natural fracture. Natural fracture length = 10 m, angle of approach = 60°, differential stress = 1000 psi, injection rate 20 bbl/min. | 107 |
| Fig. 3.43: Effective tangential stress vs. angular position at the surfaces of the natural | |

| | |
|---|-----|
| fracture. Natural fracture length = 10 m, angle of approach = 30° , differential stress = 1000 psi, injection rate 20 bbl/min. | 108 |
| Fig. 3.44: Effective tangential stress vs. angular position at the surfaces of the natural fracture. Natural fracture length = 10 m, angle of approach = 60° , differential stress = 500 psi, injection rate 20 bbl/min. | 108 |
| Fig. 3.45: Effective tangential stress vs. angular position at the surfaces of the natural fracture. Natural fracture length = 20 m, angle of approach = 90° , differential stress = 1000 psi, injection rate 20 bbl/min. | 109 |
| Fig. 3.46: Effective tangential stress vs. angular position at the surfaces of the natural fracture. Natural fracture length = 20 m, angle of approach = 90° , differential stress = 1000 psi, injection rate 35 bbl/min. | 109 |
| | |
| Fig. A.1: Superposition to show the effect of fluid stress on bulk. | 139 |
| Fig. A.2: Superposition of stress and fluid pressure acting on bulk. | 139 |
| | |
| Fig. B.1: Decomposition of total problem. | 151 |
| Fig. B0.2: Schematic representation of classical KGD model. | 152 |
| | |
| Fig. C.1 Intact wellbore reservoir model. | 165 |
| Fig. C.2 Quarter reservoir model. | 165 |
| Fig. C.3 Schematic of the mesh of the Quarter model. | 166 |
| Fig. C.4 (a) Exact mesh of the Quarter model, wellbore radius is 0.1 m, outer boundary radius 1500 m, first element showing in coloured. | 166 |
| Fig. C.4 (b) Exact mesh of the Quarter model zoom in from 0 meter to 0.3 meter. Last number of element showing in coloured. | 167 |
| Fig. C.5 Four noded square element with local coordinates. | 167 |
| Fig. C.6 Eight noded square element with local coordinates. | 168 |
| Fig. C.7 Three noded triangular element with local coordinates. | 168 |

| | |
|---|-----|
| Fig. C.8 Schematic of a patch for eight noded square elements. | 169 |
| Fig. E.1: Schematic of the pressurized wellbore in a dry rock with isotropic horizontal stress and finite outer boundary. | 191 |
| Fig. E.2: Schematic of the pressurized wellbore in an unstressed dry rock. | 191 |
| Fig. E.3: Schematic of the intact dry rock with anisotropic in situ horizontal stress. | 192 |
| Fig. E.4: Schematic of the pressurized wellbore in a dry rock with isotropic in situ horizontal stress. | 192 |
| Fig. E.5: Schematic of the pressurized wellbore in a dry rock with anisotropic in situ horizontal stress. | 193 |
| Fig. E.6: Schematic of the pressurized wellbore in a drained rock with anisotropic in situ horizontal stress. | 193 |
| Fig. E.7: Schematic of the pressurized wellbore in an unstressed rock at zero pressure. | 194 |
| Fig. E.8: Schematic of the pressurized wellbore in an unstressed rock with zero fluid pressure. | 194 |
| Fig. E.9: Schematic of the wellbore with balanced pressure in a drained rock with anisotropic horizontal stress. | 195 |
| Fig. E.10: Schematic of the pressurized wellbore in a drained rock with anisotropic horizontal stress. | 195 |

Chapter 1: Introduction

1.1 Background Knowledge:

The main objective of this thesis is to investigate the fracture propagation pathway of an induced hydraulic fracture in the presence of a pre-existing natural fracture in a poroelastic medium. Several field and lab experimental studies have shown that a hydraulically induced fracture can propagate in a naturally fractured reservoir in different modes. It can intersect and cross a natural fracture, turn into a natural fracture (fracture arrest) or turn into the natural fracture for a short distance and breaks out again to propagate in direction dictated by perturbed local stress state (Blanton, 1982; Lammont and Jessen, 1963; Potluri et al., 2005). These possibilities are dependent on the magnitude of stress differential and the angle at which the induced fracture approaches the natural fracture (Daneshy, 1974; Warpinski and Teufel, 1987). One of these possibilities is shear dilation of natural fractures which can enhance reservoir permeability (Chen et al., 1995).

Analytical solutions are developed for predicting the direction of a propagating fracture in naturally fractured reservoirs. Most notable of which is Blanton's criterion (Blanton, 1986) which is primarily based on angle of approach of an induced fracture towards the natural fracture and differential stress field. Under this criterion low angle of approach associated with low to intermediate differential stress tends to open the natural fracture and divert fracturing fluid and/or arrest the propagation of the hydraulic fracture, whereas under high differential stress and high angle of approach hydraulic fracture most likely crosses the natural fracture. Warpinski and Teufel (1987) presented criteria for shear slippage (based on Mohr- Coulomb failure criterion) and shear dilation (based on the relationship between fracture pressure and normal stress) of the natural fracture. If the hydraulic fracture has already crossed the natural fracture, shear slippage or dilation of the natural fracture are affected by perturbed stress state of the region around the fracture. Warpinski and Teufel (1987) also presented a simplified analytical approximation of stress field around a natural fracture by taking into account for the effect of fluid leak-off mainly through the natural fracture.

Numerous studies are also carried out on the interaction of hydraulic fracture and layered formations. Renshaw and Pollard (1995) introduced a criterion for fracture propagation across unbounded frictional interfaces in linear elastic media. Studies based on

the elastic theory have shown that a fracture initiated in a stiff layer of two perfectly bounded interfaces is able to advance towards and enter into the softer layer under favorable stress conditions. In an opposite situation, a fracture that has grown in a softer rock cannot propagate into stiff rocks (Bear, 1991; Erdogan and Biricikoglu, 1973; Helgeson and Aydin, 1991). Recently, Zhang et al. (2006a) presented a numerical simulation of hydraulic fracture propagation at the bedding interfaces using a two-dimensional boundary element model.

As far as numerical studies are concerned, only a few works have been carried out on the interaction between hydraulically induced fracture and natural fractures. Heuze (1990) used FEFFLAP model (Finite Element Fracture and Flow Analysis Program) to investigate fluid-driven crack in jointed rock. Dong and de Pater (2001) applied a displacement discontinuity method to study the effect of a fault on hydraulic fracture reorientation. Zhang and Jeffrey (2006b) also applied a displacement discontinuity method to study the role of friction and secondary flaws on deflection and re-initiation of hydraulic fractures at orthogonal pre-existing fractures. Koshelev (2003) developed a numerical elastic model to study crack propagation near natural discontinuities such as joints and faults based on complex variable boundary element method. Potluri (2005) developed a numerical elastic model to predict the dynamic fracture dimension in the presence of natural fracture based on the PKN model. Akulich et al. (2008) developed a numerical elastic model to investigate the interaction of a hydraulic fracture with fault. They suggested that the fault slows down the propagation of a hydraulic fracture. An increase in differential stresses and the angle of inclination of the fault leads to a decreased likelihood of fault activation and decrease in the relative normal and tangential displacements of the fault faces. Modeling of interaction between induced fracture and fault did not include fracture intersections; however, it gives an idea about the slippage along the fault and how it affects the stress intensity factors at the tip of the growing hydraulic fractures. Lecampion (Lecampion, 2008) attempted to use the Extended Finite Element Methods (XFEM) to solve this problem. He sought the elasticity solution via XFEM for a given fracture geometry with either specified pressure distribution or opening profile.

1.2 Aims and significance:

In all the aforementioned works interaction (diversion, arrest and/or crossing) of an approaching induced fracture with an arbitrarily oriented natural fracture in a poroelastic medium has not been addressed. In this study the influence of angle of approach, differential

stress and natural fracture properties on the interaction between pre-existing natural fractures and an induced hydraulic fracture in a poroelastic environment is studied. First a numerical model that is capable of dealing with fracture propagation near natural fracture in poroelastic environment is developed and then a number of case studies are presented. Due to the computational complexity of three dimensional analysis of fractures, all the analyses will be limited to the two dimensional geometries. A finite element mesh generator is developed using FORTRAN 90 in part of this thesis to accurately implement the natural fracture into the model and the zone of interaction.

Large volumes of natural gas are stored in low-permeable fractured reservoirs around the world. Tight gas reservoirs, which form a significant part of low permeable fractured rocks, include coal bed methane, shale gas and natural gas hydrates. Although hydraulic fracturing has been used for decades to enhance productivity of tight gas reservoirs, a thorough understanding of the interaction between induced hydraulic and natural fractures is still lacking. The interaction of pre-existing natural fractures and an advancing hydraulic fracture can lead to complex fracture geometry. Performing hydraulic fracture design calculations under these complex conditions requires understanding of fracture intersections and tracking of fluid fronts (fracture tip of induced hydraulic fracture). The findings in this modeling work can be used to explain different observed behaviors of hydraulic fracturing in tight gas reservoirs and in geothermal reservoir. It can be used to predict the possible reactivations of natural fracture and the possible fracture extension pathway of the induced fracture in those reservoirs. Generally, this model can be used to predict the fracture propagation pathway and optimization of hydraulic fracture treatments in naturally fractured reservoirs including tight gas reservoirs and enhanced geothermal systems. The fully coupled poroelastic model and the understandings derived from this model, have beneficial applications in the design and optimization of hydraulic fracture treatments in naturally fractured reservoirs including tight gas reservoirs and enhanced geothermal systems. The model can also be used in the design of hydraulic stimulation of naturally fractured reservoirs based on shear dilation (high pressure low injection rate).

1.3 Structure of the thesis:

This thesis is divided in four chapters including the **Chapter-1**, introduction. **Chapter-2** is divided into two sections. In section one the brief introduction of development of theory of poroelasticity, governing equations of linear elasticity and diffusivity are presented. The

coupling of these two phenomenon using Biot's theory. A model based for intact wellbore is built. For validation of the model developed, derivation of analytical solutions is discussed. Finite element method is used to solve the poroelastic equations. The results produced are illustrated at the end of the chapter and supporting discussion is also provided. In section two detailed review of existing current fracturing models and different modes and criteria for fracture are outlined. The effects of poroelasticity and fracture treatment parameters such as formation permeability, rock strength, and fluid viscosity on the hydraulic fracture propagation are analysed. The results produced are illustrated at the end of the chapter and supporting discussion is also provided.

In **Chapter-3**, a fracture propagation model is presented to simulate the induced hydraulic fracture propagation in presence of a natural fracture in poroelastic environment. A two dimensional model is presented to study the effect of natural fracture on hydraulic fracture propagation. Also a model for analysing the induced fracture arrest by and/or breakout of natural fracture is presented. Results produced are illustrated at the end of the chapter and supporting discussion is also provided.

In **Chapter-4** conclusions are made, major findings observed through the study are presents and recommendations for future work are outlined.

Chapter 2: Modelling of Fracture Propagation in Poroelastic Formation

The purpose of this chapter is to develop a fully coupled numerical model to simulate fracture propagation in a poroelastic medium. For this purpose an intact wellbore model is first developed and validated. Then a fracture is brought in to study its propagation.

2.1 Intact Wellbore Modelling

Poroelastic modeling involves two processes: deformation of the rock due to change in pore pressure, and change of pore pressure due to deformation of the rock in undrained condition. These two processes are coupled and hence impart an obvious time dependent character to the mechanical properties of the rock.

The reciprocal impact of the processes of diffusion and deformation is first developed by Terzaghi in 1923 who proposed a model for one dimensional consolidation. This theory is generalized to three dimensions by Rendulic in 1936. Biot developed the theory of linear poroelasticity in 1935, 1941 and extended in 1956. This theory is then further extended by Verruijt (1969) in the context of soil mechanics. Rice and Cleary (1976) related the parameters of rocks and soils to poroelasticity. In petroleum engineering, poroelastic theory is first applied to study subsidence by Geerstma (1966) and hydraulic fracturing by Haimson and Fairhurst (1969).

According to Longuemare et al. (2002), governing equations of the poroelasticity include two components: fluid flow and rock deformation. These can be solved by using partially coupled method or fully coupled method. In partially coupled approach, two separate simulators (reservoir simulator and geomechanics simulator) are used for each part of the problem. A conventional reservoir simulator is first employed to calculate pore pressure for a certain time step, and this result (pore pressure) is then brought into a geomechanics simulator that produces stress distribution. The procedure is then repeated for different time steps to generate results of displacement and pore pressure. Since there is no iteration involved in this method, it is named “one way coupling approach”. In one way coupling, the effect of geomechanics on fluid flow is not taken into account. The outputs of two simulators are exchanged at each time step in an explicit or iterative manner (Fung et al., 1992; Koutsabeloulis and Hope, 1998; Settari and Walters, 1999; Tortike and Farouq Ali,

1993). In a fully coupled method the governing equations are simultaneously solved by one simulator. This approach gives more accurate and consistent results. Therefore, less computational time is required in compare to iteratively one way coupling approach.

Poroelastic governing equations

In conventional reservoir simulators the diffusivity equation is used as the governing equation of pressure (Aghighi 2007). The coupled fluid flow equations used in the model are as follows:

$$\phi c_t \frac{\partial p}{\partial t} - \alpha \frac{\partial(\nabla \cdot \vec{u})}{\partial t} = \nabla \cdot \left(\frac{\vec{k}}{\mu} \nabla p \right) + c_f \nabla p \cdot \left(\frac{\vec{k}}{\mu} \nabla p \right) \quad (2.1)$$

$$\phi c_t \frac{\partial p}{\partial t} - \alpha \frac{\partial(\nabla \cdot \vec{u})}{\partial t} = \nabla \cdot \left(\frac{\vec{k}}{\mu} \nabla p \right) \quad (2.2)$$

Where ϕ = porosity, c_t =total compressibility, α =Biot coefficient k =permeability tensor, μ = fluid viscosity, c_f = the fluid compressibility and p =fluid pressure (See **Nomenclature**).

The governing equations for displacement which contain the fluid pressure as a coupling variable are as follows:

$$G \nabla^2 u_x + (\lambda + G) \frac{\nabla \cdot u_x}{\partial x} - \alpha \frac{\partial p}{\partial x} = 0 \quad (2.3)$$

$$G \nabla^2 u_y + (\lambda + G) \frac{\nabla \cdot u_y}{\partial y} - \alpha \frac{\partial p}{\partial y} = 0 \quad (2.4)$$

$$G \nabla^2 u_z + (\lambda + G) \frac{\nabla \cdot u_z}{\partial z} - \alpha \frac{\partial p}{\partial z} = 0 \quad (2.5)$$

$$\text{in which } \nabla^2 u_a = \frac{\partial^2 u_a}{\partial x^2} + \frac{\partial^2 u_a}{\partial y^2} + \frac{\partial^2 u_a}{\partial z^2}$$

Here, c_t is the total compressibility, λ and 'G' is Lamé's parameters, u_x , u_y and u_z is displacement along x, y and z axis respectively. The detail derivations of these equations are given in **Appendix-2.1 B**.

Equations 2.1 to 2.5 are the constitutive equations of poroelasticity with four unknowns: u_x , u_y , u_z and p . Coupling occurs among these equations because pore pressure

appears in the force equilibrium equations and mean stress/strain(derivative of displacement) appears in the fluid flow equation. The richness and verities of poroelastic phenomena arise from interactions between the mechanical requirement of force equilibrium and the fluid flow requirement of continuity (H.F Wang, 2000).

Simplification of poroelastic equations

Under specific conditions Eq. 2.1 or 2.2 is decoupled from the equation of equilibrium to make easier to solve. These conditions require assumptions for change in stress and loading conditions. Some of the conditions are non-deformable porous medium (no change in volumetric deformation $\frac{\partial(\varepsilon_{kk})}{\partial t} = 0$), Oedometric depletion also known as uniaxial strain compaction ($\Delta\sigma_{zz} = 0$ and $\varepsilon_{kk} = \varepsilon_{zz}$). For this purpose, the coupling term $-\alpha \frac{\partial(\nabla \cdot \vec{u})}{\partial t}$ of Equation Eq. 2.1, which is in fact equal to $-\alpha \frac{\partial(\varepsilon_{kk})}{\partial t}$, must be removed or changed to $\frac{\partial p}{\partial t}$ (Aghighi, 2007). So the, Eq. 2.1 turns into:

$$\phi c_i \frac{\partial p}{\partial t} = \nabla \cdot \left(\frac{\vec{k}}{\mu} \nabla p \right) + c_f \nabla p \cdot \left(\frac{\vec{k}}{\mu} \nabla p \right) \quad (2.6)$$

Undrained response

Poroelastic coupling in a physical situation depends on the rate of pore fluid movement relative to the rate of change of stress conditions. Normally when flow is restricted to move there is an undrained conditions. When the well is drilled, rock is replaced by a wellbore and pressurized by a fluid column. The stress acting on wellbore becomes different from the stresses in its previous condition. Rocks deforms in response to this stress change. Fluid flow is initiated if the wellbore pressure is different than pore pressure. Due to viscous effect fluid needs time to flow whereas solid deforms faster than fluid flow. In an undrained response solid deformation is not associated with fluid flow, which is often the case of drilling.

Hydraulic fracture is conducted relatively long time after drilling. The drained situation ($p=p_r$, reservoir pressure) is considered as initial condition for hydraulic fracturing.

For undrained case the constitutive equations of poroelasticity can be expressed as (Aghighi 2008):

$$\partial p = \frac{K_u - K_b}{\alpha} \partial \varepsilon_{kk} \quad (2.7)$$

where ε_{kk} = the volumetric strain, K_u and K_b are undrained and drained bulk modulus respectively. Substituting this value in the Eqs.2.3-2.5 one can write:

$$G \nabla^2 u_x + (\lambda_u + G) \frac{(\nabla \cdot u_x)}{\partial x} = 0 \quad (2.8)$$

$$G \nabla^2 u_y + (\lambda_u + G) \frac{(\nabla \cdot u_y)}{\partial y} = 0 \quad (2.9)$$

$$G \nabla^2 u_z + (\lambda_u + G) \frac{(\nabla \cdot u_z)}{\partial z} = 0 \quad (2.10)$$

where λ_u is undrained first Lamé's parameter.

Plane strain

Plane strain assumption can be used when one of the dimensions is very large as compared to other two. According to Jaeger (Jaeger and Cook, 1969) the principal strain in the direction of longest dimension is constrained and can be assumed to be zero. Thus, in this case the principal stress in the direction of longest axis (vertical axis) can be excluded from the calculations. This allows reducing three dimensional analyses to two dimensional analyses of stresses. These assumptions are widely used in the study of hydraulic fracturing and stress reorientation by various authors (Biot et al., 1986; Garagash and Detournay, 2005; Geerstma and De Klerck, 1969; Hidayati et al., 2001; Nouri et al., 2002; Sato and Hashida, 2000). Using the stress-displacement relationship Eqs.2.3 to 2.5 is reduced into two dimensions. The two dimensional stress-displacement relationships can be expressed as follows (Zienkiewicz and Taylor, 2000):

$$\vec{S}^T \vec{D}_e \vec{S} \Delta \vec{u} + \alpha \nabla \Delta \vec{p} = \vec{0} \quad (2.11)$$

where D_e is the elastic modulus tensor, $\Delta \vec{\sigma}$ is change in total stress and $\Delta \vec{p}$ is change in pressure. The detail derivations of these equations are given in Appendix-2.1 B.

Description of the model

The poroelastic intact wellbore model presented here includes a reservoir which is intercepted by a vertical wellbore. It is assumed that the reservoir surface is horizontal, at initial condition the system is at rest and that the reservoir is in drained situation in which pore pressure is stabilized. Vertical stress is a principal stress and other two principal stresses (minimum and maximum horizontal in-situ stresses) are in horizontal plane and are aligned in the same direction of Cartesian coordinates of the reservoir. Initial value of displacement, pore pressure and stress components are obtained from Kirsh's analytical solutions for a poroelastic rock as shown in **Appendix-2 E.5**. At the outer boundary of the reservoir no-flow (Neumann type) condition is applied. The two in-situ stresses are applied as force at the outer boundary of the reservoir. A constant wellbore pressure (Dirichlet type boundary condition) is applied as force at inner boundary (wellbore) of reservoir. Young's modulus, Poisson's ratio, porosity, permeability, total system compressibility and the viscosity of fluid are assumed to be independent of time and space. The model geometry is shown in **Fig.2.1**. The elastic properties of reservoir, formation fluid properties and in-situ stresses are given in **Table 2.1**. Structural boundary conditions are applied on the x and y axis of the model in order to take advantage of symmetry. This boundary condition is applied to restrict the displacement of the nodes along the x and y axis. A large outer radius is used and the time steps are chosen such a way that the change in pore pressure or stress state is not felt at the outer boundary. In this study the sign convention of conventional rock mechanics have been used and applied to all phases. Thus, all forms of stress, strain and pressure are positive when compressive and negative when tensile. Displacement (strain) resulted from compression is, therefore, positive and tension negative.

Numerical solution procedure

Formulations of finite element equations as a result of discretization of the governing equations of poroelasticity are discussed in **Appendix-2D**. Finite element equations are solved for change in displacement and pressure. These changes are then added to the previous time step to achieve the total displacement and pressure at the current time step. Super convergent patch recovery technique (Zienkiewicz and Zhu 1992) is employed as a method of obtaining the gradient from the displacements to calculate the nodal stresses.

To achieve high accuracy, 8-noded quadrilateral elements are employed as recommended by Zienkiewicz and Taylor (2000). Moreover, in order to get more stable result 8-noded elements are used for solution of displacement and 4-noded elements are used for pressure solution. To reduce the required computational resources, a quarter of the domain is modeled by taking advantage of symmetry. Code optimization is used to speed up the solution. Besides, matrices are stored in banded form wherever possible; nodes and elements are numbered efficiently to minimize the bandwidth of the matrices. Furthermore, to reduce the instability caused by the huge difference in scale among the nonzero values in the mass matrices involved in coupling process, a scaling factor is used to make a custom system of units. By using this unit system the cell values of the matrices roughly come into the same order of magnitude and stability is greatly improved. Stress components are calculated using the relation between displacement gradient (strain) through material properties ($\vec{\sigma} = \vec{D}\vec{\epsilon}$). Stresses are first calculated at Gauss points (G. R. Cowper, 1973; TR Chandrupatla 2002) using standard shape functions over the entire domain then nodal stresses are evaluated by determining a polynomial expansion over a patch of elements sharing the node. Pressure gradients are also evaluated using the same procedure.

2.2 Validation of Intact Wellbore Model

The numerical poroelastic model is the base model for this study. Therefore, numerical results of this model need to be verified against analytical solutions. Analytical equations to verify the numerical results for displacement, stress and pore pressure are acquired using the theory of superimposition and are given in **Appendix-2.2B**. Derivation of analytical solutions for problems related to linear elasticity and poroelasticity are discussed in **Appendix-2E**. Time steps are managed by an input file generated by using Excel. In first time step time increment was 29 sec and then change geometrically that finally reaches 1 year. Model read the time from that text file.

Pore pressure

Wellbore pressure is set maintained a lower value than the reservoir pressure. Thus, fluid flows towards the wellbore and the pore pressure progressively decreases. In **Fig.2.2** the results of pore pressure obtained from the numerical model are compared with that of

analytical solutions (Eqn. E73). As can be seen from Fig.2.2, the numerical results match well with the analytical solutions.

Similarly contour plots of pore pressure for a range of time (one minute to one month) for stress values of 6000 psi (σ_H), 5000 psi (σ_h), wellbore pressure 2000 psi and pore pressure of 4000 psi are shown in **Fig.2.3** to **2.6**, please note that Fig.2.3 (b), Fig.2.4 (b), Fig.2.5 (b) and Fig.2.6 (b) is presented to provide detail information on changes in pressure within one meter. . As expected pore pressure changes linearly to wellbore pressure near the wellbore region.

Total and effective stress

In two dimension stress tensor has two normal and one shear components which are referred to σ_x , σ_y and σ_{xy} . The three components of total stresses remain same as the original state if the poroelastic effect is neglected. However if the poroelastic effect is taken into account the change in pore pressure due to injection or production of fluids, alters the stress state of the reservoir in the vicinity of the wellbore. In this section, the numerical result of the time dependent stresses along X-axis, Y-axis and 45 degrees are verified.

Change in x-component of total and effective stress

Numerical results of change in x component of total stress and effective stress for different time and for 0° (along X-axis), 45° and 90° (along Y-axis) are compared with that of analytical solutions. To visualize the change in stress very clearly the results of entire region, wellbore region and far field region are presented separately. The numerical results show a good agreement with the exact solutions for different time and orientations. For all cases, as expected, x-component of total stress approaches the maximum horizontal in-situ stress (6000 psi) at far field.

It is assumed that wellbore pressure is equal to the reservoir pressure at zero time, so an instantaneous change in wellbore pressure is considered at the first time step which is very small. Change in x-component of total stress, induced change (due to poroelastic effect) in x-component along x-axis (0°) and change in x-component of effective stress along x-axis (0°) are presented in **Figs.2.7**, **2.8** and **2.9** respectively. It can be observed from these figures that for a given wellbore pressure the value of the stress at the wellbore do not change with time. It is also observed that as time progresses, the size of the area, which is affected by the

change in x-component of total stress increases. This is due to change in pore pressure. It is also evident from Fig.2.7 that x-component of total stress along x-axis decreases with time while the x-component of effective stress, along x-axis increases (See Fig.2.9c) with time.

Change in x-component of total stress, induced change (due to poroelastic effect) in x-component and change in x-component of effective stress along 45 degree are plotted in **Figs.2.10, 2.11** and in **2.12** respectively. Results for x-component of total and effective stress change along y-axis are also presented in **Figs.2.13, 2.14** and **2.15**. It can be seen from **Figs.2.10** through **2.15** that same trend for stresses are observed with time along 45 degree and along y-axis. The numerical results show a good agreement with the exact solutions for different time and orientations presented by Detournay and Cheng (1988). For all cases, as expected, x-component of total stress approaches the maximum horizontal in-situ stress (6000 psi) at far field.

Change in y-component of total and effective stress

Numerical results of change in y-component of total stress and effective stress for different time and for 0° (along X-axis), 45° and 90° (along Y-axis) are compared with that of analytical solutions and presented in **Figs.2.16** to **2.24**. In this case also the results of entire region, wellbore region and far field region are presented separately. The numerical results show a good agreement with the exact solutions for different time and orientations. For all cases, as expected, y-component of total stress approaches the minimum horizontal in-situ stress (5000 psi) at far field.

Change in shear stress

In this model the horizontal principal stresses are coincided with x and y axes. Thus shear stress along these directions becomes zero. Numerical results of change in shear stress for different time for 45 degree are presented in **Fig.2.25**. The results of induced change in shear stress, $(\Delta\sigma_{xy})$ are also present in **Fig.2.26**. It can be seen from Fig.2.25, that shear stress is not zero for 45 degrees in the wellbore vicinity as the stress field is anisotropic. Numerical results are in good agreement with analytical solutions for 45 degrees.

2.3 Modelling and Validation of Fracture Propagation

Hydraulic fracturing process is controlled by three major mechanisms which include crack opening, penetration of fracturing fluid into the formation (leak-off) and fluid flow in the fracture. The first simplified theoretical models for hydraulic fracturing are developed in the 1950s (Crittendon 1950, Harrison et al. 1954 and Hubbert and Willis 1957). The method of fracture mechanics is first applied to hydraulic fracturing by Barenblatt (1956 and 1962). One of the pioneering works in fracture mechanics in this era is a paper by Perkins and Kern (1961) who adapted the classic Sneddon (1946) elasticity plane-strain crack solution to establish PK model. Nordgren (1972) modified the PK model to devise the PKN (Perkins and Kern 1961; Nordgren 1972), which included the effects of fluid loss to the formation. Nordgren's formulation is based on substituting the elliptic fracture opening relation into the lubrication equation. Khristianovic and Zheltov (1955), and Geertsma and de Klerk (1969) independently developed the so-called KGD model (plane strain). Estimates of the fracture growth rate based on simple elastic model and the approximate integration of Reynold's equation have been reviewed extensively by Geertsma and Haafkens (1979). Daneshy (1973) extended the KGD model for the case of power-law fluid. Spence and Sharp (1985) introduced fracture toughness into the extended version of KGD model.

The earliest 2D models are KGD (Khristianovic and Zheltov 1955; Geertsma and De Klerk 1969), PKN (Perkins and Kern 1961; Nordgren 1972) and radial model (Valko and Economides, 1995). First two models assume constant height and constant elastic modulus. PKN model assumes plane strain on the vertical plane, whereas KGD model assumes plane strain on the horizontal plane. Due to these assumptions PKN has longer half lengths as compared to KGD. These models are initially developed to determine the fracture width for a given injection rate and initial fracture half length (one wing of the two coplanar fracture which extends from the wellbore). The mass balance is later introduced using Carters (1957) equation. The KGD model assumed that the fluid behaves similar to that of Newtonian fluids as presented by Lamb (1932). Nolte (Nolte 1979, Nolte 1991) introduced the power law fluid model to PKN model. In both PKN and KGD models the rock is assumed to behave as isotropic linear elastic solid. In this study KGD fracture mechanics principle is used to model the fracture geometry.

Fracture opening and propagation criteria

Finite element method can be applied to determine fracture width for any fracture shape and for both homogenous and inhomogeneous formations. In this study finite element method is used to determine the deformation of the formation, i.e. fracture opening. There are three basic modes of crack tip opening/displacement (See Fig.2.27).

- 1) Mode- I: Fracture opening by tensile failure,
- 2) Mode- II: Fracture opening by plane shear failure also known as sliding mode and
- 3) Mode- III: Fracture opening by anti-plane shear also known as tearing mode.

Fracture opening and propagation is primarily dominated by tensile failure in isotropic medium (Pak 1997). In this current model tensile mode is used for fracture opening. The stresses and displacements around the fracture are calculated using the following equations (Smith 1991).

$$\sigma_x = \frac{K_I}{\sqrt{2\pi r}} \cos \frac{\theta}{2} \left(1 - \sin \frac{\theta}{2} \sin \frac{3\theta}{2}\right) \quad (2.12)$$

$$\sigma_y = \frac{K_I}{\sqrt{2\pi r}} \cos \frac{\theta}{2} \left(1 + \sin \frac{\theta}{2} \sin \frac{3\theta}{2}\right) \quad (2.13)$$

$$\tau_{xy} = \frac{K_I}{\sqrt{2\pi r}} \cos \frac{\theta}{2} \sin \frac{\theta}{2} \sin \frac{3\theta}{2} \quad (2.14)$$

$$u = \frac{K_I}{4G} \sqrt{\frac{r}{2\pi}} \left[(2k-1) \cos \frac{\theta}{2} - \cos \frac{3\theta}{2} \right] \quad (2.15)$$

$$v = \frac{K_I}{4G} \sqrt{\frac{r}{2\pi}} \left[(2k-1) \sin \frac{\theta}{2} - \sin \frac{3\theta}{2} \right] \quad (2.16)$$

where, K_I is the mode-I stress intensity factor, ν = Poisson's ratio, $k = 3- 4\nu$ for plane stress, $k = (3- 4\nu)/ (1+\nu)$ for plane strain, G = shear modulus, r , θ = polar coordinates with respect to the crack tip and u , v , w = displacements in x, y and z planes respectively.

In most hydraulic fracture simulators, fracture propagation criterion is derived from linear elastic fracture mechanics (LEFM) which is established based on the Griffith's concepts of crack stability (Griffith, 1920; Griffith, 1924). He studied the stress field around an elliptical crack and proposed a criterion for crack propagation. Based on the Griffith ideas for crack stability, fracture propagation is simulated through a sequence of steps. First stress

intensity factor is calculated for a given geometry and loading condition. Then the crack propagation criterion is applied to see whether the fracture is stable or not. In the third step, if fracture is unstable, propagation occurs to a certain distance. The crack is extended if the stress intensity factor is equal to or greater than a critical value known as fracture toughness, K_{IC} or critical stress intensity factor (Clifton and Abou-Sayed, 1979) which is a material property.

The criterion applied in the current model for propagation is based on the critical width. Instead of critical stress intensity factor, critical width is used that is a function of fracture toughness of the rock (Vandamme, 1986 and Gidely et al., 1989). The authors also suggested that for a crack to be stable, the value of width obtained due to pressurizing of well bore should not exceed this critical width. The critical width for a fracture is shown in **Fig.2.28** and is calculated using the following equation:

$$W_c = \frac{8K_{IC}(1-\nu^2)}{E} \sqrt{\frac{r}{2\pi}} \quad (2.17)$$

Where, W_c = Critical width,

K_{IC} = Fracture toughness, E = Young's modulus of elasticity, r = distance from the crack tip and ν = Poisson's ratio.

When the obtained width reaches a value equal or greater than the critical width, fracture is extended and a new element is added to the current fracture.

Modeling of fluid flow in fracture

In order to model fluid flow the continuity and momentum equations across the width of the fracture are integrated. Two dimensional fluid flow equations are derived along the fracture plane. The injected fluid volume into the formation to create a fracture comprises of the volume of the created fracture and the volume of fluid leaked off into the formation from the fracture. So one can write the following:

$$V_i = V_f + V_l \quad (2.18)$$

where, V_i = volume of fluid injected, V_f = volume of fracture created and V_l = volume of fluid leaked off.

Considering the fact that the flow of fracturing fluid in the direction normal to the fracture face inside the fracture is negligible, the governing equation for fluid flow of a Newtonian fluid in a fracture can be obtained from the combination of equations of pressure loss in fracture (cubic law) and material balance as follows (Charlez, 1997):

$$\frac{\partial}{\partial x} \left(\frac{w^3}{12\mu} \frac{\partial p}{\partial x} \right) = \frac{\partial w}{\partial x} + V_l(x, t) \quad (2.19)$$

Where, w = fracture width; x, y = Cartesian coordinates, μ = fluid viscosity, v_l = leak-off velocity and p = fluid pressure.

In this study Eq. 2.19 is discretized and solved using finite element method to model the fluid flow inside the fracture. At first time step a guess wellbore pressure is used as a boundary condition at the fracture surface. For this guess wellbore pressure and a given pumping rate, an iterative procedure is carried out to satisfy material balance and to achieve a numerical convergence for time increment.

Modeling of fluid leak-off

To determine the fracture geometry the rate of fluid leak-off into the formation needs to be calculated correctly. The volume of fluid loss during the treatment determines the fracturing fluid efficiency. Carter(1957) introduced the leak off term as stated below:

$$\frac{\partial V_L}{\partial t} = \frac{C_L}{\sqrt{t - \tau}} \partial A \quad (2.20)$$

or

$$V_L = \frac{C_L}{\sqrt{t - \tau}} \quad (2.21)$$

Where, τ = the opening time of the element of interest (at which the element is exposed to fluid), A = the fracture surface, V_L = leak-off velocity, C_L = leak-off coefficient and t = actual (leak-off) time.

Another approach to characterize fracturing fluid leak-off is to evaluate the rate of fluid loss through fluid flow equation (Valko and Economides, 1995). In this approach, the rate of fluid loss through the fracture surfaces can be expressed from Darcy's law. Assuming one-dimensional flow in the direction normal to the fracture faces, one can obtain:

$$V_L = -\frac{k_y}{\mu} \frac{\partial P}{\partial y} \quad (2.22)$$

Where, k_y = formation permeability (at fracture surface) in the direction normal to the fracture faces μ = fracturing fluid viscosity, $\frac{\partial P}{\partial y}$ = pressure gradient (at fracture surface) normal to the fracture surface

This current model is capable of modeling leak-off using either leak-off as a material property (Carter leak-off model) or the fluid flow approach based on Darcy's law. In this study however the first approach (Carter leak-off model based on Eq. 2.21) is used to calculate the fluid leak-off. The fracture pressure and the leak off coefficient are two additional boundary conditions being incorporated in this model. The model initiates with a small crack and after successful iteration it calculates the width and pressure profile of the fracture for an extended length of fracture generated. The finite element mesh for this system is presented in the **Fig.2.29**.

Algorithm of fully coupled hydraulic fracture propagation model

For fracture propagation model it is essential to tackle nonlinearity issues. Other issues, such as modularity, robustness, computational time and resources and accuracy are needs to be considered. Computational procedure used to couple the governing equations of fluid flow and displacement of the formation with the fracture fluid flow equation assured the accuracy of the model. The algorithm of the model is presented in **Figs.2.30** and **2.31** include the following steps. This procedure is build upon previous work done by Aghighi (2007).

- i. Initially the reservoir data and fracturing parameters are read from external files into the model.
- ii. Using the physical description of boundaries of the reservoir and the wellbore, a mesh is generated and read from external files and used as input into the model.
- iii. Using the mesh data and the initial condition of the reservoir, the initial displacement and pressures are calculated. Based on the drained or undrained assumptions, the poroelastic model calculates the displacement and initializes the model variables.
- iv. Wellbore breakdown pressure can be calculated analytically or numerically. Once the breakdown pressure is calculated, a bottom hole pressure (BHP, which is the pressure

at the fracture mouth) is estimated to extend the fracture into next stage. The well bore pressure is calculated as a function of fracture toughness.

- v. Using this bottom hole pressure as a boundary condition at the wellbore and inside the fracture, change in pore pressure and displacements are calculated.
- vi. Using this deformation a new pressure profile for the fracture is calculated. In order to solve the fluid flow equation inside the fracture a guess time increment is used.
- vii. Fracture pressure profile obtained in previous step is used to calculate a new time increment based on material balance equation and the given injection rate. The fluid flow equation is solved again for a new fracture pressure profile in a loop until the convergence criterion for time increment is satisfied.
- viii. The fracture pressure profile is again applied as boundary condition for the formation in a similar manner to step 'i'.
- ix. The displacement then compared with the previous solution. Since the nodes at the fracture surface are only nodes that are directly subjected to the fracturing fluid pressure, it is assumed that when a convergence achieved for the displacement of these nodes, the entire displacement solution is converged. If the convergence criterion for the previous step is not met, program iterates the step ii through viii. Upon convergence it proceeds to the next step.
- x. Once the displacement convergence is successful, the critical width using equation 2.17 at the fracture tip calculated. If the critical width is numerically equal (based on a reasonable tolerance) to the deformation calculated from the model of the fracture tip , then a new element is added to the existing fracture and the model returns to the first step with a new fracture geometry for next iteration.

In this study a short fracture is considered as the initial fracture in the orthogonal direction to the minimum principal stress, i.e. minor horizontal stress herein. It is also noteworthy that the simulation time of creating a fracture of given length depends on the mesh size, accuracy needed and the length of fracture growth at each time step.

Validation of fully coupled hydraulic fracture propagation model

In this section, results of fully coupled fracture propagation model in isotropic medium are presented. The reservoir and fracture data are given in Table 2.2. Plots of fracture

profile for selected time (when fracture is at equilibrium, i.e. when numerical width, $W_{NM} = \text{Critical width, } W_{IC}$) and corresponding fracturing fluid pressure profile are shown in Figs.2.32 and 2.33. As can be seen from Fig.2.33, fracturing fluid pressure drop is higher for earlier time steps than those of late time steps. As fracture propagates deeper into the reservoir the fracturing fluid pressure profile flattens.

Comparison of fully coupled poroelastic model with KGD-C model

KGD-C model is chosen to compare with the current numerical model as both assume plain strain in horizontal plane. The key differences between the two models are the application of boundary condition and propagation criterion. KGD-C model assumes that fracture is uniformly pressurized and the criterion for propagation is based on Barenblatt's(1962) hypothesis. Whereas in the proposed model, fracture fluid pressure is a function of nodal position in the fracture and the fracture propagation is based on LEFM.

A closed system of equations for KGD-C model can be found in the Appendix-2.3 B (Equations B-63 to B-68). The well bore pressure, fracture half length and fracture width at the well bore can be obtained by using a numerical root finding method. Data used to compare the results of the current numerical model and the KGD-C model is presented in Table 2.2. A low value for permeability is chosen, so that the effect of diffusion could be minimised around the wellbore and fracture. The results of fracture half length, fracture width and fracture propagation pressure are presented in **Figs.2.34 to 2.36**. It can be shown from these figures that the trends of the values obtained from numerical result are similar to the KGD-C model. This is due to the fact that in both poroelastic and KGD-C model, fluid-leak-off is considered. In poroelastic model fluid leak-off is considered by using Darcy's equation, while the KGD-C models a laboratory drive empirical equation. Some differences, which are observed between the models, are due to the different propagation criteria and the tolerance set for the numerical simulation. Also note that results from the numerical elastic model (effect of pore pressure ignored) are also presented in order to have a good comparison with KGD-C model which is an elastic model.

Parametric study of poroelastic fracturing model

A sensitivity analysis on parameters affecting fracture propagation in a poroelastic medium is presented in this section. The reservoir parameters and the fluid data are presented

in **Table 2.3**. In simulating the propagation of this fracture, the effect of various parameters such as Biot's coefficient, formation permeability, and fluid viscosity are studied and presented.

Effect of formation permeability

High permeability of fracture face leads to large volume of fluid loss which in turn results in a low fracturing fluid efficiency and slow fracture growth. It also affects back stress by controlling change in pore pressure in the vicinity of the fracture. Assumed that the fracture face has the same permeability as the formation, a clean fracturing fluid is used so that no filter cake is built up. To study the effect of formation permeability, two different permeability of 0.1 and 5 mD are considered. Other reservoir, wellbore and fracture data are given in Table 2.3. Results of fracture length, width and propagation pressure are shown in **Figs.2.37 to 2.39**.

The effect of formation permeability on fracture half length is presented in Fig.2.37. It can be seen from the figure that high permeability results in short fracture half length. For example, after 30 seconds of injection, fracture half length is 18.5 m for $k=0.1$ mD and about 16 m for $k = 5$ mD. This means that the fracture half length is about 13.5% shorter for $k = 5$ mD than that for $k = 0.1$ mD. From Fig.2.38, it can be also observed that higher reservoir permeability yields considerably narrower fracture (about 6.6 % narrower for $k = 5$ mD than that for $k = 0.1$ mD). This is due to higher fracturing fluid loss as well as higher back stress effect due to high formation permeability. Fig.2.39 also shows that higher fracture propagation pressure is needed for high permeable reservoir. These results are in good agreement with results reported by Charlez and Aghighi (Charlez 1997, Aghighi 2007).

Effect of Biot's coefficient

To study the effect of Biot's coefficient on the hydraulic fracture propagation, two cases of Biot's coefficient 1.0 and 0.85 are considered. All other parameters are kept constant. Result of this study is presented in **Fig.2.40**. It is found that the Biot's coefficient has negligible effect on fracture propagation pressure. These results are in good agreement with the published results (Ghassemi 1997; Aghighi 2007).

Effect of pumping rate

In order to study the effect of pumping rate on hydraulic fracture propagation, two cases of pumping rates: 10 bbl/min and 20 bbl/min are chosen. All other parameters are kept constant. Results of fracture geometry and propagation pressure for two pumping rates are shown in **Figs.2.41 to 2.43**. It can be seen from the Fig.2.41 that higher pumping rate results in higher fracture growth. After 20 second of injection time at a pumping rate of 10 bbl/min fracture propagates to about 14 m. For same time and at an injection rate of 20 bbl/min fracture propagates up to 19.5 m. This means that increased pumping rate yields longer fracture half length and wider fracture width as shown in Fig.2.41 and 2.42. From Fig.2.43 it can be observed that injection rate has no significant effect on fracture propagation pressure. These results are in good agreements with those of Ghassemi (1997) and Aghighi (Aghighi 2007).

Effect of fracture toughness

In order to study the effect of fracture toughness on hydraulic fracture propagation in poroelastic media, two fracture toughness of 500 psi.ft^{0.5} and 1000 psi.ft^{0.5} are considered. All other parameters are kept constant. Fracture half length, fracture width and fracture propagation pressure profiles in terms of elapse time are shown in **Figs.2.44 through 2.46**. It can be observed from these figures that, fracture propagation process in poroelastic environment is highly sensitive to the material fracture toughness. Lower fracture toughness can lead to longer and narrower fracture (see Fig.2.44 and 2.45), while higher fracture toughness lead to shorter and wider fracture. It can be also observed that the rate of fracture growth is considerably higher for the case with lower fracture toughness. As illustrated in Fig.2.44 for fracture toughness of 500 psi.ft^{0.5} it takes about 30.5 seconds for fracture to reach a target of 18.5 meter compared to about 49.5 seconds (about 30% longer) for fracture toughness of 1000 psi.ft^{0.5}. Fracture width at the wellbore is wider for higher fracture toughness (1000 psi.ft^{0.5}) than that for low value of fracture toughness (500 psi.ft^{0.5}) (See Fig.2.45). It can be also observed that fracture propagation pressure is lower for the case of lower fracture toughness. The fracture propagation pressure difference at the early time is somewhat equal to 250 psi and later on nearly 65-70 psi that coincide with Aghighi's (2007) result. Results of this study suggest that fracture toughness of formation is a critical parameter in the design of hydraulic fracture treatment.

Effect of fracturing fluid viscosity

In order to study the effect of fracturing fluid viscosity on fracture propagation process two values of 1 and 100 cp (mPa.s) are used. All the other parameters listed in Table 2.3 are kept constant. Results of fracture geometry and propagation pressure are presented in **Figs.2.47 to 2.49**. It can be seen from the Fig.2.47 that high viscous fracturing fluid causes a lower fracture half length. It also seen from the Fig.2.48 that, the created fracture at a given injection time is considerably wider for the higher viscous fracturing fluid than that of low viscous fluid. The difference in fracture width increases with the progress of time which leads to higher fracture volume. This is due to the fact that less fluid loss (high fracturing fluid efficiency) for $\mu=100\text{cp}$. Fracture propagation pressure at the wellbore is considerably higher for $\mu=100\text{cp}$ than that of $\mu=1\text{cp}$ as shown in Fig.2.49.

2.4 Summary

In this chapter, a fully coupled poroelastic model is presented to study the fracture propagation in a homogenous medium. In order to achieve this, first an intact wellbore model is developed and the result of pore pressure, total and effective stresses are validated against analytical equations. It is observed that when the wellbore pressure is maintained lower than the initial reservoir pressure, the pore pressure with time decreases and change in pore pressure results in change in total stress. Next a hydraulically induced fracture is introduced to the intact wellbore model to study the induced fracture propagation. The results of fracture geometry (half length and width) and propagation pressure are validated against KGD-C model. Finally a parametric study of various parameters which can affect the process of hydraulic fracturing is conducted and discussed with supporting plots. It is observed that higher injection rate and high value of fracture toughness yields wider fracture. High fracturing fluid viscosity can result in shorter and wider fractures. The rate of fracture growth can significantly lower in high permeable reservoirs due to high injection fluid loss.

Table 2.1: Parameter used for verification of intact wellbore model

| Properties | Values |
|--|--------------------------|
| Young's modulus of elasticity | 2.18E+6 psi |
| Poisson's ratio | 0.25 |
| Formation porosity, ϕ | 0.2 |
| Reservoir fluid compressibility, c_f | 1.0E-5 psi ⁻¹ |
| Reservoir fluid viscosity, μ | 1 cp |
| Biot's coefficient, α | 1.0 |
| Maximum horizontal stress, σ_H | 6000 psi |
| Minimum horizontal stress, σ_h | 5000 psi |
| Initial reservoir pressure, p_i | 4000 psi |
| Wellbore pressure, p_w | 2000 psi |
| Formation permeability, k_x | 1.0 mD |
| Formation permeability, k_y | 1.0 mD |
| Wellbore radius, r_w | 0.1 m |
| Reservoir outer radius, r_e | 1500 m |

Table 2.2: Parameter used for the study of hydraulic fracture propagation

| Properties | Values |
|-----------------------------------|---------------|
| Young's modulus of elasticity | 2.18 E+6 psi |
| Bulk Poisson's ratio | 0.25 |
| Formation permeability, k_x | 0.1 mD |
| Formation permeability, k_y | 0.1 mD |
| Formation Porosity, ϕ | 0.1 |
| Reservoir fluid compressibility | 1 E-5 1/psi |
| Reservoir fluid viscosity, μ | 1 cP |
| Fracture fluid viscosity, μ_f | 1 cP |
| Biot's coefficient, α | 1.0 |
| Initial reservoir pressure, p_i | 4500 psi |

| | |
|---------------------------------------|--------------------------------|
| Maximum horizontal stress, σ_H | 6000 psi |
| Minimum horizontal stress, σ_h | 5000 psi |
| Wellbore radius, r_w | 0.1 m |
| Drainage radius, r_e | 500.0 m |
| Injection rate, q | 10 bbl/min |
| Leak-off coefficient, C_L | 0.00025 ft.min ^{-0.5} |
| Fracture toughness | 500 psi.ft ^{0.5} |

Table 2.3: Parameter used for the sensitivity analysis of hydraulic fracture propagation in poroelastic media.

| Properties | Values |
|---------------------------------------|--------------------------------|
| Young's modulus of elasticity | 1.45 E+6 psi |
| Bulk Poisson's ratio | 0.25 |
| Formation permeability, k_x | 0.1 – 5 mD |
| Formation permeability, k_y | 0.1 – 5 mD |
| Formation Porosity, | 0.1 |
| Reservoir fluid compressibility | 1 E-5 1/psi |
| Reservoir fluid viscosity, μ | 1 cP |
| Fracture fluid viscosity, μ_f | 1~100 cP |
| Biot's coefficient, α | 1.0~0.85 |
| Initial reservoir pressure, p_i | 4500 psi |
| Maximum horizontal stress, σ_H | 6000 psi |
| Minimum horizontal stress, σ_h | 5000 psi |
| Wellbore radius, r_w | 0.1 m |
| Drainage radius, r_e | 500.0 m |
| Injection rate, q | 10~20 bbl/min |
| Leak-off coefficient, C_L | 0.00025 ft.min ^{-0.5} |
| Fracture toughness | 500-1000 psi.ft ^{0.5} |
| Pay zone height, h | 100 ft |

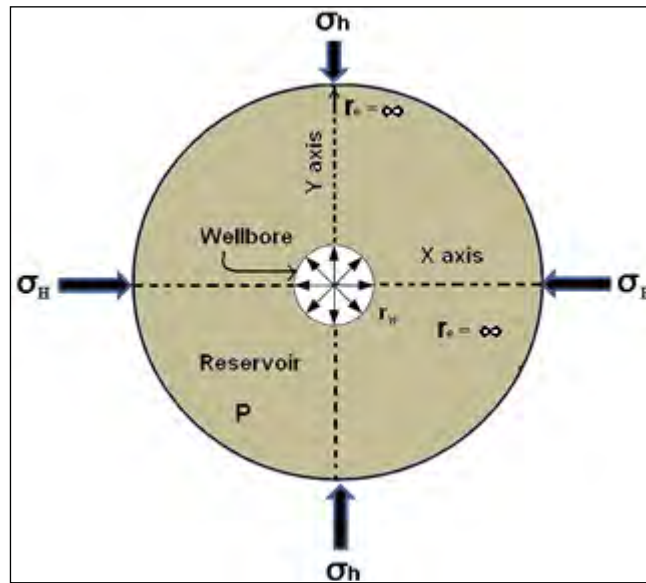


Fig. 2.1: Model geometry of pressurized intact wellbore and reservoir

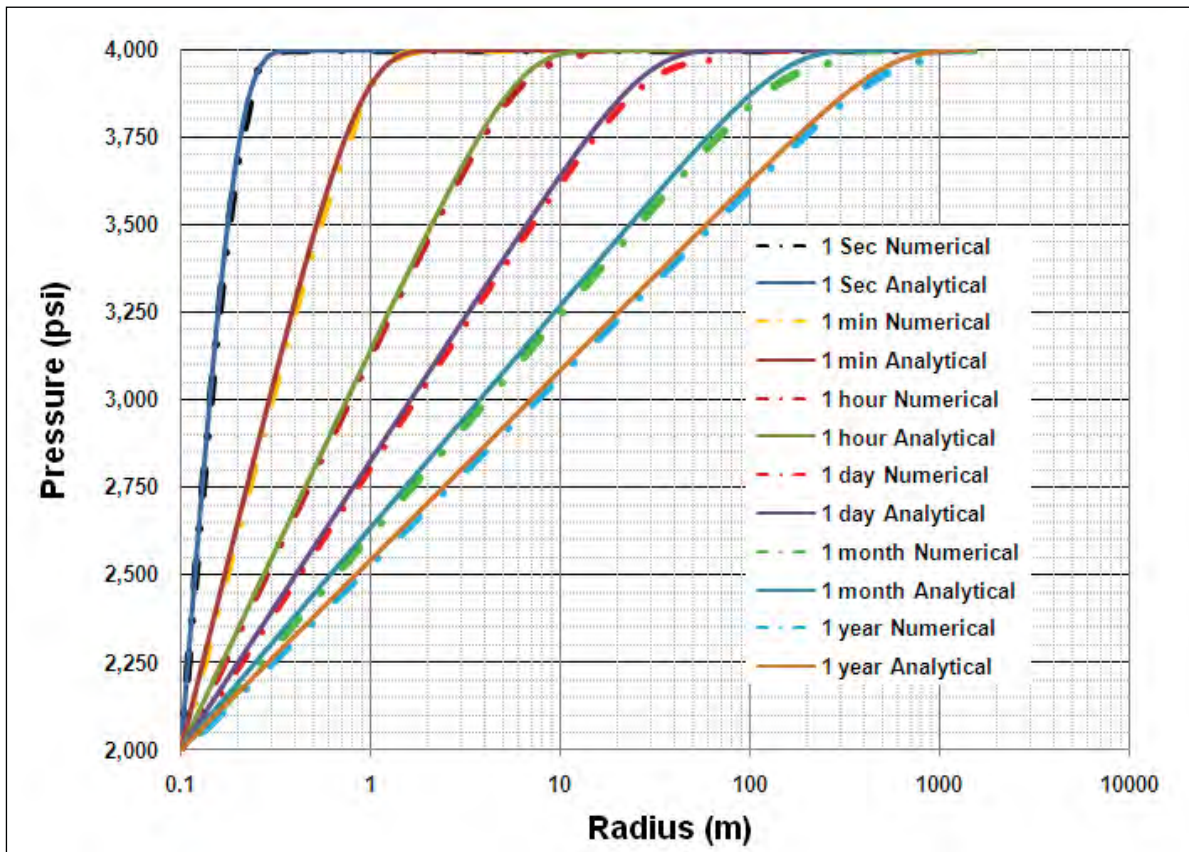


Fig. 2.2: Pore pressure as a function of radius and time in poroelastic medium for $\sigma_H = 6000$ psi, $\sigma_v = 5000$ psi, $P_i = 4000$ psi, $P_w = 2000$ psi, $k_x = 1.0$ mD, $k_y = 1.0$ mD (See Eqn E73 for analytical solution).

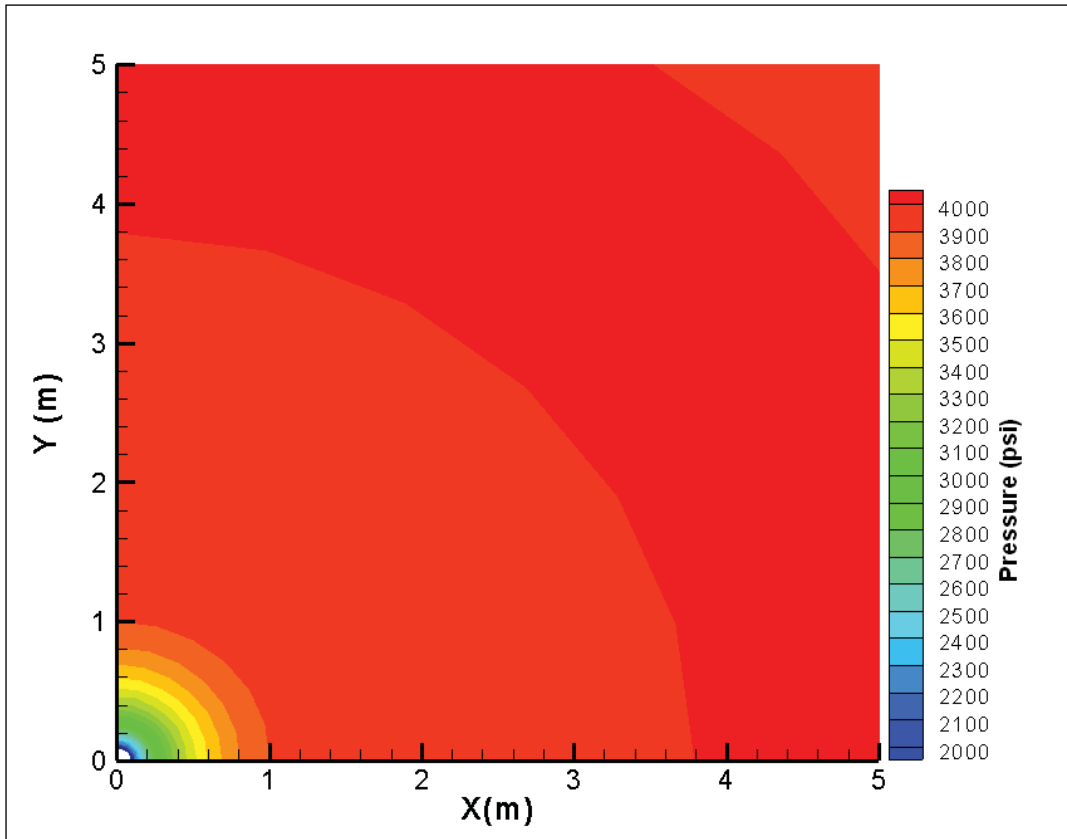


Fig. 2.3(a): Pore pressure contour map after 1 min (Numerical results, $\sigma_H = 6000$ psi, $\sigma_h = 5000$ psi, $p_i = 4000$ psi, $p_w = 2000$ psi, $k_x = 1.0$ mD, $k_y = 1.0$ mD.)

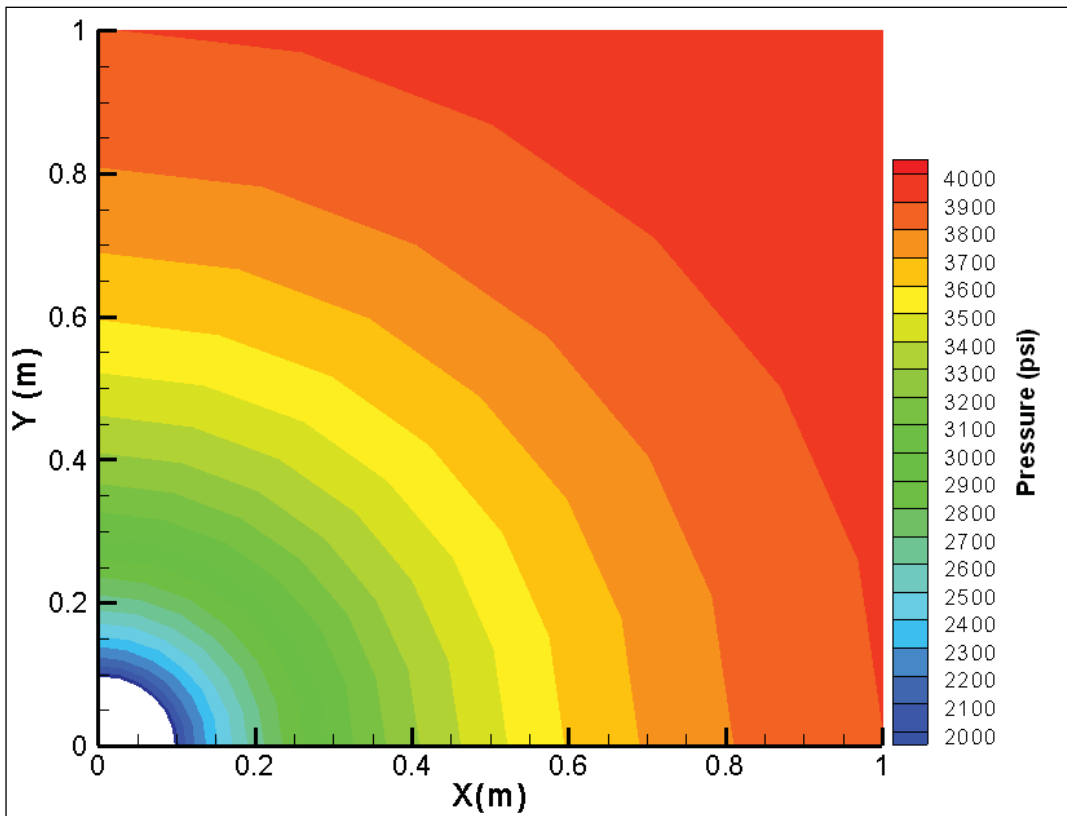


Fig. 2.3(b): Pore pressure contour map after 1 min (Numerical results, $\sigma_H = 6000$ psi, $\sigma_h = 5000$ psi, $p_i = 4000$ psi, $p_w = 2000$ psi, $k_x = 1.0$ mD, $k_y = 1.0$ mD).

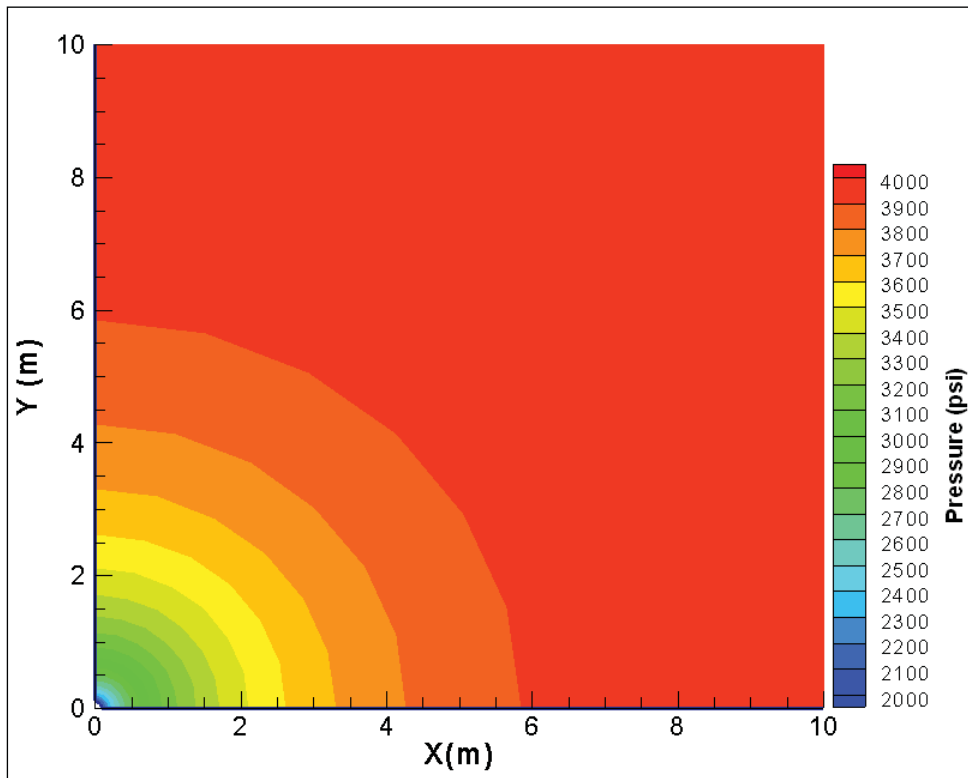


Fig. 2.4(a): Pore pressure contour map after 1hr (Numerical results, $\sigma_H = 6000$ psi, $\sigma_h = 5000$ psi, $p_i = 4000$ psi, $p_w = 2000$ psi, $k_x = 1.0$ mD, $k_y = 1.0$ mD).

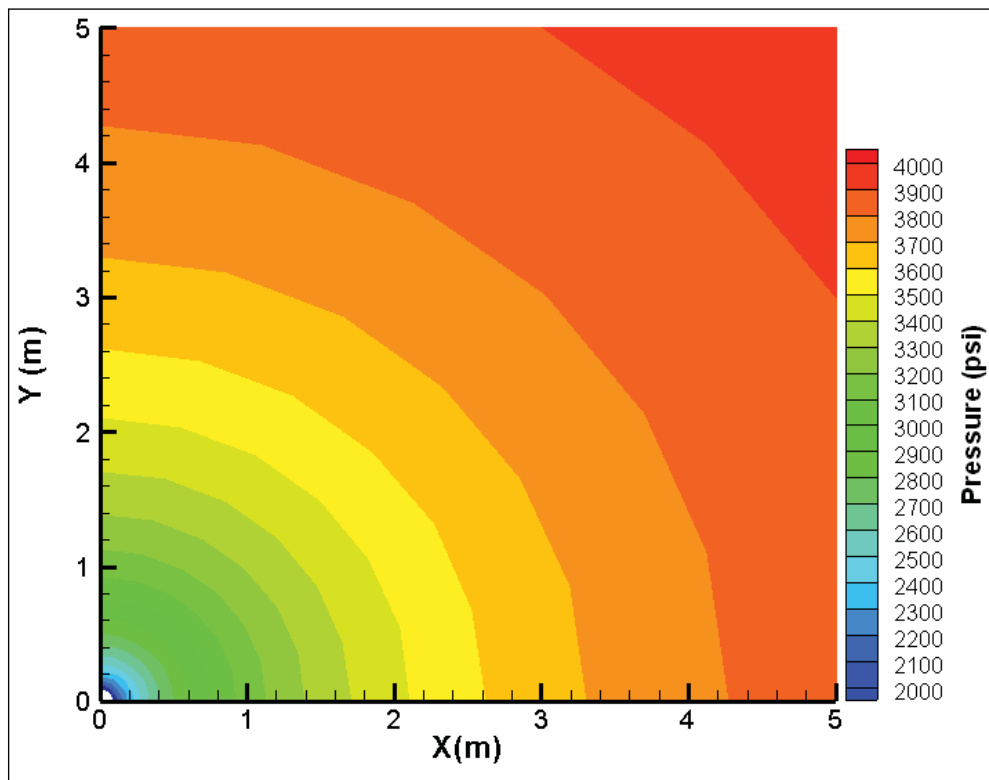


Fig. 2.4(b): Pore pressure contour map after 1hr (Numerical results, $\sigma_H = 6000$ psi, $\sigma_h = 5000$ psi, $p_i = 4000$ psi, $p_w = 2000$ psi, $k_x = 1.0$ mD, $k_y = 1.0$ mD).

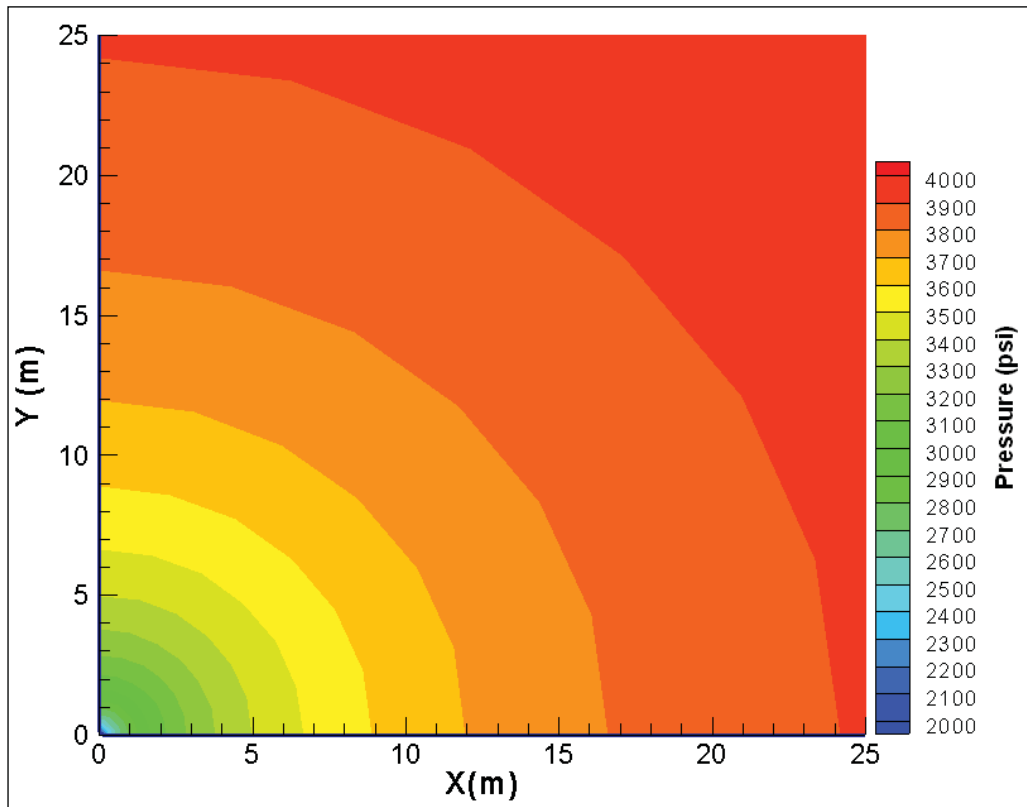


Fig. 2.5(a): Pore pressure contour map after 1 day (Numerical results, $\sigma_H = 6000$ psi, $\sigma_h = 5000$ psi, $p_i = 4000$ psi, $p_w = 2000$ psi, $k_x = 1.0$ mD, $k_y = 1.0$ mD).

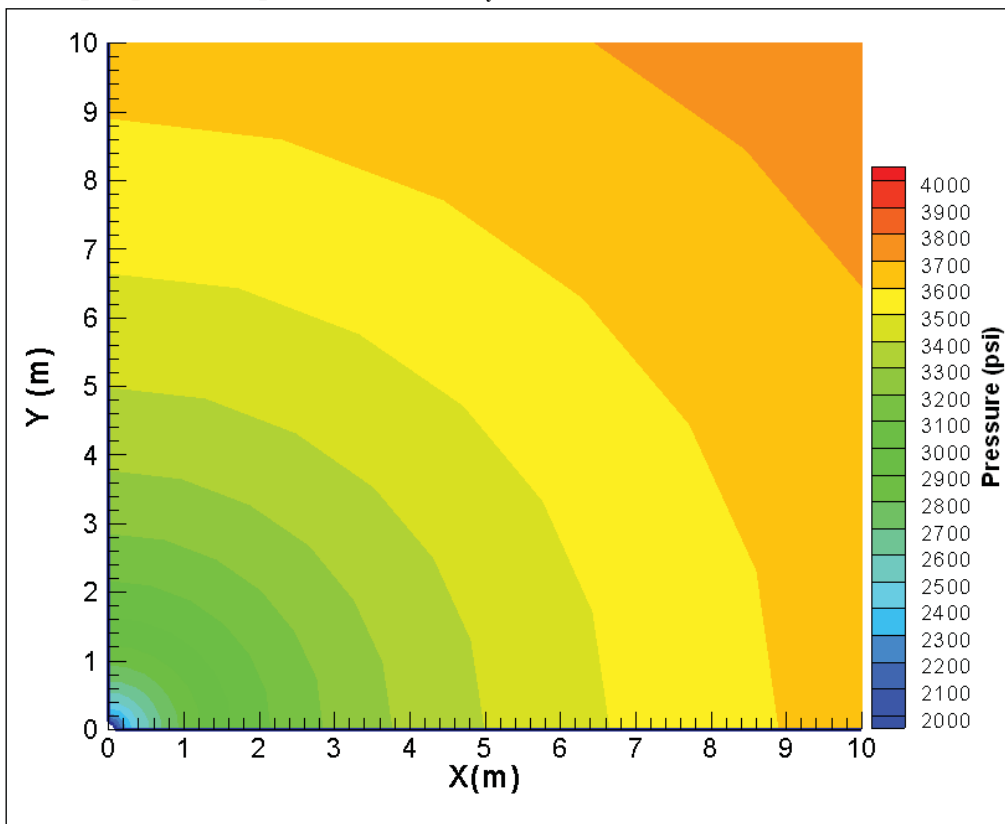


Fig.2.5(b): Pore pressure contour map after 1 day (Numerical results, $\sigma_H = 6000$ psi, $\sigma_h = 5000$ psi, $p_i = 4000$ psi, $p_w = 2000$ psi, $k_x = 1.0$ mD, $k_y = 1.0$ mD).

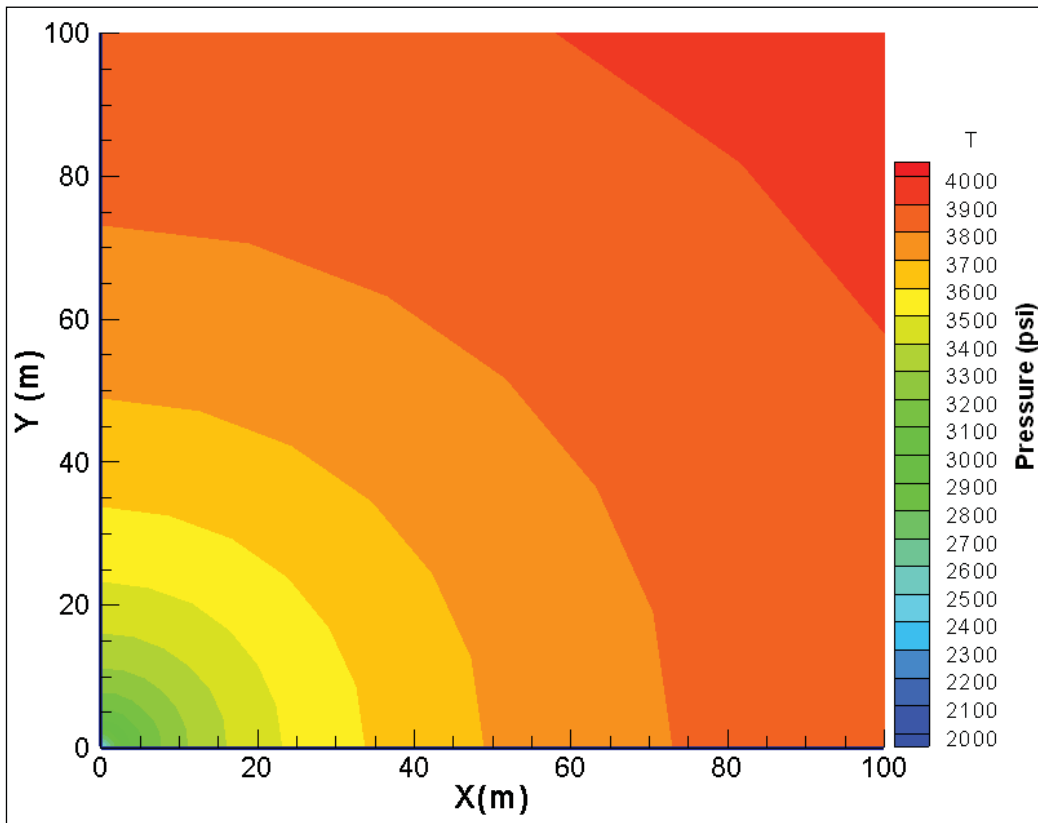


Fig. 2.6(a): Pore pressure contour map after 1 month (Numerical results, $\sigma_H = 6000$ psi, $\sigma_h = 5000$ psi, $p_i = 4000$ psi, $p_w = 2000$ psi, $k_x = 1.0$ mD, $k_y = 1.0$ mD).

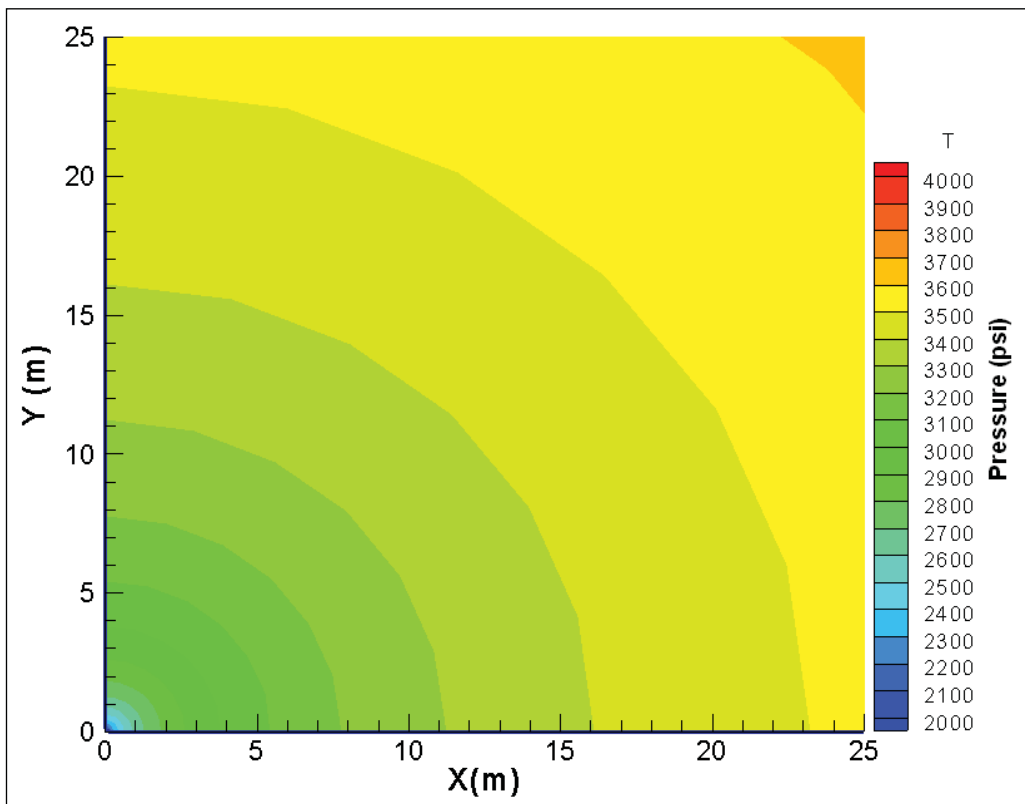


Fig. 2.6(b): Pore pressure contour map after 1 month (Numerical results, $\sigma_H = 6000$ psi, $\sigma_h = 5000$ psi, $p_i = 4000$ psi, $p_w = 2000$ psi, $k_x = 1.0$ mD, $k_y = 1.0$ mD).

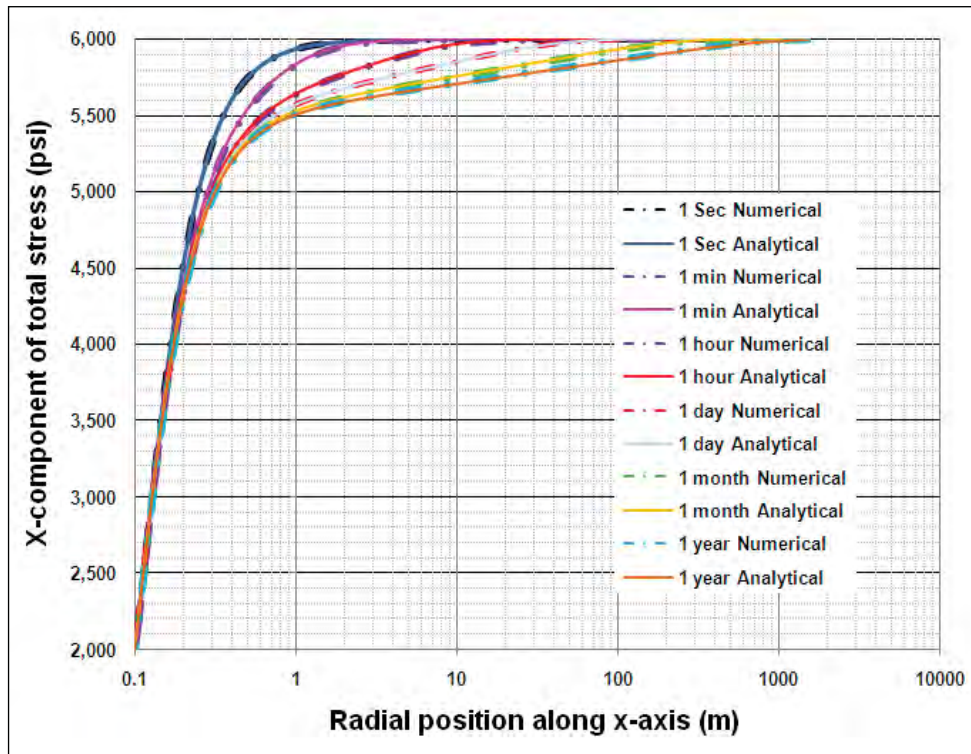


Fig. 2.7 (a): X-component of total stress (σ_x) as a function of time and radial position along X-axis for entire region (poroelastic reservoir, $\sigma_H = 6000$ psi, $\sigma_h = 5000$ psi, $p_i = 4000$ psi, $p_w = 2000$ psi, $k_x = 1.0$ mD, $k_y = 1.0$ mD).

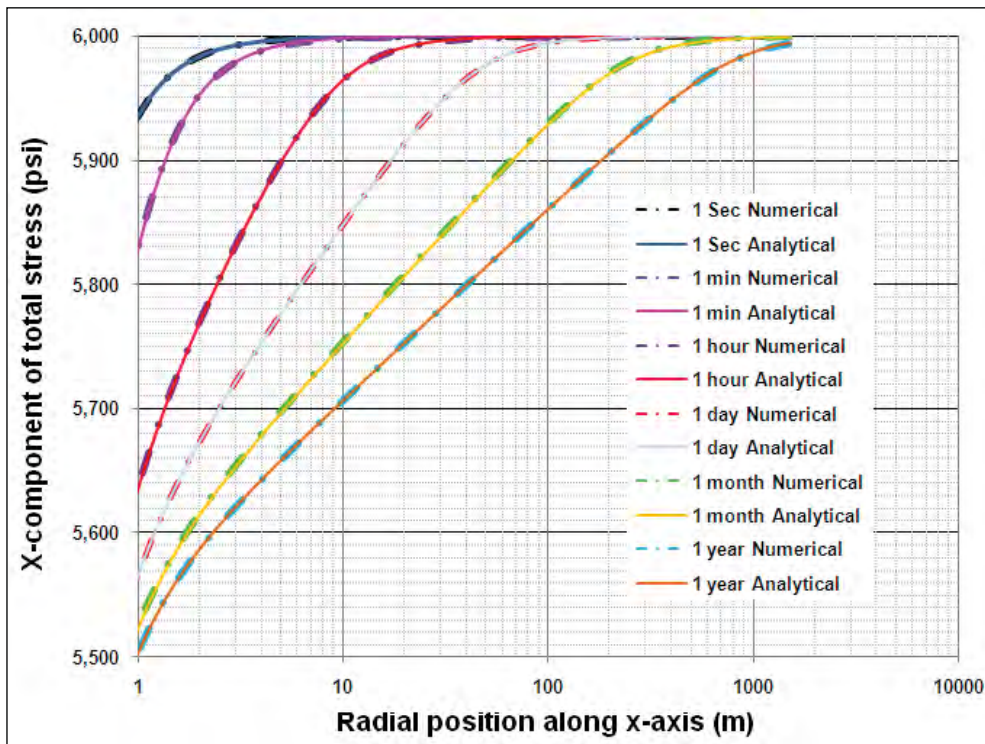


Fig. 2.7 (b): X-component of total stress (σ_x) as a function of time and radial position along X-axis for far field region (poroelastic reservoir, $\sigma_H = 6000$ psi, $\sigma_h = 5000$ psi, $p_i = 4000$ psi, $p_w = 2000$ psi, $k_x = 1.0$ mD, $k_y = 1.0$ mD).

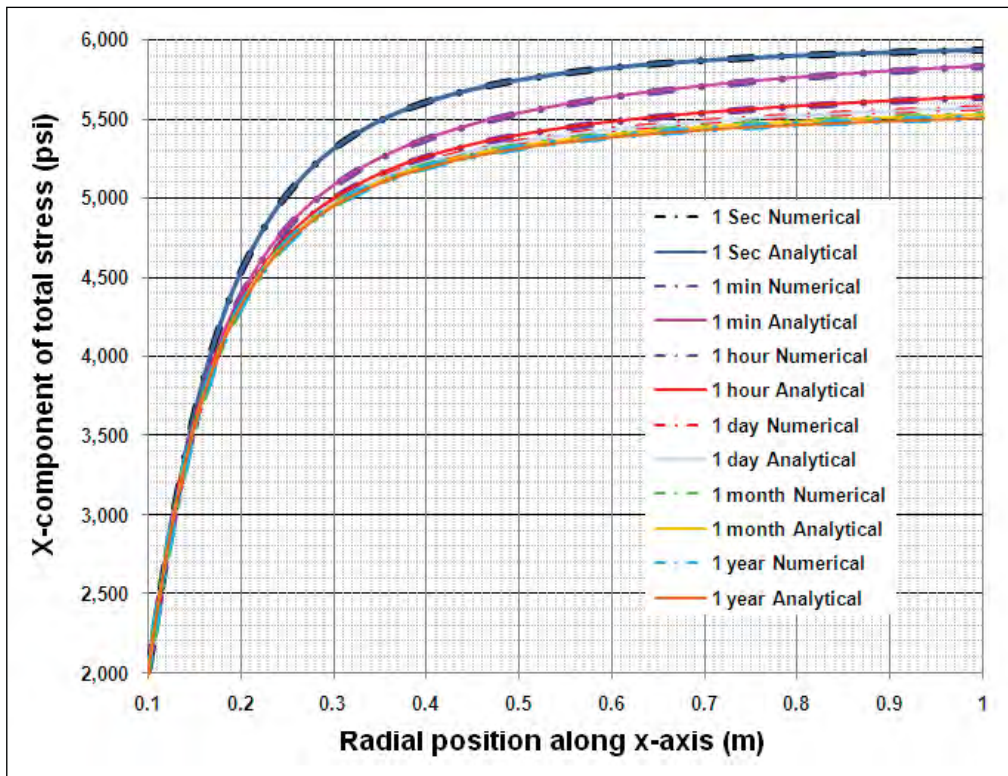


Fig. 2.7 (c): X-component of total stress (σ_x) as a function of time and radial position along X-axis for near wellbore region (poroelastic reservoir, $\sigma_H = 6000$ psi, $\sigma_h = 5000$ psi, $p_i = 4000$ psi, $p_w = 2000$ psi, $k_x = 1.0$ mD, $k_y = 1.0$ mD).

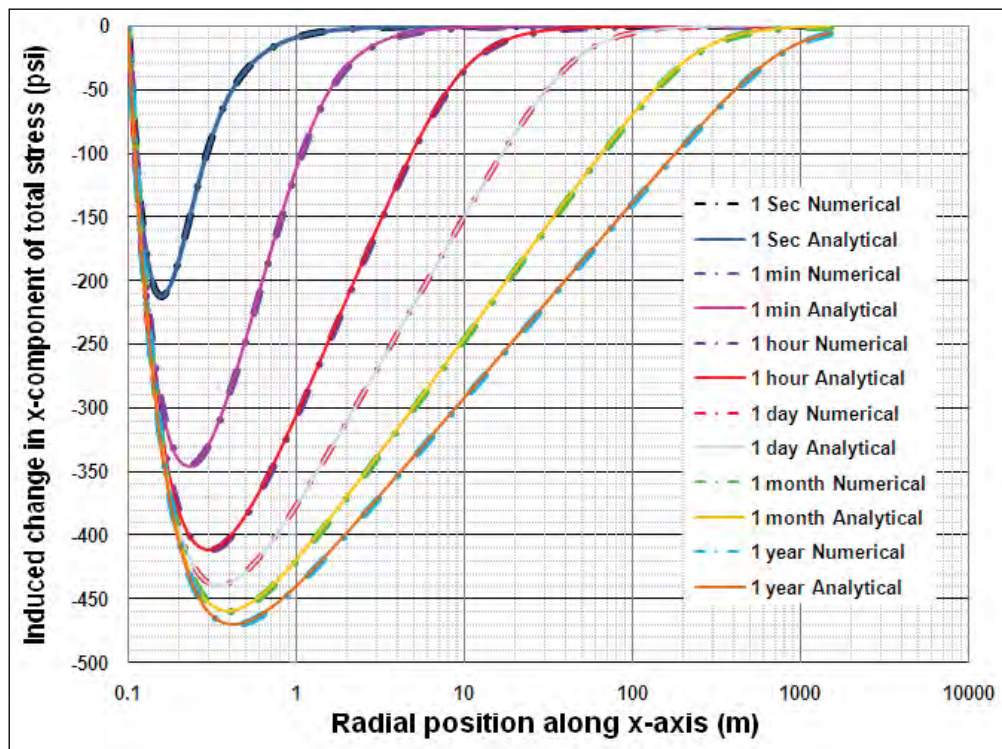


Fig. 2.8: Change in x-component of total stress ($\Delta\sigma_x$) as a function of time and radial position along X-axis (poroelastic reservoir, $\sigma_H = 6000$ psi, $\sigma_h = 5000$ psi, $p_i = 4000$ psi, $p_w = 2000$ psi, $k_x = 1.0$ mD, $k_y = 1.0$ mD).

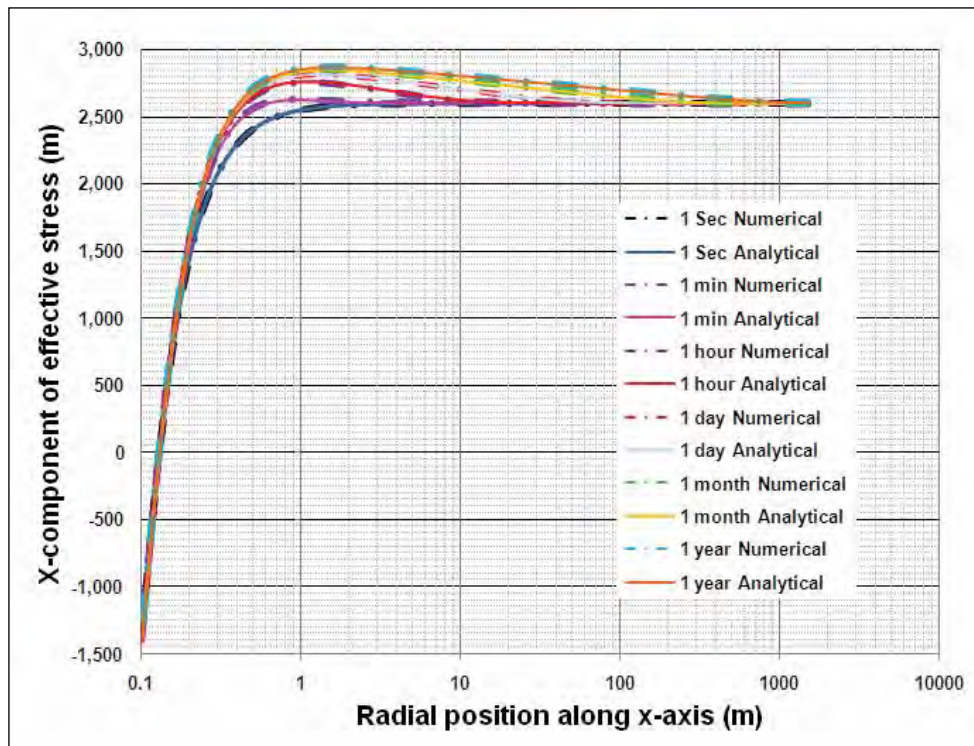


Fig. 2.9(a): X-component of effective stress (σ'_x) as a function of time and radial position along X-axis for entire region (poroelastic reservoir, $\sigma_H = 6000$ psi, $\sigma_h = 5000$ psi, $p_i = 4000$ psi, $p_w = 2000$ psi, $k_x = 1.0$ mD, $k_y = 1.0$ mD).

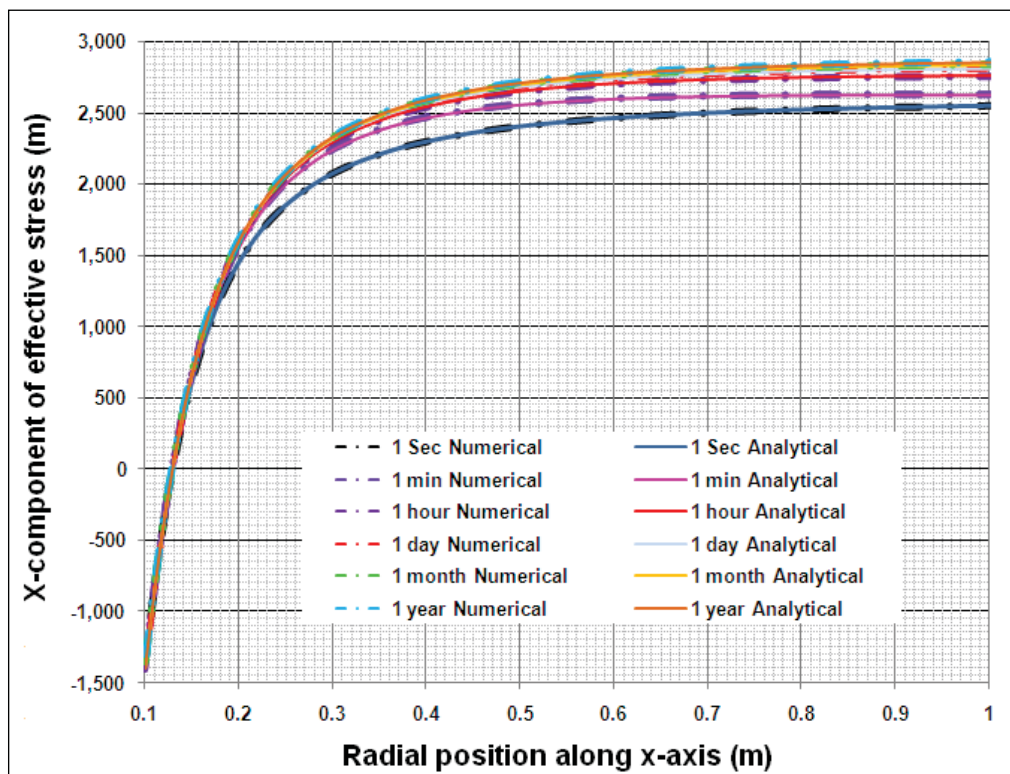


Fig. 2.9(b): X-component of effective stress (σ'_x) as a function of time and radial position along X-axis for near wellbore region (poroelastic reservoir, $\sigma_H = 6000$ psi, $\sigma_h = 5000$ psi, $p_i = 4000$ psi, $p_w = 2000$ psi, $k_x = 1.0$ mD, $k_y = 1.0$ mD).

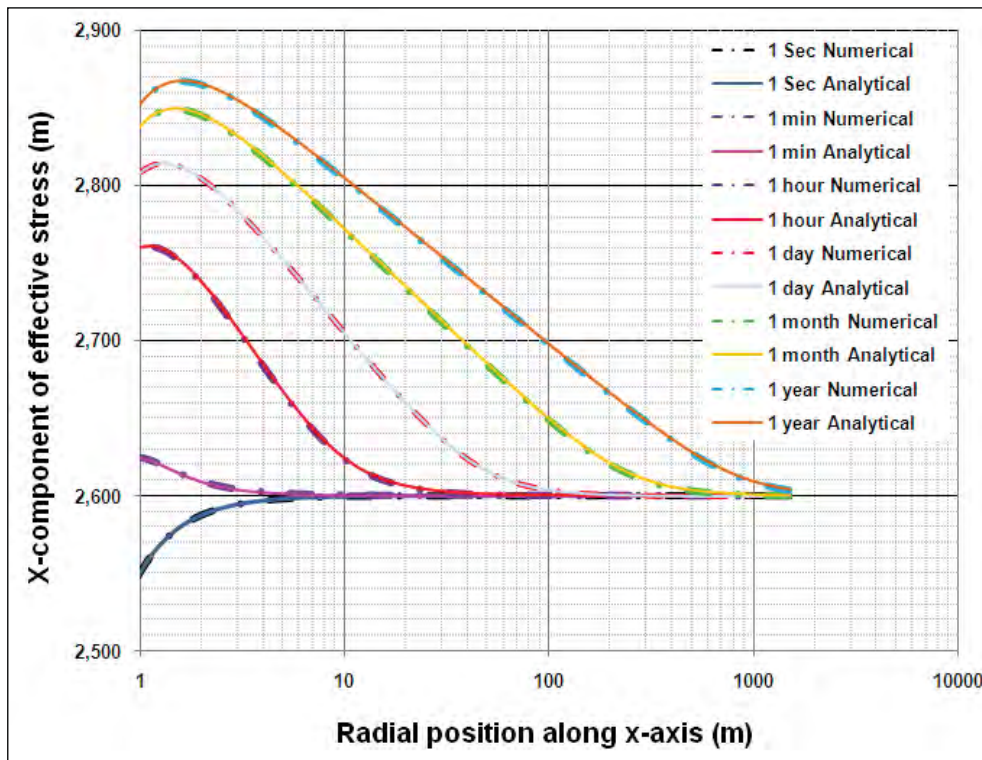


Fig. 2.9(c): X-component of effective stress (σ'_x) as a function of time and radial position along X-axis for far field region (poroelastic reservoir, $\sigma_H = 6000$ psi, $\sigma_h = 5000$ psi, $p_i = 4000$ psi, $p_w = 2000$ psi, $k_x = 1.0$ mD, $k_y = 1.0$ mD).

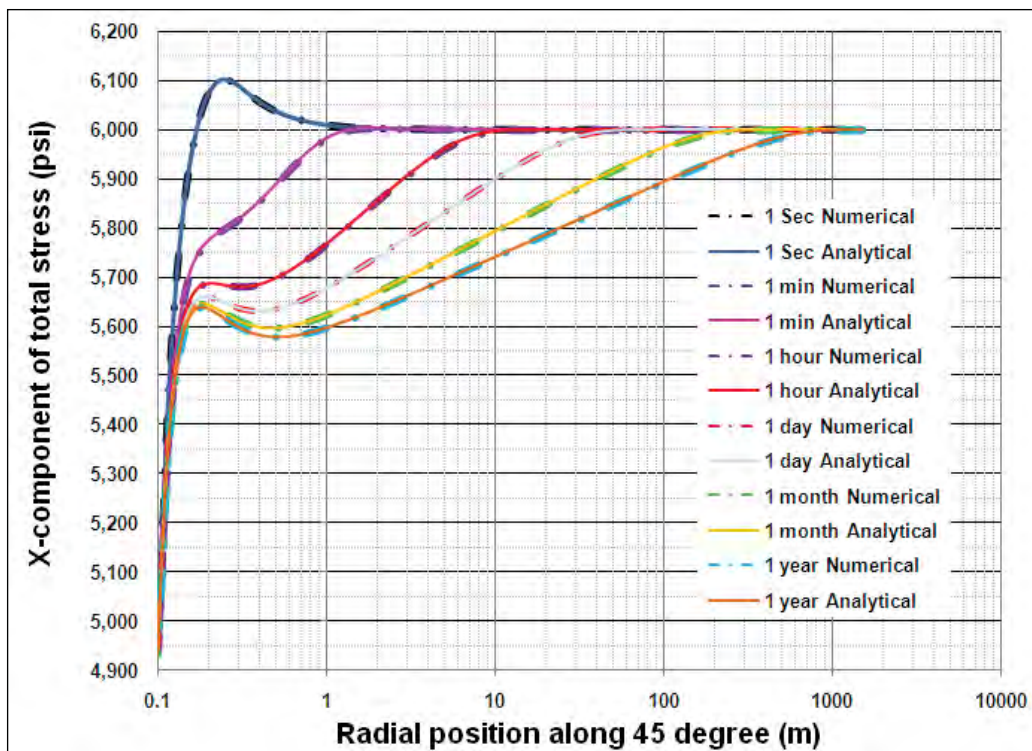


Fig. 2.10(a): X-component of total stress (σ_x) as a function of time and radial position along 45° for entire region (poroelastic reservoir, $\sigma_H = 6000$ psi, $\sigma_h = 5000$ psi, $p_i = 4000$ psi, $p_w = 2000$ psi, $k_x = 1.0$ mD, $k_y = 1.0$ mD).

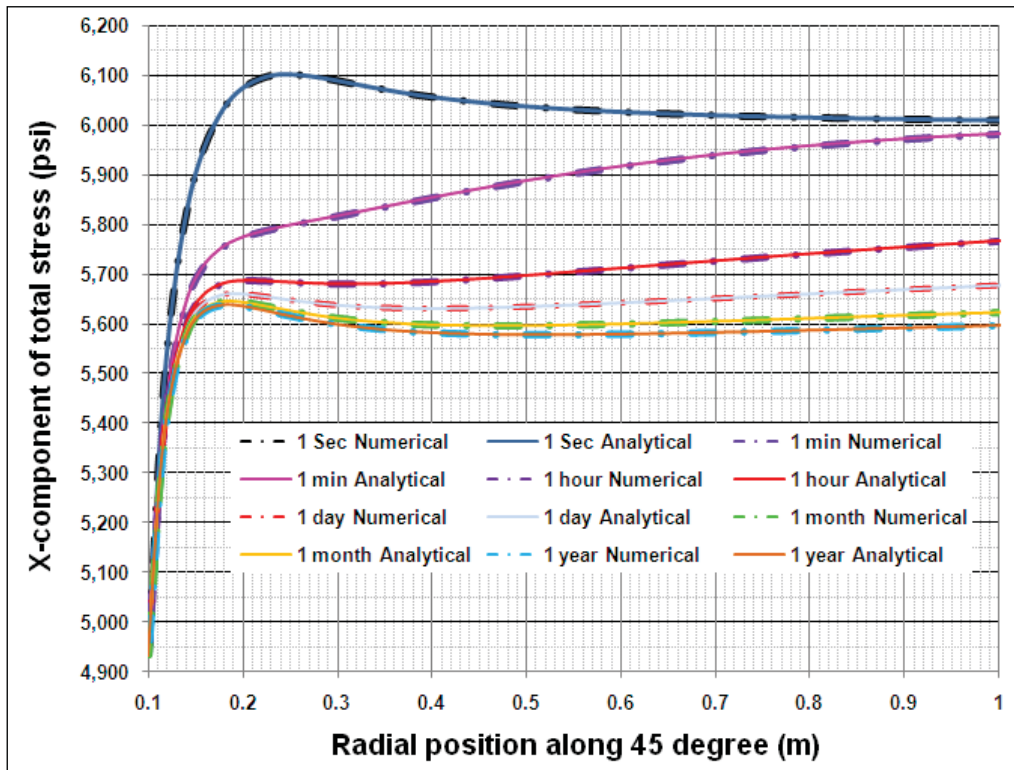


Fig. 2.10(b): X-component of total stress (σ_x) as a function of time and radial position along 45° for near wellbore region (poroelastic reservoir, $\sigma_H = 6000$ psi, $\sigma_h = 5000$ psi, $p_i = 4000$ psi, $p_w = 2000$ psi, $k_x = 1.0$ mD, $k_y = 1.0$ mD).

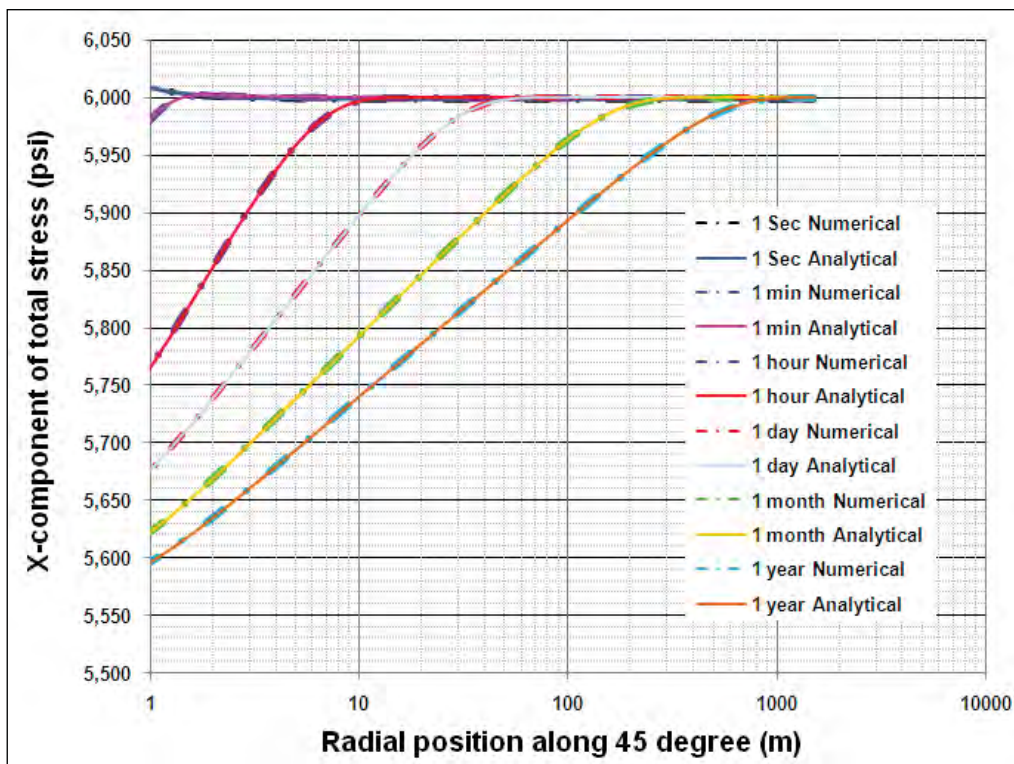


Fig. 2.10(c): X-component of total stress (σ_x) as a function of time and radial position along 45° for far field region (poroelastic reservoir, $\sigma_H = 6000$ psi, $\sigma_h = 5000$ psi, $p_i = 4000$ psi, $p_w = 2000$ psi, $k_x = 1.0$ mD, $k_y = 1.0$ mD).

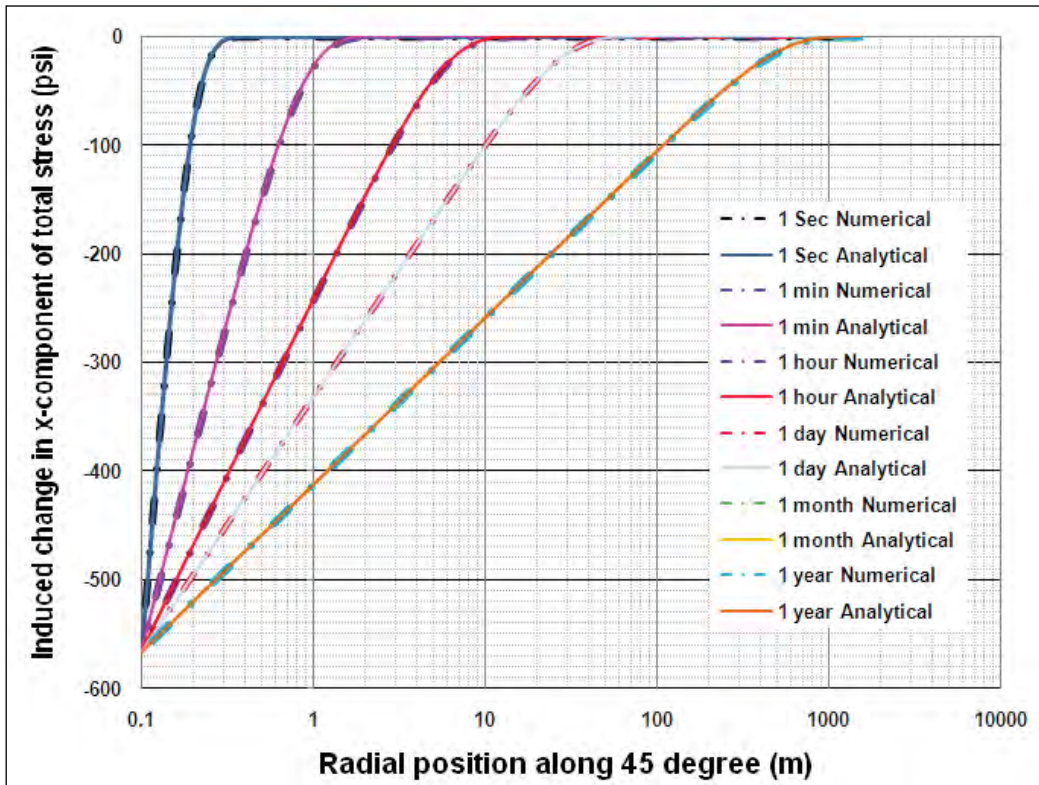


Fig. 2.11: Change in x-component of total stress ($\Delta\sigma_x$) as a function of time and radial position along 45° (poroelastic reservoir, $\sigma_H = 6000$ psi, $\sigma_h = 5000$ psi, $p_i = 4000$ psi, $p_w = 2000$ psi, $k_x = 1.0$ mD, $k_y = 1.0$ mD).

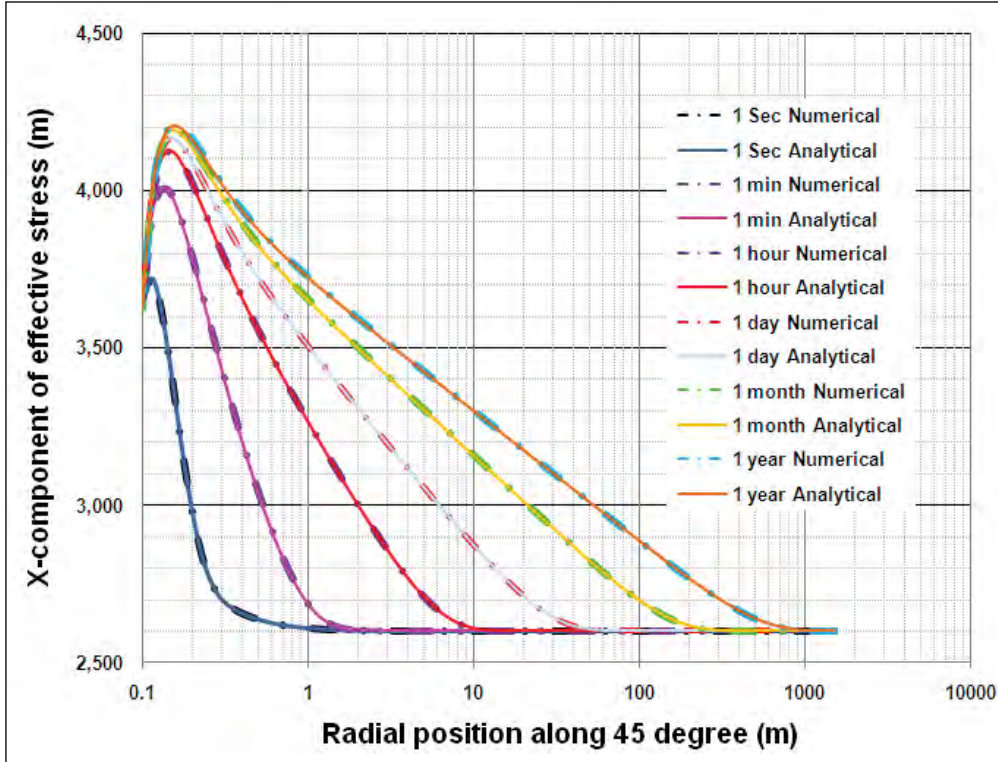


Fig. 2.12(a): X-component of effective stress (σ'_x) as a function of time and radial position along 45° for entire region (poroelastic reservoir, $\sigma_H = 6000$ psi, $\sigma_h = 5000$ psi, $p_i = 4000$ psi, $p_w = 2000$ psi, $k_x = 1.0$ mD, $k_y = 1.0$ mD).

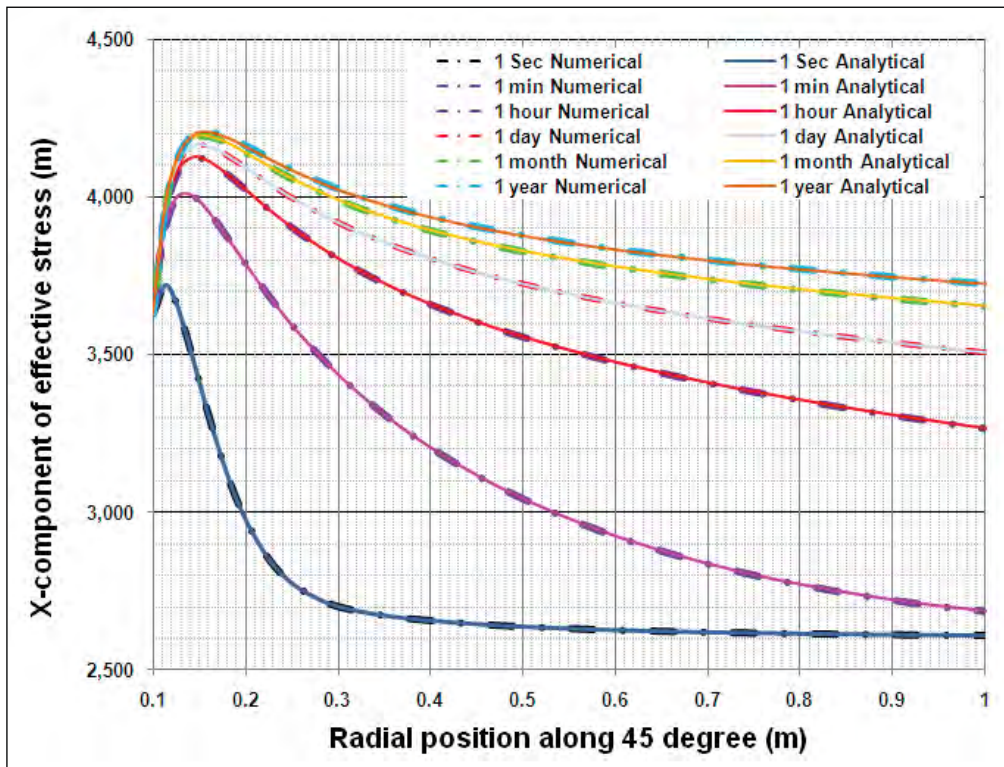


Fig. 2.12(b): X-component of effective stress (σ'_x) as a function of time and radial position along 45° for near wellbore region (poroelastic reservoir, $\sigma_H = 6000$ psi, $\sigma_h = 5000$ psi, $p_i = 4000$ psi, $p_w = 2000$ psi, $k_x = 1.0$ mD, $k_y = 1.0$ mD).

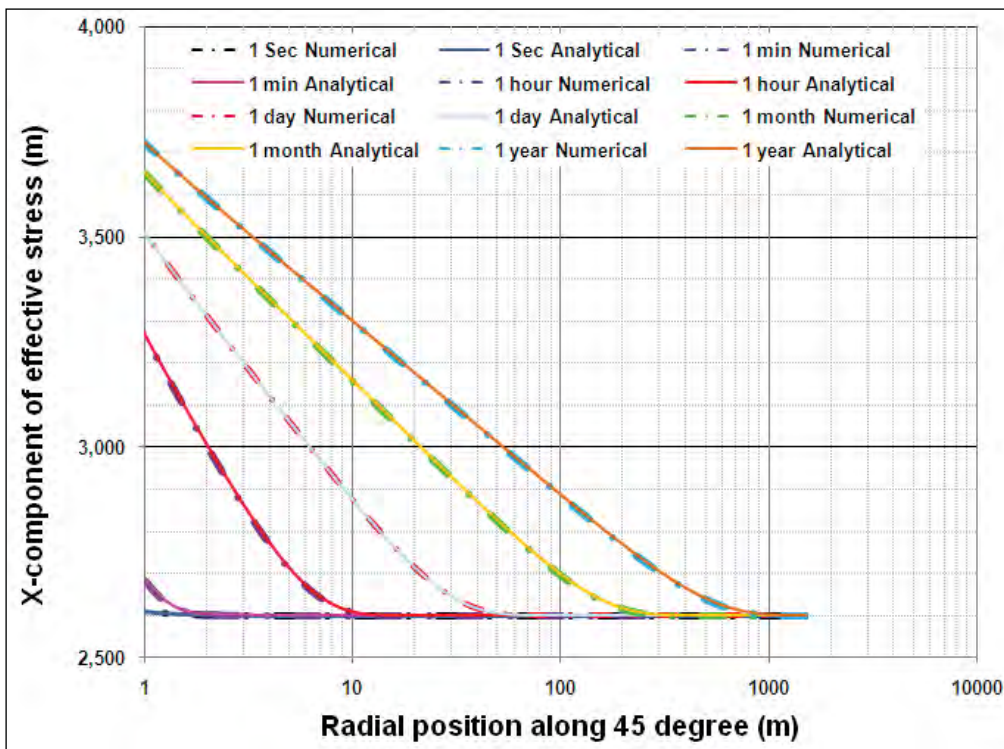


Fig. 2.12(c): X-component of effective stress (σ'_x) as a function of time and radial position along 45° for far field region (poroelastic reservoir, $\sigma_H = 6000$ psi, $\sigma_h = 5000$ psi, $p_i = 4000$ psi, $p_w = 2000$ psi, $k_x = 1.0$ mD, $k_y = 1.0$ mD).

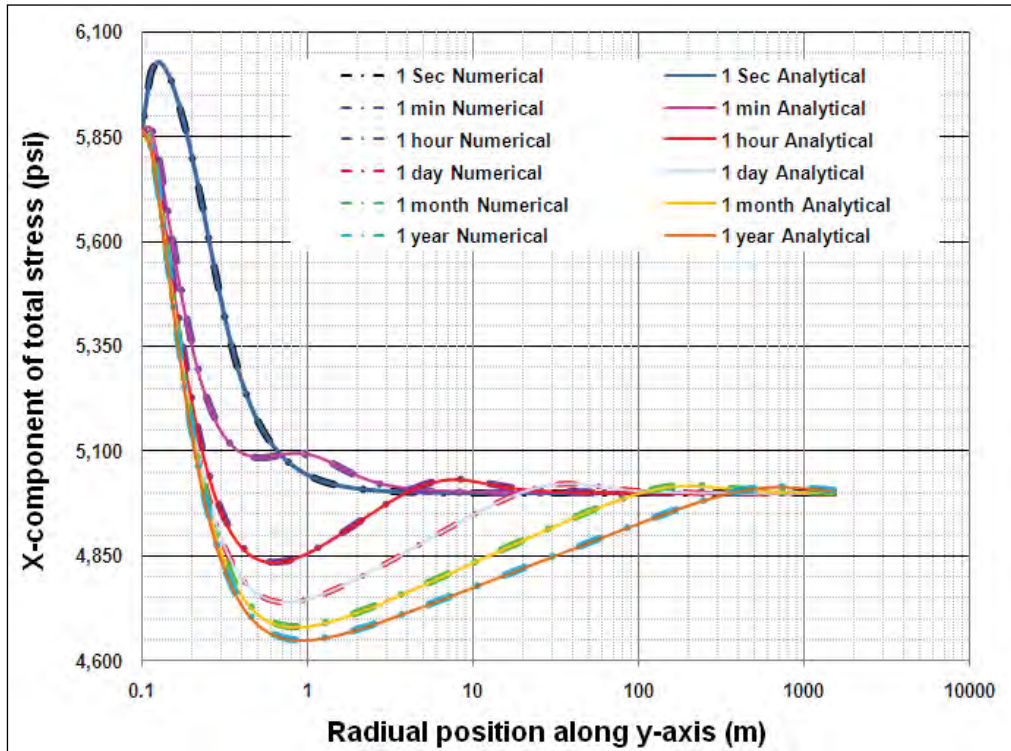


Fig. 2.13(a): X-component of total stress (σ_x) as a function of time and radial position along y-axis (90°) for entire region (poroelastic reservoir, $\sigma_H = 6000$ psi, $\sigma_h = 5000$ psi, $p_i = 4000$ psi, $p_w = 2000$ psi, $k_x = 1.0$ mD, $k_y = 1.0$ mD).

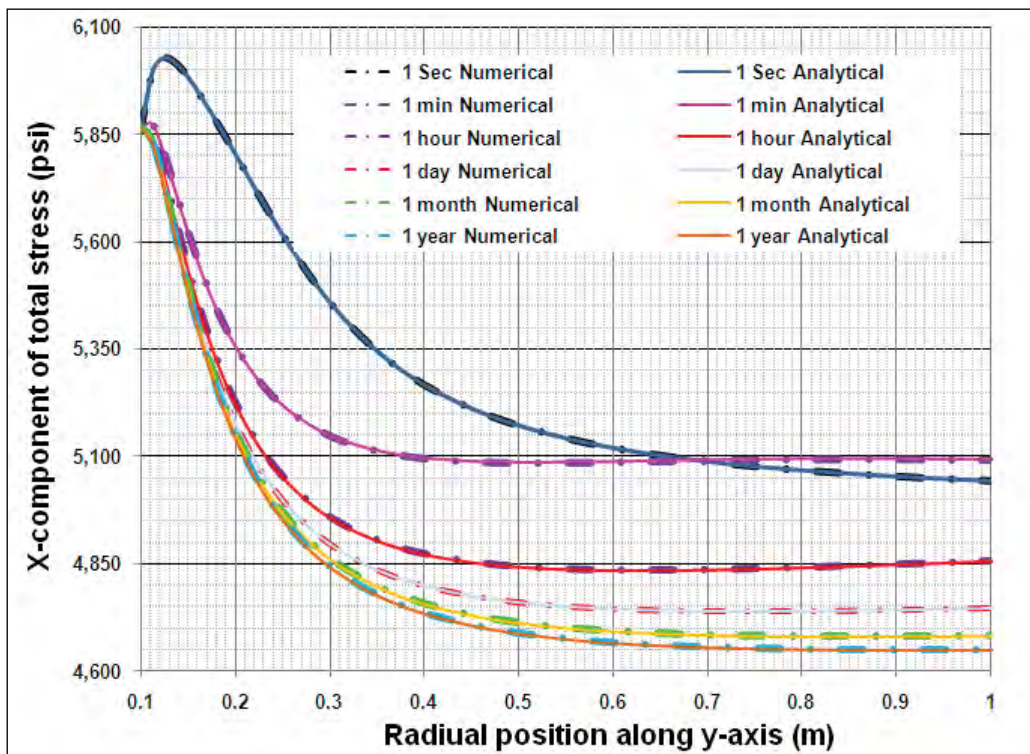


Fig. 2.13(b): X-component of total stress (σ_x) as a function of time and radial position along y-axis (90°) for near wellbore region (poroelastic reservoir, $\sigma_H = 6000$ psi, $\sigma_h = 5000$ psi, $p_i = 4000$ psi, $p_w = 2000$ psi, $k_x = 1.0$ mD, $k_y = 1.0$ mD).

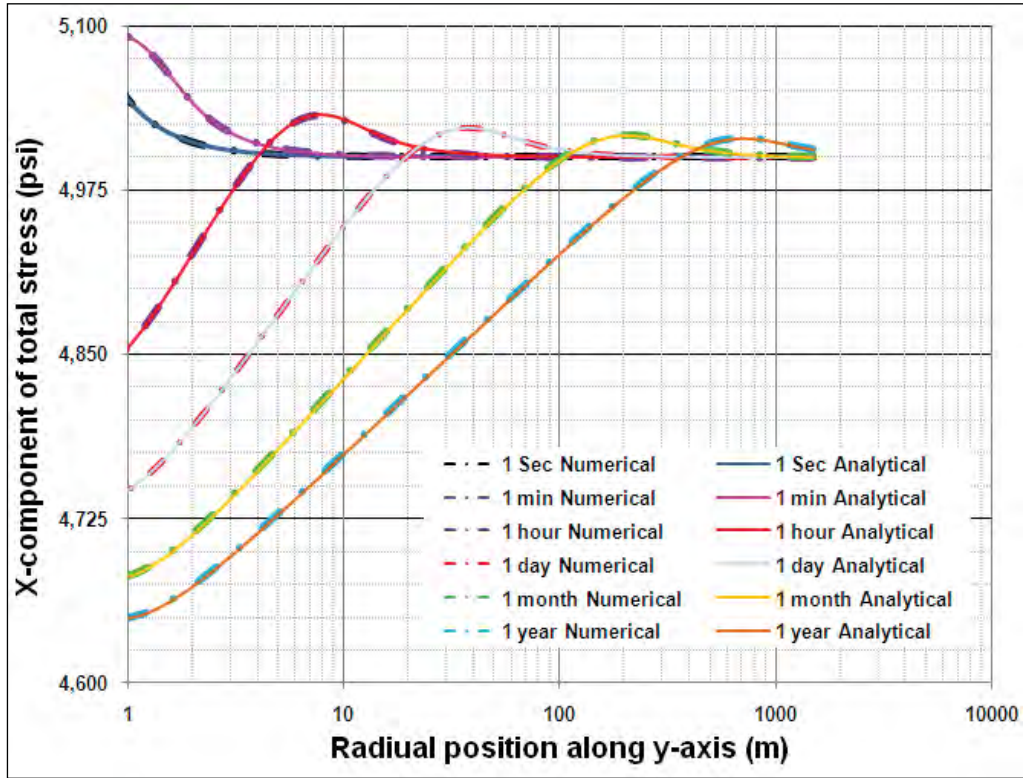


Fig. 2.13(c): X-component of total stress (σ_x) as a function of time and radial position along y-axis (90°) for far field region (poroelastic reservoir, $\sigma_H = 6000$ psi, $\sigma_h = 5000$ psi, $p_i = 4000$ psi, $p_w = 2000$ psi, $k_x = 1.0$ mD, $k_y = 1.0$ mD).

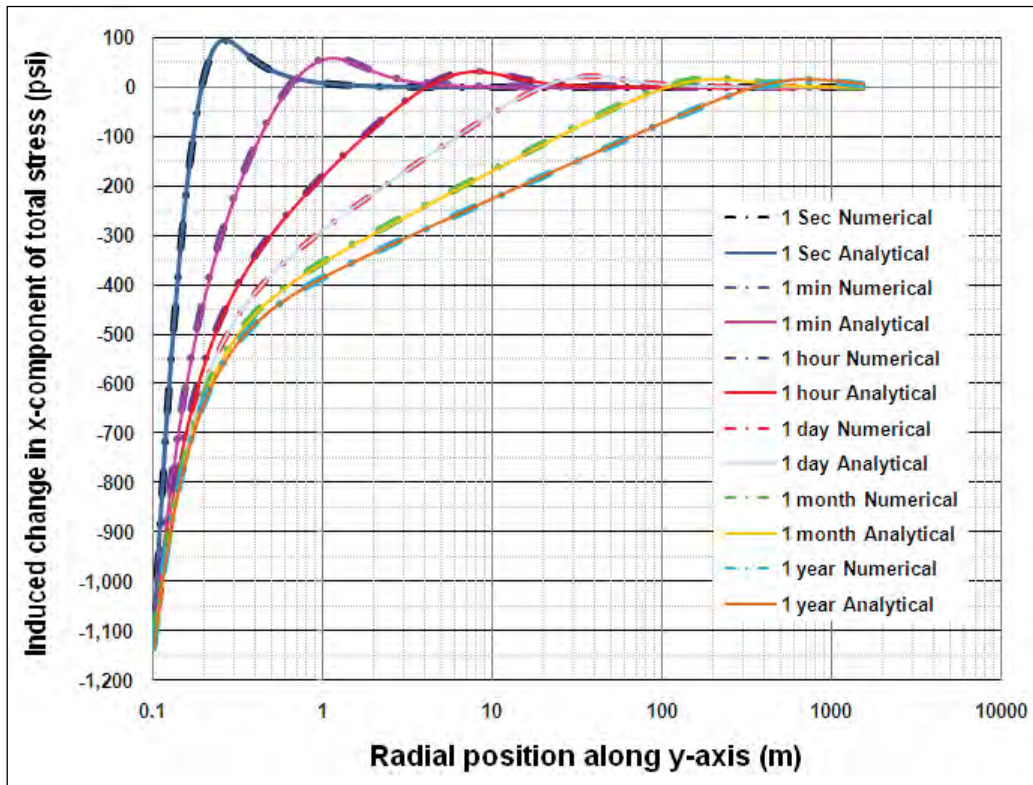


Fig. 2.14: Change in x-component of total stress ($\Delta\sigma_x$) as a function of time and radial position along y-axis (poroelastic reservoir, $\sigma_H = 6000$ psi, $\sigma_h = 5000$ psi, $p_i = 4000$ psi, $p_w = 2000$ psi, $k_x = 1.0$ mD, $k_y = 1.0$ mD).

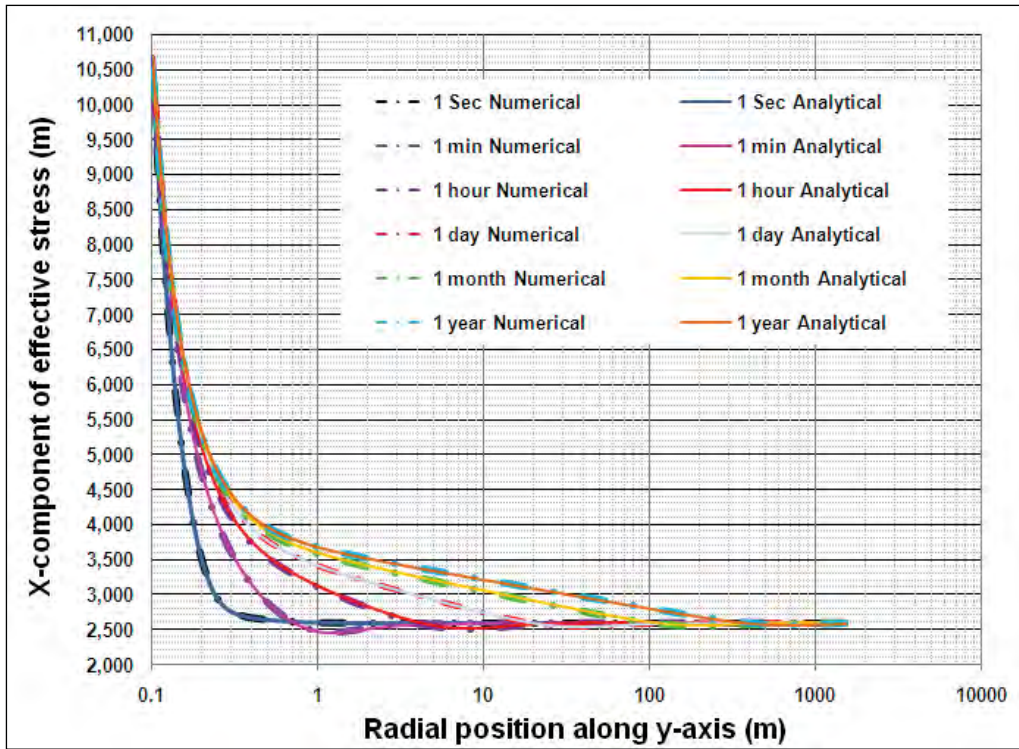


Fig. 2.15(a): X-component of effective stress (σ'_x) as a function of time and radial position along y-axis (90°) for entire region (poroelastic reservoir, $\sigma_H = 6000$ psi, $\sigma_h = 5000$ psi, $p_i = 4000$ psi, $p_w = 2000$ psi, $k_x = 1.0$ mD, $k_y = 1.0$ mD).

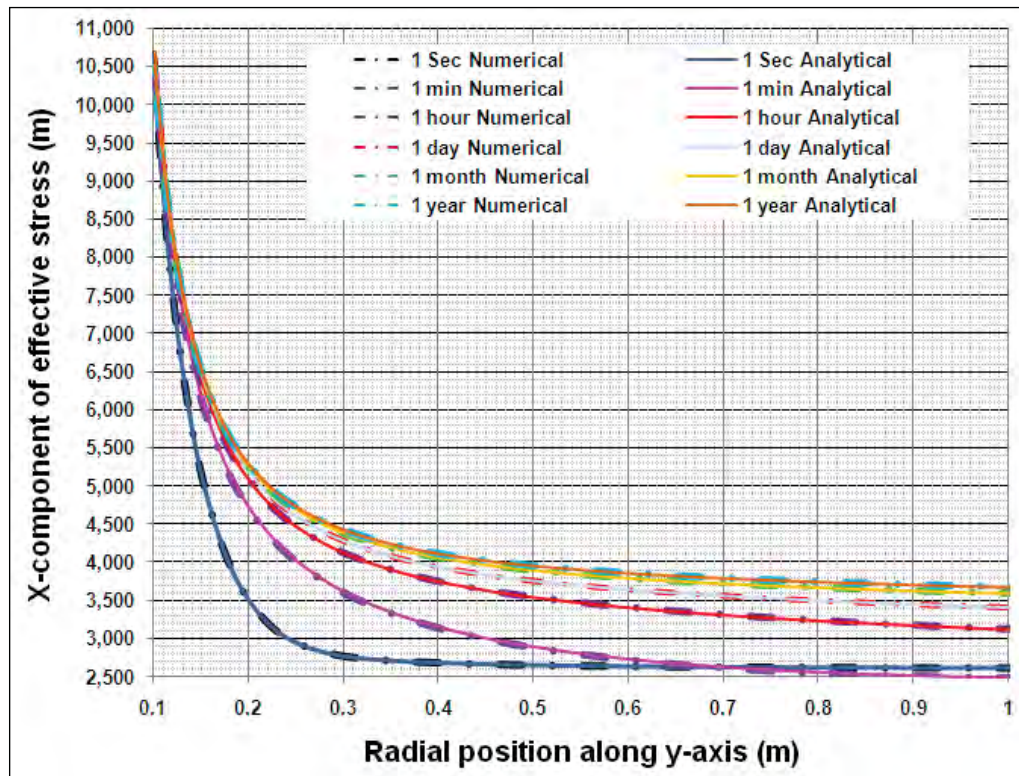


Fig. 2.15(b): X-component of effective stress (σ'_x) as a function of time and radial position along y-axis (90°) for near wellbore region (poroelastic reservoir, $\sigma_H = 6000$ psi, $\sigma_h = 5000$ psi, $p_i = 4000$ psi, $p_w = 2000$ psi, $k_x = 1.0$ mD, $k_y = 1.0$ mD).

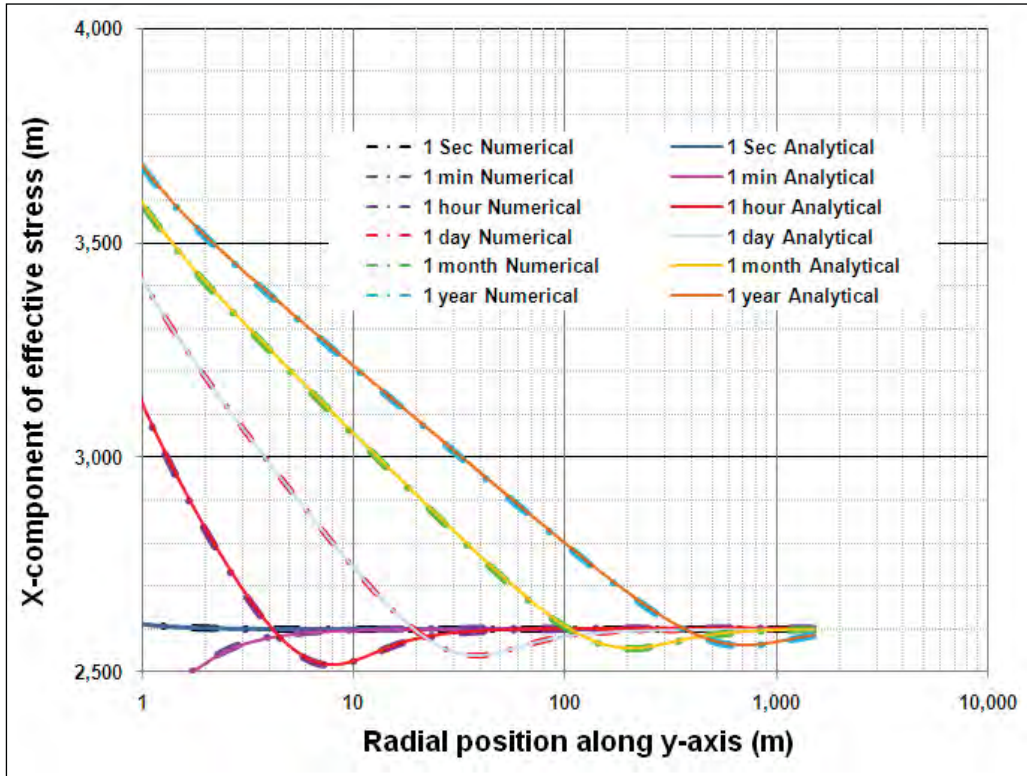


Fig. 2.15(c): X-component of effective stress (σ'_x) as a function of time and radial position along y-axis (90°) for far field region (poroelastic reservoir, $\sigma_H = 6000$ psi, $\sigma_h = 5000$ psi, $p_i = 4000$ psi, $p_w = 2000$ psi, $k_x = 1.0$ mD, $k_y = 1.0$ mD).

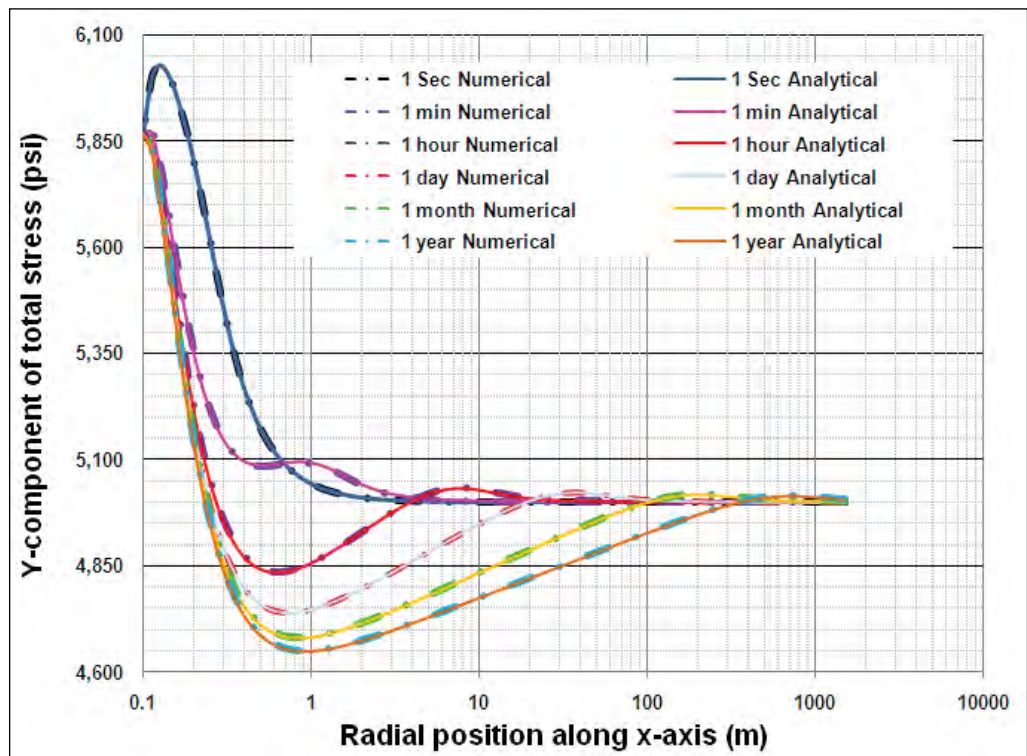


Fig. 2.16(a): Y-component of total stress (σ_y) as a function of time and radial position along x-axis for entire region (poroelastic reservoir, $\sigma_H = 6000$ psi, $\sigma_h = 5000$ psi, $p_i = 4000$ psi, $p_w = 2000$ psi, $k_x = 1.0$ mD, $k_y = 1.0$ mD).

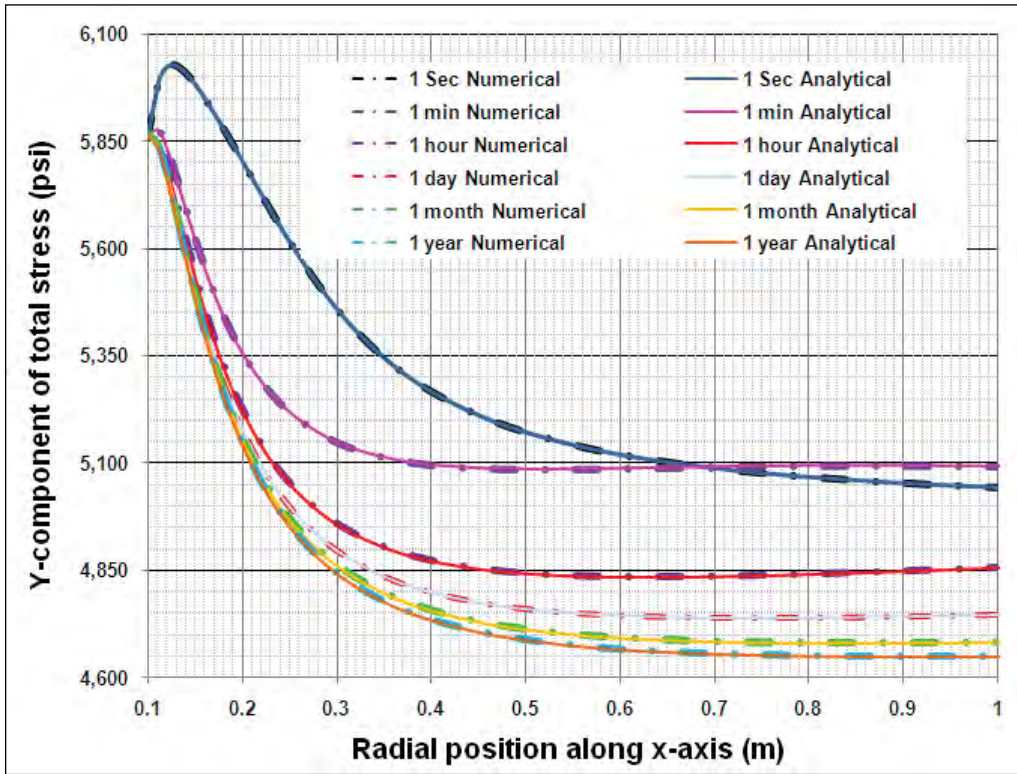


Fig. 2.16(b): Y-component of total stress (σ_y) as a function of time and radial position along x-axis for near wellbore region (poroelastic reservoir, $\sigma_H = 6000$ psi, $\sigma_h = 5000$ psi, $p_i = 4000$ psi, $p_w = 2000$ psi, $k_x = 1.0$ mD, $k_y = 1.0$ mD).

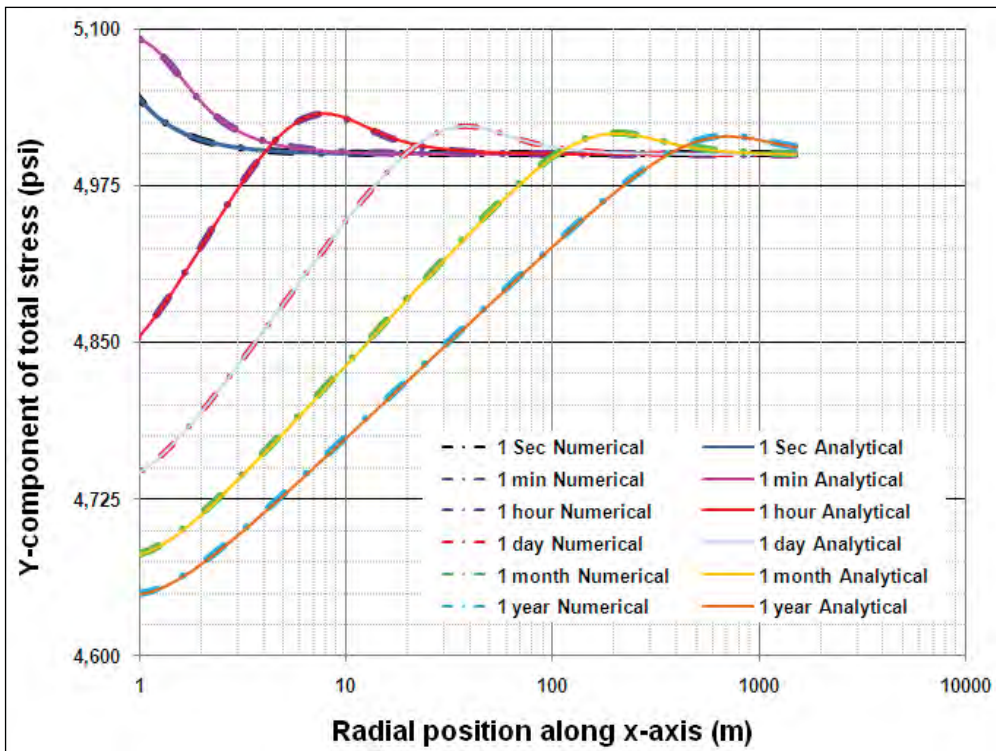


Fig. 2.16(c): Y-component of total stress (σ_y) as a function of time and radial position along x-axis for far field region (poroelastic reservoir, $\sigma_H = 6000$ psi, $\sigma_h = 5000$ psi, $p_i = 4000$ psi, $p_w = 2000$ psi, $k_x = 1.0$ mD, $k_y = 1.0$ mD).

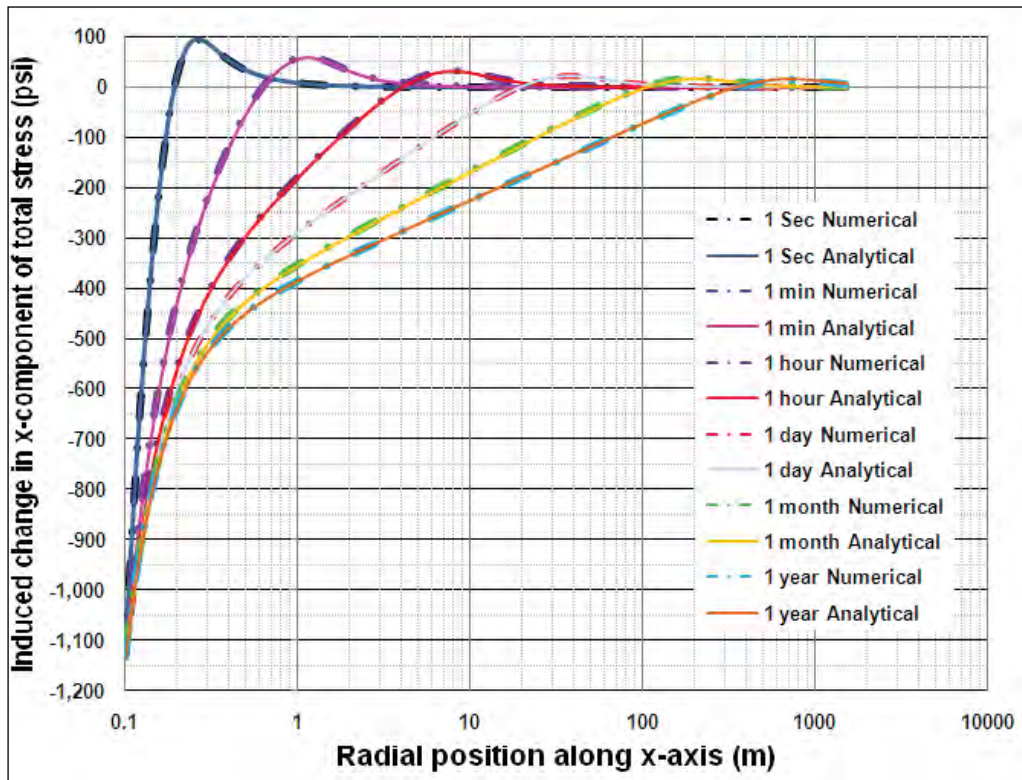


Fig. 2.17: Change in y-component of total stress ($\Delta\sigma_y$) as a function of time and radial position along y-axis (poroelastic reservoir, $\sigma_H = 6000$ psi, $\sigma_h = 5000$ psi, $p_i = 4000$ psi, $p_w = 2000$ psi, $k_x = 1.0$ mD, $k_y = 1.0$ mD).

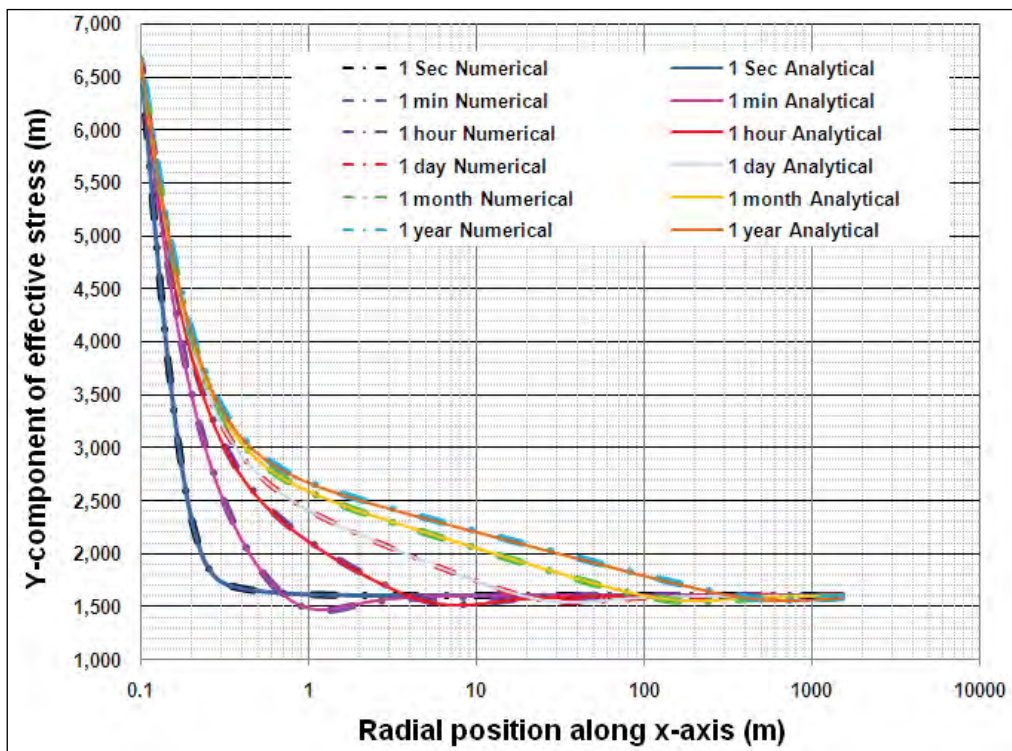


Fig. 2.18(a): Y-component of effective stress (σ'_y) as a function of time and radial position along X-axis for entire region (poroelastic reservoir, $\sigma_H = 6000$ psi, $\sigma_h = 5000$ psi, $p_i = 4000$ psi, $p_w = 2000$ psi, $k_x = 1.0$ mD, $k_y = 1.0$ mD).

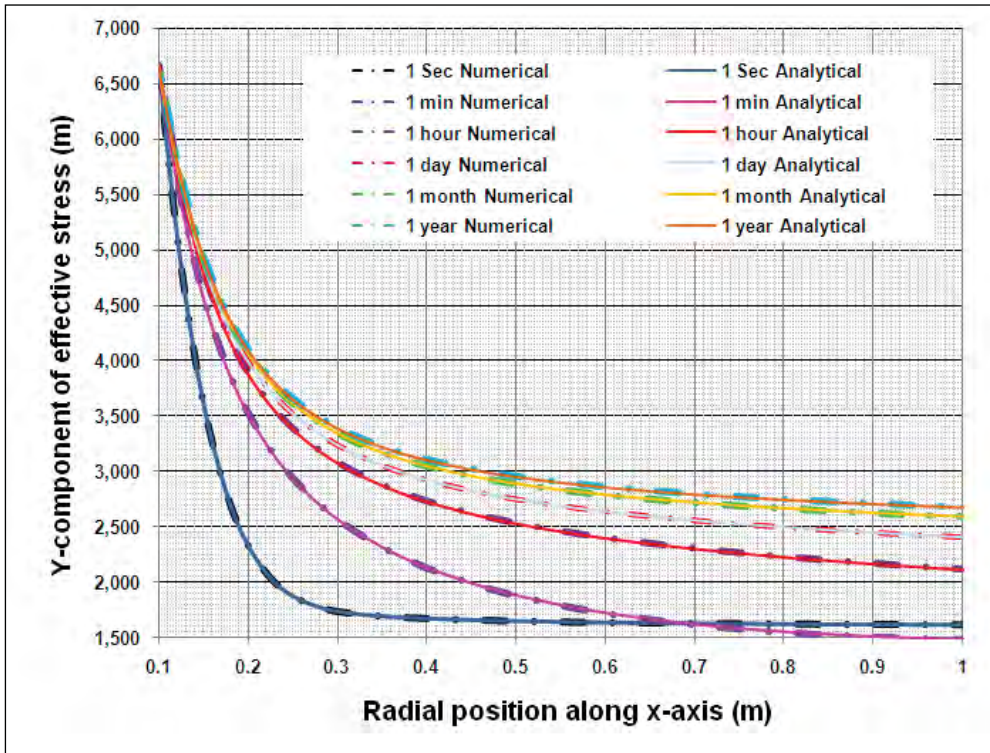


Fig. 2.18(b): Y-component of effective stress (σ'_y) as a function of time and radial position along X-axis for near wellbore region (poroelastic reservoir, $\sigma_H = 6000$ psi, $\sigma_h = 5000$ psi, $p_i = 4000$ psi, $p_w = 2000$ psi, $k_x = 1.0$ mD, $k_y = 1.0$ mD).

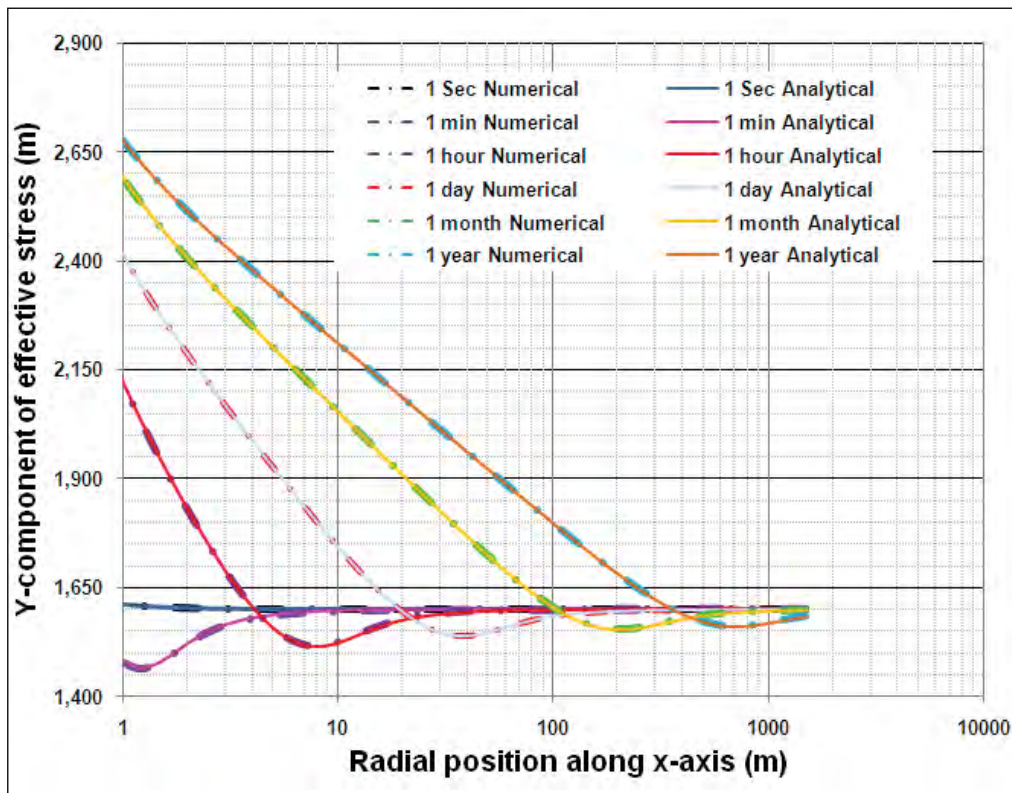


Fig. 2.18(c): Y-component of effective stress (σ'_y) as a function of time and radial position along X-axis for far field region (poroelastic reservoir, $\sigma_H = 6000$ psi, $\sigma_h = 5000$ psi, $p_i = 4000$ psi, $p_w = 2000$ psi, $k_x = 1.0$ mD, $k_y = 1.0$ mD).

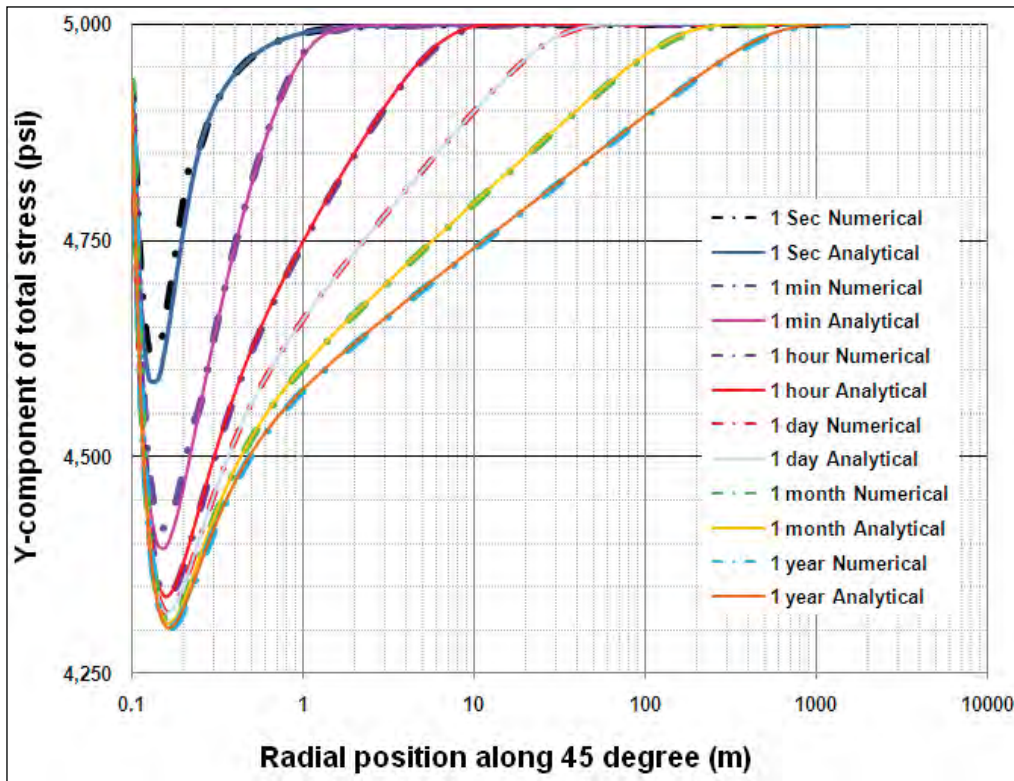


Fig. 2.19(a): Y-component of total stress (σ_y) as a function of time and radial position along 45° for entire region (poroelastic reservoir, $\sigma_H = 6000$ psi, $\sigma_h = 5000$ psi, $p_i = 4000$ psi, $p_w = 2000$ psi, $k_x = 1.0$ mD, $k_y = 1.0$ mD).

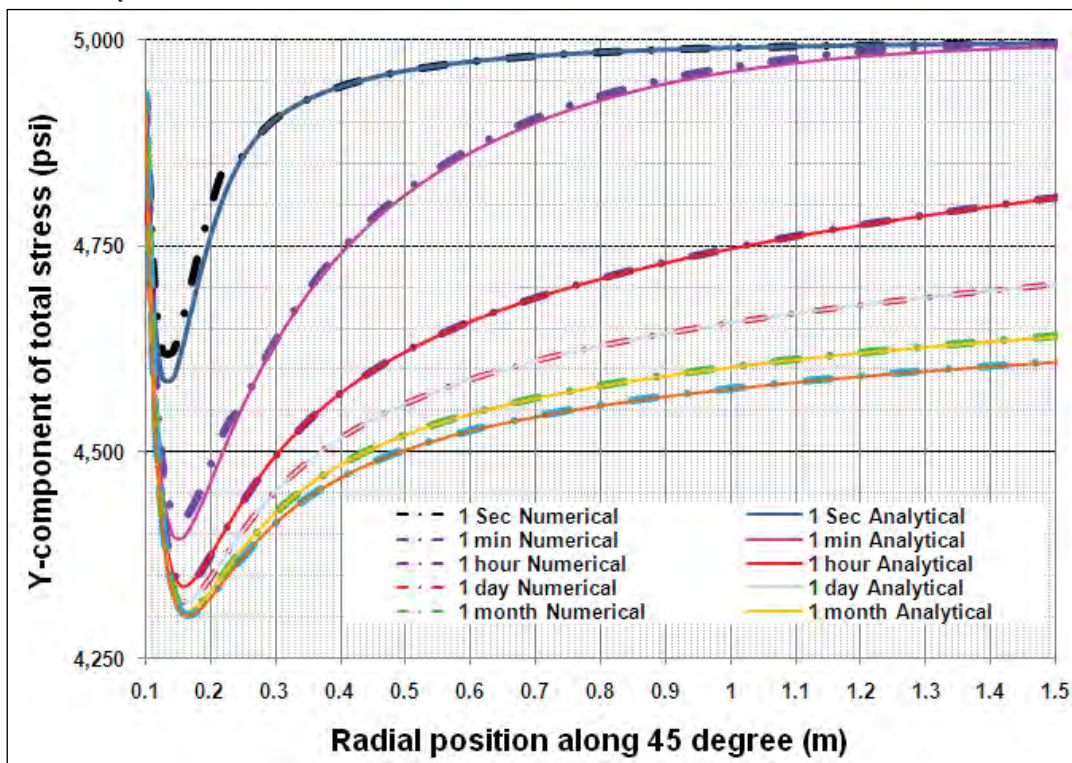


Fig. 2.19(b): Y-component of total stress (σ_y) as a function of time and radial position along 45° for near wellbore region (poroelastic reservoir, $\sigma_H = 6000$ psi, $\sigma_h = 5000$ psi, $p_i = 4000$ psi, $p_w = 2000$ psi, $k_x = 1.0$ mD, $k_y = 1.0$ mD).

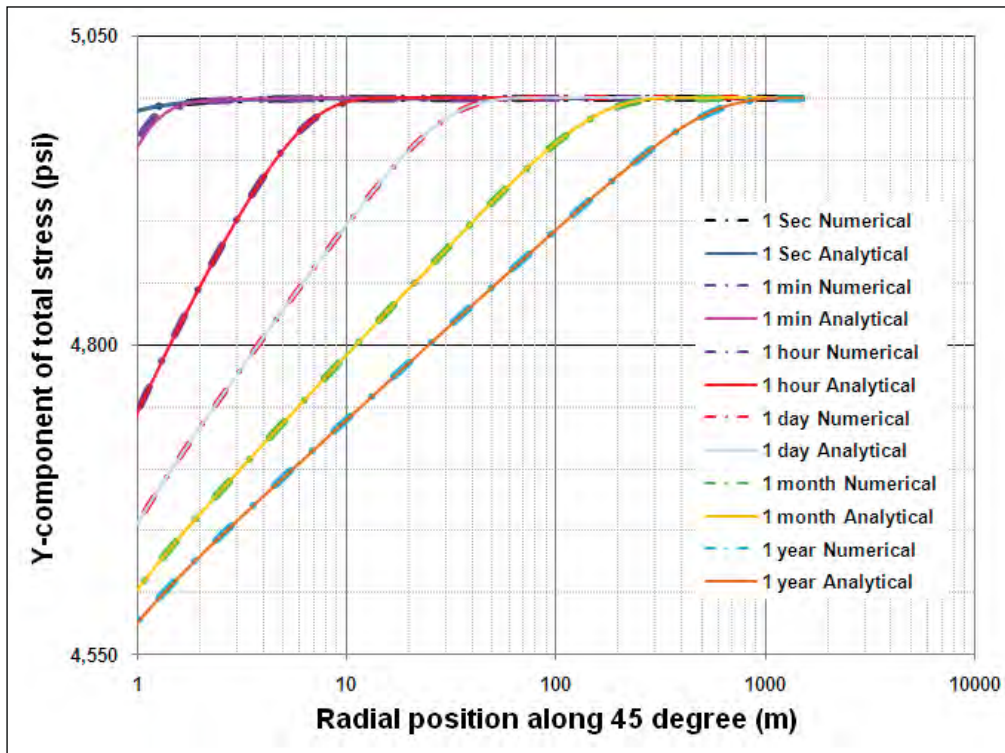


Fig. 2.19(c): Y-component of total stress (σ_y) as a function of time and radial position along 45° for far field (poroelastic reservoir, $\sigma_H = 6000$ psi, $\sigma_h = 5000$ psi, $p_i = 4000$ psi, $p_w = 2000$ psi, $k_x = 1.0$ mD, $k_y = 1.0$ mD).

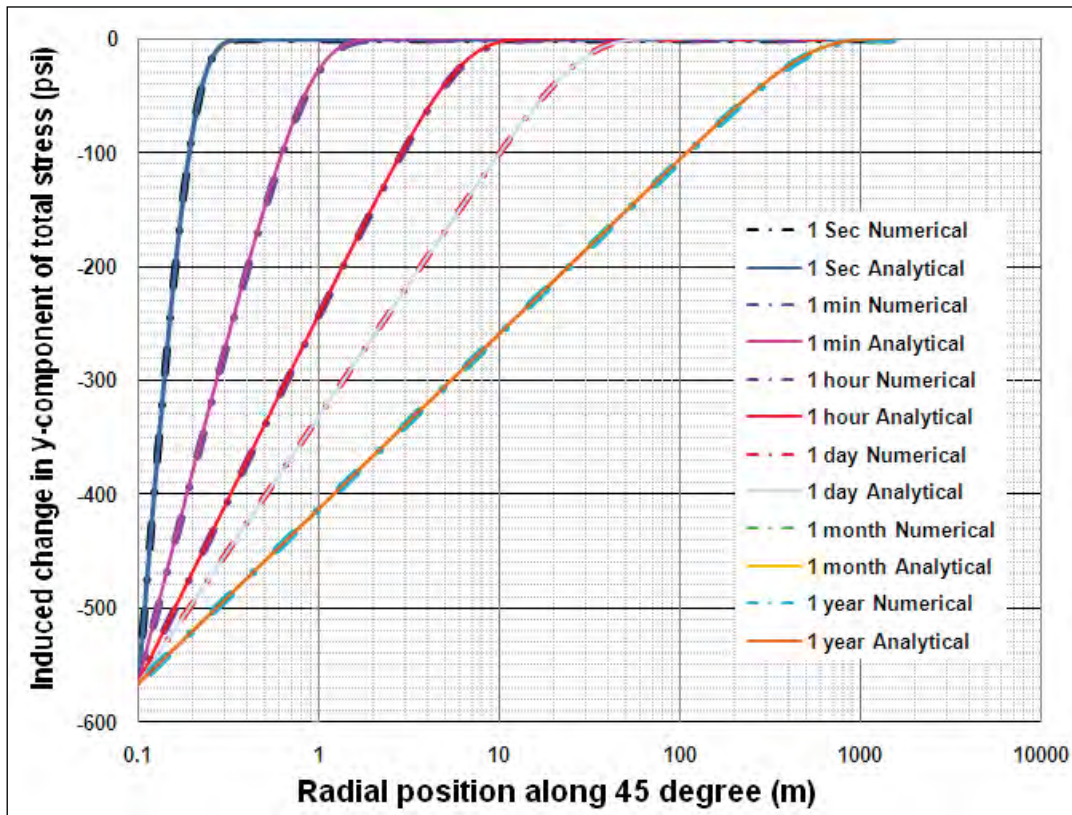


Fig. 2.20: Change in y-component of total stress ($\Delta\sigma_y$) as a function of time and radial position along 45° (poroelastic reservoir, $\sigma_H = 6000$ psi, $\sigma_h = 5000$ psi, $p_i = 4000$ psi, $p_w = 2000$ psi, $k_x = 1.0$ mD, $k_y = 1.0$ mD).

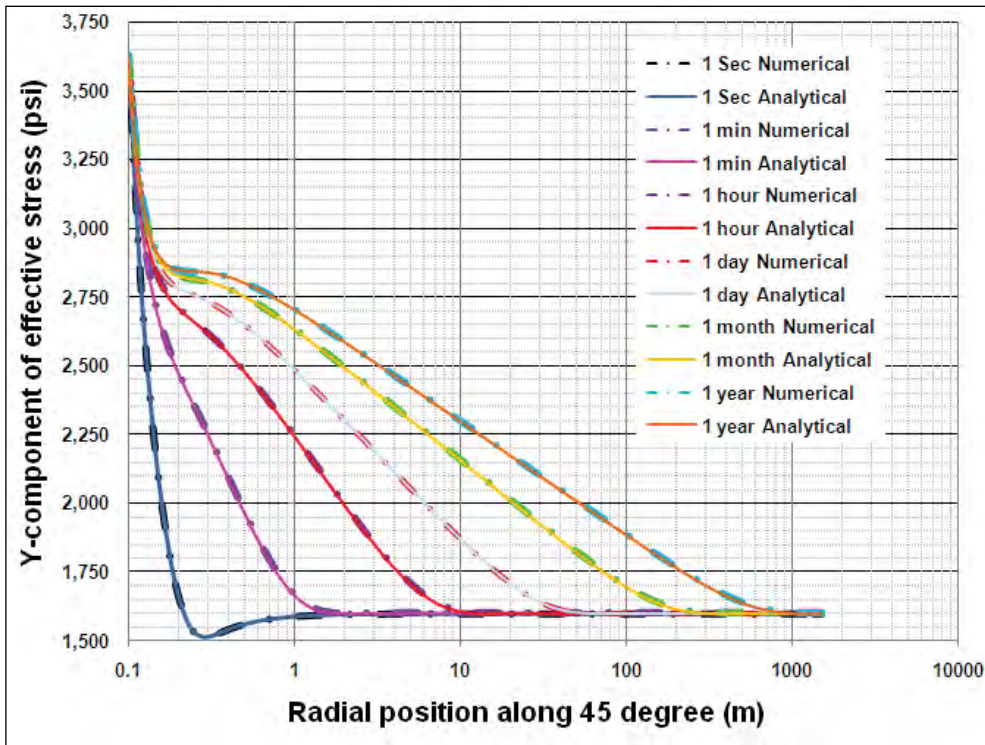


Fig. 2.21(a): Y-component of effective stress (σ'_y) as a function of time and radial position along 45° for entire region (poroelastic reservoir, $\sigma_H = 6000$ psi, $\sigma_h = 5000$ psi, $p_i = 4000$ psi, $p_w = 2000$ psi, $k_x = 1.0$ mD, $k_y = 1.0$ mD).

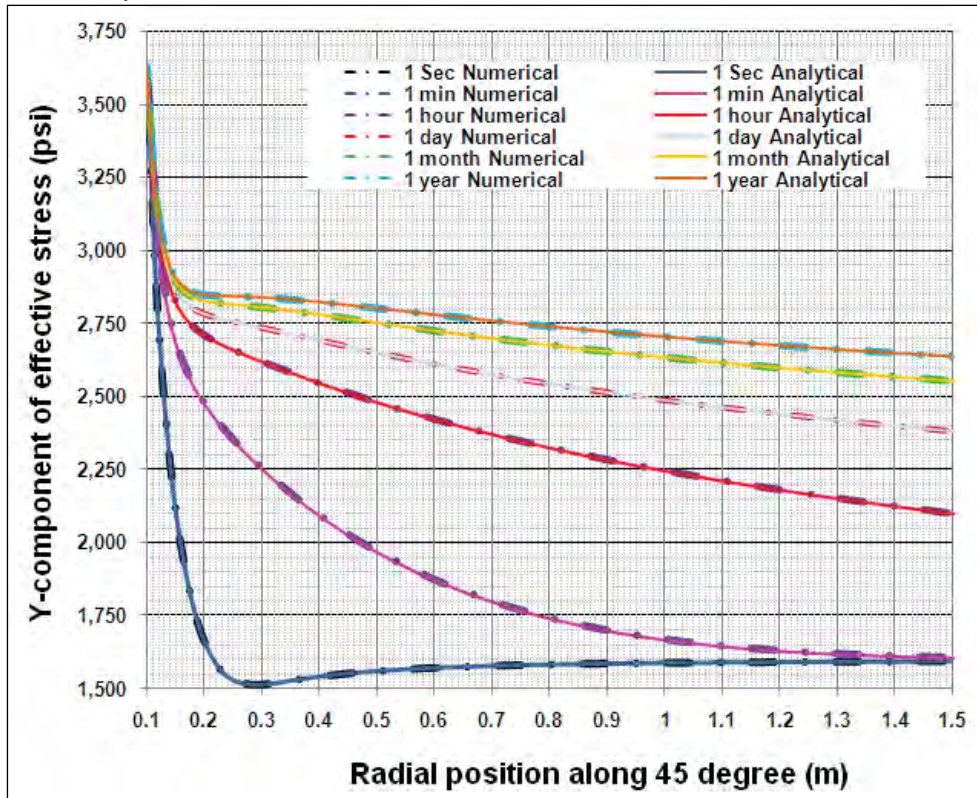


Fig. 2.21(b): Y-component of effective stress (σ'_y) as a function of time and radial position along 45° for near wellbore region (poroelastic reservoir, $\sigma_H = 6000$ psi, $\sigma_h = 5000$ psi, $p_i = 4000$ psi, $p_w = 2000$ psi, $k_x = 1.0$ mD, $k_y = 1.0$ mD).

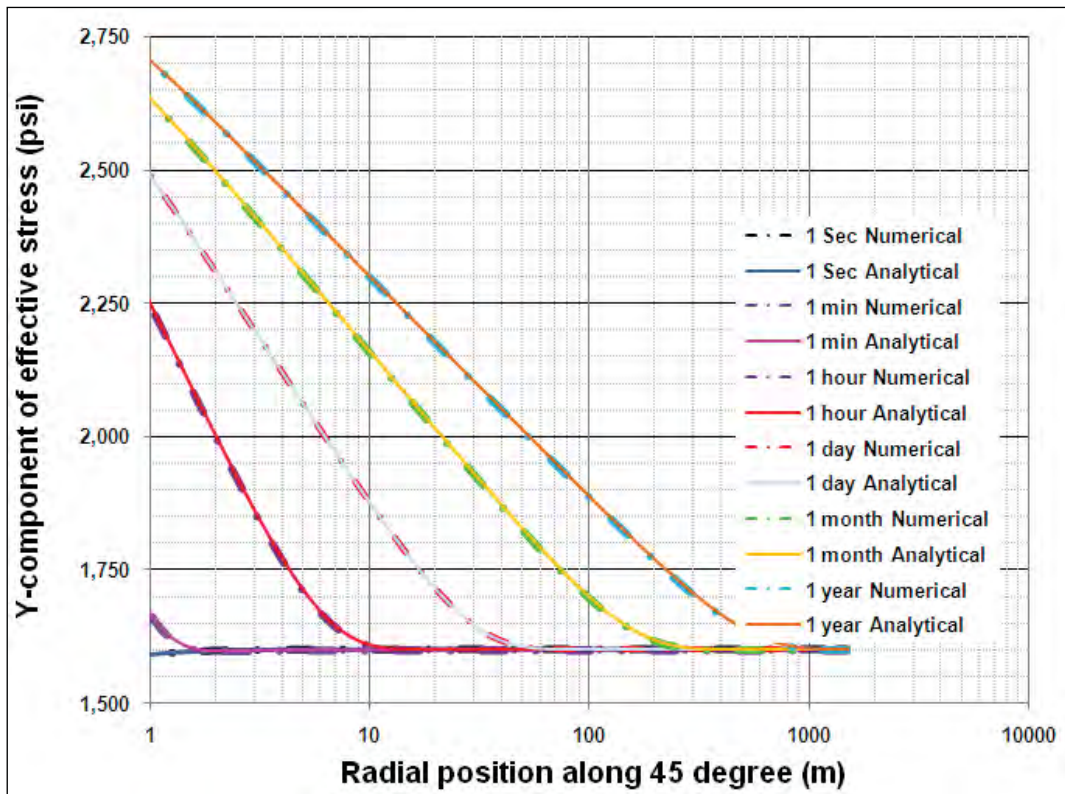


Fig. 2.21(c): Y-component of effective stress (σ'_y) as a function of time and radial position along 45° for far field region (poroelastic reservoir, $\sigma_H = 6000$ psi, $\sigma_h = 5000$ psi, $p_i = 4000$ psi, $p_w = 2000$ psi, $k_x = 1.0$ mD, $k_y = 1.0$ mD).

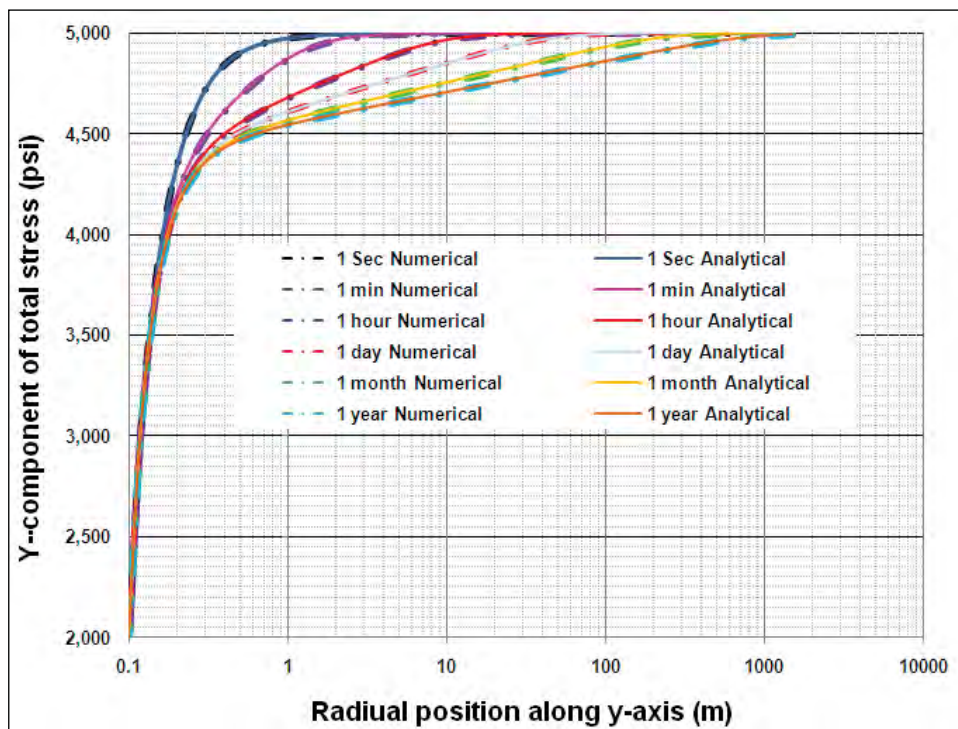


Fig. 2.22(a): Y-component of total stress (σ_y) as a function of time and radial position along y-axis (90°) for entire region (poroelastic reservoir, $\sigma_H = 6000$ psi, $\sigma_h = 5000$ psi, $p_i = 4000$ psi, $p_w = 2000$ psi, $k_x = 1.0$ mD, $k_y = 1.0$ mD).

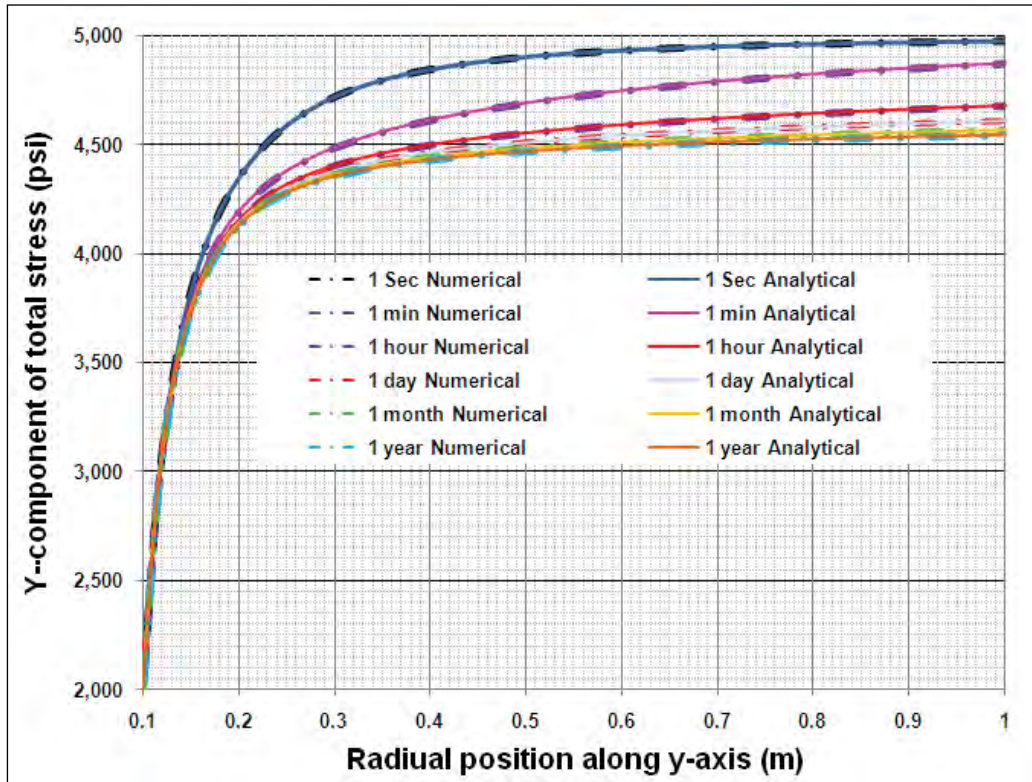


Fig. 2.22(b): Y-component of total stress (σ_y) as a function of time and radial position along y-axis (90°) for near wellbore region (poroelastic reservoir, $\sigma_H = 6000$ psi, $\sigma_h = 5000$ psi, $p_i = 4000$ psi, $p_w = 2000$ psi, $k_x = 1.0$ mD, $k_y = 1.0$ mD).

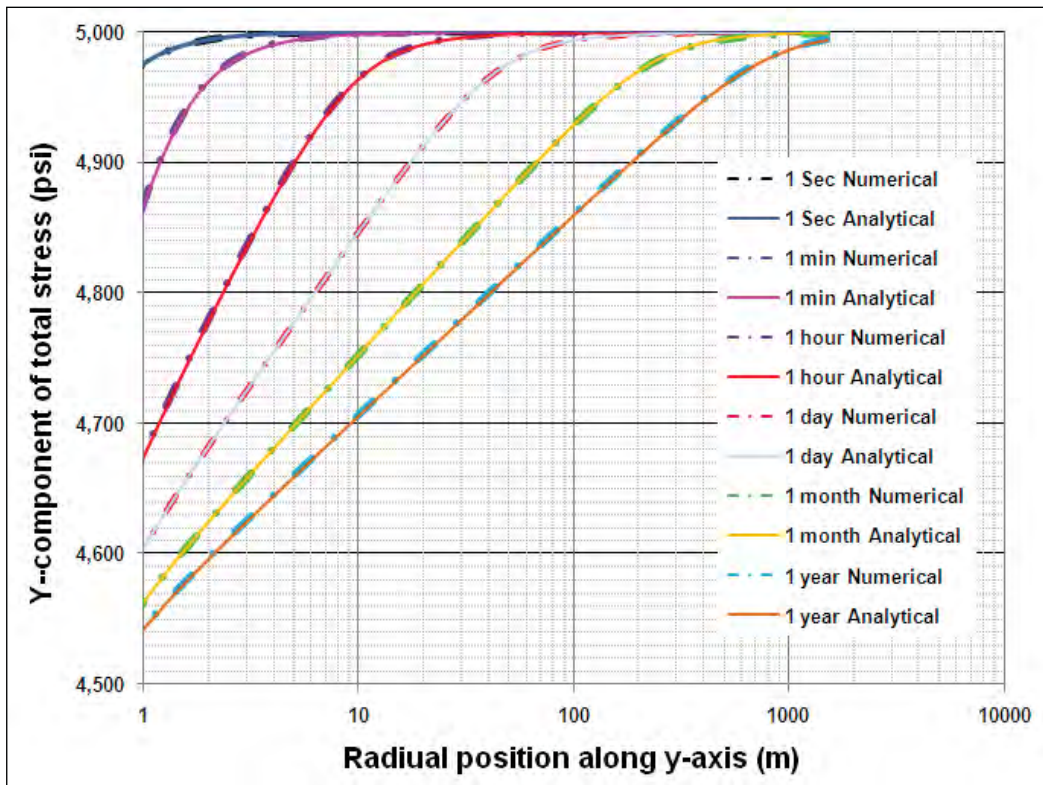


Fig. 2.22(c): Y-component of total stress (σ_y) as a function of time and radial position along y-axis (90°) for far field region (poroelastic reservoir, $\sigma_H = 6000$ psi, $\sigma_h = 5000$ psi, $p_i = 4000$ psi, $p_w = 2000$ psi, $k_x = 1.0$ mD, $k_y = 1.0$ mD).

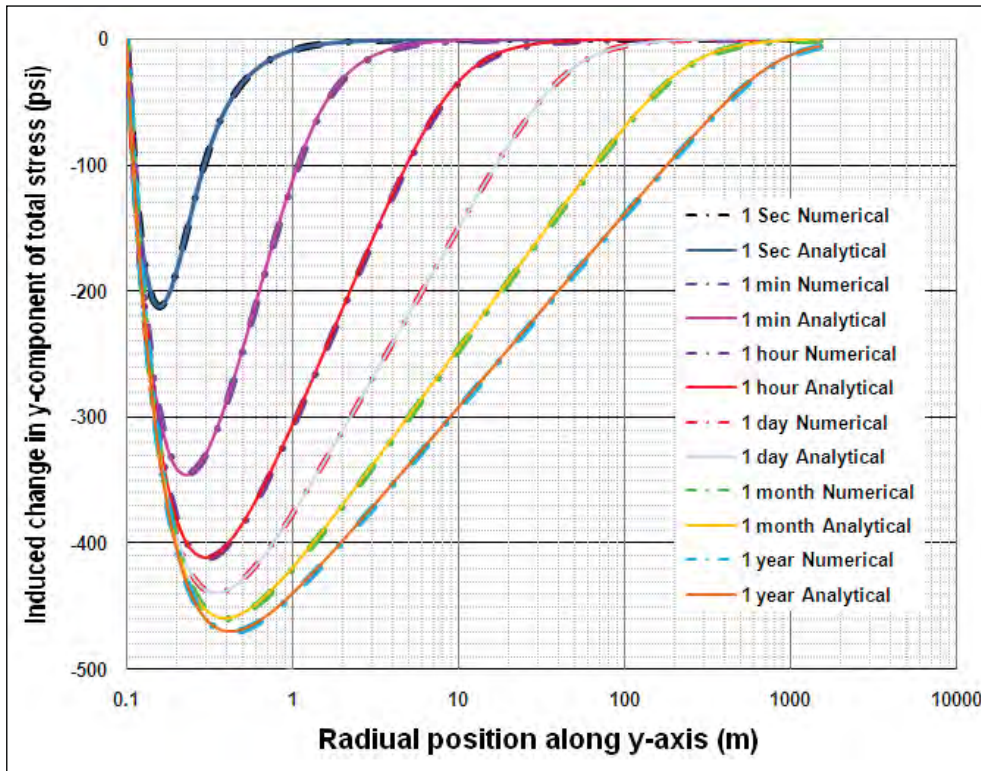


Fig. 2.23: Change in y-component of total stress ($\Delta\sigma_y$) as a function of time and radial position along y-axis (poroelastic reservoir, $\sigma_H = 6000$ psi, $\sigma_h = 5000$ psi, $p_i = 4000$ psi, $p_w = 2000$ psi, $k_x = 1.0$ mD, $k_y = 1.0$ mD).

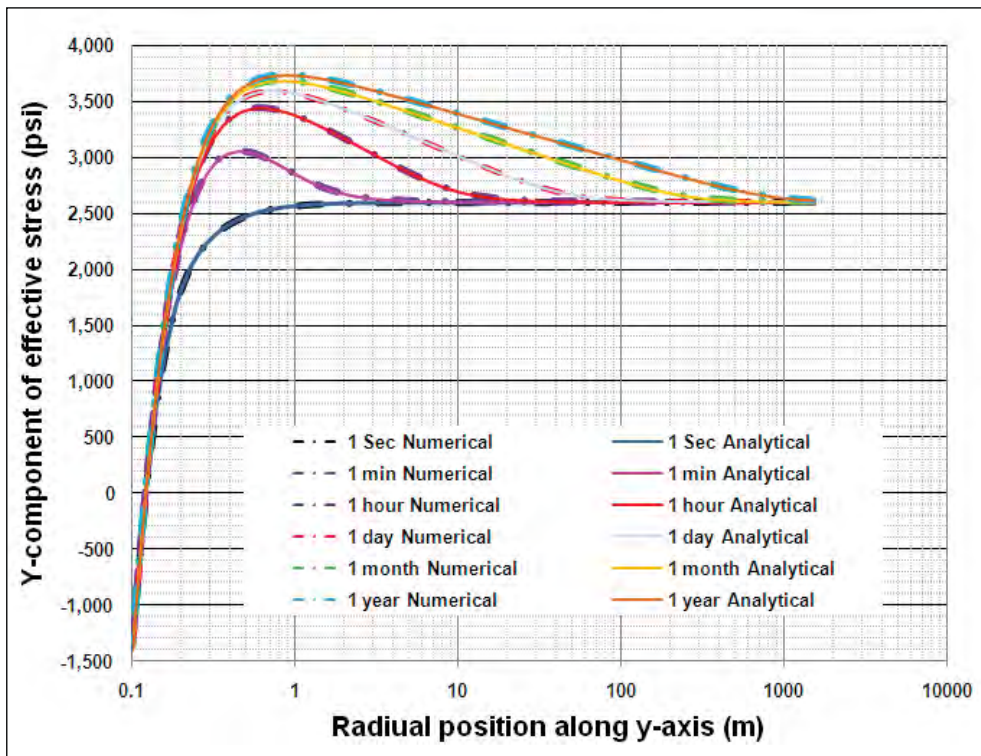


Fig. 2.24(a): Y-component of effective stress (σ'_y) as a function of time and radial position along y-axis (90°) for entire region (poroelastic reservoir, $\sigma_H = 6000$ psi, $\sigma_h = 5000$ psi, $p_i = 4000$ psi, $p_w = 2000$ psi, $k_x = 1.0$ mD, $k_y = 1.0$ mD).

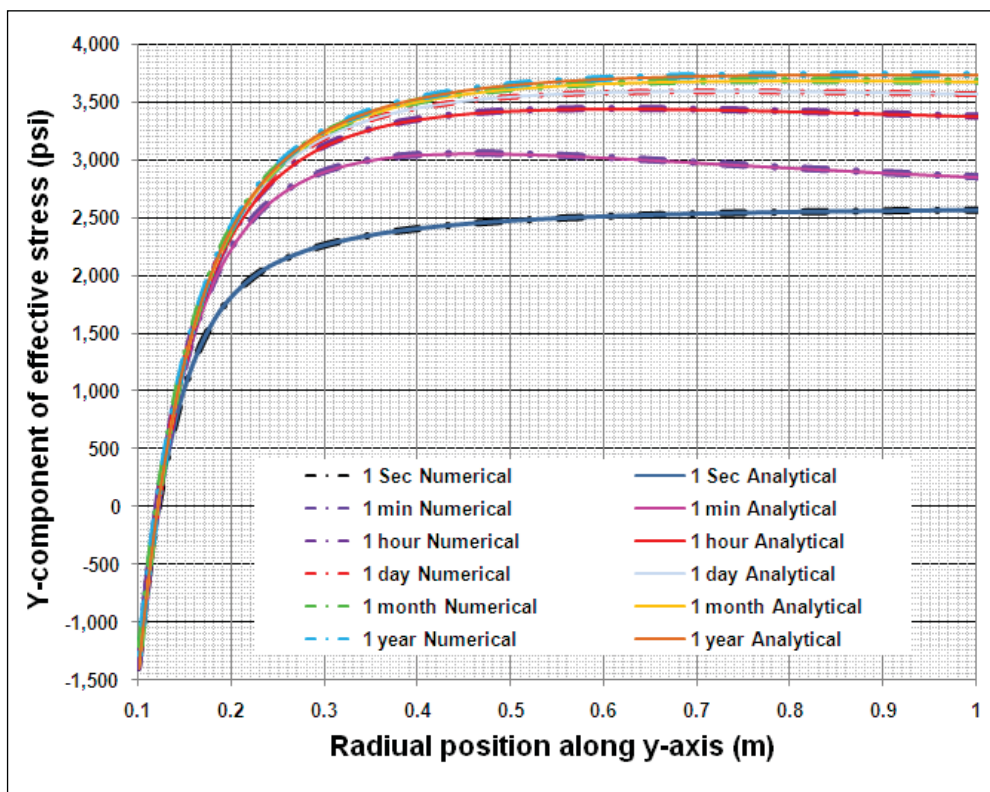


Fig. 2.24(b): Y-component of effective stress (σ'_y) as a function of time and radial position along y-axis (90°) for near wellbore region (poroelastic reservoir, $\sigma_H = 6000$ psi, $\sigma_h = 5000$ psi, $p_i = 4000$ psi, $p_w = 2000$ psi, $k_x = 1.0$ mD, $k_y = 1.0$ mD).

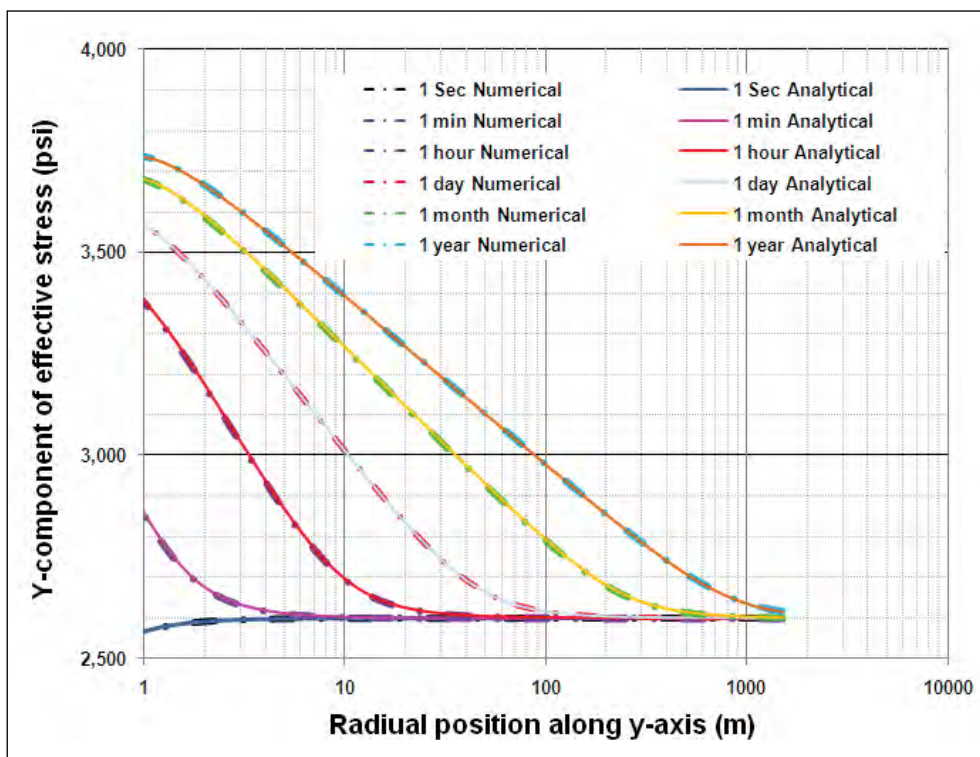


Fig. 2.24(c): Y-component of effective stress (σ'_y) as a function of time and radial position along y-axis (90°) for far field region (poroelastic reservoir, $\sigma_H = 6000$ psi, $\sigma_h = 5000$ psi, $p_i = 4000$ psi, $p_w = 2000$ psi, $k_x = 1.0$ mD, $k_y = 1.0$ mD).

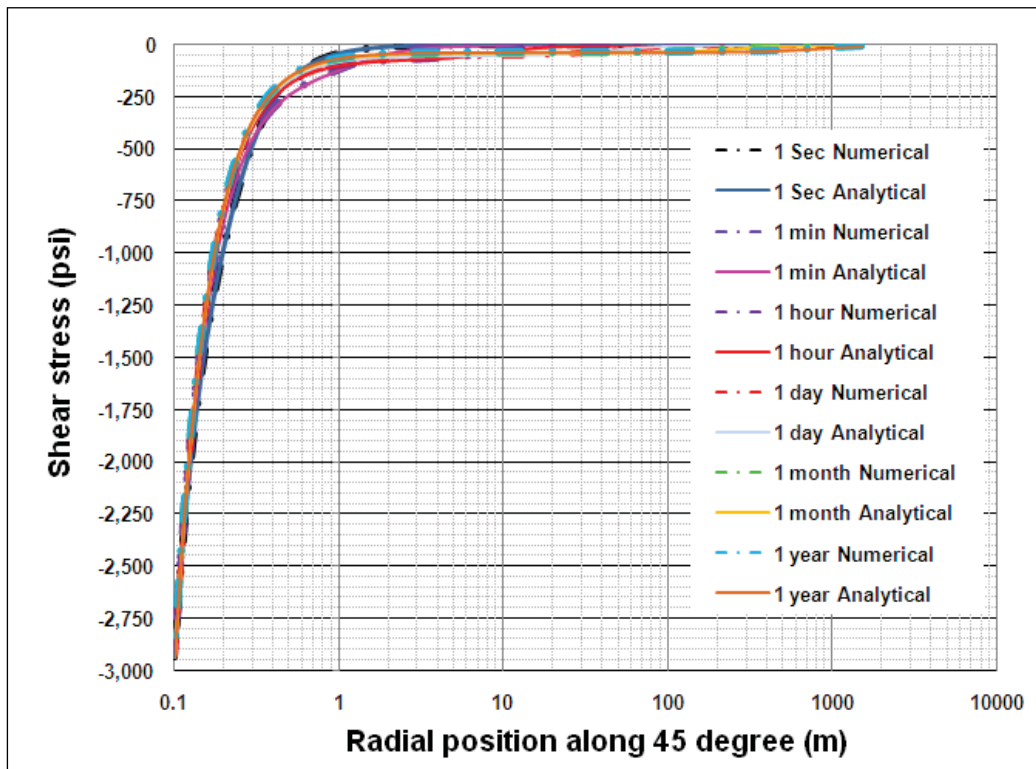


Fig. 2.25(a): Shear stress (σ_{xy}) as a function of time and radial position along 45° for entire region (poroelastic reservoir, $\sigma_H = 6000$ psi, $\sigma_h = 5000$ psi, $p_i = 4000$ psi, $p_w = 2000$ psi, $k_x = 1.0$ mD, $k_y = 1.0$ mD).

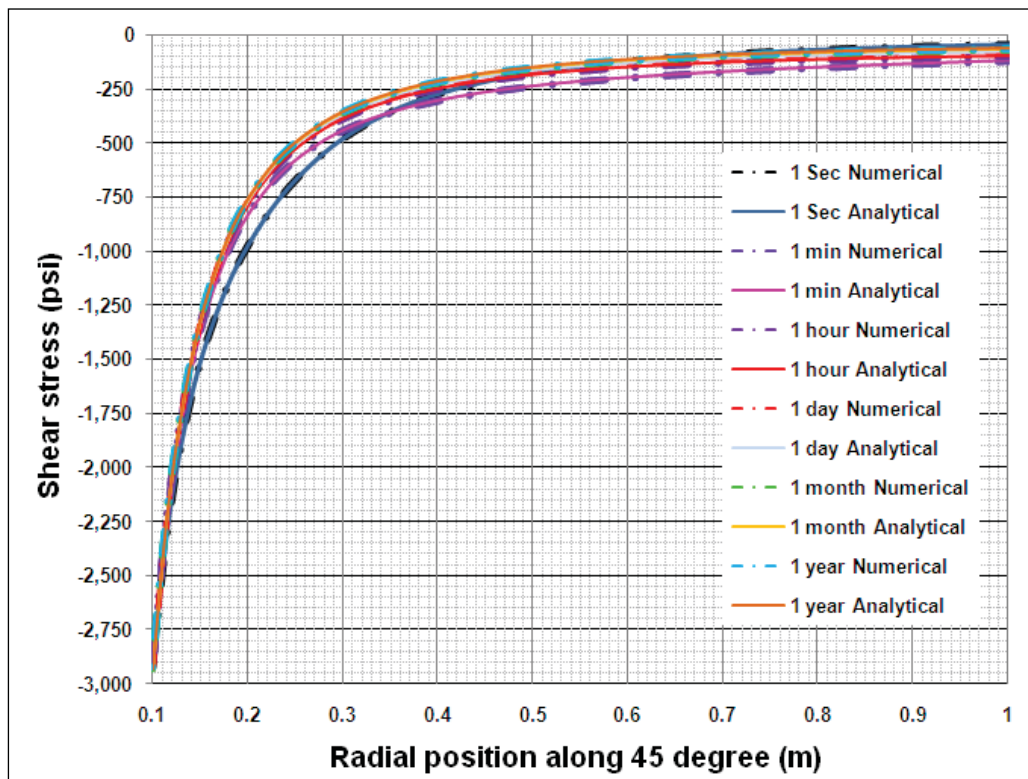


Fig. 2.25(b): Shear stress (σ_{xy}) as a function of time and radial position along 45° for near wellbore region (poroelastic reservoir, $\sigma_H = 6000$ psi, $\sigma_h = 5000$ psi, $p_i = 4000$ psi, $p_w = 2000$ psi, $k_x = 1.0$ mD, $k_y = 1.0$ mD).

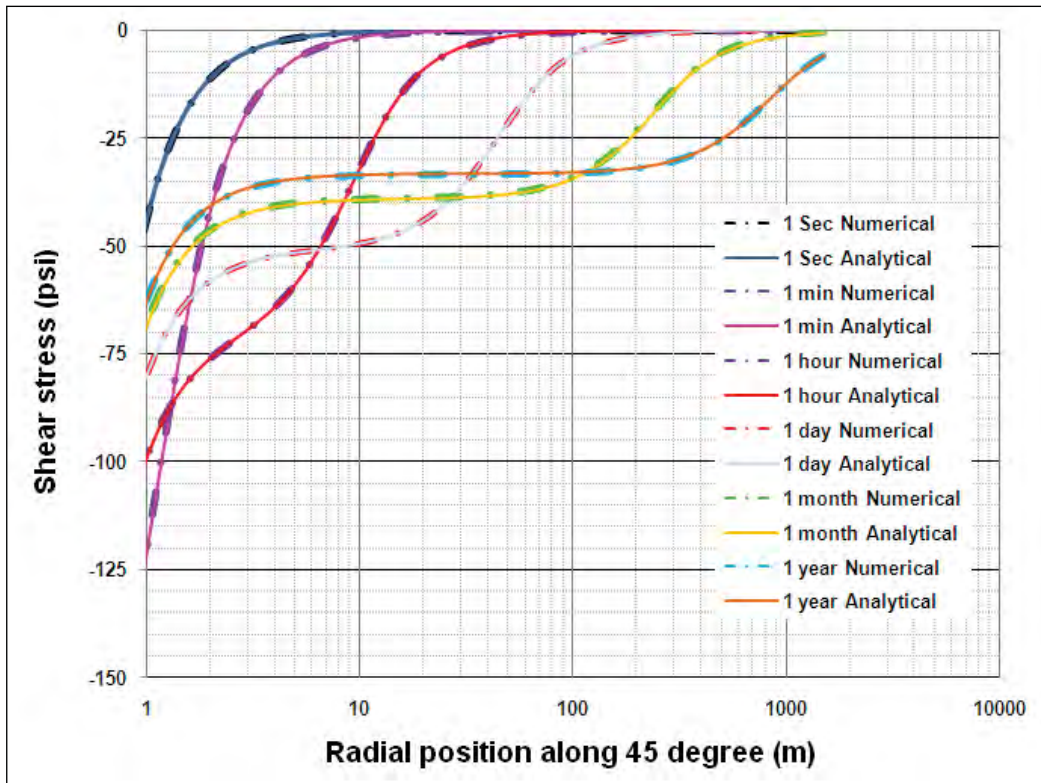


Fig .2.25(c): Shear stress (σ_{xy}) as a function of time and radial position along 45° for far field region (poroelastic reservoir, $\sigma_H = 6000$ psi, $\sigma_h = 5000$ psi, $p_i = 4000$ psi, $p_w = 2000$ psi, $k_x = 1.0$ mD, $k_y = 1.0$ mD).

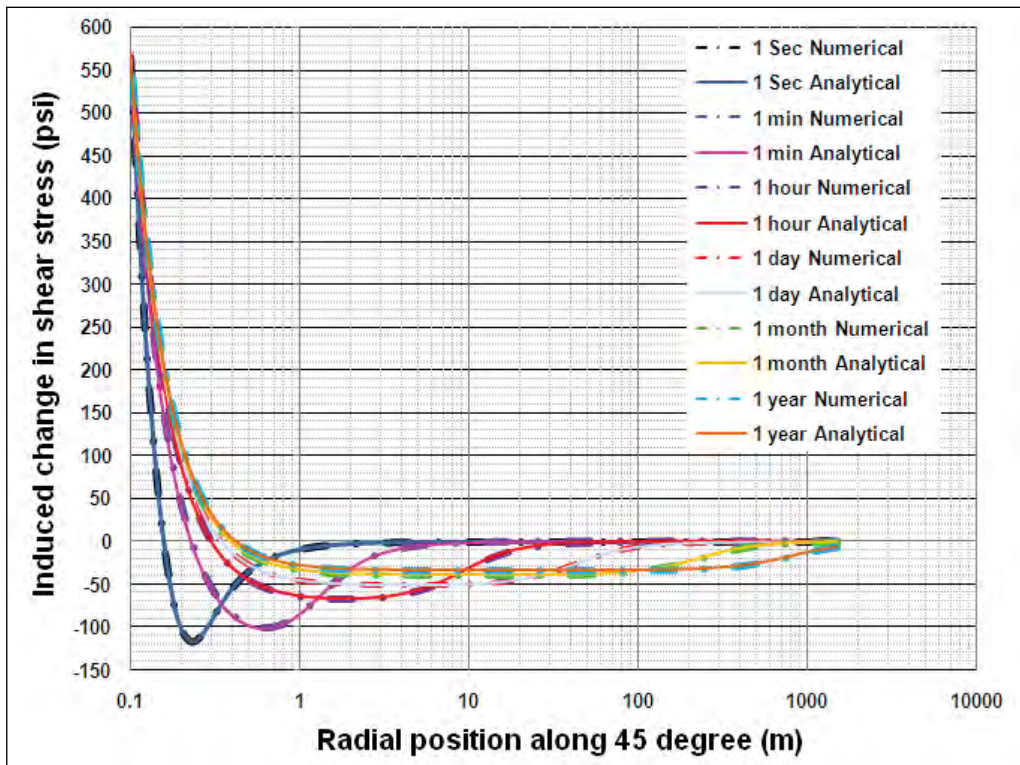


Fig. 2.26: Change in shear stress (σ_{xy}) as a function of time and radial position along 45° (poroelastic reservoir, $\sigma_H = 6000$ psi, $\sigma_h = 5000$ psi, $p_i = 4000$ psi, $p_w = 2000$ psi, $k_x = 1.0$ mD, $k_y = 1.0$ mD).

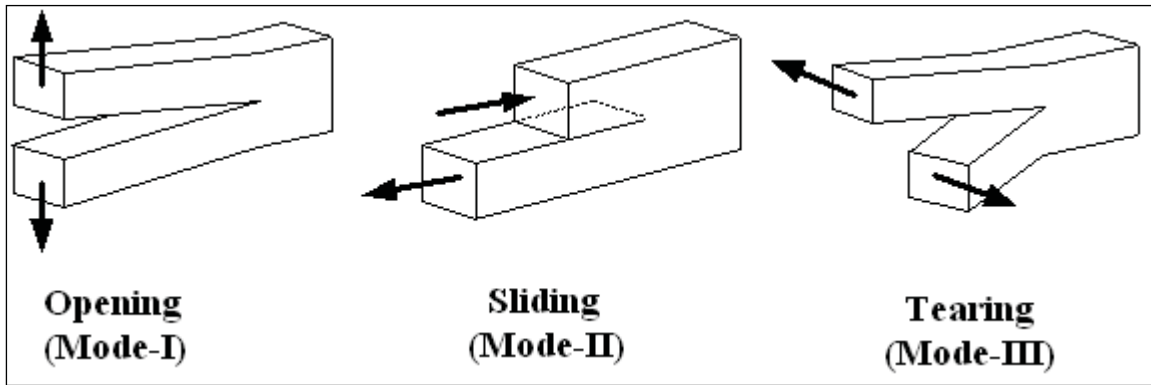


Fig .2.27: Schematic illustration of three basic modes of fracture extension.

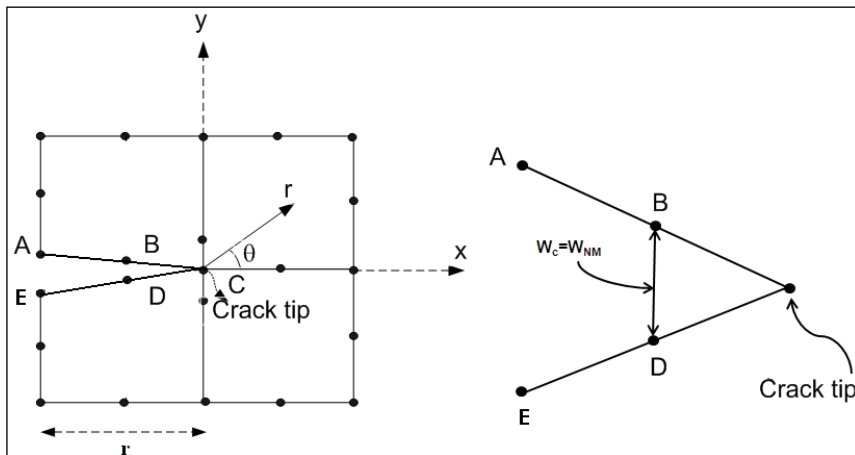


Fig. 2.28: Nodal arrangement of fracture tip element for calculation of critical width.

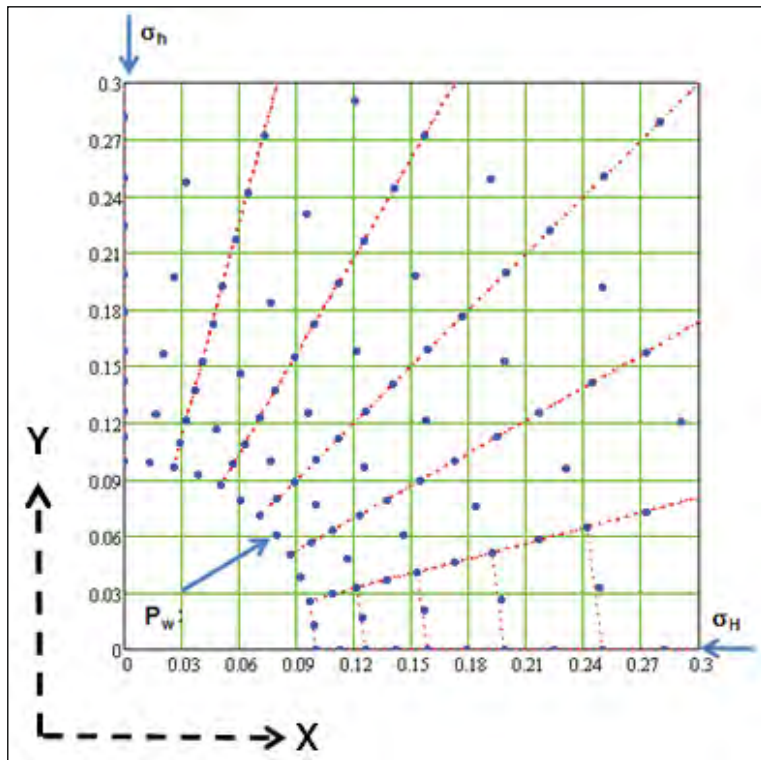


Fig. 2.29: Finite element mesh used for simulation.

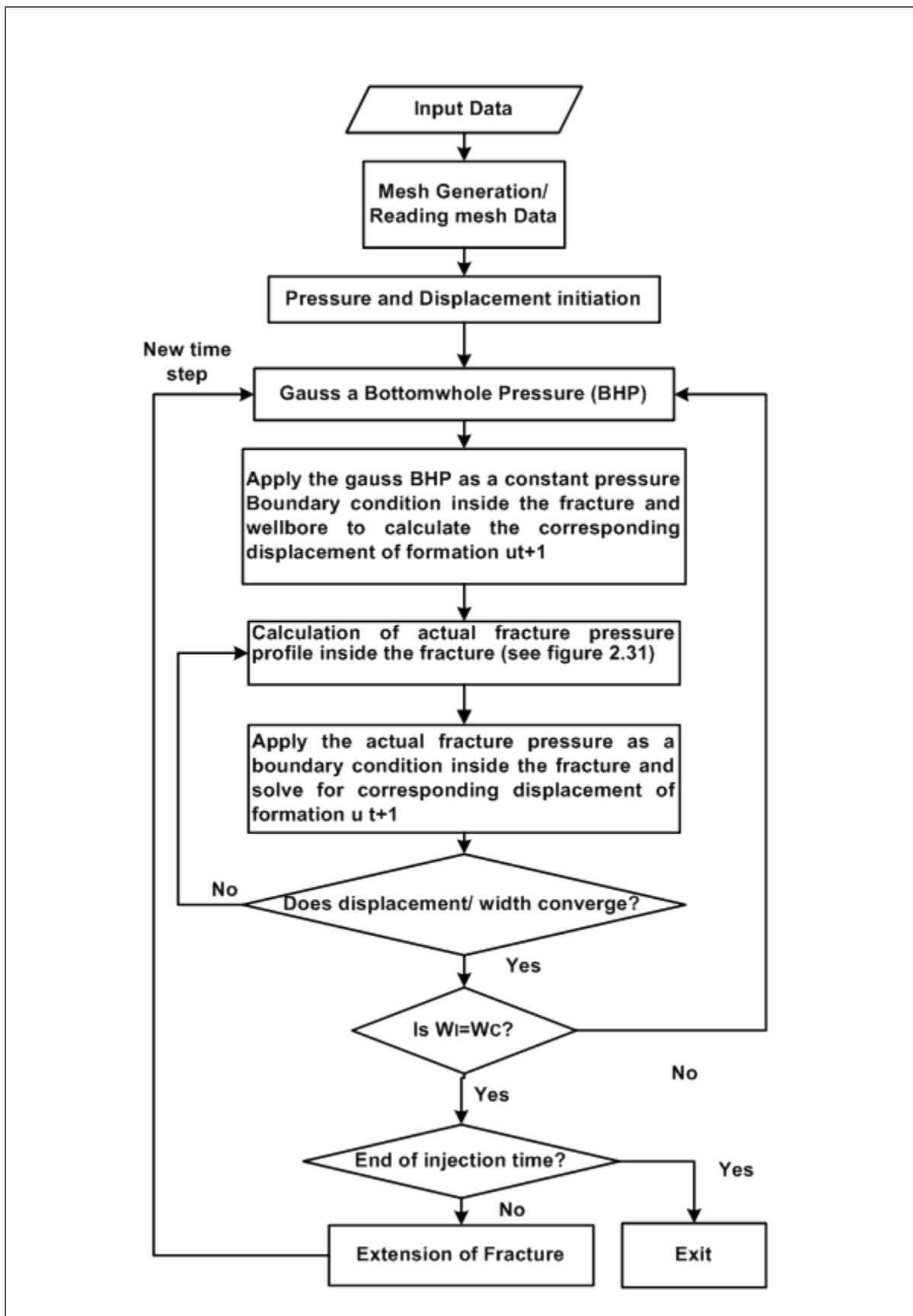


Fig. 2.30: Algorithm of hydraulic fracture propagation model.

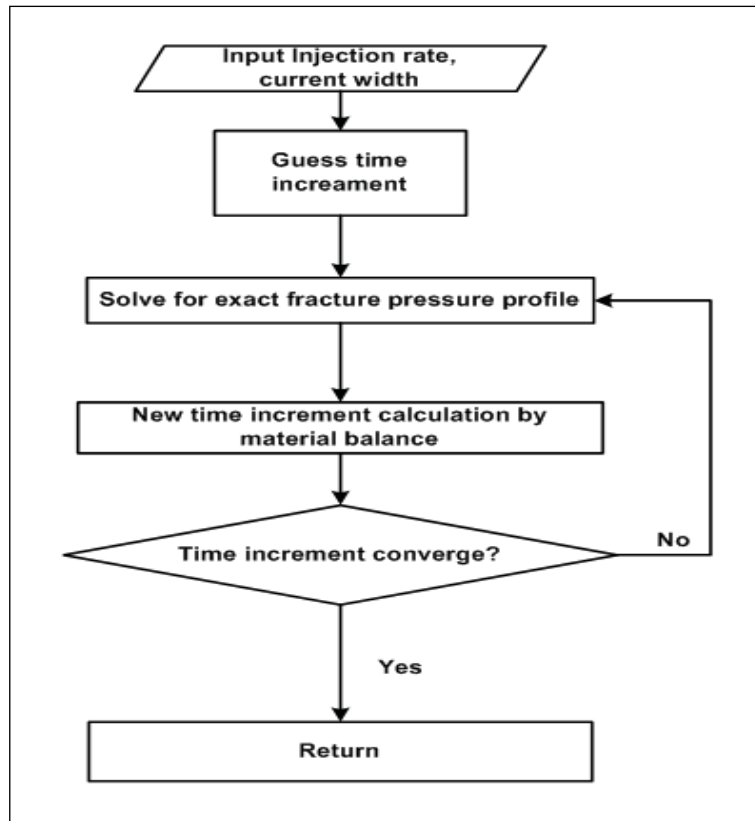


Fig. 2.31: Algorithm of fracture pressure profile calculation.

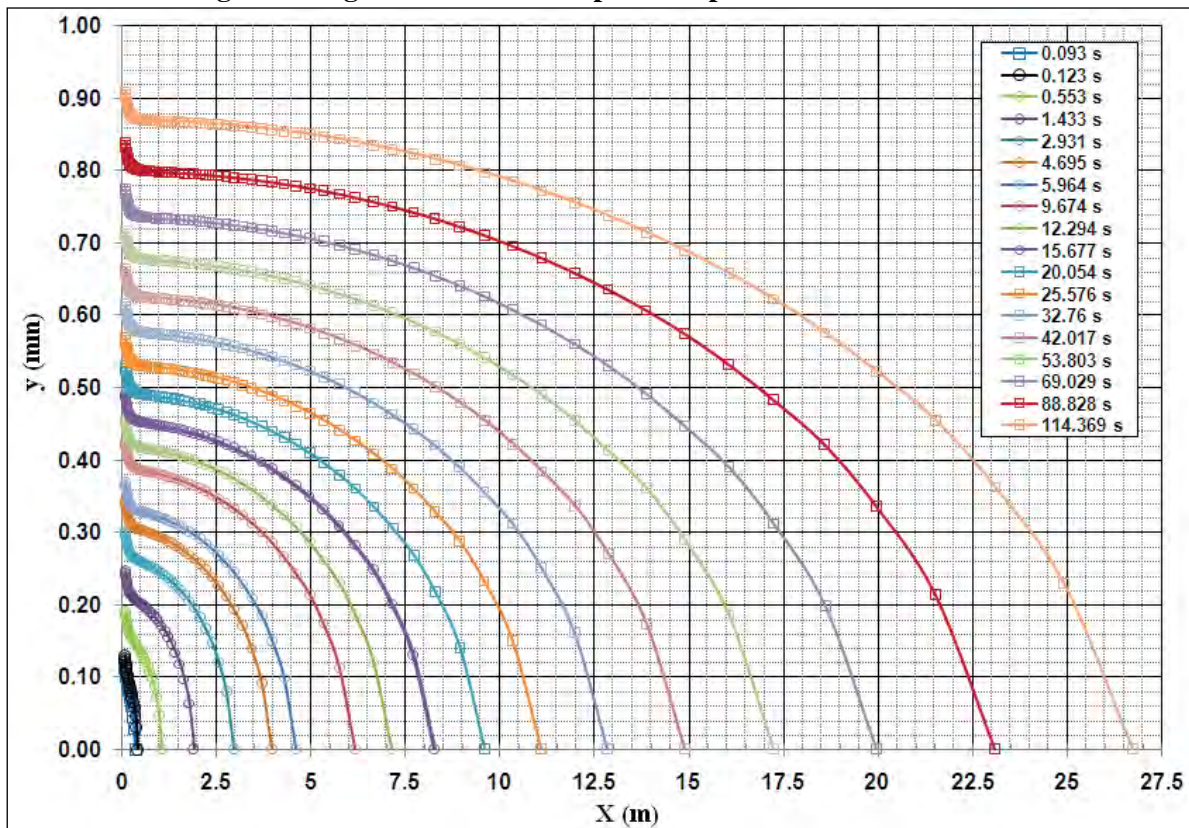


Fig .2.32: Fracture profile for selected time steps (poroelastic reservoir, $\sigma_H = 6000$ psi, $\sigma_h = 5000$ psi, $p_i = 4500$ psi, $\mu_f = 1$ cp, $q = 10$ bbl/min, $k = 0.1$ mD, $K_{IC} = 500$ psi.ft^{0.5}).

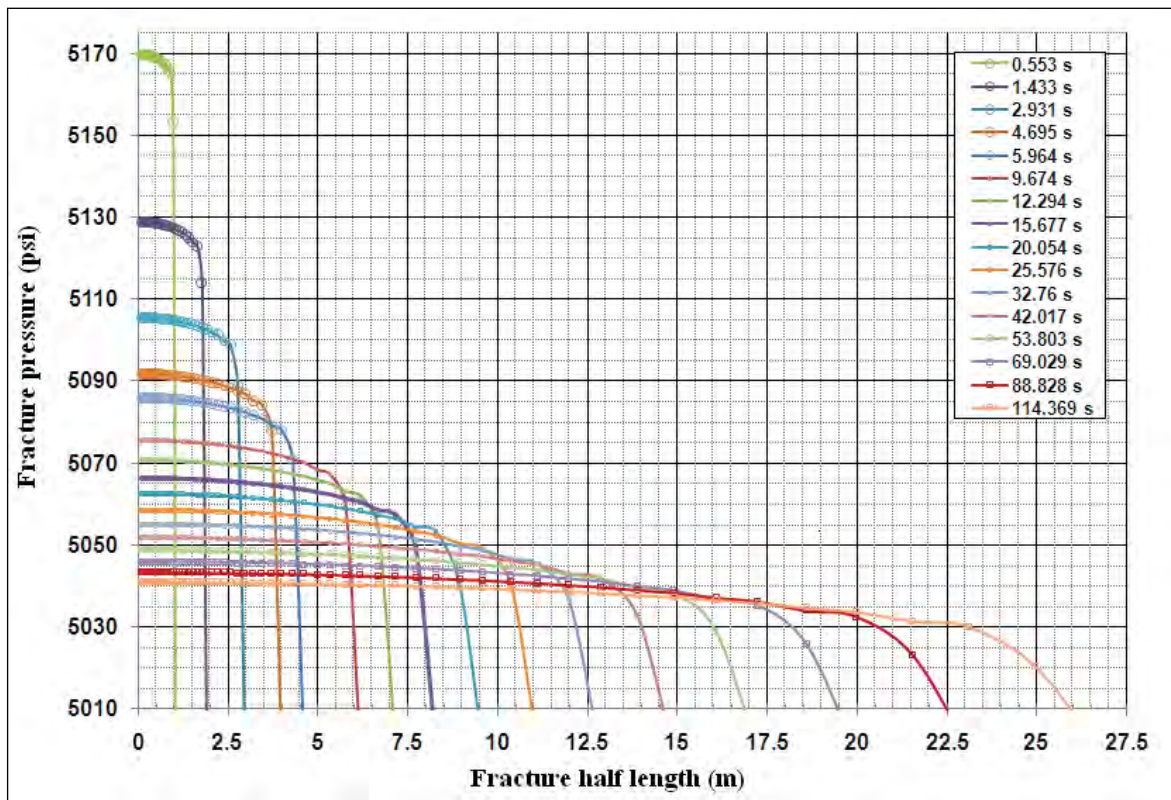


Fig .2.33: Fracturing fluid pressure profile for selected time steps (poroelastic reservoir, $\sigma_H = 6000$ psi, $\sigma_h = 5000$ psi, $p_i = 4500$ psi, $\mu_f = 1$ cp, $q = 10$ bbl/min, $k = 0.1$ mD, $K_{IC} = 500$ psi.ft^{0.5}).

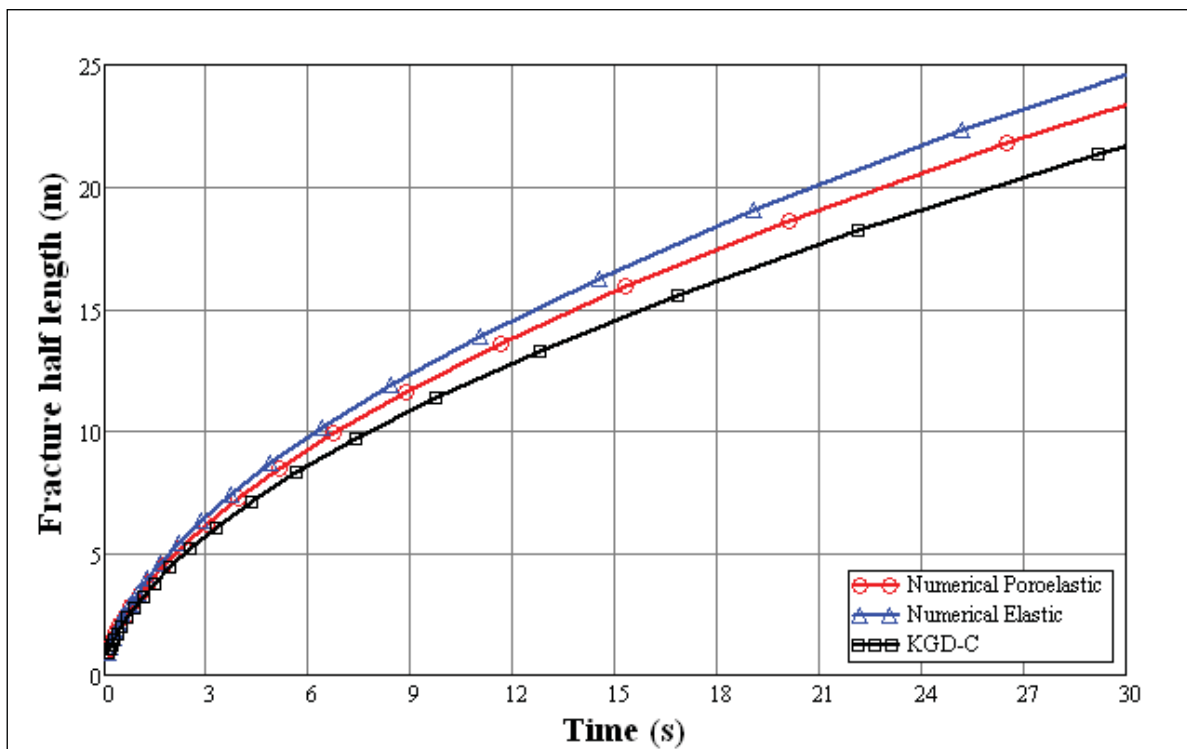


Fig .2.34: Fracture half length vs., pumping time for the numerical poroelastic and elastic fracturing models as well as KGD-C model ($\sigma_H = 6000$ psi, $\sigma_h = 5000$ psi, $p_i = 4500$ psi, $\mu_f = 1$ cp, $q = 10$ bbl/min, $k = 0.1$ mD, $K_{IC} = 500$ psi.ft^{0.5}).

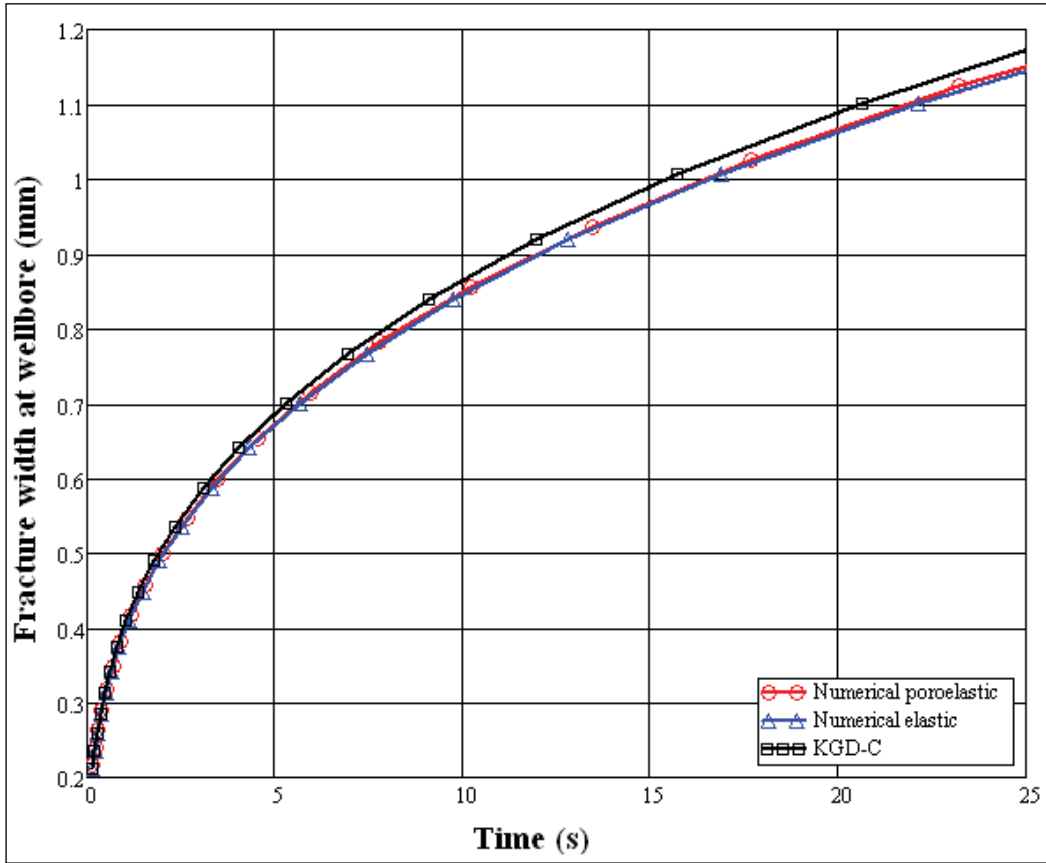


Fig. 2.35: Fracture width vs. pumping time for the numerical poroelastic, elastic fracturing models and KGD-C model ($\sigma_H = 6000$ psi, $\sigma_h = 5000$ psi, $p_i = 4500$ psi, $\mu_f = 1$ cp, $q = 10$ bbl/min, $k = 0.1$ mD, $K_{IC} = 500$ psi.ft^{0.5}).

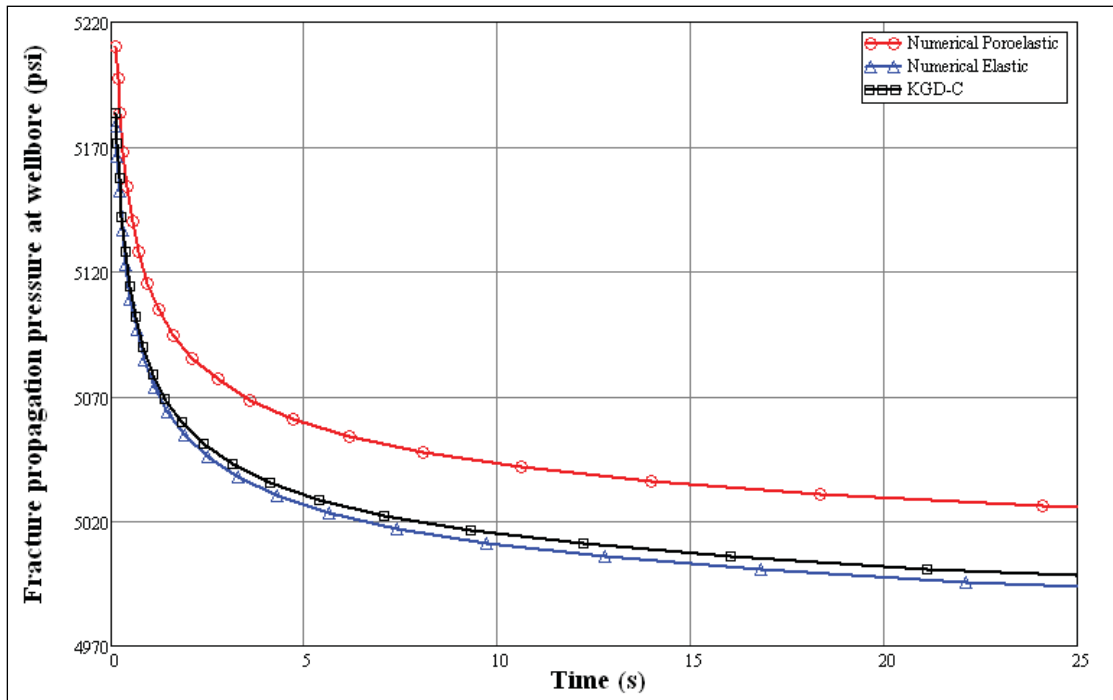


Fig. 2.36: Fracture propagation pressure vs. pumping time for the numerical poroelastic, elastic fracturing models and KGD-C model ($\sigma_H = 6000$ psi, $\sigma_h = 5000$ psi, $p_i = 4500$ psi, $\mu_f = 1$ cp, $q = 10$ bbl/min, $k = 0.1$ mD, $K_{IC} = 500$ psi.ft^{0.5}).

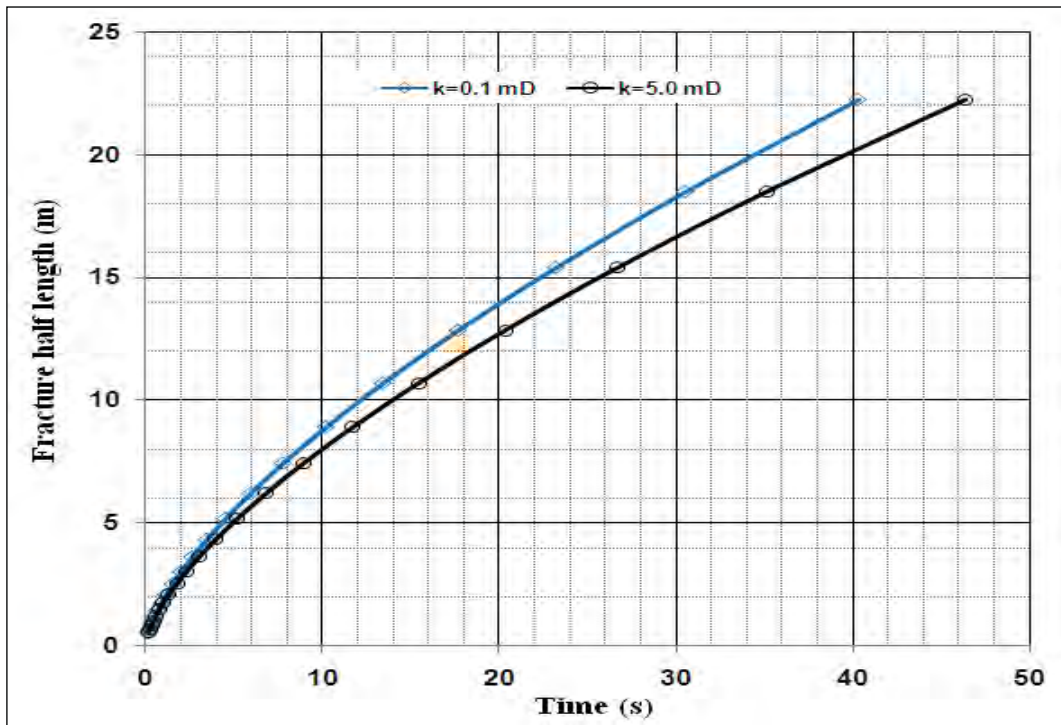


Fig. 2.37: Fracture half length vs., pumping time for two permeability of 0.1 mD and 5 mD (poroelastic reservoir, $\sigma_H = 6000$ psi, $\sigma_h = 5000$ psi, $p_i = 4500$ psi, $\mu_f = 1$ cp, $q = 10$ bbl/min, $K_{IC} = 500$ psi.ft^{0.5}).

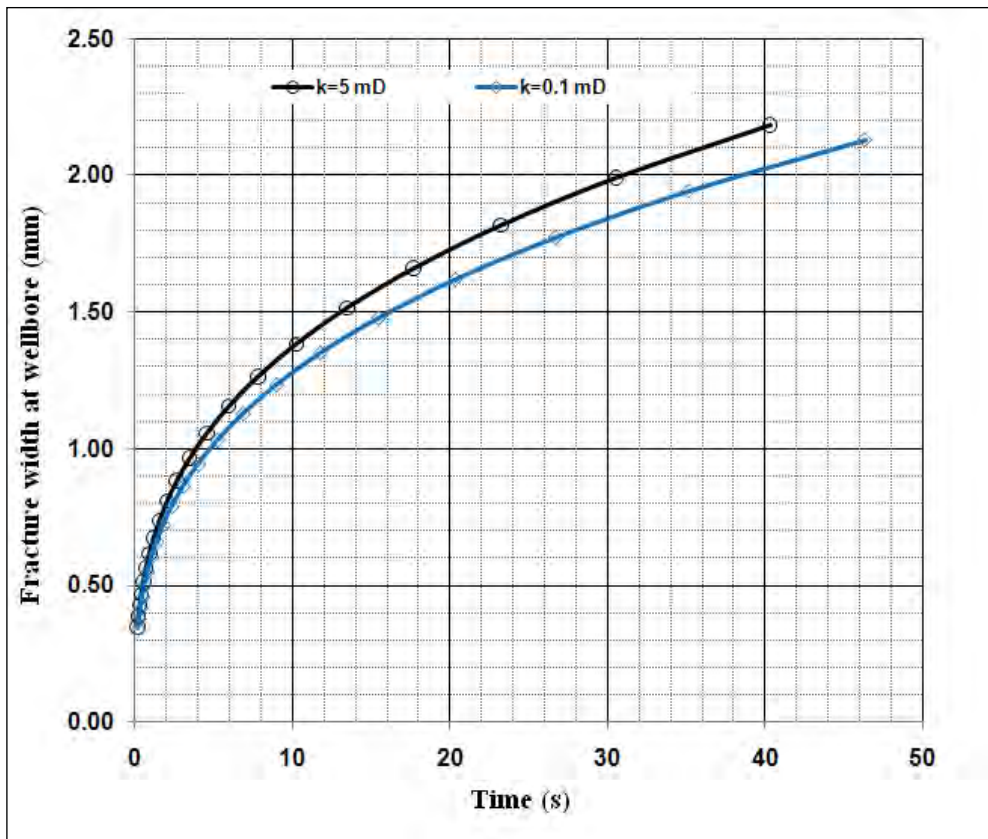


Fig. 2.38: Fracture width vs. pumping time for two permeability of 0.1 mD and 5 mD (poroelastic reservoir, $\sigma_H = 6000$ psi, $\sigma_h = 5000$ psi, $p_i = 4500$ psi, $\mu_f = 1$ cp, $q = 10$ bbl/min, $K_{IC} = 500$ psi.ft^{0.5}).

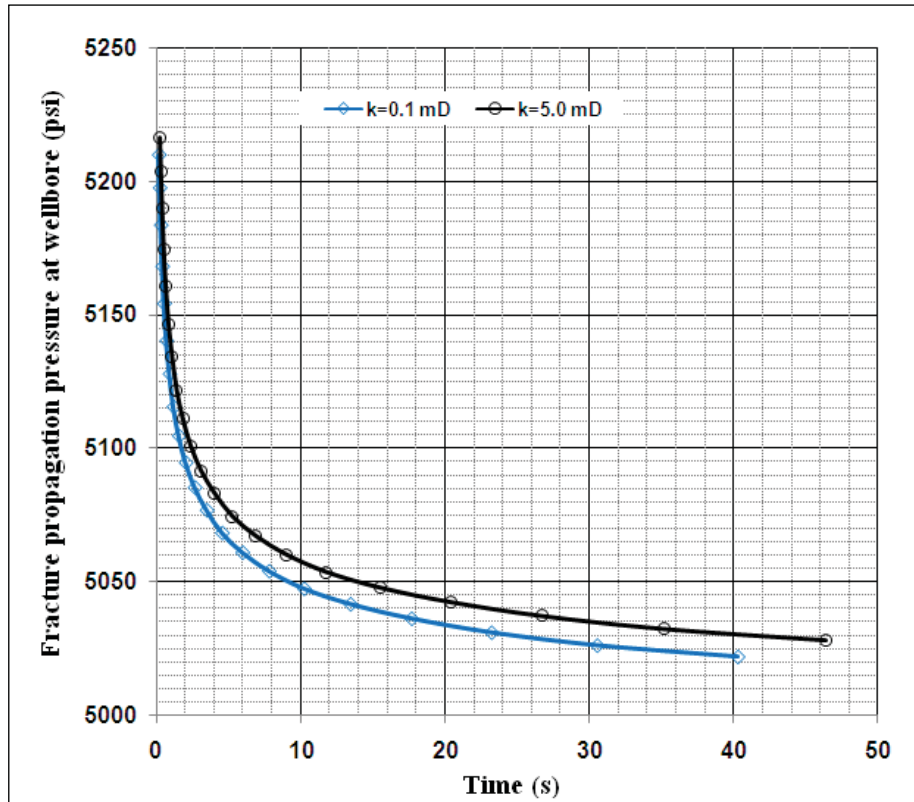


Fig. 2.39: Fracture propagation pressure vs. pumping time for two permeability of 0.1 mD and 5 mD (poroelastic reservoir, $\sigma_H = 6000$ psi, $\sigma_h = 5000$ psi, $p_i = 4500$ psi, $\mu_f = 1$ cp, $q = 10$ bbl/min, $K_{IC} = 500$ psi.ft^{0.5}).

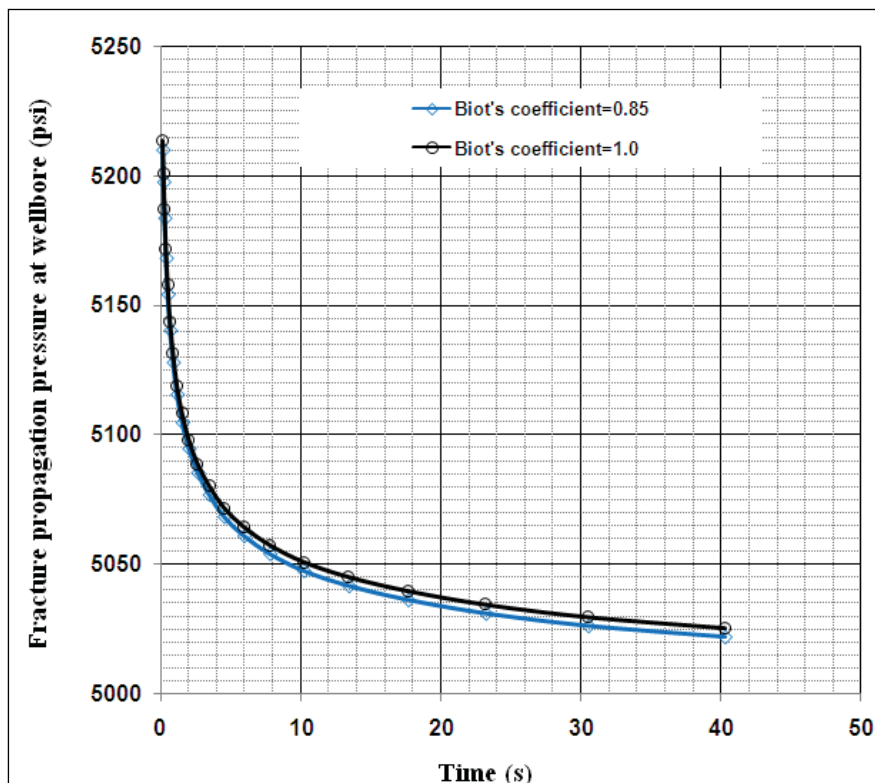


Fig. 2.40: Fracture propagation pressure vs. pumping time for two Biot's coefficient of 1.0 and 0.85 (poroelastic reservoir, $\sigma_H = 6000$ psi, $\sigma_h = 5000$ psi, $p_i = 4500$ psi, $\mu_f = 1$ cp, $q = 10$ bbl/min, $k = 0.1$ mD, $K_{IC} = 500$ psi.ft^{0.5}).

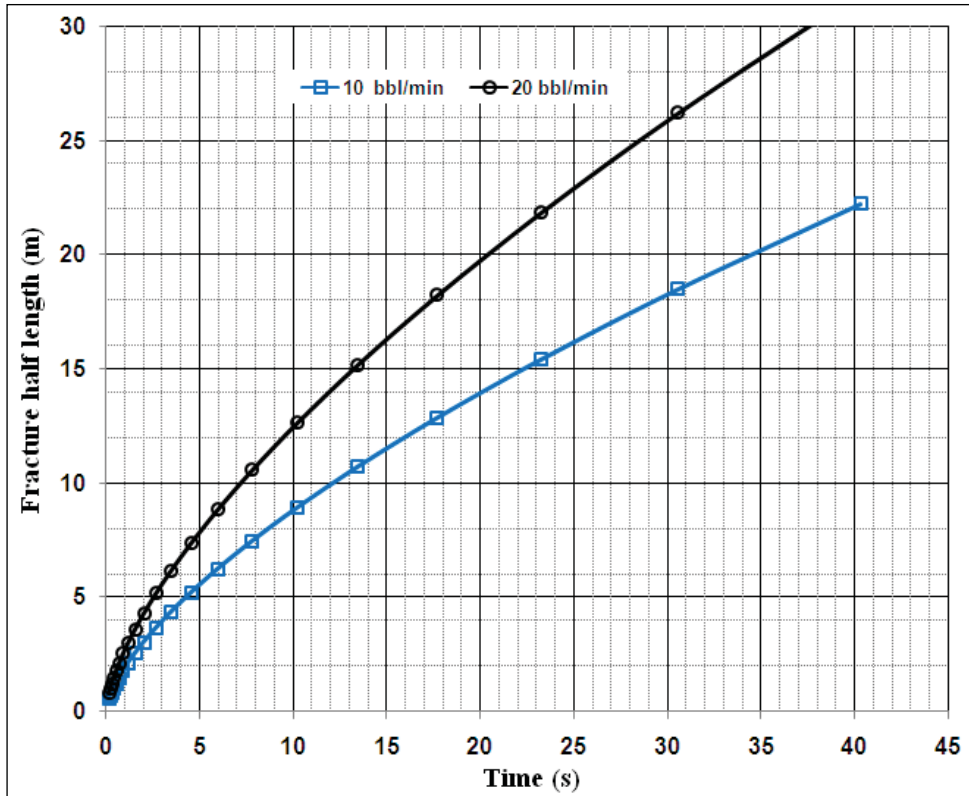


Fig. 2.41: Fracture half length vs., pumping time for two pumping rate of 10 bbl/min and 20 bbl/min (poroelastic reservoir, $\sigma_H = 6000$ psi, $\sigma_h = 5000$ psi, $p_i = 4500$ psi, $\mu_f = 1$ cp, $k = 0.1$ mD, $K_{IC} = 500$ psi.ft^{0.5}).

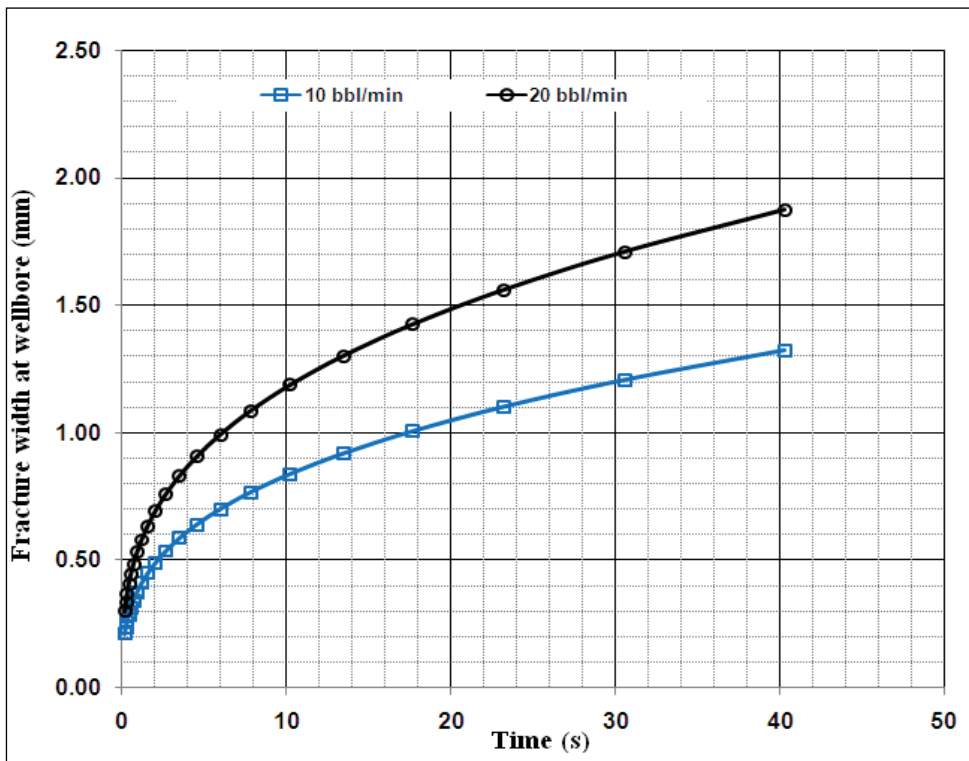


Fig. 2.42: Fracture width vs. pumping time for two pumping rate of 10 bbl/min and 20 bbl/min (poroelastic reservoir, $\sigma_H = 6000$ psi, $\sigma_h = 5000$ psi, $p_i = 4500$ psi, $\mu_f = 1$ cp, $k = 0.1$ mD, $K_{IC} = 500$ psi.ft^{0.5}).

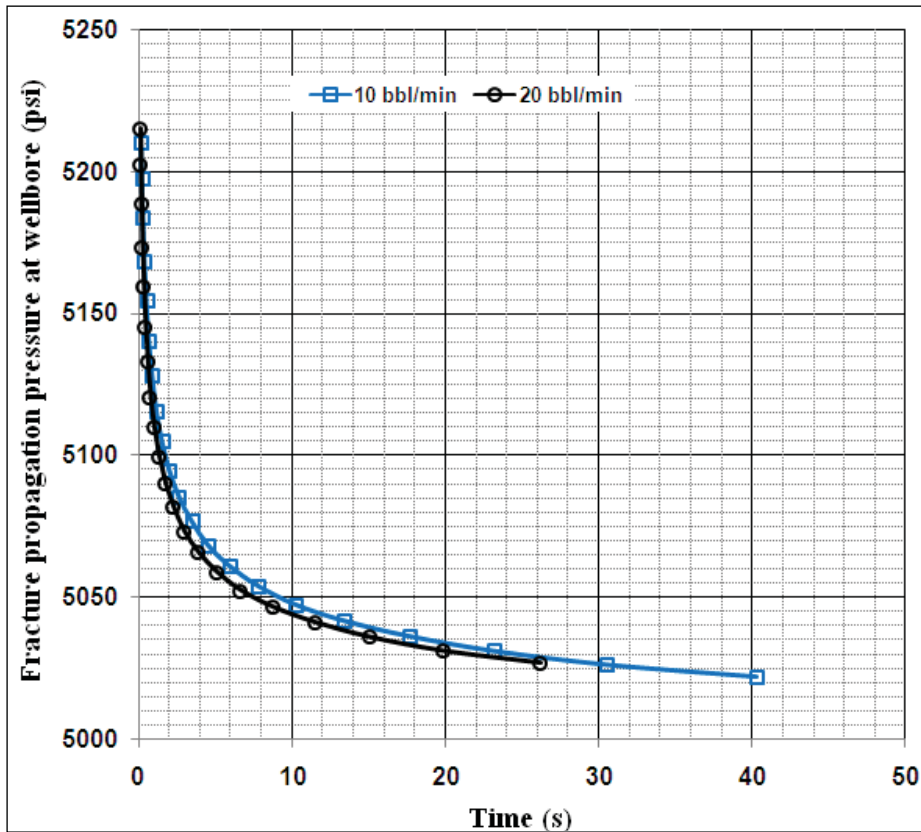


Fig. 2.43: Fracture propagation pressure vs. pumping time for two pumping rate of 10 bbl/min and 20 bbl/min (poroelastic reservoir, $\sigma_H = 6000$ psi, $\sigma_h = 5000$ psi, $p_i = 4500$ psi, $\mu_f = 1$ cp, $k = 0.1$ mD, $K_{IC} = 500$ psi.ft^{0.5}).

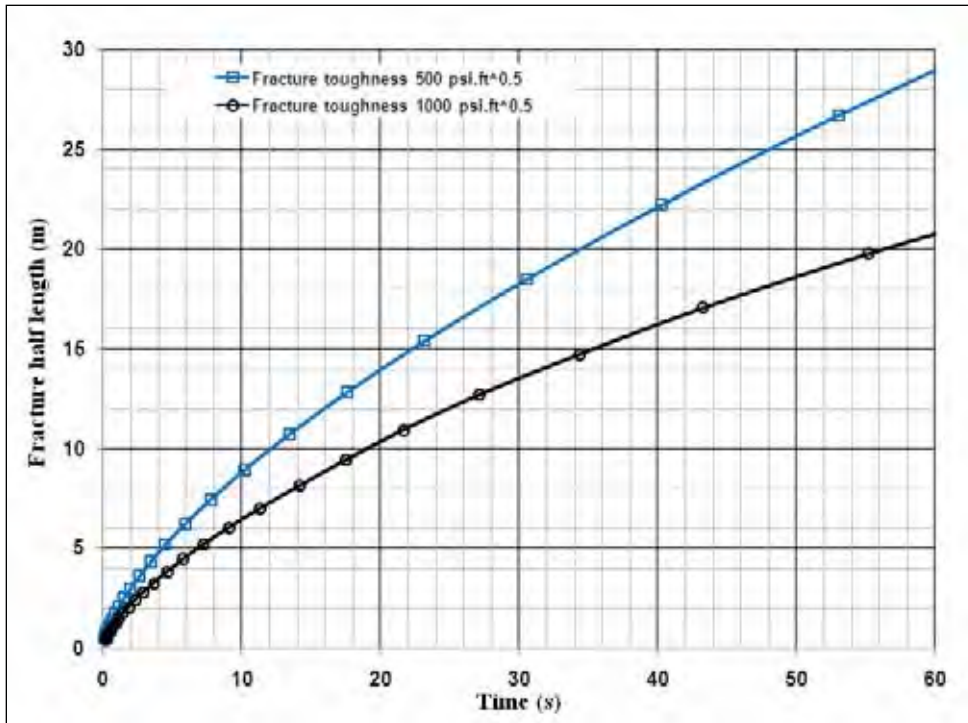


Fig. 2.44: Fracture half length vs., pumping time for two fracture toughness of 500 psi.ft^{0.5} and 1000 psi.ft^{0.5} (poroelastic reservoir, $\sigma_H = 6000$ psi, $\sigma_h = 5000$ psi, $p_i = 4500$ psi, $\mu_f = 1$ cp, $k = 0.1$ mD, $q = 10$ bbl/min).

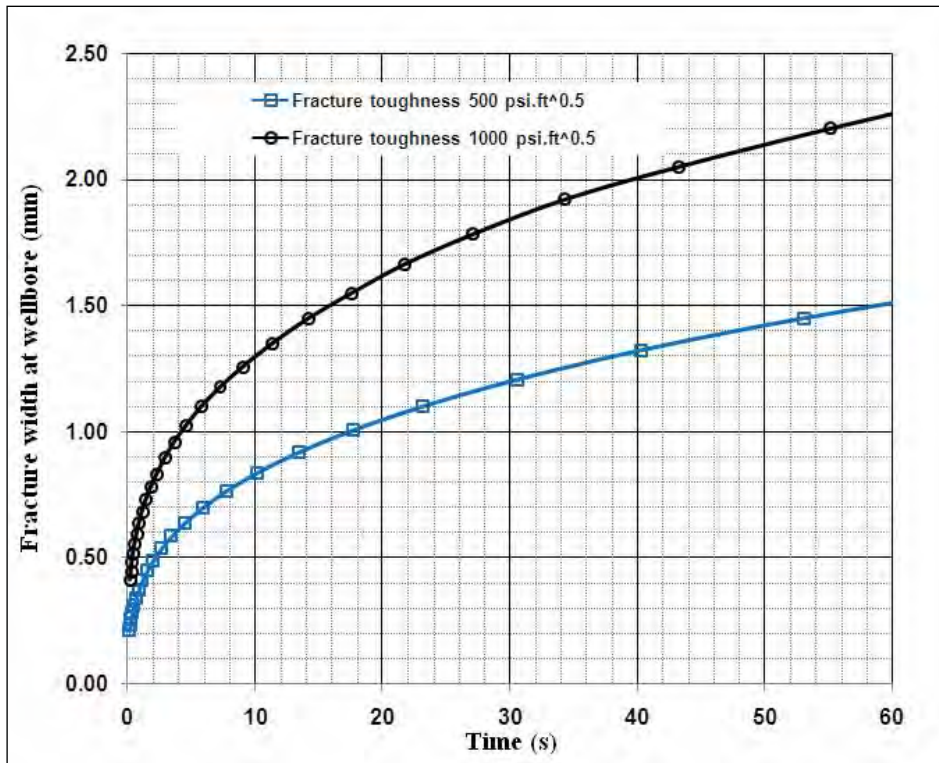


Fig. 2.45: Fracture width vs. pumping time for two fracture toughness of 500 psi.ft^{0.5} and 1000 psi.ft^{0.5} (poroelastic reservoir, $\sigma_H = 6000$ psi, $\sigma_h = 5000$ psi, $p_i = 4500$ psi, $\mu_f = 1$ cp, $k = 0.1$ mD, $q = 10$ bbl/min).

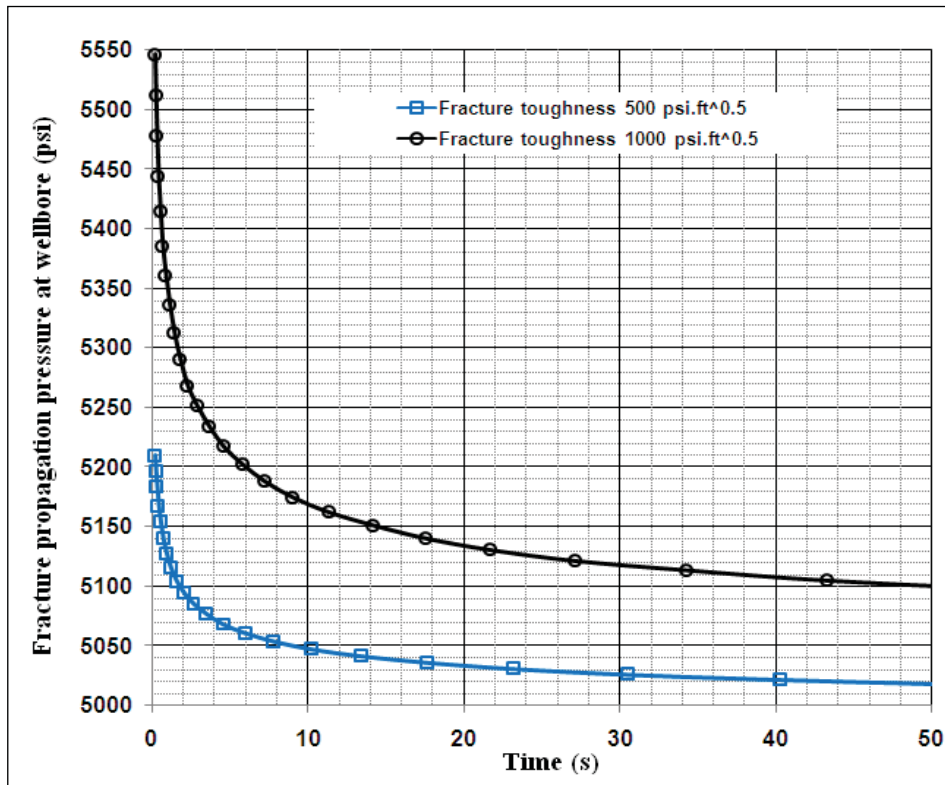


Fig. 2.46: Fracture propagation pressure vs. pumping time for two fracture toughness of 500 psi.ft^{0.5} and 1000 psi.ft^{0.5} (poroelastic reservoir, $\sigma_H = 6000$ psi, $\sigma_h = 5000$ psi, $p_i = 4500$ psi, $\mu_f = 1$ cp, $k = 0.1$ mD, $q = 10$ bbl/min).

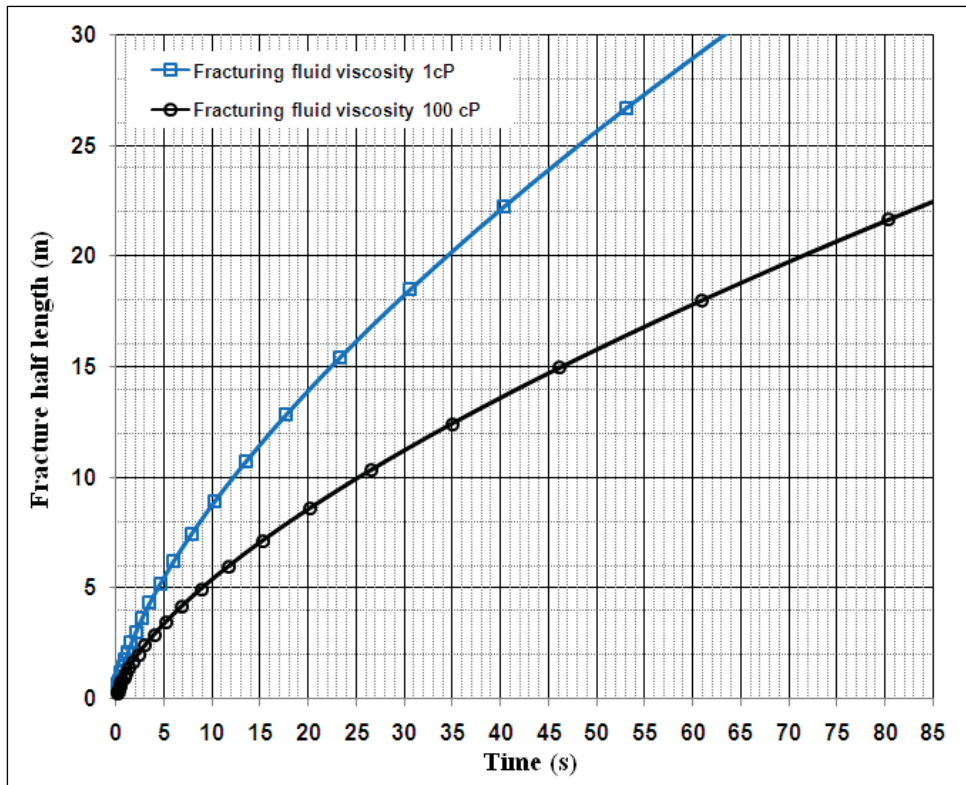


Fig. 2.47: Fracture half length vs., pumping time for two fracturing fluid viscosities of 1cP and 100 cP (poroelastic reservoir, $\sigma_H = 6000$ psi, $\sigma_h = 5000$ psi, $p_i = 4500$ psi, $\mu_f = 1$ cp, $k = 0.1$ mD, $q = 10$ bbl/min, fracture toughness = 500 psi.ft^{0.5}).

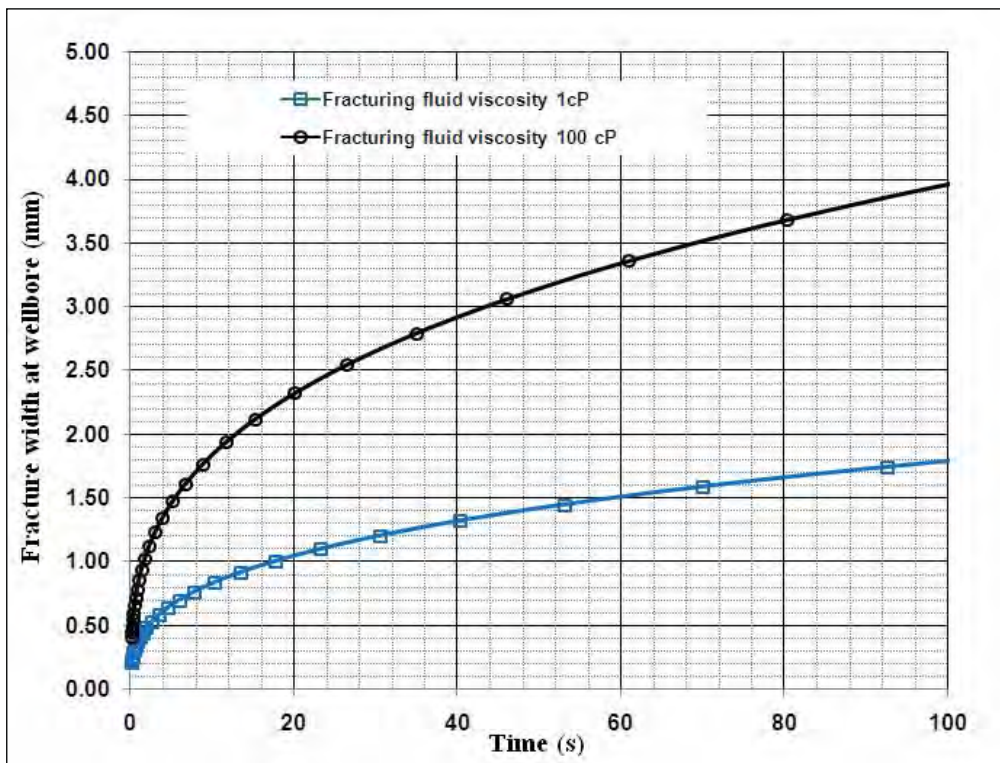


Fig. 2.48: Fracture width vs. pumping time for two fracturing fluid viscosities of 1cP and 100 cP (poroelastic reservoir, $\sigma_H = 6000$ psi, $\sigma_h = 5000$ psi, $p_i = 4500$ psi, $\mu_f = 1$ cp, $k = 0.1$ mD, $q = 10$ bbl/min, fracture toughness = 500 psi.ft^{0.5}).

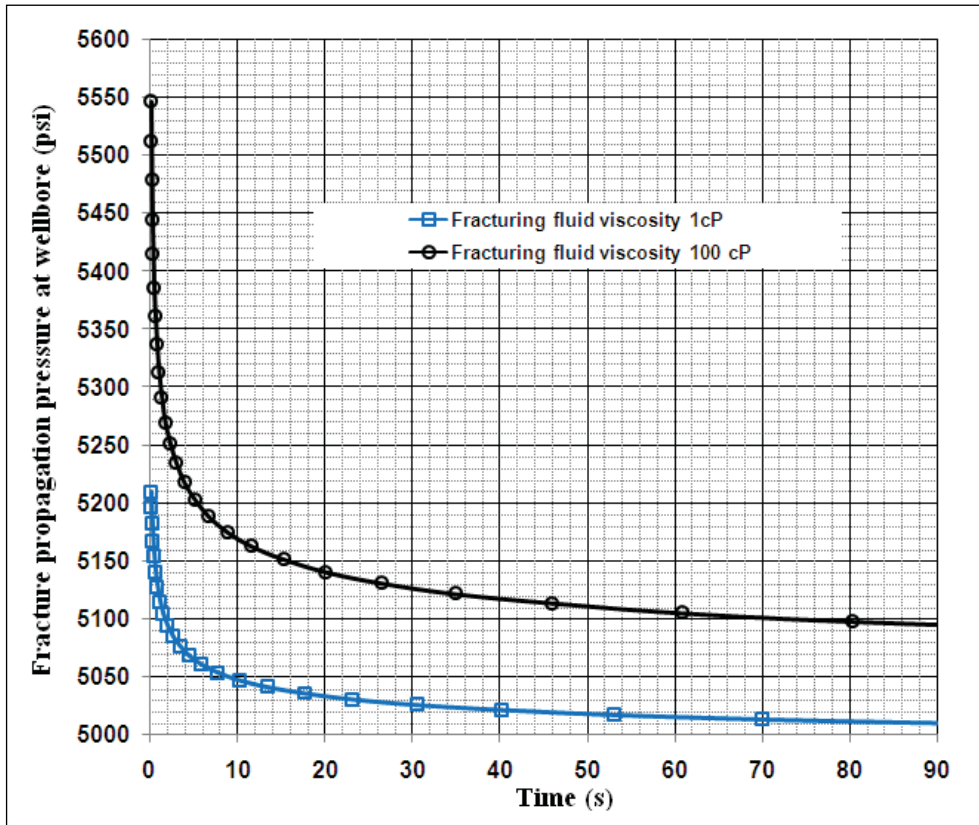


Fig. 2.49: Fracture propagation pressure vs. pumping time for two fracturing fluid viscosities of 1cP and 100 cP (poroelastic reservoir, $\sigma_H = 6000$ psi, $\sigma_h = 5000$ psi, $p_i = 4500$ psi, $\mu_f = 1$ cp, $k = 0.1$ mD, $q = 10$ bbl/min, fracture toughness = 500 psi.ft^{0.5}).

Chapter 3: Hydraulic Fracture Propagation in Presence of a Natural Fracture

The objective of this chapter is to extend the numerical poroelastic model developed in previous chapter to simulate hydraulic fracture propagation in presence of a natural fracture. For this purpose an arbitrarily oriented natural fracture is incorporated in the numerical poroelastic model. Possibilities of fracture deviation, arrest and fracture crossing for various angles of approach are investigated under different scenarios of in-situ stress contrast, rock strength, natural fracture geometry and injection rate.

Several field and lab experimental studies have investigated the presence of natural fractures on the propagation of an induced hydraulic fracture. In 1943 Lammont and Jessen (Norman Lamont and F.W. Jessen 1963) conducted a series of experiments in different types of rock (cement, Austin stone, Leuders lime, Berea sandstone, Boise sandstone and Millsap sandstone). Experiments are conducted under tri-axial compression. All samples are pre-fractured and angle of inclination, bearing and width are varied from specimen to specimen. Widths are also varied from hairline to a large open fracture. The loading conditions for the experiment are showing in **Fig.3.1** and results are shown in **Fig.3.2** to **Fig.3.4**. Authors reported that the hydraulic fracture tends to turn and intersect the existing fracture at right angles or deviates from its existing extension path. They also observed that after intersecting a natural fracture the hydraulic fracture exit with an offset angle.

Daneshy (1974) has shown that fracture follows the local path of least resistance, not the global path, and this leads to substantial branching. The works of Blanton (1982; 1986) have shown that the propagating fracture crosses the natural fracture, turns into the natural fracture, or in some cases, turns into the natural fracture for a short distance, and then breaks out again to propagate in a mechanically more favorable direction depending primarily on the approach angle. The author does not provide any threshold for the approach angle to predict fracture arrest or fracture diversion. Studies by Azeemuddin et al., 2002; Blanton, 1982; 1986; Britt and Hager, 1995; Daneshy, 1974; Vinod et al., 1997; Zhou et al., 2008 suggest that hydraulic fractures tend to cross existing fractures at high differential stress and high angles of approach. At low angle of approach and low differential stress the natural fracture

opens, diverting the fracturing fluid and preventing the induced fracture from crossing, at least temporarily. A propagating hydraulic fracture deviates after reaching the vicinity of a natural fracture or it turns into the natural fracture and breaks out from the tip of the natural fracture because of the altered stress around the natural fracture. It is likely that the width of the hydraulic fracture becomes substantially smaller than its initial width. Warpinski and Teufel (1987) conducted mine back experiments to study the effect of geologic discontinuities on hydraulic fracture propagation. However, mine back experiments have several major differences from hydraulic fracturing, such as shallow depth and low confining stresses. On the other hand, it is not feasible to monitor hydraulic fractures in the subsurface with great precision, because of the limited access to the subsurface.

More recently, L. Casas et al. (2006) performed hydraulic fracturing experiments in the laboratory on a large block of high modulus and low permeability rock (Colton sandstone) with artificial discontinuities. Authors concluded that in a high confining stress condition, planar fracture propagation follows the expected trend and the fluid net pressure inside the induced fracture becomes slightly higher than expected due to fluid lag zones. Difference in stiffness between the grout and Colton sandstone interface (artificial discontinuity), as well as joint orientation do not arrest fracture growth.

As far as numerical studies are concerned, only a few works have been carried out on the interaction between hydraulically induced fracture and natural fractures. Heuze (1990) used FEFFLAP (Finite Element Fracture and Flow Analysis Program) to investigate fluid-driven crack in jointed rock. Dong and de Pater (2001) applied a displacement discontinuity method to study the effect of a fault on hydraulic fracture reorientation. Zhang and Jeffrey (2006b) also applied a displacement discontinuity method to study the role of friction and secondary flaws on deflection and re-initiation of hydraulic fractures at orthogonal to pre-existing fractures. Ghassmi, (V. Koshelev and A. Ghassmi 2003) developed a numerical elastic model using boundary element method to study crack propagation near natural discontinuities such as joints and faults based on complex variable boundary element method. Potluri (2005) developed a numerical elastic model to predict the dynamic fracture dimension in the presence of natural fracture based on the PKN model. Akulich et al. (2008) developed a numerical elastic model to investigate the interaction of a hydraulic fracture with fault. They suggested that the fault slows down the propagation of a hydraulic fracture. An increase in differential stresses and the angle of inclination of the fault lead to a decreased likelihood of fault activation and decrease in the relative normal and tangential displacements of the fault

faces. Modeling of interaction between induced fracture and fault do not include fracture intersections; however, it gives an idea about the slippage along the fault and how it affects the stress intensity factors at the tip of the growing hydraulic fractures.

In all the aforementioned works interaction (diversion, arrest and/or crossing) of an approaching induced fracture with an arbitrarily oriented natural fracture in a poroelastic medium has not been addressed. In this study the poroelastic medium is considered to model and used to study the interaction of a hydraulically induced fracture and a natural fracture.

3.1 Modelling of fracture propagation in the presence of natural fracture (fracture arrest and/or deviation)

In the poroelastic model finite element technique is conveniently adopted to develop incremental approaches for the solution of moving boundary of the hydraulically induced fracture. The computational technique accommodates the situations where the induced fracture interacts with natural fracture. Propagation of hydraulic fracture takes place along the trajectory governed by mixed mode (mode-I and mode-II) fracture extension concept. The incremental nature of the iterative scheme allows for the time dependent analysis where pore pressure and deformation are appropriately adjusted by using 8-noded displacement element and 4-noded pressure element. The schematic of the system of an induced hydraulic fracture approaching/intersecting a pre existing natural fracture is shown in **Fig.3.5**.

Modeling fluid leak-off

Natural fractures (closed or mineralized) can still act as weak paths for fracture growth. One common observation in naturally fractured reservoirs is a high leak-off rate and in some cases it is as high as 60 times more than that of in non-fractured reservoirs (Valkó and Economides, 1996). Leak-off rate in a permeable medium without natural fractures is dependent on formation permeability, net treatment pressure and fracture fluid parameters (Valkó and Economides, 1996). Whereas field observation during hydraulic fracturing in naturally fractured reservoirs shows that leak-off primarily depends on net treatment pressure and fracture fluid parameters does not depend on formation permeability (Barree 1996, Britt et al. 1994). For every fracture system there is a threshold for net injection pressure above which natural fracture opens. If net injection pressure stays below this threshold, fractures

remain closed and do not contribute to leak-off. This mechanism makes the leak-off rate in naturally fractured reservoirs strongly injection pressure dependent.

The fluid leak-off model developed in chapter-2 is further extended here by using a modified leak-off coefficient for natural fracture. Dong et al (1999) presented a simple methodology to handle the leak-off coefficient at fracture intersection. The same methodology is applied to calculate the modified leak-off coefficient at the fracture intersection. Here the assumptions are made that the fracture conductivity is much larger than the formation permeability and the pressure inside the natural fracture is considered to be the same as the pressure at the intersection point (between induced hydraulic fracture and natural fracture). The leak-off coefficient in the affected region (near the induced fracture) is set to the matrix leak of coefficient (C_L) and the distance (distance perpendicular to the axis of the induced fracture) is referred to as l_{ref} . The leak-off coefficient at the intersection point now can be calculated using the following equation:

$$C_{nf} = \frac{l_{nf}}{l_{ref}} C_L \quad (3.1)$$

where C_L = matrix leak of coefficient, l_{nf} = length of natural fracture, l_{ref} = length of the influence zone known as reference length and C_{nf} = calculated leak-off coefficient at the intersection point used as a natural fracture leak-off coefficient.

The pressure in the region very close to the hydraulically induced fracture (main flow path) can be expressed by the diffusivity equation as follows:

$$\frac{\partial^2 p}{\partial y^2} = \frac{\phi \mu c}{k} \frac{\partial p}{\partial t} \quad (3.2)$$

where ϕ = porosity, k = formation permeability (at fracture surface), μ = fluid viscosity, c = fluid compressibility and y = distance parallel to the Y-axis from the induced fracture.

Carslaw and Jaeger (H.S. Carslaw and J.C. Jaeger, 1959) gave the solution of the above equation. For typical values for each parameter ($\phi=0.2$, $\mu = 1$, $c = 10^{-5}$ psi, $k = 50$ mD and $y = 1$ ft) they found that the pressure in the region close to the main flow path reaches 1.9 times larger than that of the main fracture within one second. Based on their solution, in this study the influence zone of 1ft is utilized as a reference length (l_{ref}) to calculate the modified leak-off coefficient at the intersection point. Replacing C_L by C_{nf} in

equation 2.20 fracturing fluid leak-off through natural fracture can be calculated using the following equation:

$$\frac{\partial V_L}{\partial t} = \frac{C_{nf}}{\sqrt{t-\tau}} \partial A \quad (3.3)$$

The rate of fluid leak-off at the natural fracture surface is controlled by viscosity of the fracturing fluid, natural fracture permeability and local pressure gradient.

Fracture propagation criteria in the presence of natural fracture

In this poroelastic model mixed mode (opening and shearing mode) fracture extension criteria is employed to simulate the induced fracture propagation in presence of natural fracture. For this purpose first opening mode criterion that is based on Griffith's concepts of crack stability is developed. Then the opening mode criterion is further extended to include the influence of shearing effects (mode-II). In order to include the shearing effect, both fracture extension and fracture orientation criteria are implemented.

According to the Griffith's concepts of crack stability (Griffith, 1920; Griffith, 1924) the fracture propagation in a poroelastic medium is assumed to take place in opening mode when the stress intensity factor in the fracture tip satisfied the following condition in terms of fracture toughness:

$$K_I = K_{IC} \quad (3.4)$$

where K_{IC} is the critical value of the stress intensity factor known as fracture toughness and K_I is the stress intensity factor for opening mode.

In this model Erdogan and Sih's (1963) crack extension criteria is used to include the shearing effects. According to authors, orientation of fracture extension ("θ") can be calculated using the following equation:

$$\cos \frac{\theta}{2} \left[\frac{K_I}{K_{IC}} \cos^2 \theta \sin \theta \frac{K_{II}}{2K_{IC}} \right] = \quad (3.5)$$

where K_{II} is the stress intensity factor for shearing mode (mode-II).

The equation 3.5 gives two directions for propagation, the one with positive tensile stress is accepted and utilized in the mixed mode fracture propagation criteria. Finally fracture orientation and extension criteria for the fracture propagation in mixed mode given

by G.C.Sih and Theocaries (1979) and G.C.Sih (1991) is adapted to model fracture propagation in presence of natural fracture. According to authors, the mixed mode fracture propagation (rock failure) criterion is as follows:

$$K_I \sin\theta - K_{II}(3 \cos\theta - 1) = 0 \quad (3.6)$$

Displacement correlation method is employed to calculate the stress intensity factors (for mode-I and mode-II) at the fracture tip. This method utilizes the quarter point singular elements (shift the mid-side nodes of an eight noded iso-parametric element to their quarter points) as shown in **Fig.3.6**. Nodal displacements at four locations *A*, *B*, *D*, and *E* of the fracture tip are shown in the **Fig.3.7**. The opening mode-I and shearing mode-II stress intensity factors can be calculated using the following equations (Ingraffea, 1977a; Ingraffea and Manu, 1980; Murti and Valliappan, 1984, 1986):

$$K_I = \frac{G}{4(1-\nu)} \sqrt{\frac{2\pi}{l_0}} \{4[u_y(B) - u_y(D)] + u_y(E) - u_y(A)\} \quad (3.7)$$

$$K_{II} = \frac{G}{4(1-\nu)} \sqrt{\frac{2\pi}{l_0}} \{4[u_x(B) - u_x(D)] + u_x(E) - u_x(A)\} \quad (3.8)$$

where *G* is the rock shear modulus, *v* is the Poisson's ratio, *l₀* is the length of fracture tip element and *u_x* (*) and *u_y* (*) are the nodal displacements along X and Y axis calculated from the numerical model.

The meshes are made considerably fine when using the displacement correlation method. In order to have compliance with these considerations into the meshing process, a mesh generator is developed to generate this special type of geometry. The schematic of the finite element mesh is presented in Fig.3.8. It should be noted that the stress field around the fracture tip is modified by change in local pore pressure due to fracturing fluid leak off into the formation. In this study, this effect (also known as back stress) is taken into account by taking advantage of thin fluid (inside the fracture) elements.

Criteria for induced fracture interaction with natural fracture

There are some works done to provide analytical equations for predicting the intersection of a natural fracture by an induced hydraulic fracture. Blanton (Blanton T.L, 1986) and Warpinski (Warpinski and Teufel, 1987) gave a relation based on the differential stress and angle of approach. Renshaw (Renshaw C.E, and Pollard D.D, 1996) provided a

criterion for crossing across unbonded interfaces, and Dyer (Dyer R., 1988) analyzed the interaction between joints and a hydraulic fracture. In this study Blanton's and Warpinski's criteria are used and extended to model the intersection with a natural fracture and its breakout.

According to Blanton (Blanton, 1986) crossing will occur when the pressure required for re-initiation is less than the opening pressure. This critical state occurs just as the natural fracture begins to open. For the induced fracture to breakout at a point opposite to the initial intersection point, the fracture pressure, p would have to overcome the stress σ_t , plus the tensile strength of the rock, T_o . Mathematically this can be written as

$$p > \sigma_t + T_o \quad (3.9)$$

or

$$\sigma_t' \leq T_o. \quad (3.10)$$

where $\sigma_t' = \sigma_t - p$ effective stress, T_o = tensile strength of the rock, p = pressure.

Determination of σ_t is complicated by the fact that it depends not only on the far-field stresses and pressure in the fracture but also on the geometry of the interaction zone as well as frictional slippage and opening along the natural fracture. An expression for σ_t is given by Blanton (Blanton, 1986). In this model, the value of σ_t' can be obtain directly from the numerical results of displacement. Hence it is possible to calculate σ_t' at any point including at the circumference of the natural fracture. After that the value of those effective stress are investigated to evaluate points at the circumference of the natural fracture where the stress exceed the value of tensile strength of the rock. This rock tensile failure criterion is adopted to determine the crossing or break out behavior of the natural fracture based on the angular nodal position of natural fracture surface (see **Fig. 3.9**).

Algorithm of induced fracture propagation in presence of natural fracture

The computational methodologies for fracture propagation away from the natural fracture (without the influence of the natural fracture) are same as the methodologies described in chapter-2. Once the induced fracture reaches the vicinity of the natural fracture the interaction is modeled by mixed mode failure criteria. The computational procedure

presented in **Fig.3.10** which includes step 1-9 of the section “Algorithm of hydraulic fracture propagation” of chapter-2 forms the first part of the algorithm. The second part of the algorithm includes step 10 to 14.

- x. Once the displacement convergence is successful, instead of calculating critical width (as described in section “Algorithm of hydraulic fracture propagation” chapter-2) stress intensity factor K_I and K_{II} using equation 3.7 and 3.8 at the fracture tip element are calculated. This element is already made as quarter point singular element.
- xi. Then fracture orientation “ θ ” is calculated using equation 3.5. The equation gives two values of “ θ ” (directions for fracture propagation) which is physically unacceptable. Out of these two values only one value is accepted (which yields the positive tensile stress at fracture tip) as fracture orientation angle.
- xii. Once the fracture orientation angle (see **Fig.3.12 a**) is found, fracture extension criteria (using equation 3.6) is then checked. If the extension criteria meet the requirement, then a new element is added to the existing fracture which locates the new fracture tip (See Fig.3.12 b and c).
- xiii. If the fracture extension criteria for mixed mode not met, the criterion for opening mode (mode-I) is checked before next iteration. If the opening mode criteria ($K_{IC}=K_I$) fulfills the requirement, then a new element is added to the existing fracture to locate the new fracture tip. Otherwise the process sends back to the step “iv” for next iteration. In this case decision is to be made whether the propagation is opening mode or mixed mode driven.
- xiv. The double nodes of the new element in step xii or xiii is split to generate the quarter point singular element. Then the model returns to the first step with a new fracture geometry for next iteration (new time step).

3.2 Parametric study of hydraulic fracture propagation in presence of a natural fracture:

According to Daneshy (1974) natural fractures can be divided as: small (up to 1.27 cm), medium (up to 10 m) and large (more than 10 m). It is found in literature (Daneshy, 1974; Blanton, 1982, 1986) that small natural fracture does not have any impact on induced

hydraulic fracture propagation. Hence, in this study only the medium natural and large natural fractures are considered. Angle of approach ' θ ' (as shown in **Fig.3.5**) and combinations of σ_H and σ_h (differential stress, $\sigma_H - \sigma_h$) are varied.

In order to study the influence of natural fracture on hydraulic fracture propagation, four parameters are varied: angle of approach, differential stress, natural fracture length and injection rate. Angles of approaches are set at 90° , 60° and 30° respectively. Fluid injection rates used in this study are 20 bbl/min and 35 bbls/min and differential stress 1000 psi and 500 psi respectively. A natural fracture is placed 20 meter away from the wellbore. Lengths of natural fracture used in this study are 10 m and 20 m long. Reservoir rock properties, fracture properties, rock mechanical properties and stress data are presented in **Table 3.1**. All propagation results discussed in this section are mix of opening mode (mode-I, near the wellbore region) and mixed mode (Mode-I and mode-II, in the vicinity of natural fracture) driven.

Effect of angle of approach on fracture interaction

Results of the effect of a 10 m long natural fracture with an angle of approach of 90° and differential stress of 1000 psi on fracture interaction are presented in **Figs.3.13** through **3.16**. It can be seen from Fig.3.13 that the induced fracture reaches the vicinity of the natural fracture after 42 sec of its initiation. Propagation of the induced hydraulic fracture ceases at this time temporarily. From Fig.3.14 it can be seen that the width of induced fracture increases until it reaches natural fracture (42 sec). After this time the width at the fracture mouth continues to decrease for about 65 sec (117 s from the initiation). During this time, fracture propagation pressure increased by about 30 psi. As the injection of fracturing fluid continues the propagation pressure begins to drop sharply from 117 sec until 142 sec and then flattens out. It is also important to note that during the same period of 42 sec-117 sec fracture pressure at the fracture tip (inside the induced fracture) drops from 5095 psi to 5070 psi (See **Fig.3.15**). This phenomenon can be explained by the fact that as the induced fracture propagates and reaches the vicinity of the natural fracture a significant amount of fracture fluid leaks into the natural fracture, thus reducing the width of the induced fracture at the wellbore and fracture pressure near the fracture tip (See Fig.3.13 and 3.14). As the pumping continues pressure inside the natural fracture builds up and at about 117 sec (from the initiation of induced fracture) the tangential stress at angular position of 90° and 270° of the natural fracture surface exceeds its tensile strength (See Fig.3.16 where effective tangential

stress as a function of angular position of the natural fracture is presented). At this time induced fracture crosses the natural fracture and continues to propagate further into the formation. As the fracture propagates the fracture propagation pressure continues to decrease.

Results of the effect of a 10 m long natural fracture with an angle of approach of 60° and differential stress of 1000 psi on fracture interaction are presented in **Figs.3.17** through **3.20**. Results of this study show very similar behavior to that of a 90° angle of approach but with following exceptions. Pressurization time required for tangential stress exceeds the tensile strength of the rock and the tangential stress at the point of interception for the case of 60° angle of approach are much greater (about 2.5 times) than that of 90° angle of approach. This means that the angle of approach of 90° provides a most favorable condition for the induced fracture to intercept and cross the natural fracture. As the angle of approach decreases the pressurization time and the tangential stress at the circumference of the natural fracture required for the induced fracture to breakout increases.

Results of the effect of a 10 m long natural fracture with an angle of approach of 30° and differential stress of 1000 psi on fracture interaction are presented in **Figs.3.21** through **3.22**. In this case the induced fracture intersected the natural fracture. With continuous injection of fracturing fluid the induced fracture reorients and propagates along the axis of the natural fracture. It can be observed that the propagation pressure after the induced fracture intersects the natural fracture is greater (by 20 psi) for 30° angle of approach than that for 90° angle of approach. This means that at low angle of approach it is less likely that the induced fracture to cross the natural fracture.

Effect of differential stress on fracture interaction

Results of the effect of a 10 m long natural fracture with an angle of approach of 60° and differential stress 500 psi on fracture interaction are presented in **Figs.3.23** through **3.25**. From the result it can be seen that the induced fracture propagates and intersects the natural fracture. As the injection of fracturing fluid continues the induced fracture reorient and propagate along the axis of natural fracture. In previous case where differential stress is 1000 psi and angle of approach 60° , the induced fracture crossed the natural fracture (see Fig. 3.17-3.20). It can be seen from Fig.3.23 that the fracture propagation pressure in current case (propagate along the axis of natural fracture) is higher than that for 1000 psi differential stress (see Fig.3.17 and 3.18). This additional fracture propagation pressure is required to reorientation for the induced fracture. From Fig.3.24 it is observed that, during the

reorientation of induced fracture along the axis of natural fracture the width of the induced fracture at the wellbore decreases due to the increase fluid leak-off into the surrounding and into the natural fracture. Fracture pressure profiles for two differential stresses (1000 psi and 500 psi and angle of approach 60°) are presented in **Fig.3.25**. It can be seen from the figure that at higher differential stress (1000 psi) less fluid pressure inside the fracture is needed to cross the natural fracture. While at low differential stress (500 psi) higher fluid pressure is observed inside the fracture.

Results of the effect of a 10 m long natural fracture with an angle of approach of 30° and differential stress of 500 psi on fracture propagation are presented in **Figs.3.26** through **3.27**. Results of this study show very similar behavior to that of a 60° angle of approach (500 psi differential stress). When the results of this study are compared with 30° angle of approach and 1000 psi differential stress, it can be seen that the behavior is very similar, but the pressurization time required to re-orient along the axis of natural fracture is much greater (about 2.5 times) than that for 1000 psi differential stress.

From the above discussion one can conclude that, at high differential stress and high angle of approach the induced fracture is likely to cross the natural fracture. As the differential stress and angle of approach decreases it is unlikely for the induced fracture to cross the natural fracture.

Effect of natural fracture length on fracture interaction

In order to investigate the effect of the natural fracture length on fracture interaction a natural fracture of 20 m is placed at a distance of 20 meter away from the wellbore (fracture half length). The angles of approach are set at 90° and 60° . The wellbore is pressurized by injecting fracturing fluid (slick water). Results of the effect of a 20 m long natural fracture with an angle of approach of 90° and differential stress 1000 psi on fracture interaction are presented in **Figs. 3.28 to 3.31** and compared with results of 10 m long natural fracture (see Figs.3.13-3.16). It can be observed from Figs.3.28 and 3.29 that the induced fracture continues to propagate until about 73.25s. After this time propagation slows down and finally stops propagating at the vicinity of the natural fracture (19.91 m from the wellbore) at about 98s. This means that an induced fracture is likely to be stopped from propagation by a natural fracture of length 20 m and greater with angle of approach 90° .

Results of the effect of a 20 m long natural fracture with an angle of approach of 60° and differential stress 1000 psi on fracture interaction are presented in **Figs.3.31** through **3.33** and compared with results of 10 m long natural fracture (see Fig.3.17-3.20). It can be observed from Fig.3.31 that the induced fracture propagates and reaches the vicinity of the natural fracture (19.14 m from the wellbore). As the injection of the fracturing fluid continues the induced fracture reorient, deviate from its original direction and propagates along the axis of the natural fracture as it enter into the influence zone of natural fracture (see **Fig.3.32** for better view). This result is in good agreement with the result reported by Kosheleve's (2003). It also agrees with the theory that the plane of the extending hydraulic fracture should be normal to the least stress (Daneshy, 1974).

Effect of injection rate on fracture interaction

In order to study the effect of injection rate on fracture interaction the fluid injection rate is increased from 20 bbl/min (previous case) to 35 bbl/min. The length of the natural fracture and the angle of approach are kept at 20 m and 90° respectively. Results of this study are presented from **Figs.3.35** through **3.37** and compared with results presented in Figs. 3.13 to 3.16 in which the injection rate is kept at 20 bbl/min.

It can be seen from Fig.3.35 that the induced fracture requires 11.6 sec to reach the vicinity of the natural fracture from the time of its initiation compared to 71.8 sec for the case of 20 bbl/min injection rate (see Fig.3.13). Similarly time required to reach maximum width is much reduced (11.8 sec compared to about 97 sec for the case of 20 bbl/min, see Fig.3.14 and 3.15). After this time the width at the fracture mouth continues to decrease for about 15 sec (until 26.7 s from the initiation). Fracture propagation pressure increased by about 15 psi during the same period. With continuation of injection of fluid the induced fracture intercepts and breaks out of the natural fracture and propagates further into the formation (see Fig.3.5 and 3.36). Results of this study show very similar behavior to that of a 10 m long natural fracture with 90° angle of approach and 20 bbl/min injection rate but with a number of exceptions: the natural fracture pressurization time and the tangential stress at the point of interception. For the case of 20 m long natural fracture the pressurization and interception time is about 2.5 times lower than that of 10 m long natural fracture. This means that a higher injection rate can overcome the leak off of fluid from the both induced and natural fracture and maintains the stress intensity factor at the fracture tip at a level required for it to intercept, cross and further propagation into the formation.

3.3 Analysis of the induced hydraulic fracture arrest by and/or breakout of natural fracture

In order to develop a detail understanding of the mechanism by which the induced fracture breaks out of and/or arrested by the natural fracture after intersecting, the previous numerical model is modified here. The model geometry includes a poroelastic reservoir, an arbitrarily oriented natural fracture and an intersected induced fracture. The processes of induced fracture arrest and/or breakout of the natural fracture are described by the governing equations of geomechanical deformation of formation, fluid flow within the formation (reservoir) and fluid flow inside the fractures. A much larger number of meshes (nodes and elements) are generated than in the previous case to study the arrest and breakout.

The initial condition of this model is that, the induced hydraulic fracture is already intersected the natural fracture and ready to propagate within the natural fracture. Schematic representation of an induced hydraulic fracture in a medium containing a natural fracture with its initial condition is presented in **Fig.3.38**. Minimum principal stress, σ_h acts perpendicularly to the induced fracture. Fracture is driven by injecting fluid at a constant rate, Q_0 through the wellbore. It is assumed that the fracture propagates along the x-axis.

Governing Equations

Fluid flow and geomechanical deformations are coupled based on the poroelastic theory developed by Biot (1951; 1955). The governing equations, which are derived in Chapter-2(See Equation 2.1, 2.3-2.5) on the basis of mass continuity equations (for both fluids and solids), are presented as follows (Charlez, 1997; Chen et al., 1995):

$$\phi c_t \frac{\partial p}{\partial t} - \alpha \frac{\partial(\nabla \cdot u)}{\partial t} = \nabla \cdot \left(\frac{\vec{k}}{\mu} \cdot \nabla p \right) \quad (3.11)$$

$$(\lambda + G) \frac{\nabla \cdot u}{\partial x_i} + G \nabla^2 u_i - \alpha \frac{\partial p}{\partial x_i} = 0 \quad (3.12)$$

where ϕ is porosity; c_t is total system compressibility ($c_s + c_f$); p is pore pressure; t is time; α is Biot's coefficient; u is displacement vector; \vec{k} is the permeability tensor; μ is fluid viscosity; c_f is fluid compressibility; ∇ is a vector operator; λ and G are Lamé's

constants and x_i is the position vector ($i = 1, 2,$ and 3 in a 3D space to represent three spatial components).

Discretization of the above equations using finite element method (FEM) (Zienkiewicz and Taylor, 2000) results in the following coupled linear system of equations:

$$\begin{bmatrix} \overrightarrow{M5} & \overrightarrow{M3}^T \\ \overrightarrow{-M3} & \overrightarrow{M4} \end{bmatrix} \begin{bmatrix} \Delta \vec{U}^i \\ \Delta \vec{P}^i \end{bmatrix} = \begin{bmatrix} \vec{f}_2 \\ \vec{f}_1 \end{bmatrix} \quad (3.11)$$

where i is the time step; \vec{P} is the pore pressure vector; $\vec{P}^T = (p_1 \ p_2 \ \dots \ p_n)$; p is the nodal pore pressure; n is the number of nodes; \vec{U} is the displacement vector; $\vec{U}^T = (u_{x1} \ u_{y1} \ u_{x2} \ \dots \ u_{yn})$; u_x is the nodal value of x -component of displacement, u_y is the nodal value of y -component of displacement; $\Delta \vec{P} = \vec{P}^i - \vec{P}^{i-1}$; $\Delta \vec{U} = \vec{U}^i - \vec{U}^{i-1}$; and Δt represents the time increment. Additionally $\overrightarrow{M5}$, $\overrightarrow{M4}$, $\overrightarrow{M3}$, \vec{f}_1 , and \vec{f}_2 are matrices and vectors which are defined in the Appendix-2D.

Model description

The finite element mesh to represent the model geometry that includes a poroelastic reservoir, a natural fracture and an intersected induced fracture is presented in **Fig.3.39**. It is noted that different types of elements have been embedded in this mesh: a) reservoir element, b) hydraulic fracture element and c) natural fracture element. Different material properties are assigned to these elements. As the hydraulic fracture is infinite conductive a very high permeability and a very low value of young modulus are given to the respective elements (like a fluid element). Values of porosity, permeability and young modulus for the natural fracture elements are considered such that they represent more realistic properties of a mineralized natural fracture (http://en.wikipedia.org/wiki/Youngs_modulus).

It should be mentioned that in this study compressive stress is considered positive and tensile stress negative. Main assumptions made in this study are as follows:

- The maximum and minimum stresses, σ_H and σ_h act at far field along x and y axes respectively.
- No flow boundary condition is set at the outer reservoir boundary.
- Plane strain hypothesis are employed to reduce the 3D problem to 2D.

In order to simulate the induced fracture arrest by and/or breakout of natural fracture, a fluid (slick water) is injected from the wellbore into the induced fracture. This is done by applying an appropriate boundary condition at the wellbore nodes. At each time step of the injection period the system of linear equations (Eq.3.11) is solved for displacement and pore pressure. Stress tensor at each node is recovered from the numerical results of nodal displacement using super convergent patch recovery method (Boroomand and Zienkiewicz, 1997; Zienkiewicz and Zhu, 1992) which are found to be the most accurate methods of stress recovery. The algorithm of the arrest and/or breakout analysis is presented in Fig.3.40. Initially the effective tangential stress is compressive at every point on the surface of the natural fracture due to the influence of far field in situ stresses. When the induced hydraulic fracture intersects the natural fracture, pore pressure is built up inside the natural fracture which results in the dilation of the natural fracture. As the injection continues due to the increase in pressure inside the natural fracture, the effective stresses acting at the surfaces of the natural fracture decrease. In particular, tangential stress at the circumference of the natural fracture gradually transforms from compression to tensile. When the effective tangential stress exceeds the tensile strength of the rock, tensile failure takes place. Depending on the point of failure, this is called crossing or breakout (see Fig.3.38).

Parametric study of induced fracture arrest by and/or breakout of natural fracture

For the purpose of arrest and breakout analysis a number of cases are studied by varying angle of approach ' θ ' (as shown in Fig.3.38) and differential stress, $\sigma_H - \sigma_h$. In all cases it is assumed that the induced fracture has already intersected the natural fracture. The natural fracture length is varied from 10 to 20 m and the natural fracture placed 20 m away from the wellbore. Reservoir properties and natural fracture data are given in Table 3.2.

Effect of angle of approach

In order to study the influence of angle of approach on the induced fracture arrest by and/or breakout of natural fracture, three cases of 90° , 60° and 30° are considered. Differential stress and natural fracture length are kept constant at 1000 psi and 10 m respectively.

The variation of effective tangential stress at angular positions along the surface of the natural fracture for the case of 90° angle of approach is presented in **Fig.3.41**. From the figure it can be seen that the first point where the effective tangential stress exceeds the tensile strength of the rock is at 90° angular position. That means that the breakout of natural fracture occurs at the point opposite of the intersection point. Therefore, in the case of 90° angle of approach induced hydraulic fracture crosses the natural fracture and propagates further into the formation without changing its original direction.

The variation of effective tangential stress at angular positions along the surface of the natural fracture for the case of 60° angle of approach is presented in **Fig.3.42**. From the figure it can be seen that the result is very similar to that of 90° angle of approach. Variation of effective tangential stress at angular positions along the surface of the natural fracture for the case of 30° angle of approach is presented in **Fig.3.43**. From the figure it can be seen that at 180° angular position the effective tangential stress reaches the tensile strength of the rock (-150 psi). Therefore, in this case breakout takes place at the far end tip of the natural fracture.

From the above result one can conclude that at high angle of approach break out occurs at the point opposite to the initial intersecting point. At low angle of approach the induced hydraulic fracture is more likely to be arrested (at least temporarily) and/or breaks out from far end tip of the natural fracture. Results when compared with results of the Potluri

Effect of differential stress

In order to study the influence of differential stress on the induced fracture arrest by and/or breakout of natural fracture an angle of approach 60° and 500 psi differential stress are considered and compared with the case of 1000 psi differential stress. The length of the natural fracture is kept constant at 10 m.

The change in effective tangential stress at different angular positions along the surface of the natural fracture for the cases of 500 psi differential stress is presented in **Fig.3.44**. From the figure it can be seen that unlike the previous case (see Fig.3.68) induced fracture breaks out at the far end tip of the natural fracture (180° angular position). Therefore, at low differential stress the induced hydraulic fracture breaks out at the far end tip of the natural fracture.

Effect of length of the natural fracture

In order to study the influence of natural fracture length on the induced fracture arrest by and/or breakout of natural fracture a 20 m long natural fracture is considered. Angle of approach and differential stress are kept constant at 90° and 1000 psi respectively.

The change in effective tangential stress at the angular positions along the surface of the natural fracture for the cases of 20 m long natural fracture is presented in **Fig.3.45**. From the figure it can be seen that after 18 minutes of injection the effective stress at the circumference of the natural fracture remains compressive. This means that the fracture is more likely to be arrested by the 20 m long natural fracture.

Effect of injection rate

In order to study the influence of injection rate on the induced fracture arrest by and/or breakout of natural fracture the injection rate is increased from 20 bbl/min to 35 bbl/min. The length of the natural fracture, angle of approach and differential stress are kept constant at 20 m, 90° and 1000 psi respectively.

The change in effective tangential stress at the angular positions along the surface of the natural fracture for the cases of 35 bbl/min injection rate is presented in **Fig.3.46**. From the figure it can be seen that after 8.4 minutes of injecting the effective stress at the circumference of the natural fracture at 90° angular position becomes tensile and exceeds the tensile strength of the natural fracture. This means that the induced fracture is more likely to break out of natural fracture at the point opposite to the initial intersecting. When this result is compared with that of 20 bbl/min injection rate (see Fig.3.71), it is found that induced fracture is arrested by the natural fracture on that case.

3.4 Summary

In this chapter, a fully coupled poroelastic model is presented to study the fracture propagation in presence of a natural fracture. In order to achieve this, first an arbitrary oriented natural fracture is initiated to the previously developed model to study the effect of natural fracture. Next a parametric study of various parameters which can affect the process of hydraulic fracturing in presence of natural fracture is conducted and discussed with supporting plots. Numerical results have shown that natural fractures have a considerable

effect on the induced fracture propagation. In particular it is observed that for medium sized natural fracture (≤ 10 m) the angle of approach and the stress state plays an important role. At high angle of approach and high differential stress, it is more likely for the hydraulic fracture to cross the medium size natural fracture, whereas for a case where angle of approach and differential stress are low the hydraulic fracture is more likely to be arrested (at least for a short time) and then reorient and propagate along natural fracture. Results also confirmed that in the case of 90° (or close to 90°) angle of approach the hydraulic fracture always crosses the natural fracture and the differential stress (studied here) has no significant effect on the trajectory of the hydraulic fracture propagation. Crossing of the natural fracture depends on the size of the natural fracture. In the case of long (>10 m, 20 m is used in this study) natural fracture, the propagation of induced fracture is stopped by the natural fracture. If the injection rate is high enough the induced hydraulic fracture crosses the long natural fracture.

These results are compared with results published in Potluri (2004) and found that the trends are similar. Low angles of approach and low differential stress favors the induced fracture to open the natural fracture and propagates through the axis of the natural fracture, whereas high angles of approach with moderate to high differential stress favor crossing of the natural fracture. In all cases width constriction happened and as expected the magnitudes (decrease in width, increase of propagation pressure) are different as Potluri (2004) uses elastic model with no fluid leak-off.

Next the model is further modified to provide an in-depth understanding of the induced fracture arrest by and/or breakout the natural fracture in a close proximity. It is observed that at high angle of approach and high differential stress break out occurs at the point opposite to the initial intersecting point. At low angle of approach the induced hydraulic fracture is more likely to be arrested (at least temporarily) and/or breaks out from far end tip of the natural fracture.

Table 3.1: Parameter used for the study of fracture propagation and interaction

| Reservoir properties | |
|--|--------------------------------|
| Young's modulus of elasticity | 1.48 E+6 psi |
| Bulk Poisson's ratio | 0.2 |
| Biot's coefficient, α | 1.0 |
| Leak-off coefficient, C_L | 0.00025 ft.min ^{-0.5} |
| Fracture toughness | 500 psi.ft ^{0.5} |
| Fracture fluid viscosity, μ_f | 1 cP |
| Formation permeability, k_x, k_y | 0.1 mD |
| Formation porosity, ϕ | 0.1 |
| Reservoir fluid compressibility | 1 E-5 1/psi |
| Reservoir fluid viscosity, μ | 1 cP |
| Initial reservoir pressure, p_i | 4000 psi |
| Maximum horizontal stress, σ_H | 5500-6000 psi |
| Minimum horizontal stress, σ_h | 5000 psi |
| Injection rate, q | 20-35 bbl/min |
| Natural Fracture properties | |
| Length of natural fracture, l_{nf} | 10 m |
| Width of natural fracture | 0.5 mm |
| Rock tensile strength, T_o | -150.0 psi |
| Distance of natural fracture from wellbore | 20 m |
| Porosity, ϕ | 0.15 |

Table 3.2: Reservoir properties and wellbore data used for fracture arrest and breakout analysis

| | |
|---------------------------------------|---------------|
| Young's modulus of formation | 1.58 E 6 psi |
| Porosity | 0.1 |
| Biot's coefficient, α | 1.0 |
| Initial reservoir pressure, p_i | 5000 psi |
| Poisson's ratio | 0.2 |
| Viscosity of fracturing fluid | 1.0 cp |
| Maximum horizontal stress, σ_H | 5200-6000 psi |
| Minimum horizontal stress, σ_h | 5000 psi |
| Drainage area | 5000 ft |
| Formation permeability, k_x, k_y | 0.1 mD |

Table 3.3: Natural fracture data used for fracture interaction, fracture arrest and breakout analysis

| | |
|--|------------|
| Length of natural fracture, l_{nf} | 10~20 m |
| Width of natural fracture | 0.5 mm |
| Rock tensile strength, T_o | -150.0 psi |
| Distance of natural fracture from wellbore | 20 m |
| Porosity, ϕ | 0.15 |

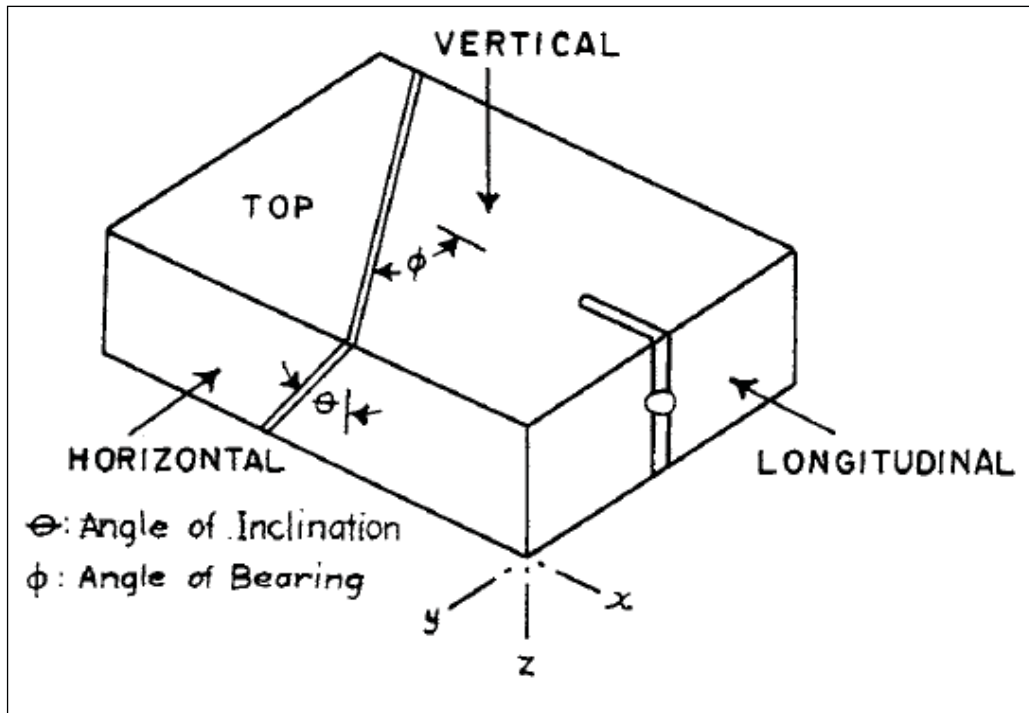


Fig. 3.1: Schematic of Lammont and Jessen's model with existing fracture showing directions of loading (from Lammont and Jessen, 1943).

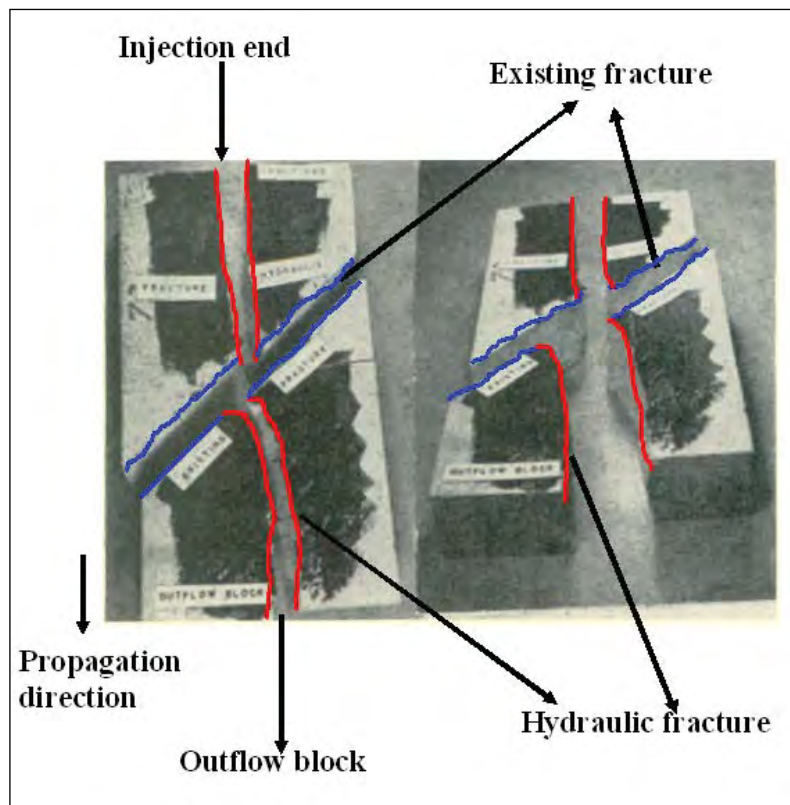


Fig. 3.2: Austin stone model with hairline fracture, angle of inclination 0° , angle of bearing 45° (from Lammont and Jessen, after Potluri, 2004).

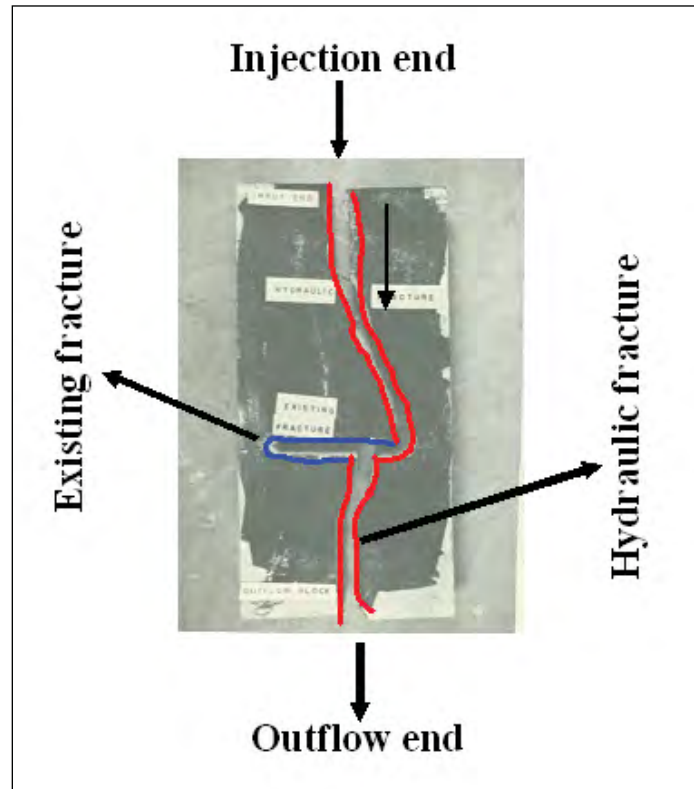


Fig. 3.3: Austin stone model with 2-IN width fracture, angle of inclination 0° , angle of bearing 90° (from Lammont and Jessen, after Potluri, 2004).

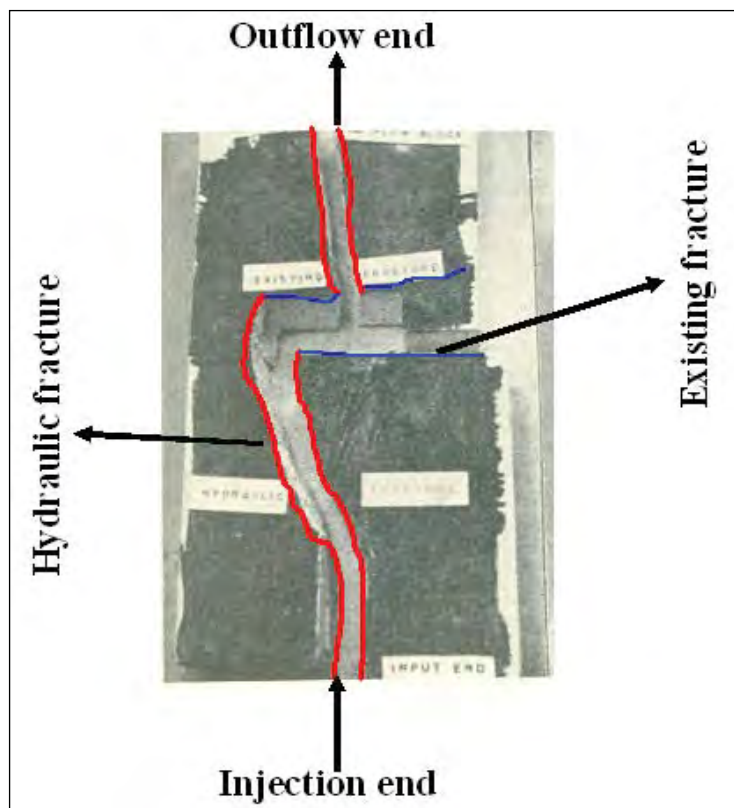


Fig. 3.4: Austin stone model with 1/2-IN width fracture, angle of inclination 0° , angle of bearing 90° (from Lammont and Jessen, after Potluri, 2004).

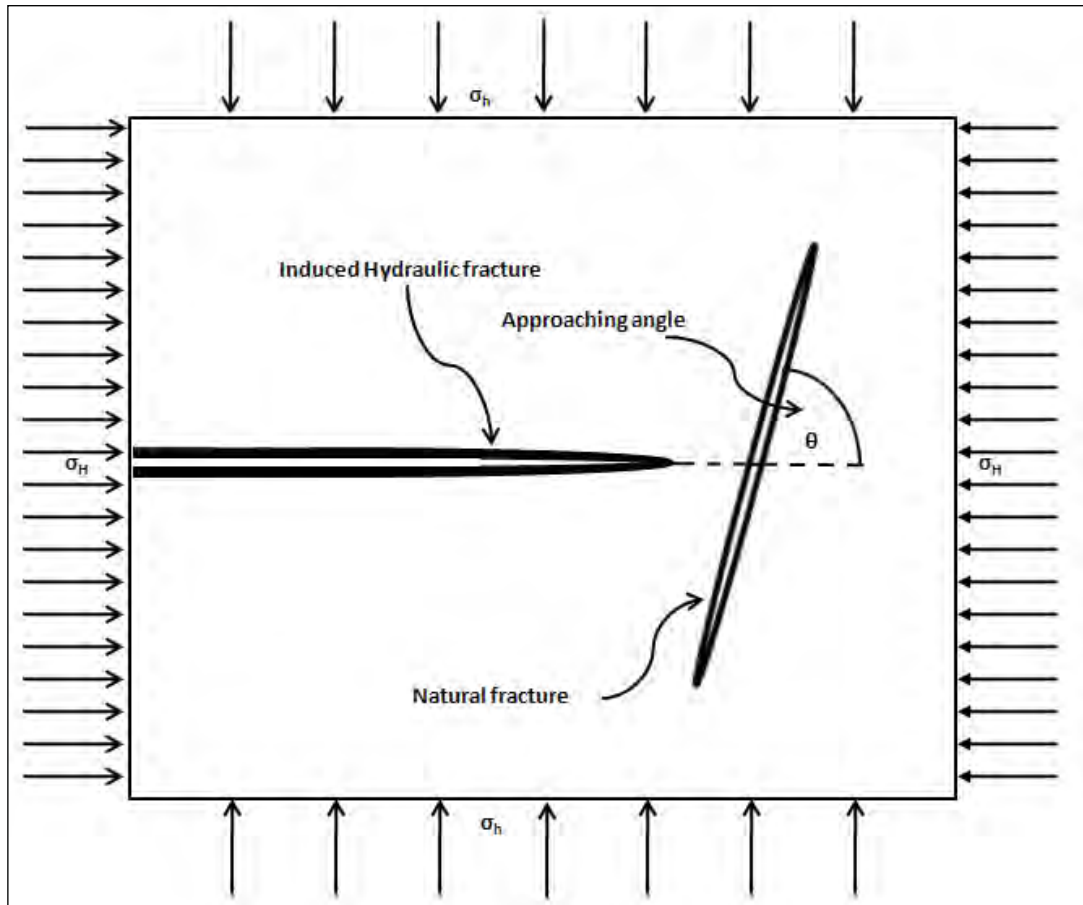


Fig. 3.5: Schematic of Induced hydraulic fracture intersecting a pre-existing natural fracture.

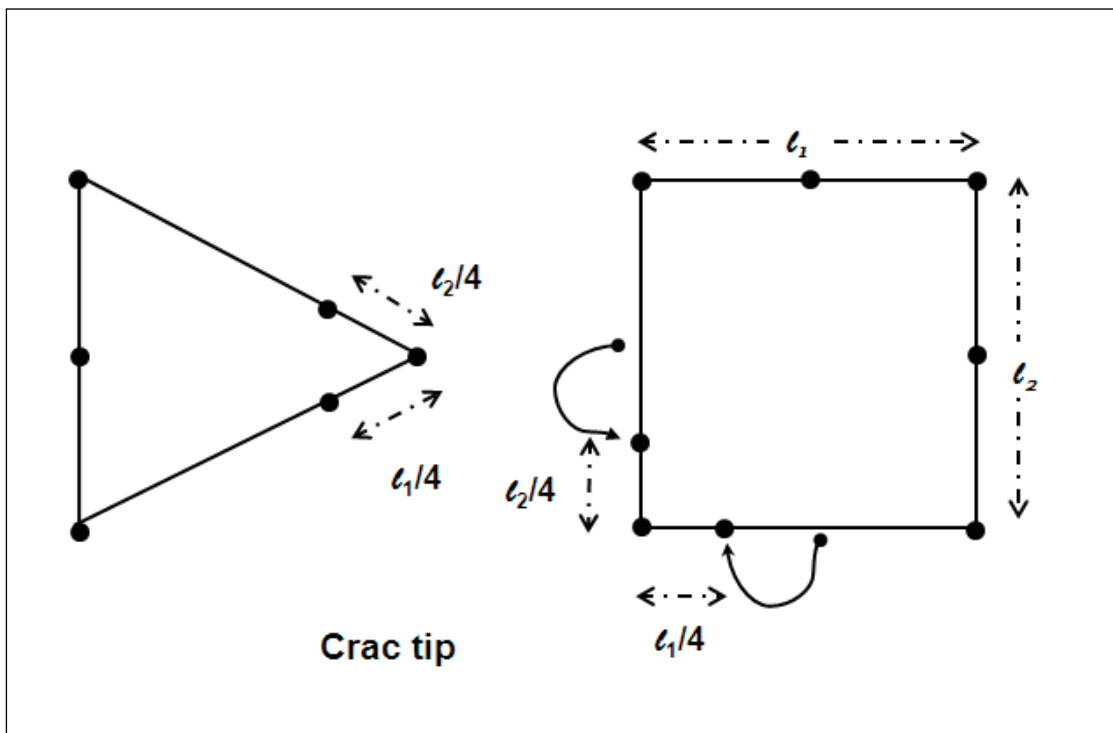


Fig. 3.6: Quarter point singular element.

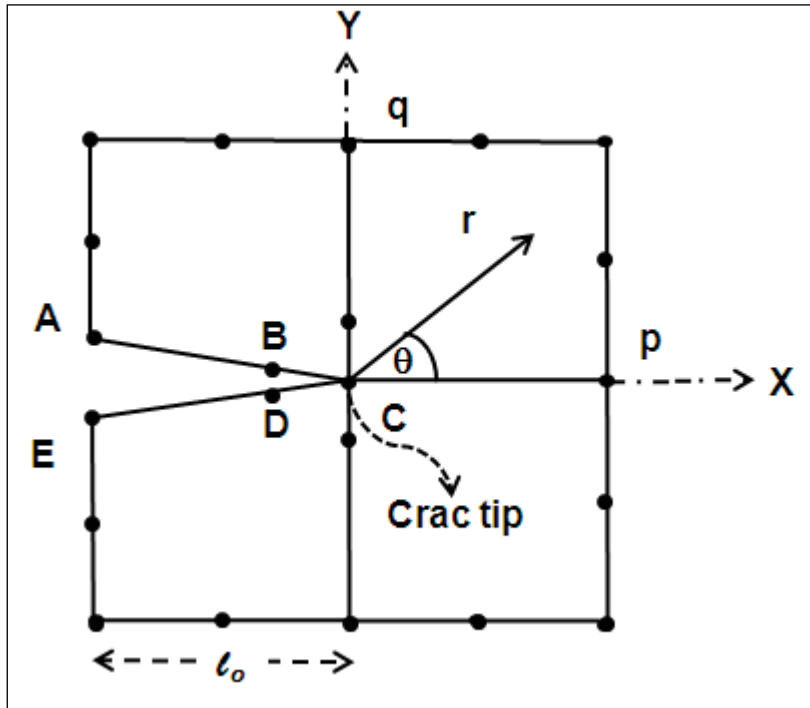


Fig. 3.7: Nodal arrangement for computation of stress intensity factor using displacement correlation method.

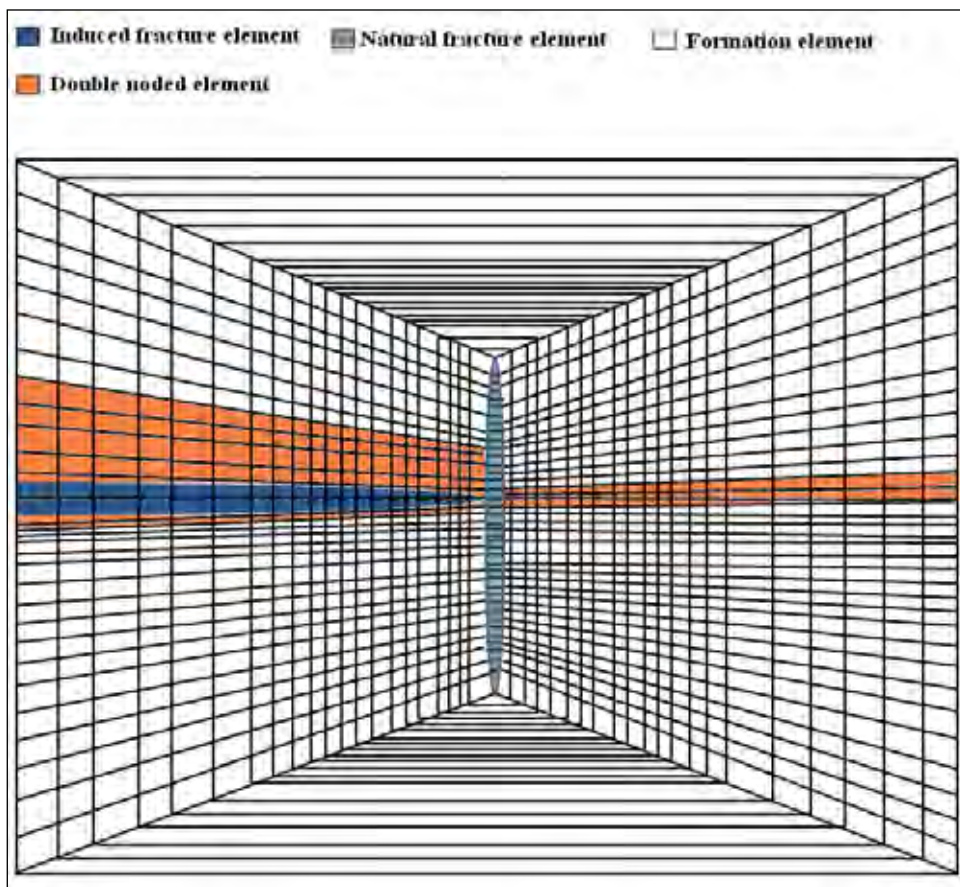


Fig. 3.8(a): Schematic of finite element 2D mesh of the induced fracture, natural fracture and the reservoir system. (A total number of nodes=47123 and total number of elements=19444 are used for this study).

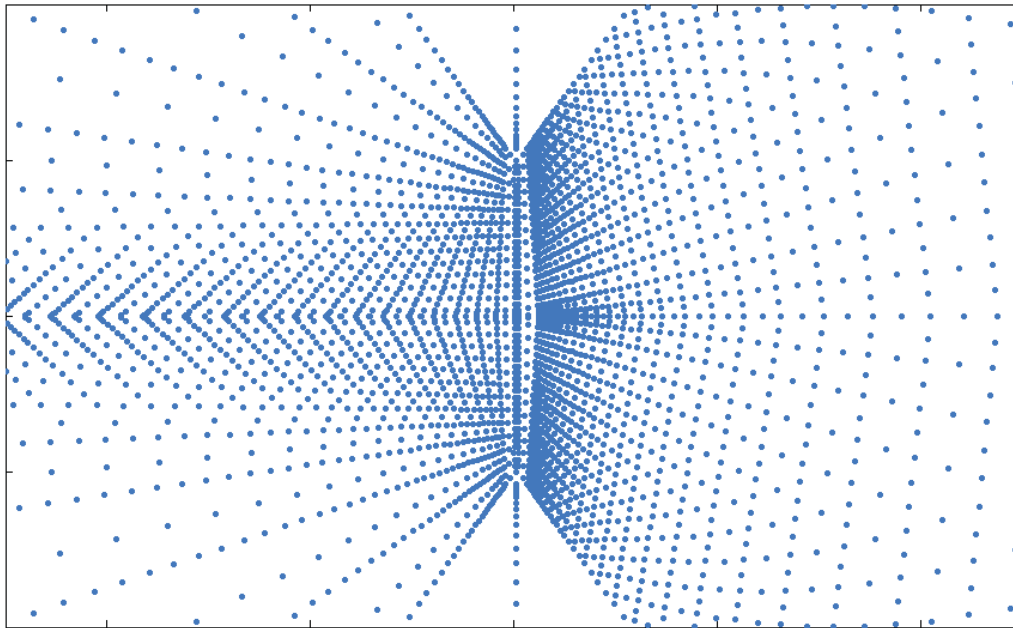


Fig. 3.8 (b): Finite element 2D mesh of the induced fracture, natural fracture and the reservoir system showing near natural fracture region (A total number of nodes=47123 and total number of elements=19444 are used for this study).

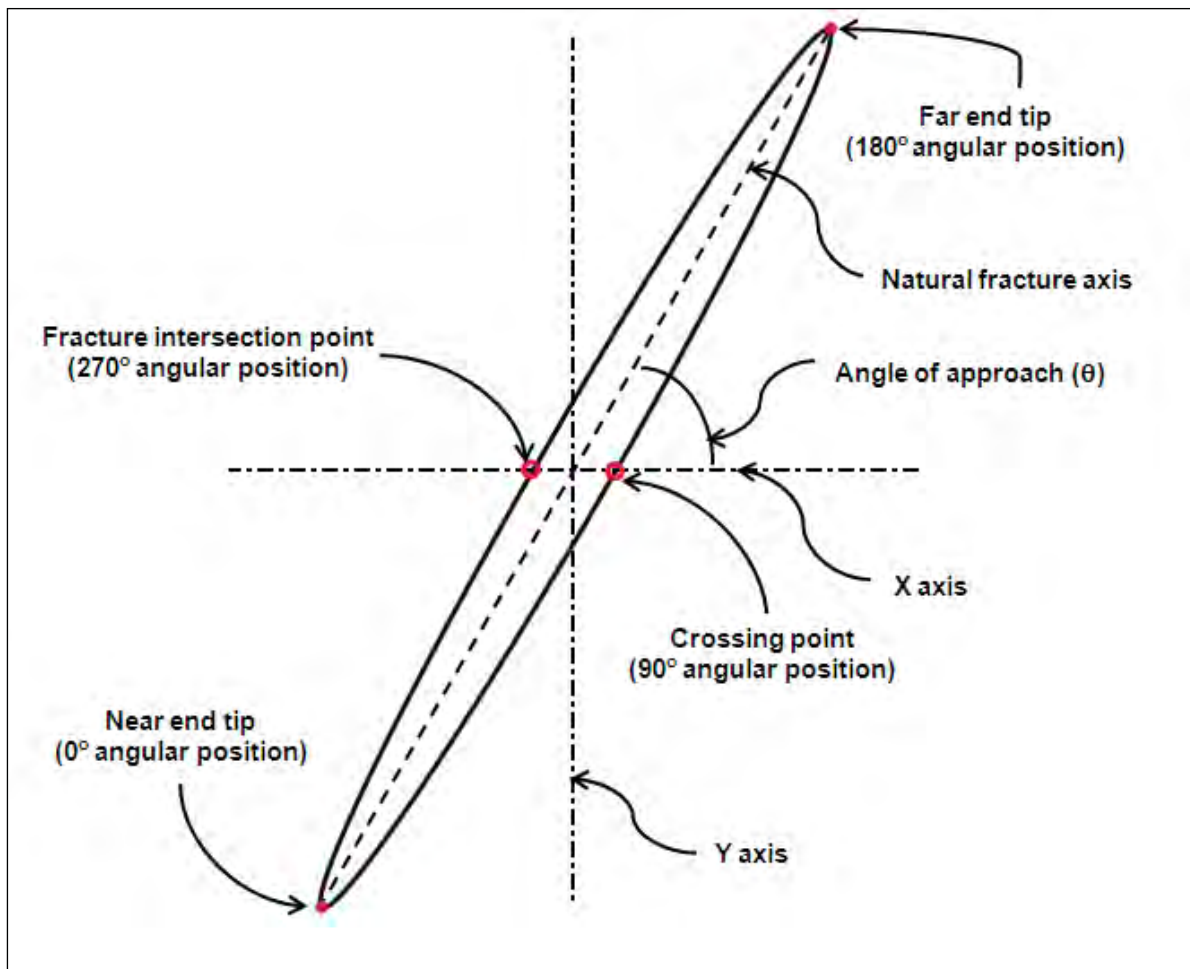


Fig .3.9: Schematic of natural fracture showing different angular positions at the surface.

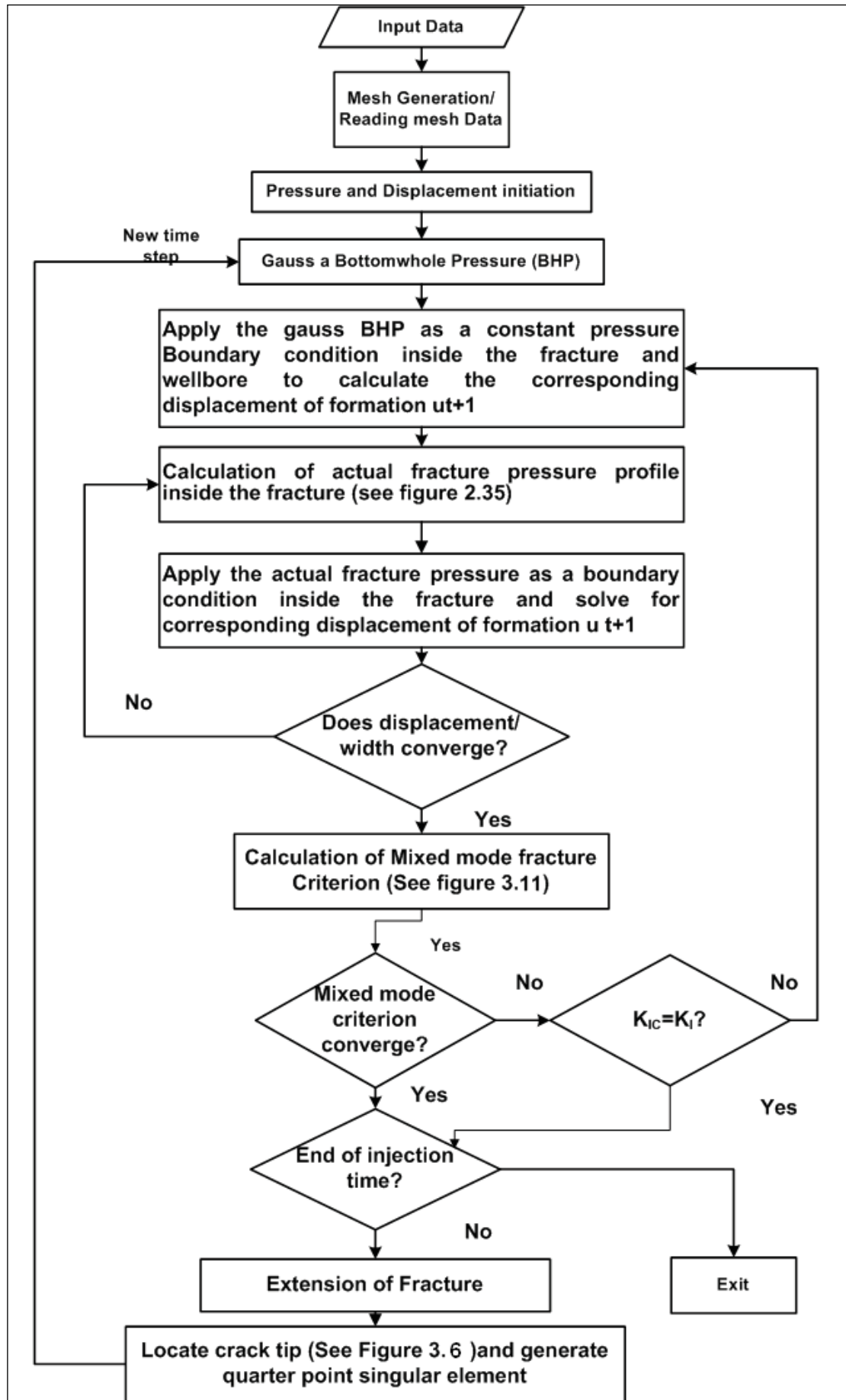


Fig .3.10: Fracture propagation/ extension algorithm using mixed mode fracture criteria.

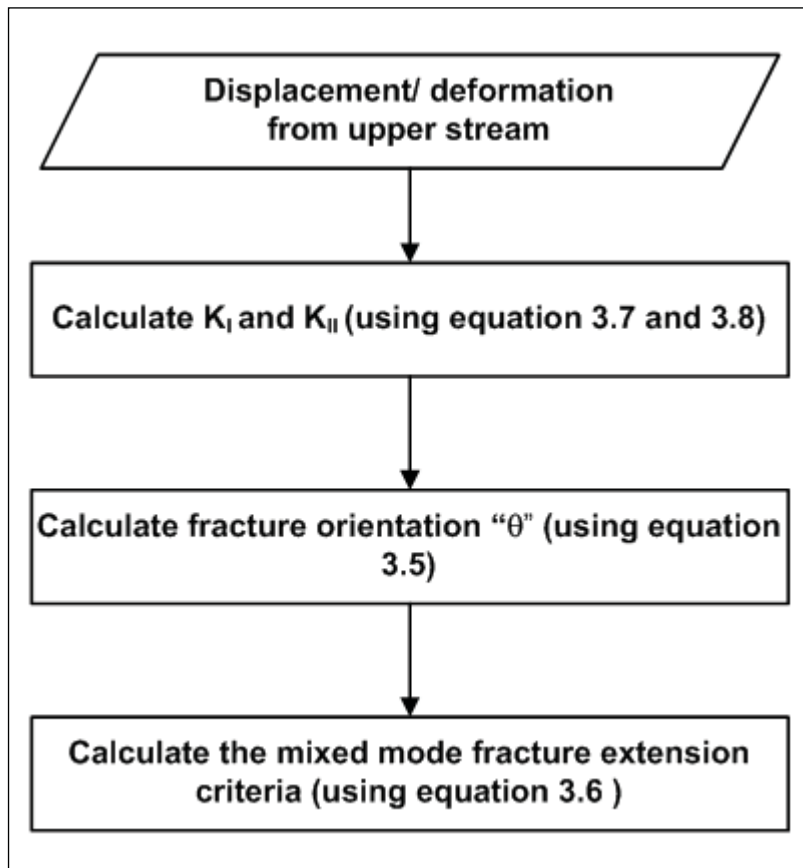


Fig .3.11: Calculation of mixed mode fracture criteria.

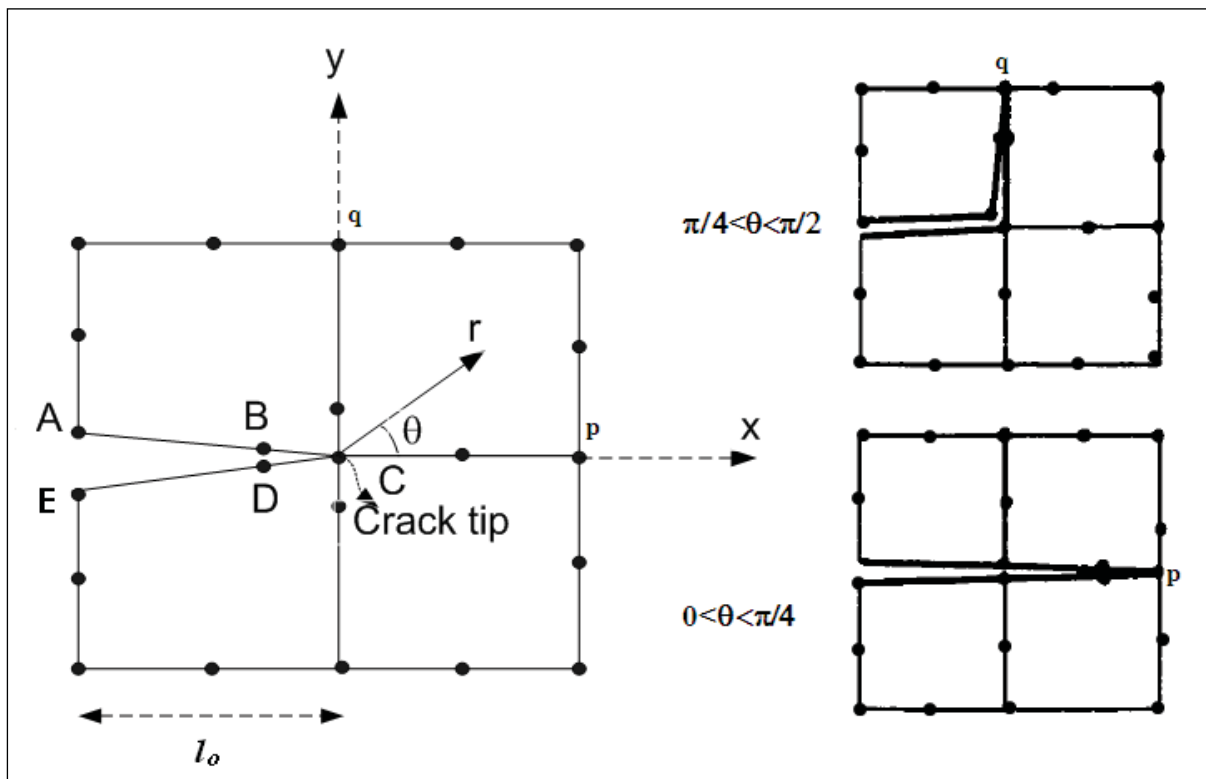


Fig. 3.12: Identification of crack orientation.

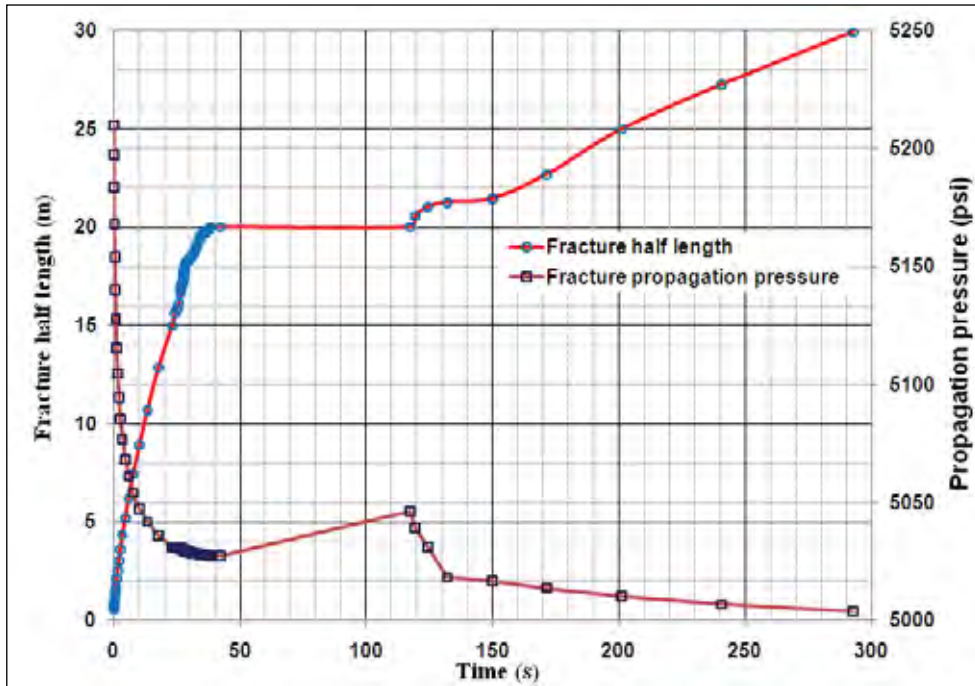


Fig. 3.13: Fracture half length and propagation pressure vs. pumping time, natural fracture length 10 m, width 0.5 mm, angle of approach 90° and natural fracture position from well bore is 20 m, differential stress 1000 psi (poroelastic reservoir, $\sigma_H = 6000$ psi, $\sigma_h = 5000$ psi, $p_i = 4500$ psi, $\mu_f = 1$ cp, $k = 0.1$ mD, $q = 20$ bbl/min, fracture toughness = 500 psi.ft^{0.5}).

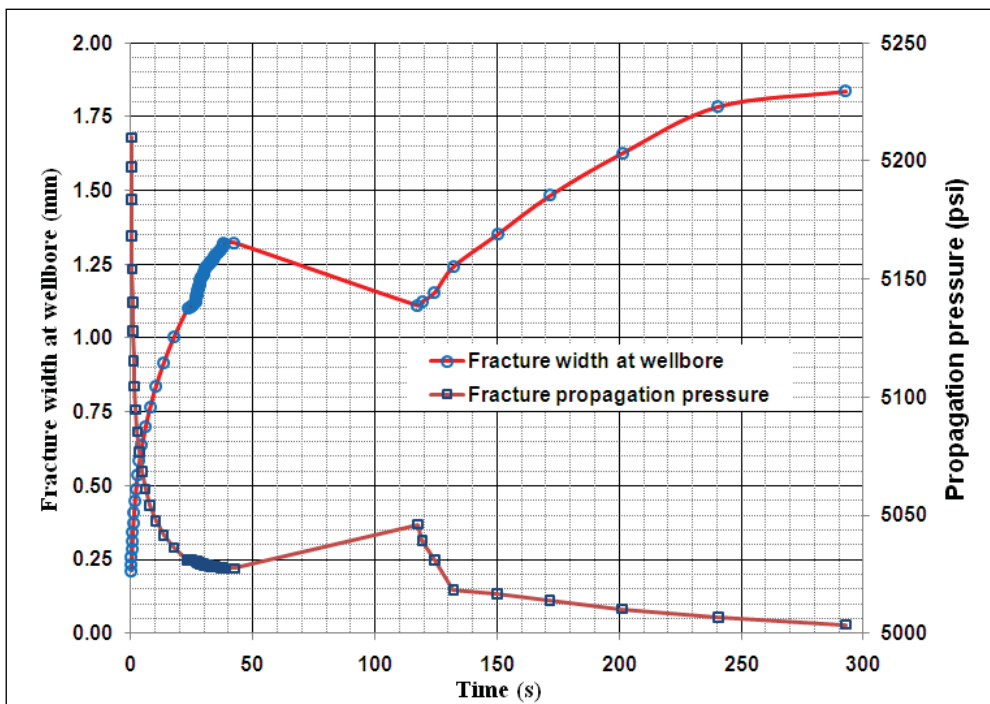


Fig. 3.14: Fracture width and propagation pressure vs. pumping time, natural fracture length 10 m, width 0.5 mm, angle of approach 90° , natural fracture position from well bore is 20 m and differential stress 1000 psi (poroelastic reservoir, $\sigma_H = 6000$ psi, $\sigma_h = 5000$ psi, $p_i = 4500$ psi, $\mu_f = 1$ cp, $k = 0.1$ mD, $q = 20$ bbl/min, fracture toughness = 500 psi.ft^{0.5}).

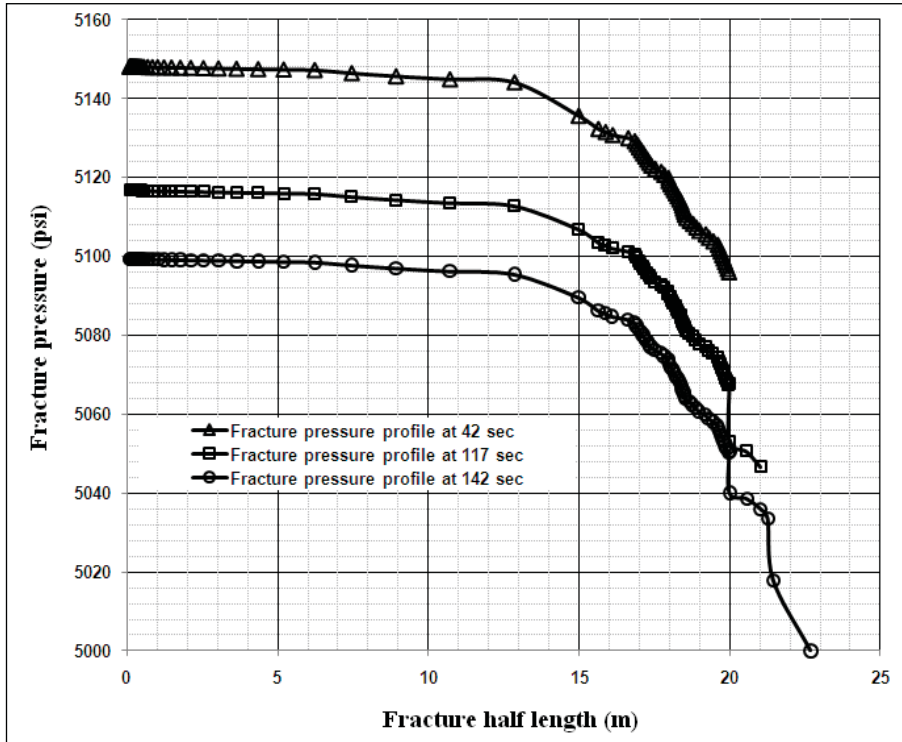


Fig. 3.15: Fracturing fluid pressure profile for selected time steps, natural fracture length 10 m, width 0.5 mm, angle of approach 90°, natural fracture position from well bore is 20 m and differential stress 1000 psi (poroelastic reservoir, $\sigma_H = 6000$ psi, $\sigma_h = 5000$ psi, $p_i = 4500$ psi, $\mu_f = 1$ cp, $k = 0.1$ mD, $q = 20$ bbl/min, fracture toughness = 500 psi.ft^{0.5}).

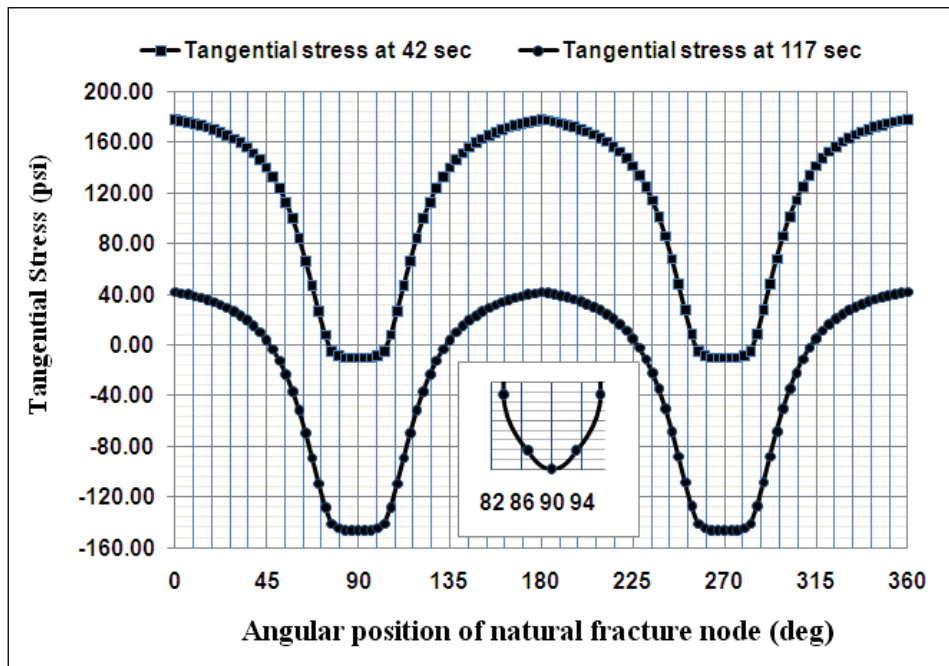


Fig. 3.16: Effective tangential stresses vs. angular position at the surfaces of the natural fracture for selected time steps, natural fracture length 10 m, width 0.5 mm, angle of approach 90°, natural fracture position from well bore is 20 m and differential stress 1000 psi (poroelastic reservoir, $\sigma_H = 6000$ psi, $\sigma_h = 5000$ psi, $p_i = 4500$ psi, $\mu_f = 1$ cp, $k = 0.1$ mD, $q = 20$ bbl/min, fracture toughness = 500 psi.ft^{0.5}).

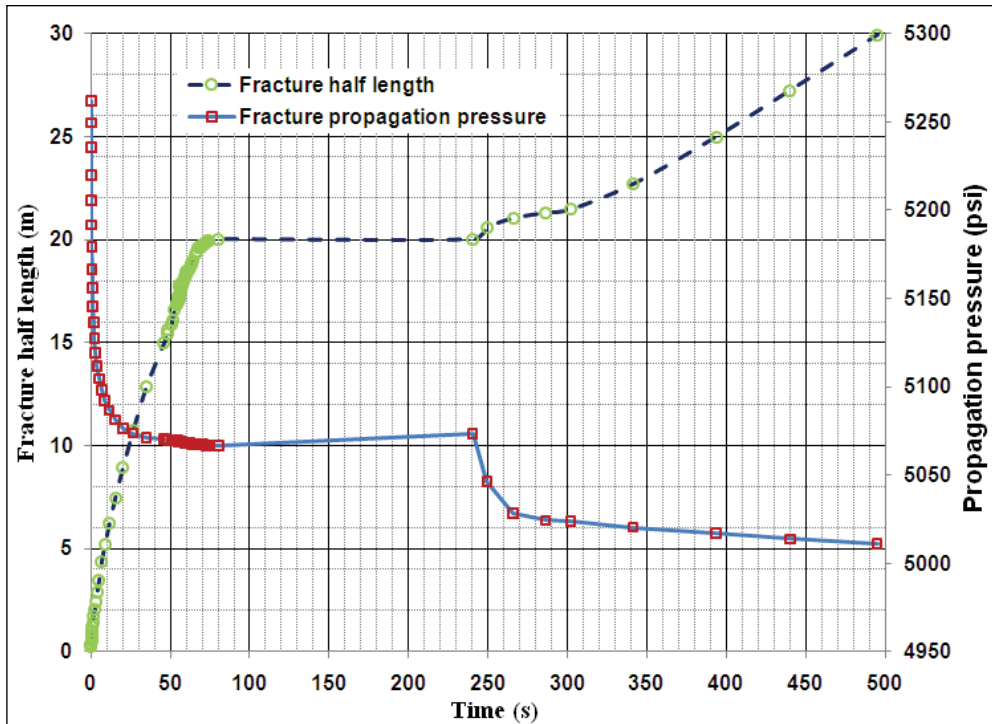


Fig. 3.17: Fracture half length and propagation pressure vs. pumping time, natural fracture length 10 m, width 0.5 mm, angle of approach 60° , natural fracture position from well bore is 20 m and differential stress 1000 psi (poroelastic reservoir, $\sigma_H = 6000$ psi, $\sigma_h = 5000$ psi, $p_i = 4500$ psi, $\mu_f = 1$ cp, $k = 0.1$ mD, $q = 20$ bbl/min, fracture toughness = 500 psi.ft $^{0.5}$).

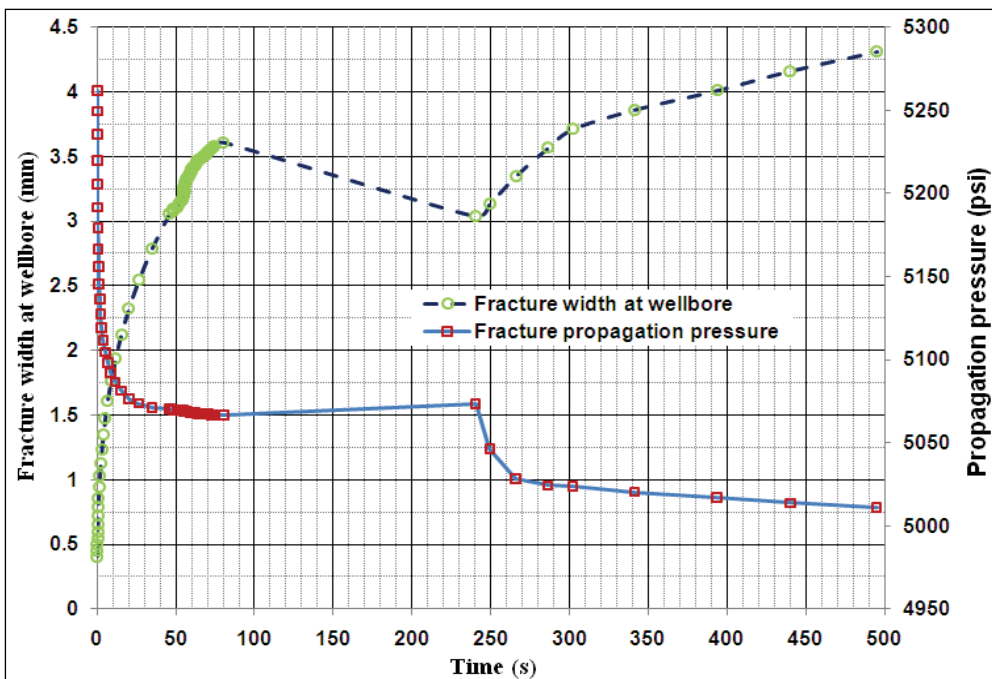


Fig. 3.18: Fracture width and propagation pressure vs. pumping time, natural fracture length 10 m, width 0.5 mm, angle of approach 60° , natural fracture position from well bore is 20 m and differential stress 1000 psi (poroelastic reservoir, $\sigma_H = 6000$ psi, $\sigma_h = 5000$ psi, $p_i = 4500$ psi, $\mu_f = 1$ cp, $k = 0.1$ mD, $q = 20$ bbl/min, fracture toughness = 500 psi.ft $^{0.5}$).

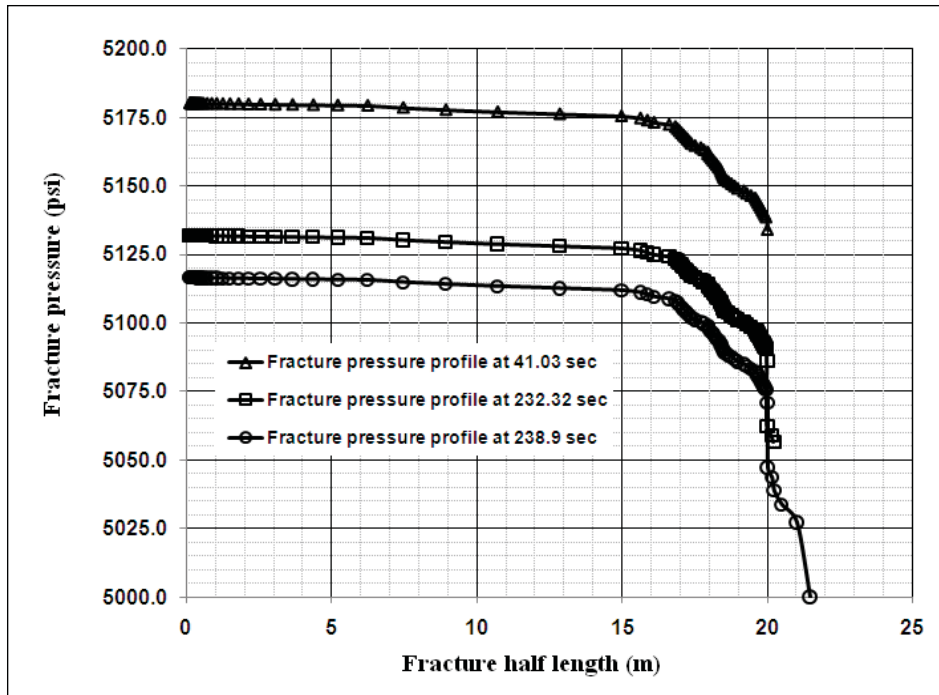


Fig. 3.19: Fracturing fluid pressure profile for selected time steps, natural fracture length 10 m, width 0.5 mm, angle of approach 60° , natural fracture position from well bore is 20 m and differential stress 1000 psi (poroelastic reservoir, $\sigma_H = 6000$ psi, $\sigma_h = 5000$ psi, $p_i = 4500$ psi, $\mu_f = 1$ cp, $k = 0.1$ mD, $q = 20$ bbl/min, fracture toughness = 500 psi.ft $^{0.5}$).

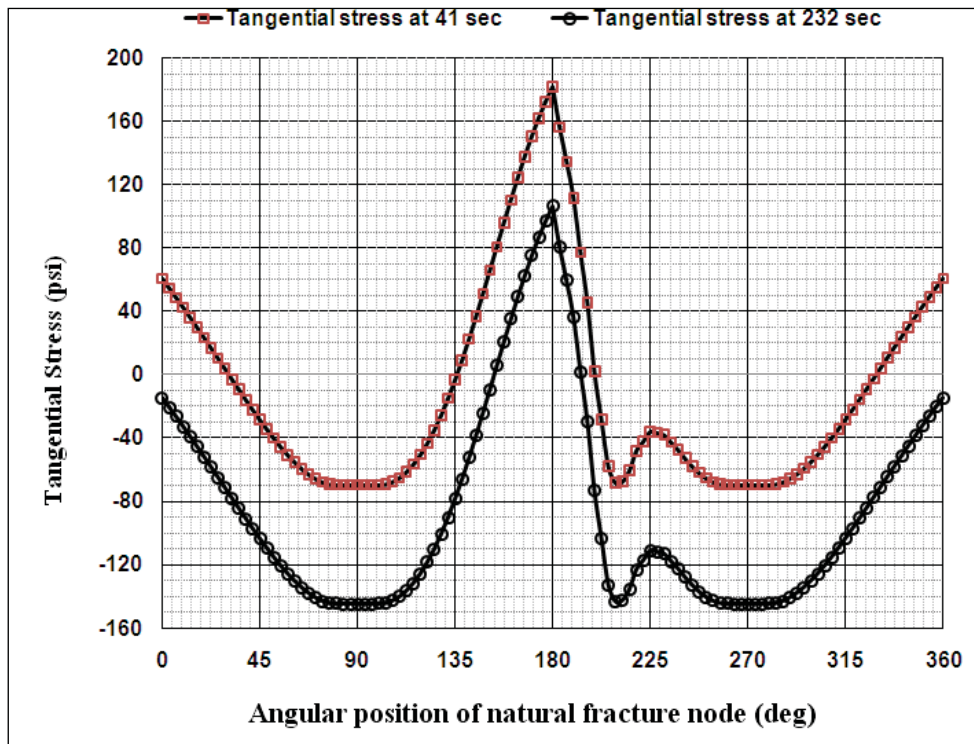


Fig. 3.20: Effective tangential stresses vs. angular position at the surfaces of the natural fracture for selected time steps, natural fracture length 10 m, width 0.5 mm, angle of approach 60° , natural fracture position from well bore is 20 m and differential stress 1000 psi (poroelastic reservoir, $\sigma_H = 6000$ psi, $\sigma_h = 5000$ psi, $p_i = 4500$ psi, $\mu_f = 1$ cp, $k = 0.1$ mD, $q = 20$ bbl/min, fracture toughness = 500 psi.ft $^{0.5}$).

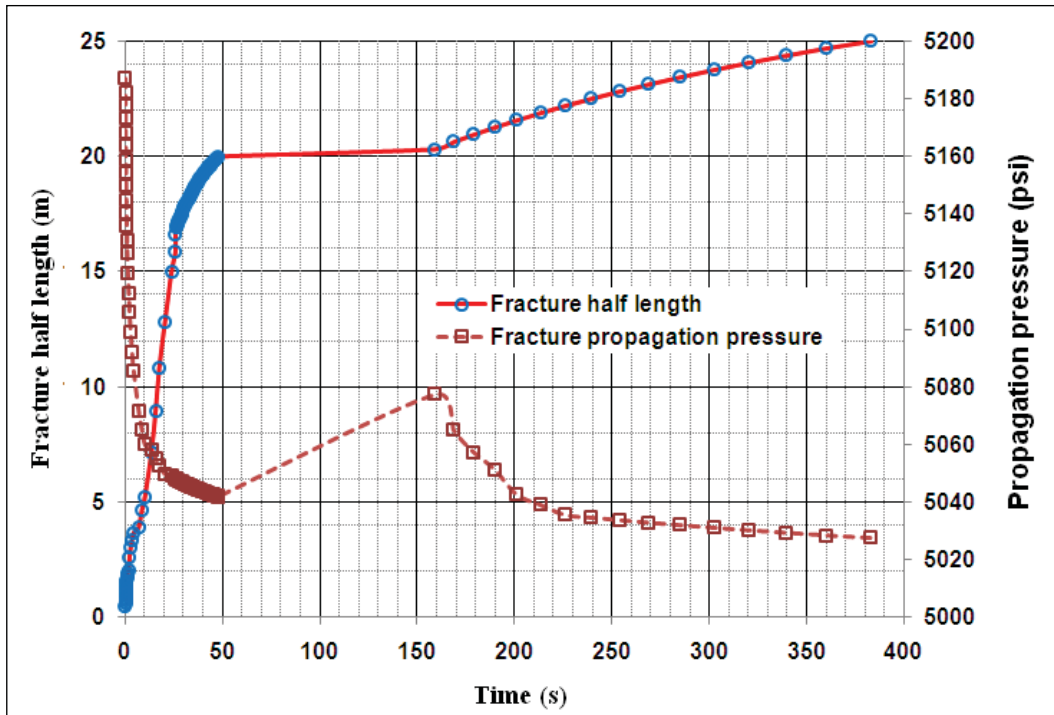


Fig. 3.21: Fracture half length and propagation pressure vs. pumping time, natural fracture length 10 m, width 0.5 mm, angle of approach 30° and natural fracture position from well bore is 20 m, differential stress 1000 psi (poroelastic reservoir, $\sigma_H = 6000$ psi, $\sigma_h = 5000$ psi, $p_i = 4500$ psi, $\mu_f = 1$ cp, $k = 0.1$ mD, $q = 20$ bbl/min, fracture toughness = 500 psi.ft^{0.5}).

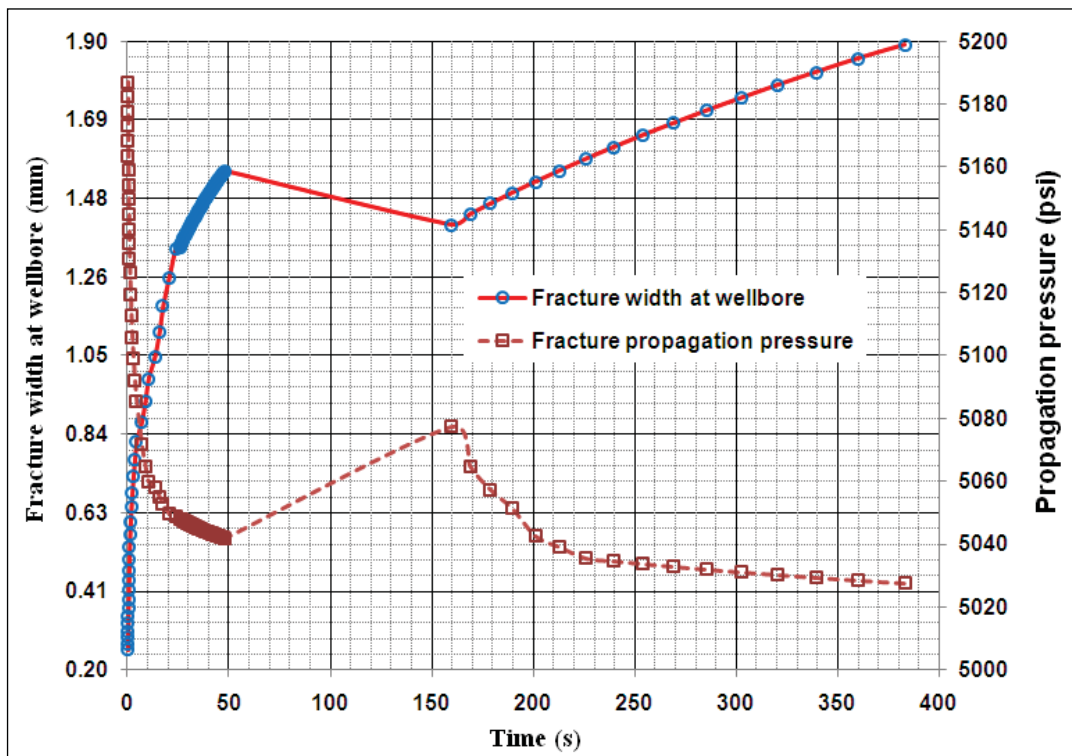


Fig. 3.22: Fracture width and propagation pressure vs. pumping time, natural fracture length 10 m, width 0.5 mm, angle of approach 30° , natural fracture position from well bore is 20 m and differential stress 1000 psi (poroelastic reservoir, $\sigma_H = 6000$ psi, $\sigma_h = 5000$ psi, $p_i = 4500$ psi, $\mu_f = 1$ cp, $k = 0.1$ mD, $q = 20$ bbl/min, fracture toughness = 500 psi.ft^{0.5}).

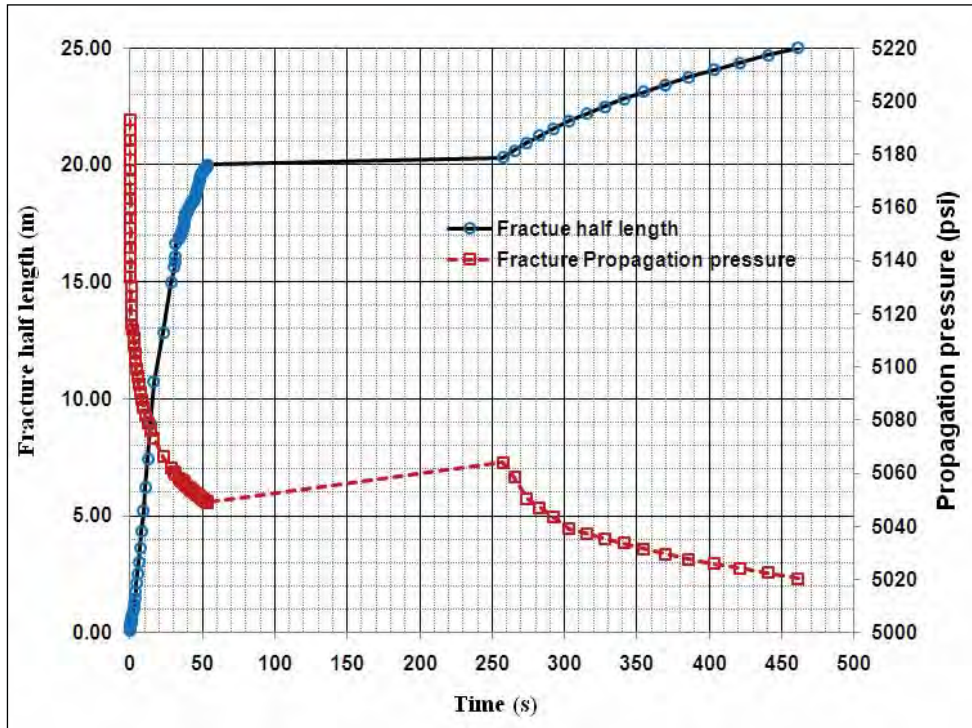


Fig. 3.23: Fracture half length vs. pumping time, natural fracture length 10 m, width 0.5 mm, angle of approach 60° and natural fracture position from well bore is 20 m (poroelastic reservoir, $\sigma_H = 6000$ psi, $\sigma_h = 5500$ psi, $p_i = 4500$ psi, $\mu_f = 1$ cp, $k = 0.1$ mD, $q = 20$ bbl/min, fracture toughness = 500 psi.ft^{0.5}).

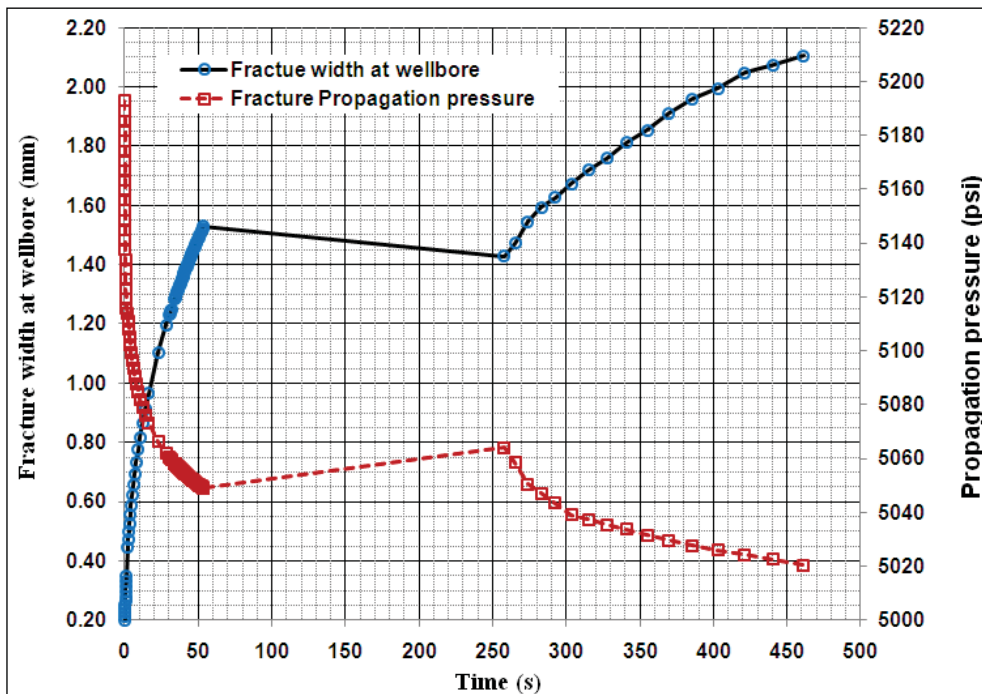


Fig. 3.24: Fracture width vs. pumping time, natural fracture length 10 m, width 0.5 mm, angle of approach 60° and natural fracture position from well bore is 20 m (poroelastic reservoir, $\sigma_H = 6000$ psi, $\sigma_h = 5500$ psi, $p_i = 4500$ psi, $\mu_f = 1$ cp, $k = 0.1$ mD, $q = 20$ bbl/min, fracture toughness = 500 psi.ft^{0.6}).

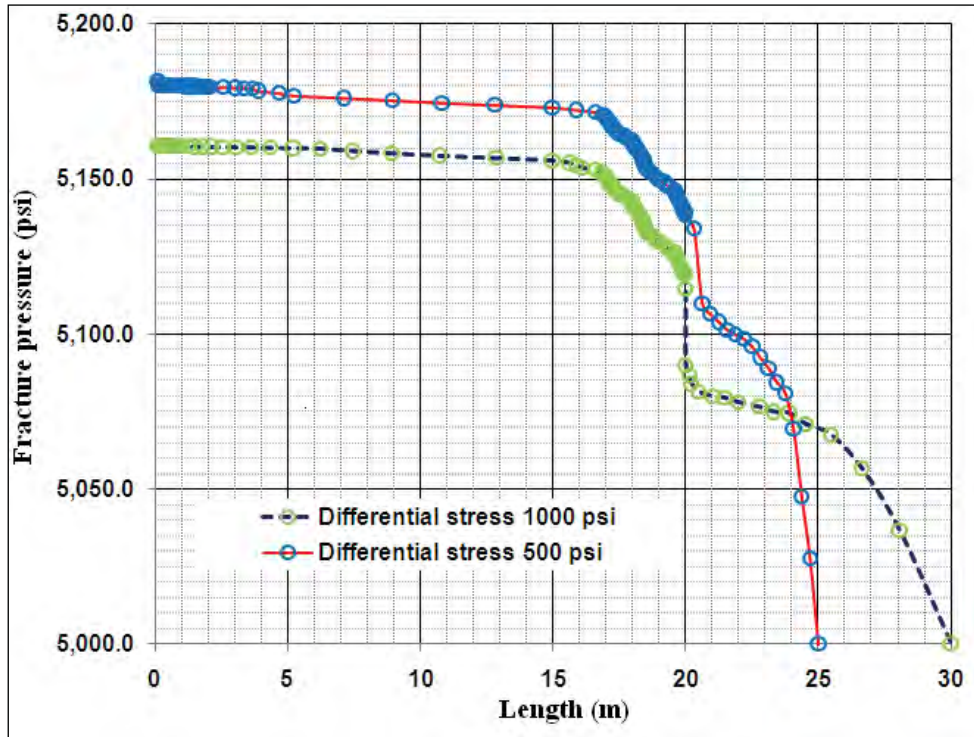


Fig. 3.25: Fracturing fluid pressure profile for two differential stress of 500.0 psi and 1000.0 psi, natural fracture length 10 m, width 0.5 mm, angle of approach 60° and natural fracture position from well bore is 20 m (poroelastic reservoir, $\sigma_H = 6000$ psi, $\sigma_h = 5500 \sim 6000$ psi, $p_i = 4500$ psi, $\mu_f = 1$ cp, $k = 0.1$ mD, $q = 20$ bbl/min, fracture toughness = 500 psi.ft^{0.5}).

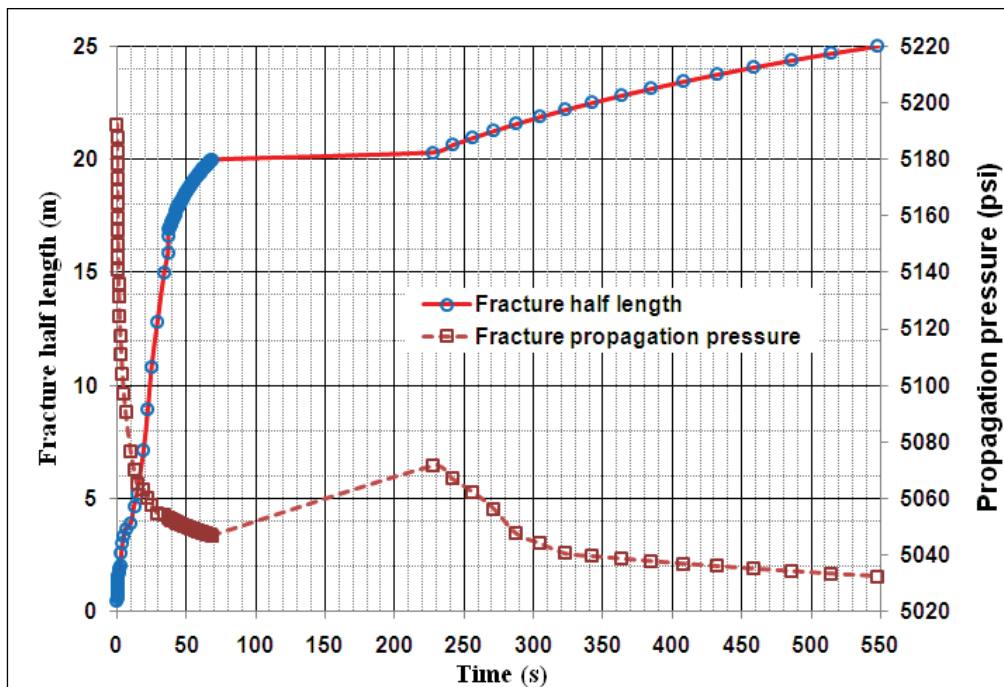


Fig. 3.26: Fracture half length and propagation pressure vs. pumping time, natural fracture length 10 m, width 0.5 mm, angle of approach 30° and natural fracture position from well bore is 20 m, differential stress 500 psi (poroelastic reservoir, $\sigma_H = 6000$ psi, $\sigma_h = 5500$ psi, $p_i = 4500$ psi, $\mu_f = 1$ cp, $k = 0.1$ mD, $q = 20$ bbl/min, fracture toughness = 500 psi.ft^{0.5}).

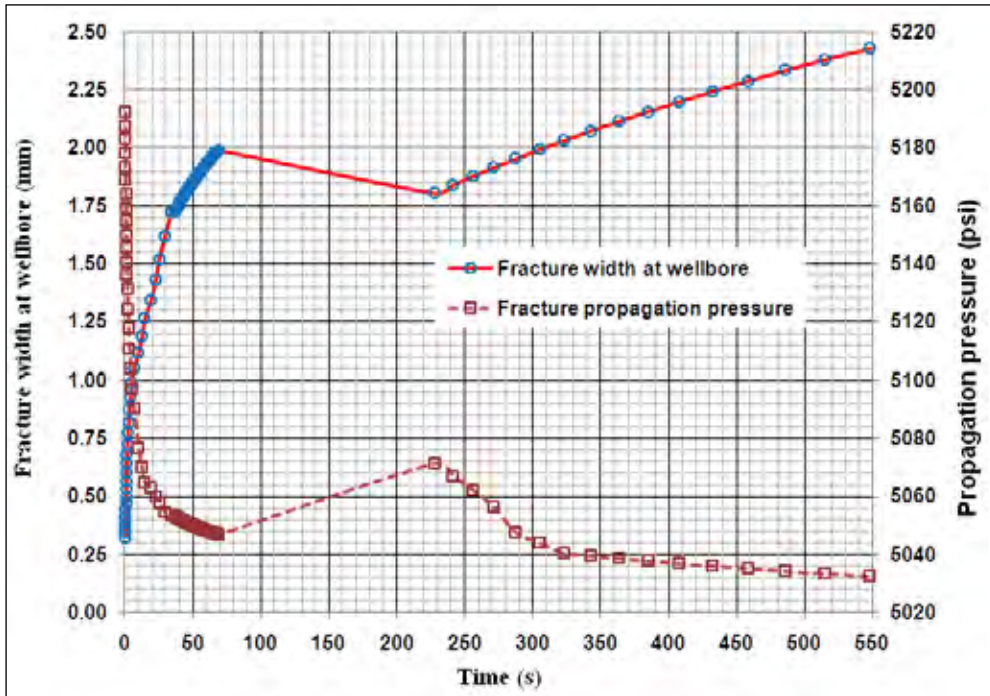


Fig. 3.27: Fracture width and propagation pressure vs. pumping time, natural fracture length 10 m, width 0.5 mm, angle of approach 30° , natural fracture position from well bore is 20 m and differential stress 500 psi (poroelastic reservoir, $\sigma_H = 6000$ psi, $\sigma_h = 5500$ psi, $p_i = 4500$ psi, $\mu_f = 1$ cp, $k = 0.1$ mD, $q = 20$ bbl/min, fracture toughness = 500 psi.ft $^{0.5}$).

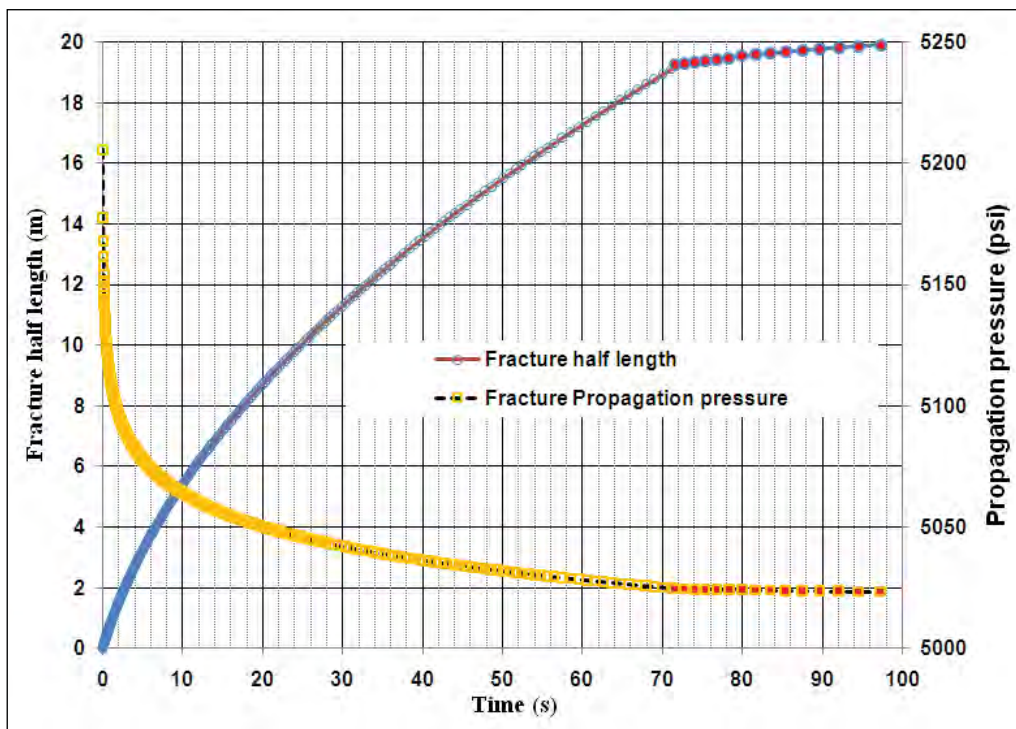


Fig. 3.28: Fracture half length and propagation pressure vs. pumping time, natural fracture length 20 m, width 0.5 mm, angle of approach 90° , natural fracture position from well bore is 20 m and differential stress 1000 psi (poroelastic reservoir, $\sigma_H = 6000$ psi, $\sigma_h = 5500$ psi, $p_i = 4500$ psi, $\mu_f = 1$ cp, $k = 0.1$ mD, $q = 20$ bbl/min, fracture toughness = 500 psi.ft $^{0.5}$).

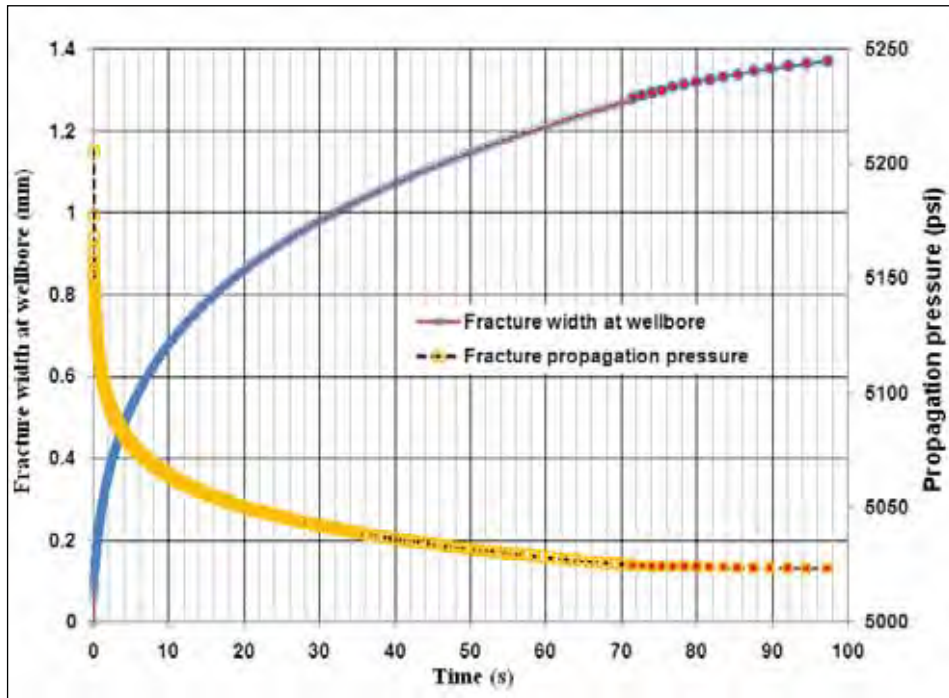


Fig. 3.29: Fracture width and propagation pressure vs. pumping time, natural fracture length 20 m, width 0.5 mm, angle of approach 90°, natural fracture position from well bore is 20 m and differential stress 1000 psi (poroelastic reservoir, $\sigma_H = 6000$ psi, $\sigma_h = 5500$ psi, $p_i = 4500$ psi, $\mu_r = 1$ cp, $k = 0.1$ mD, $q = 20$ bbl/min, fracture toughness of 500 psi.ft^{0.5}).

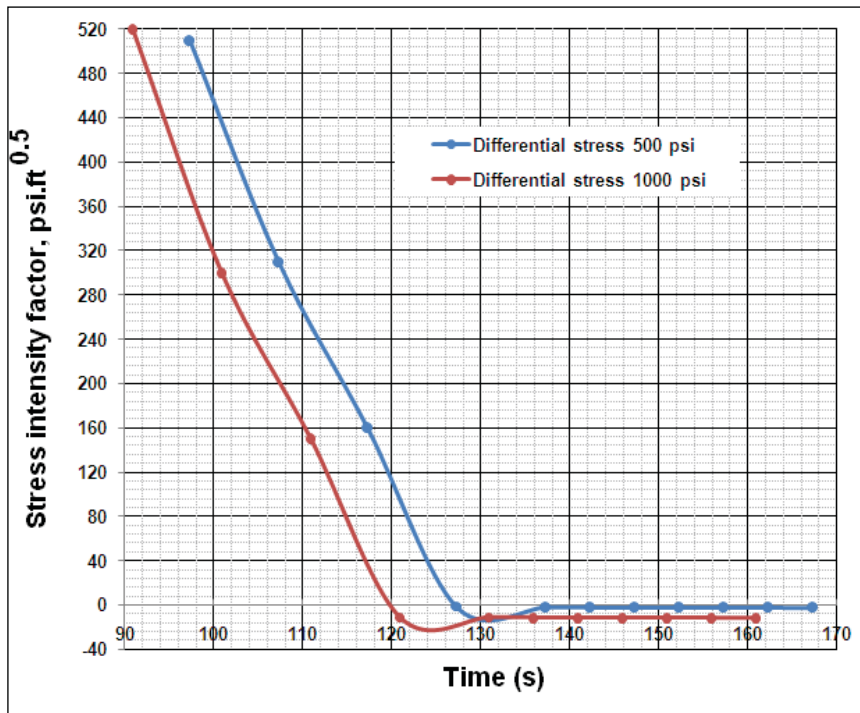


Fig. 3.30: Stress intensity factor at the fracture tip during pressurization after the induced fracture induced fracture propagation stops by the natural fracture for two differential stresses. Natural fracture length 20 m, width 0.5 mm, angle of approach 90°, natural fracture position from well bore is 20 m and differential stress 1000 psi (poroelastic reservoir, $\sigma_H = 6000$ psi, $\sigma_h = 5000\sim 5500$ psi, $p_i = 4500$ psi, $\mu_r = 1$ cp, $k = 0.1$ mD, $q = 20$ bbl/min, fracture toughness = 500 psi.ft^{0.5}).

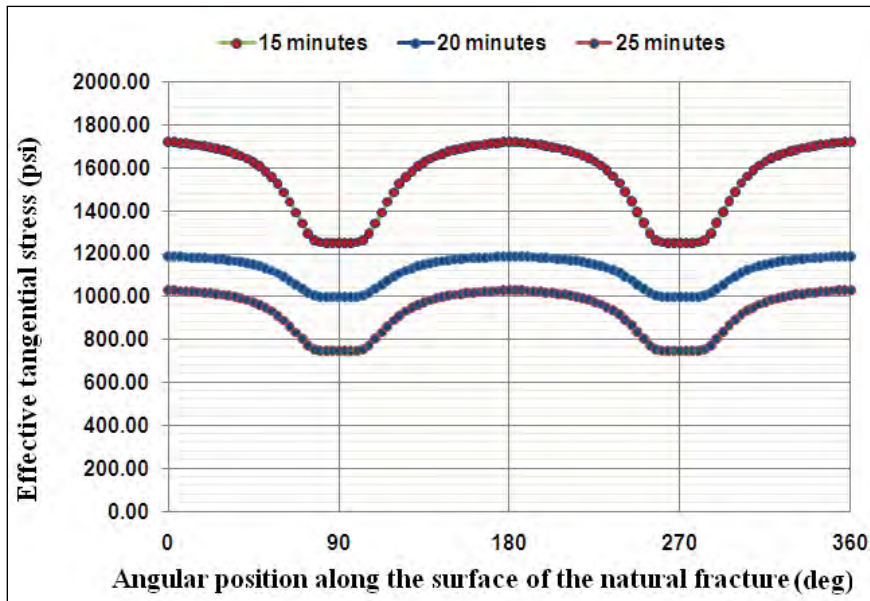


Fig. 3.31: Effective tangential stresses vs. angular position at the surfaces of the natural fracture after the induced fracture propagation stops by the natural fracture, natural fracture length 20 m, width 0.5 mm, angle of approach 90° , natural fracture position from well bore is 20 m and differential stress 1000 psi (poroelastic reservoir, $\sigma_H = 6000$ psi, $\sigma_h = 5000$ psi, $p_i = 4500$ psi, $\mu_r = 1$ cp, $k = 0.1$ mD, $q = 20$ bbl/min, fracture toughness = 500 psi.ft $^{0.5}$).

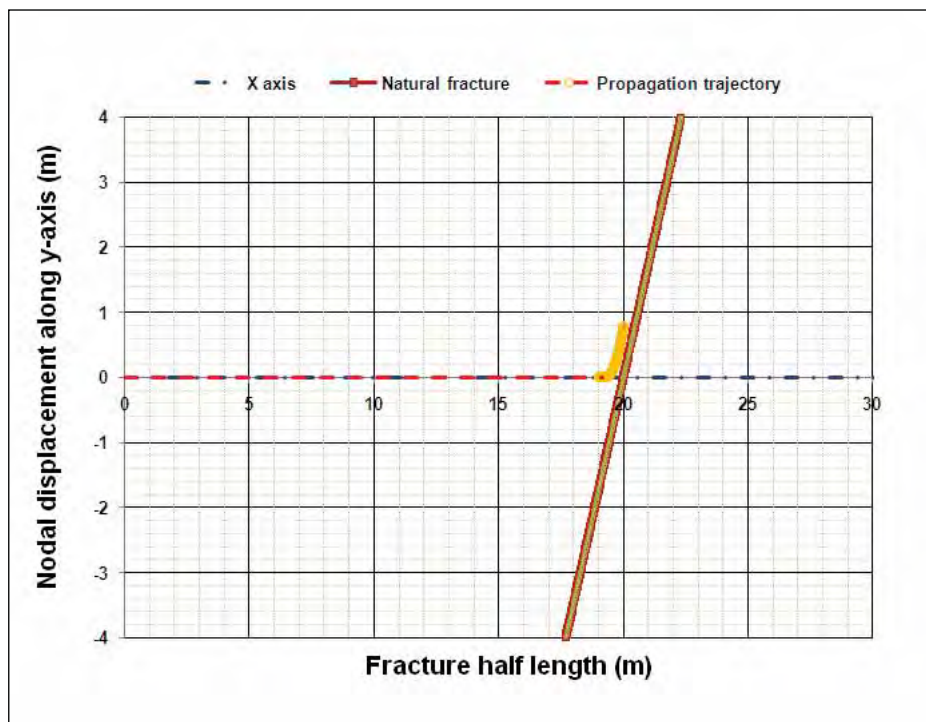


Fig. 3.32: Propagating hydraulic fracture half length vs. nodal displacement along y axis of the induced fracture, angle of approach= 60° , natural fracture position from wellbore 20 m, length of natural fracture 20 m, width of natural fracture 0.5 mm, differential stress = 500 psi (poroelastic reservoir, $\sigma_H = 6000$ psi, $\sigma_h = 5500$ psi, $p_i = 4500$ psi, $\mu_r = 1$ cp, $k = 0.1$ mD, $q = 20$ bbl/min, fracture toughness = 500 psi.ft $^{0.5}$).

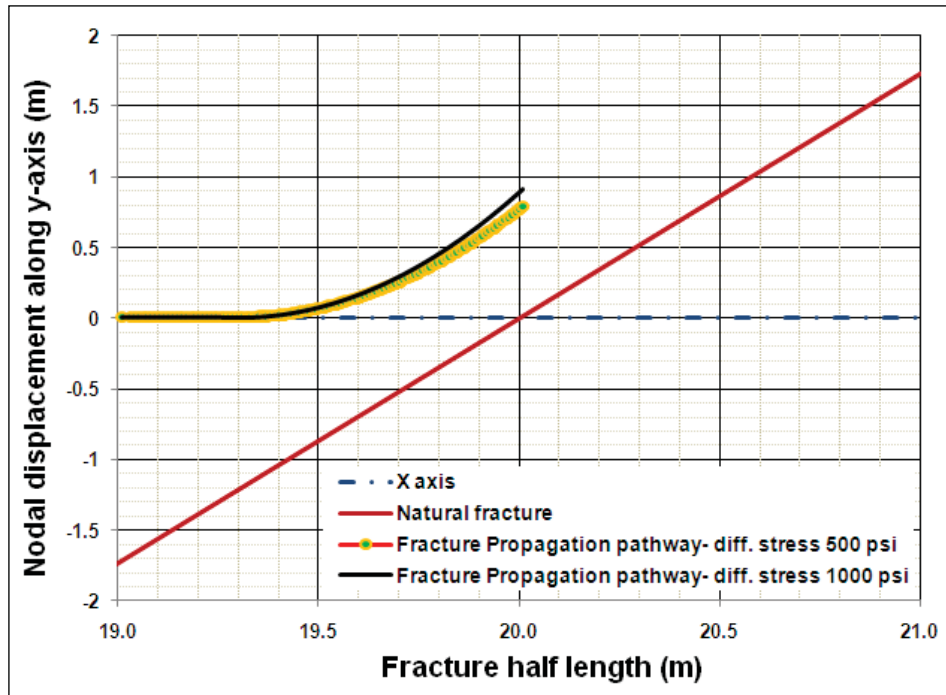


Fig. 3.33: Propagating hydraulic fracture half length vs. nodal displacement along y axis of the induced fracture, angle of approach= 60°, natural fracture position from wellbore 20 m, length of natural fracture 20 m, width of natural fracture 0.5 mm, differential stress = 500 psi and 1000psi (poroelastic reservoir, $\sigma_H = 6000$ psi, $\sigma_h = 5500\sim 5000$ psi, $p_i = 4500$ psi, $\mu_f = 1$ cp, $k = 0.1$ mD, $q = 20$ bbl/min, fracture toughness = 500 psi.ft^{0.5}).

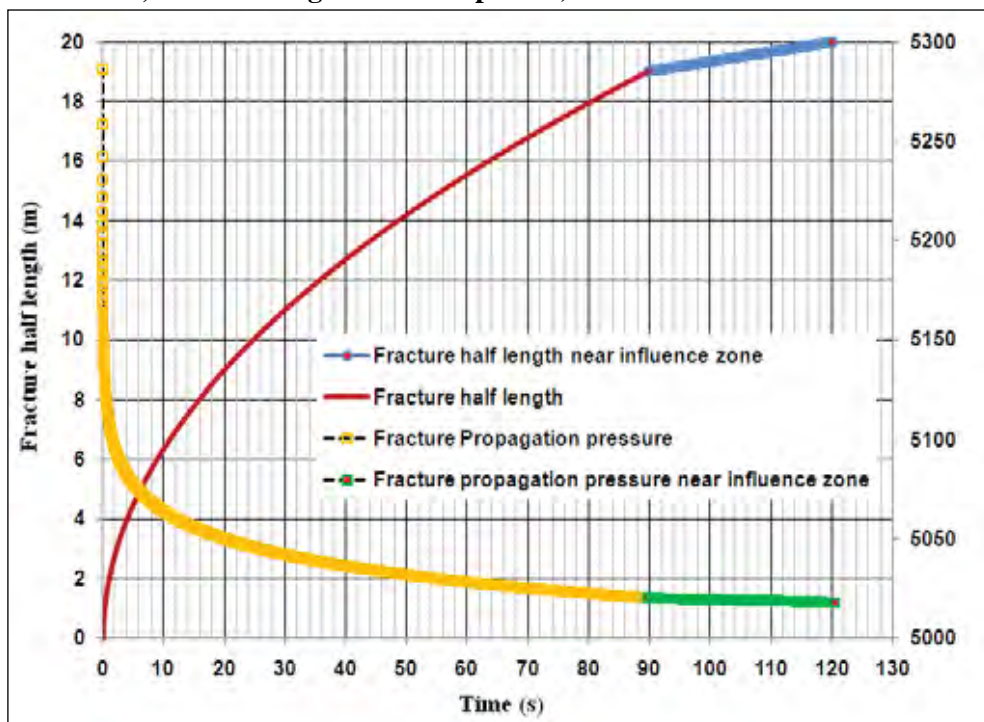


Fig. 3.34: Fracture half length and propagation pressure vs. pumping time, natural fracture length 20 m, width 0.5 mm, angle of approach 60°, natural fracture position from well bore is 20 m and differential stress 500 psi (poroelastic reservoir, $\sigma_H = 6000$ psi, $\sigma_h = 5500$ psi, $p_i = 4500$ psi, $\mu_f = 1$ cp, $k = 0.1$ mD, $q = 20$ bbl/min, fracture toughness = 500 psi.ft^{0.5}).

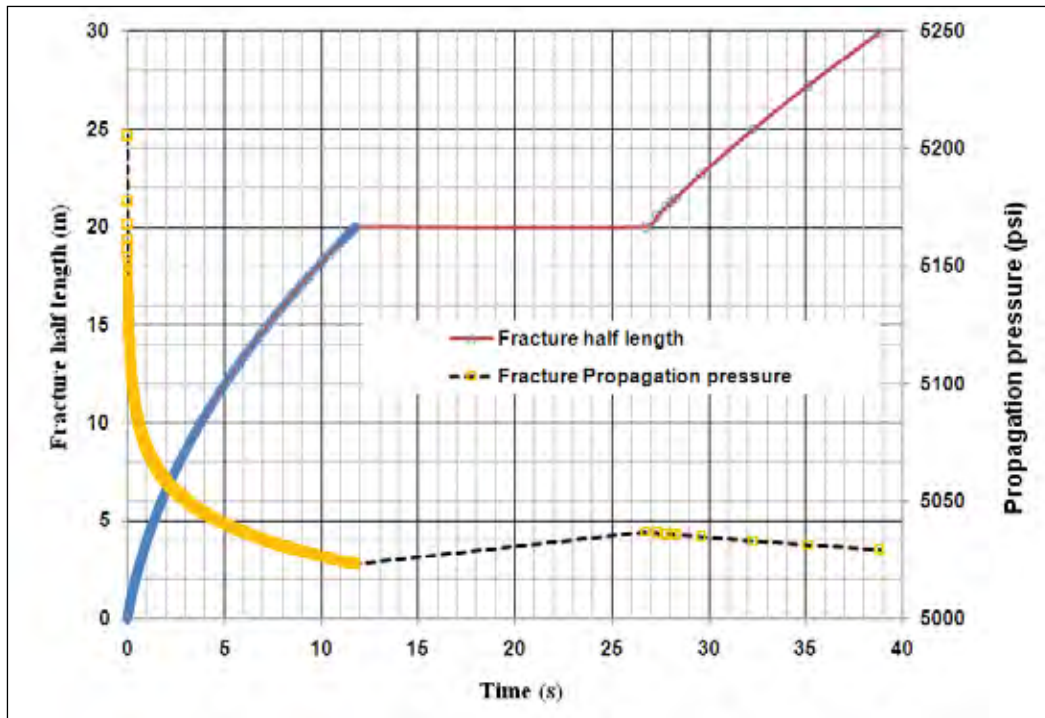


Fig. 3.35: Fracture half length and propagation pressure vs. pumping time, natural fracture length 20 m, width 0.5 mm, angle of approach 90°, natural fracture position from well bore is 20 m and differential stress 1000 psi (poroelastic reservoir, $\sigma_H = 6000$ psi, $\sigma_h = 5000$ psi, $p_i = 4500$ psi, $\mu_f = 1$ cp, $k = 0.1$ mD, $q = 35$ bbl/min, fracture toughness = 500 psi.ft^{0.5}).

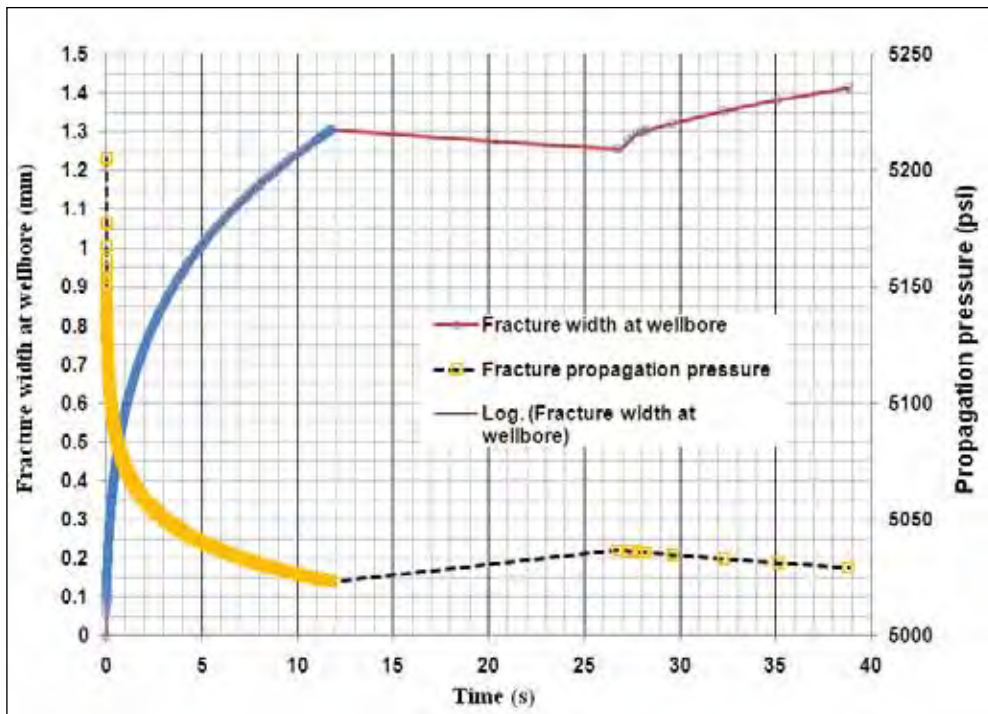


Fig. 3.36 Fracture width and propagation pressure vs. pumping time, natural fracture length 20 m, width 0.5 mm, angle of approach 90°, natural fracture position from well bore is 20 m and differential stress 1000 psi (poroelastic reservoir, $\sigma_H = 6000$ psi, $\sigma_h = 5000$ psi, $p_i = 4500$ psi, $\mu_f = 1$ cp, $k = 0.1$ mD, $q = 35$ bbl/min, fracture toughness = 500 psi.ft^{0.5}).

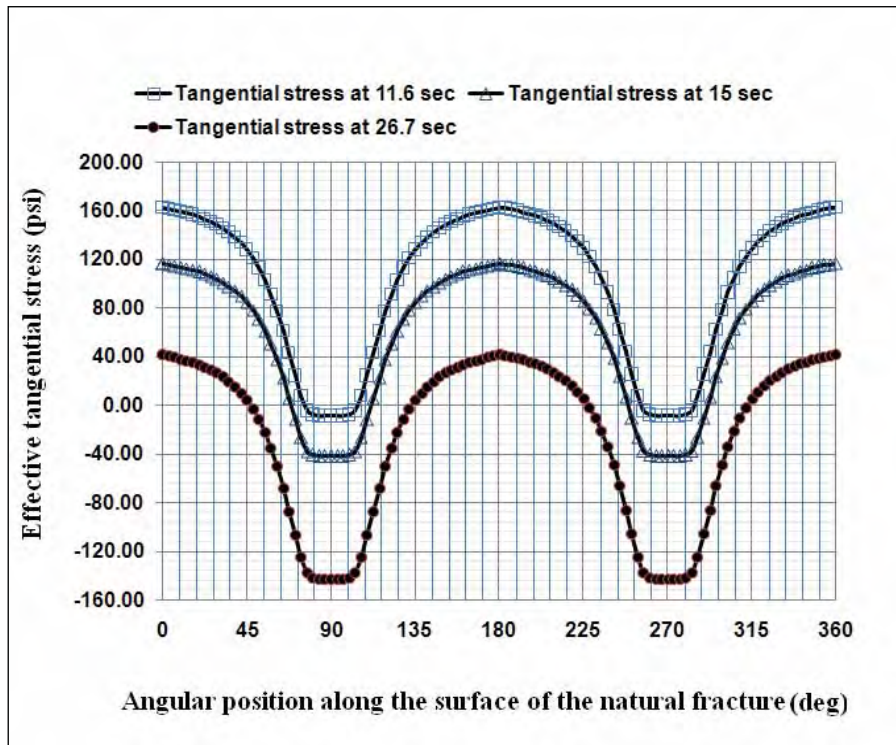


Fig. 3.37: Effective tangential stresses vs. angular position at the surfaces of the natural fracture after the induced fracture propagation stops by the natural fracture, natural fracture length 20 m, width 0.5 mm, angle of approach 90° , natural fracture position from well bore is 20 m and differential stress 1000 psi (poroelastic reservoir, $\sigma_H = 6000$ psi, $\sigma_h = 5000$ psi, $p_i = 4500$ psi, $\mu_f = 1$ cp, $k = 0.1$ mD, $q = 35$ bbl/min, fracture toughness = 500 psi.ft^{0.5}).

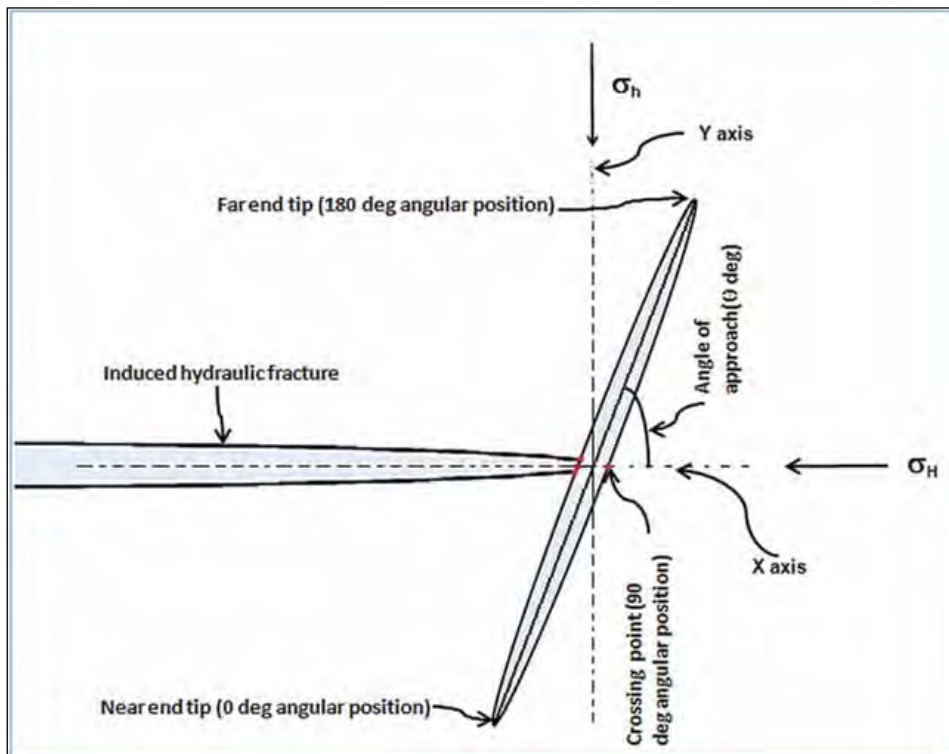


Fig. 3.38: Schematic of initial condition of induced hydraulic and natural fracture intersection showing the angular positions at the natural fracture surface.

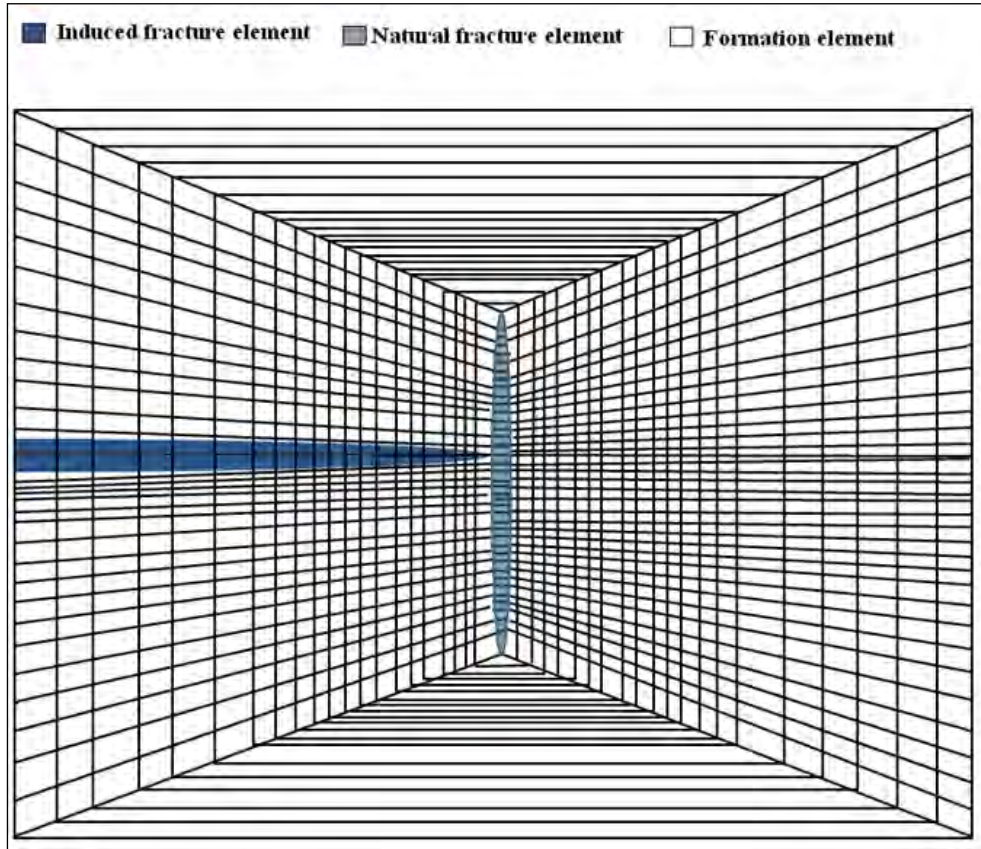


Fig. 3.39(a): Schematic of finite element mesh of the induced fracture, natural fracture and the reservoir system.

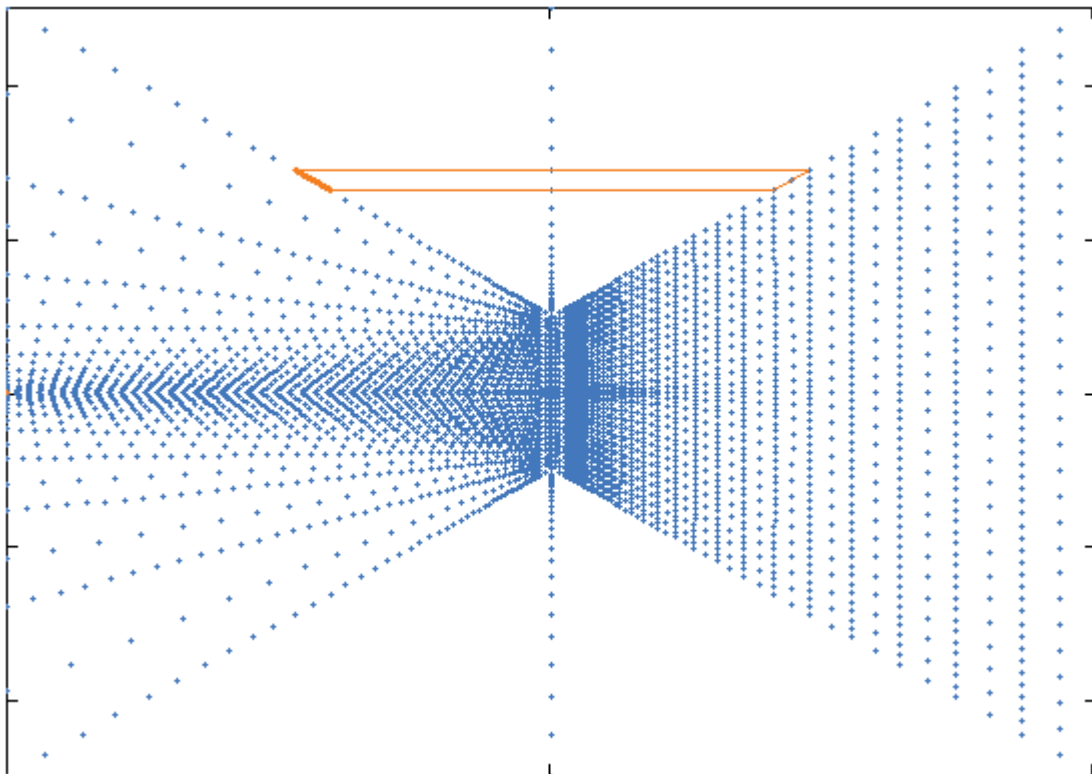


Fig. 3.39(b): Finite element 2D mesh of the induced fracture, natural fracture and the reservoir system showing a thin element near natural fracture region (angle of approach 90°).

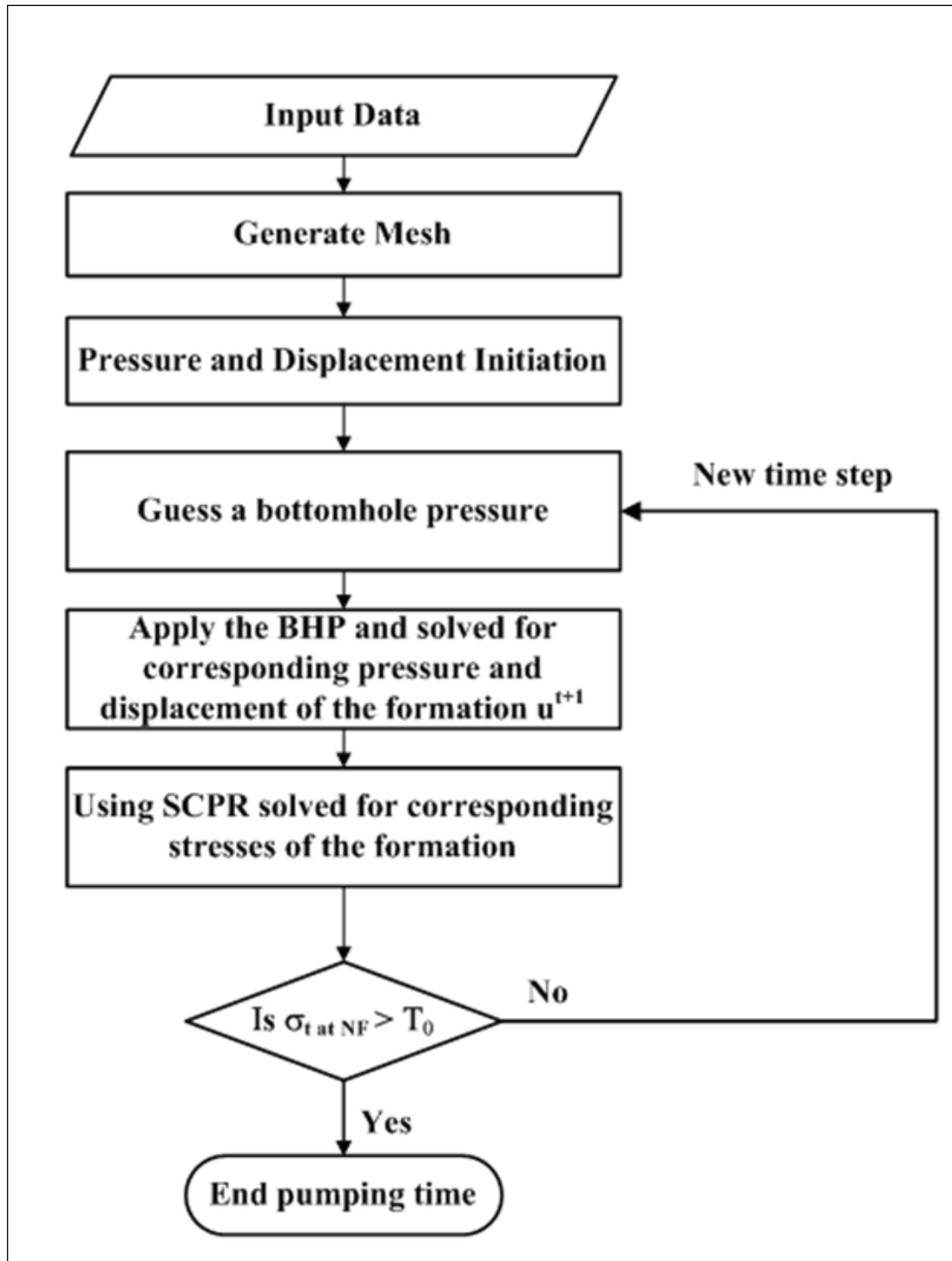


Fig .3.40: Algorithm of the induced fracture arrest and/or breakout (BHP=bottom hole pressure, σ_t is the tangential stress around natural fracture and T_0 is the tensile strength of the natural fracture rock).

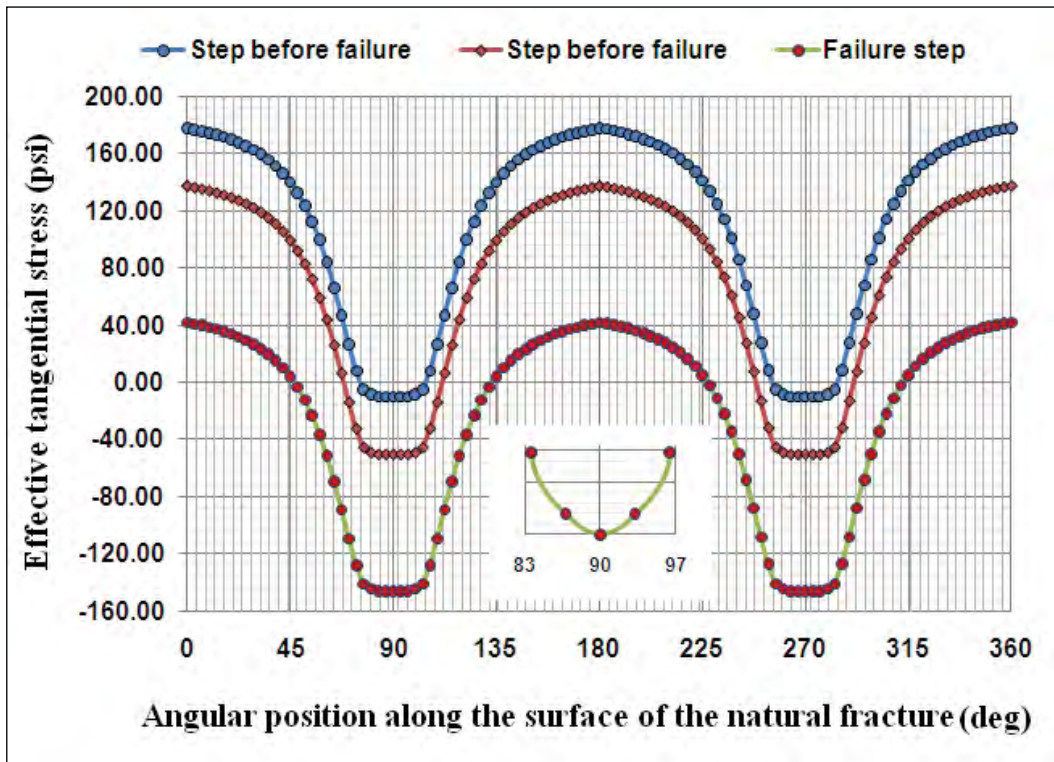


Fig. 3.41: Effective tangential stress vs. angular position at the surfaces of the natural fracture. Natural fracture length = 10 m, angle of approach = 90° , differential stress = 1000 psi, injection rate 20 bbl/min.

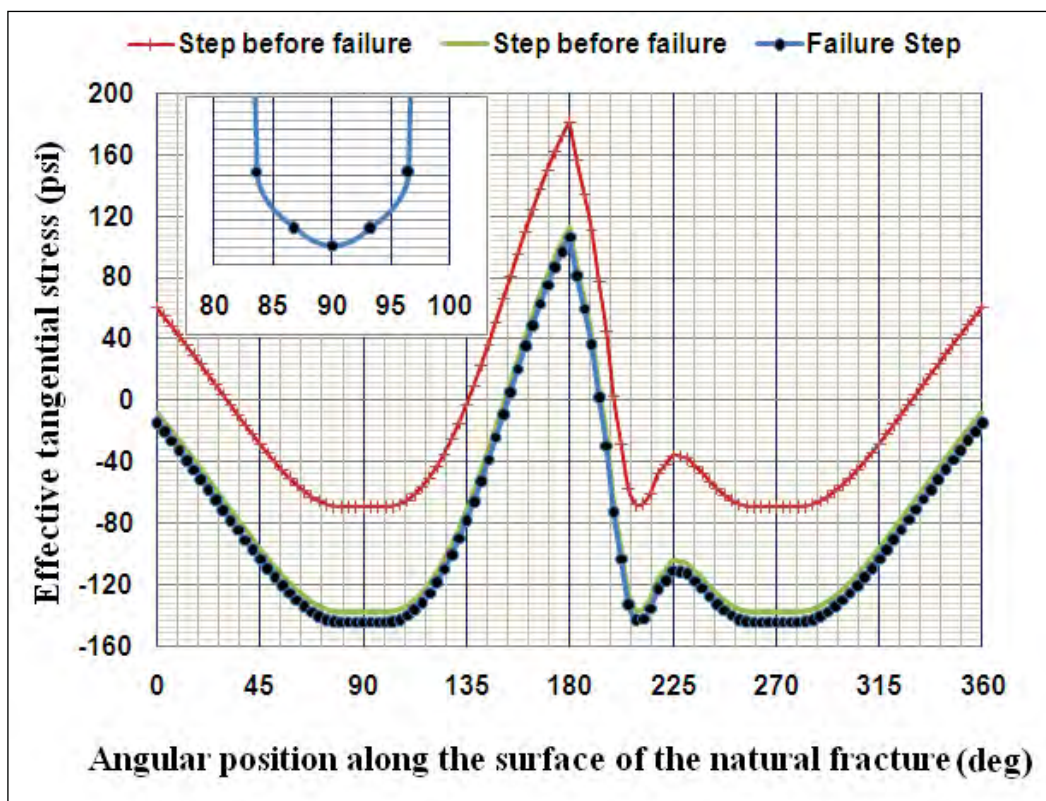


Fig. 3.42: Effective tangential stress vs. angular position at the surfaces of the natural fracture. Natural fracture length = 10 m, angle of approach = 60° , differential stress = 1000 psi, injection rate 20 bbl/min.

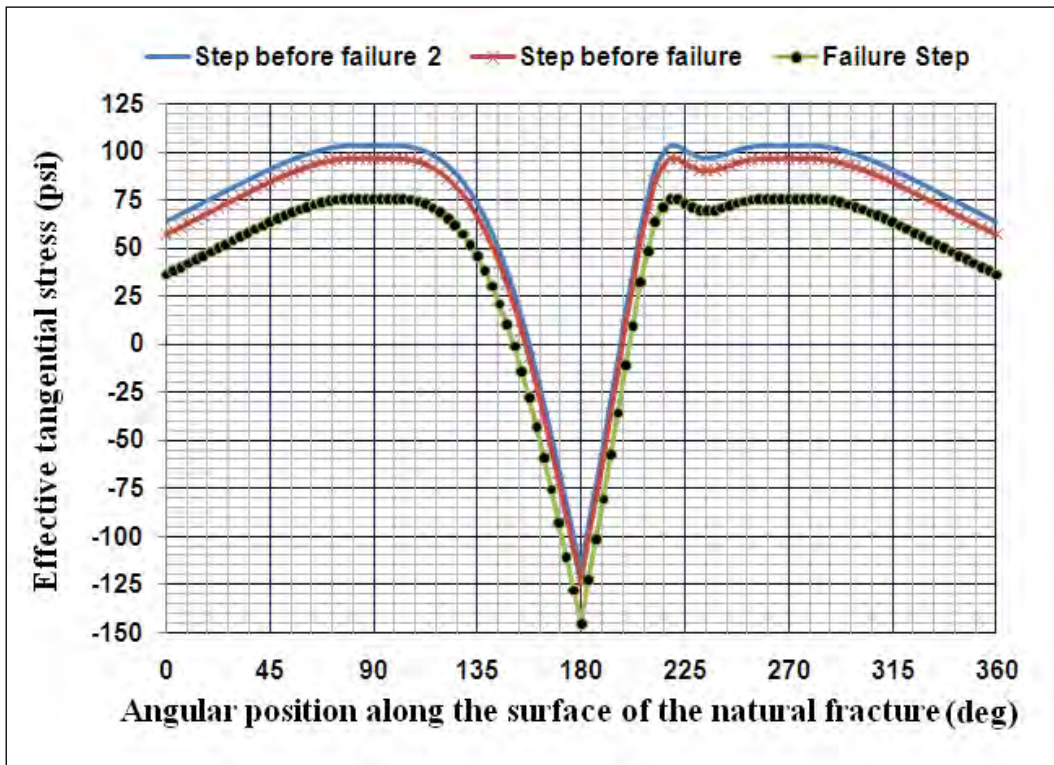


Fig. 3.43: Effective tangential stress vs. angular position at the surfaces of the natural fracture. Natural fracture length = 10 m, angle of approach = 30° , differential stress = 1000 psi, injection rate 20 bbl/min.

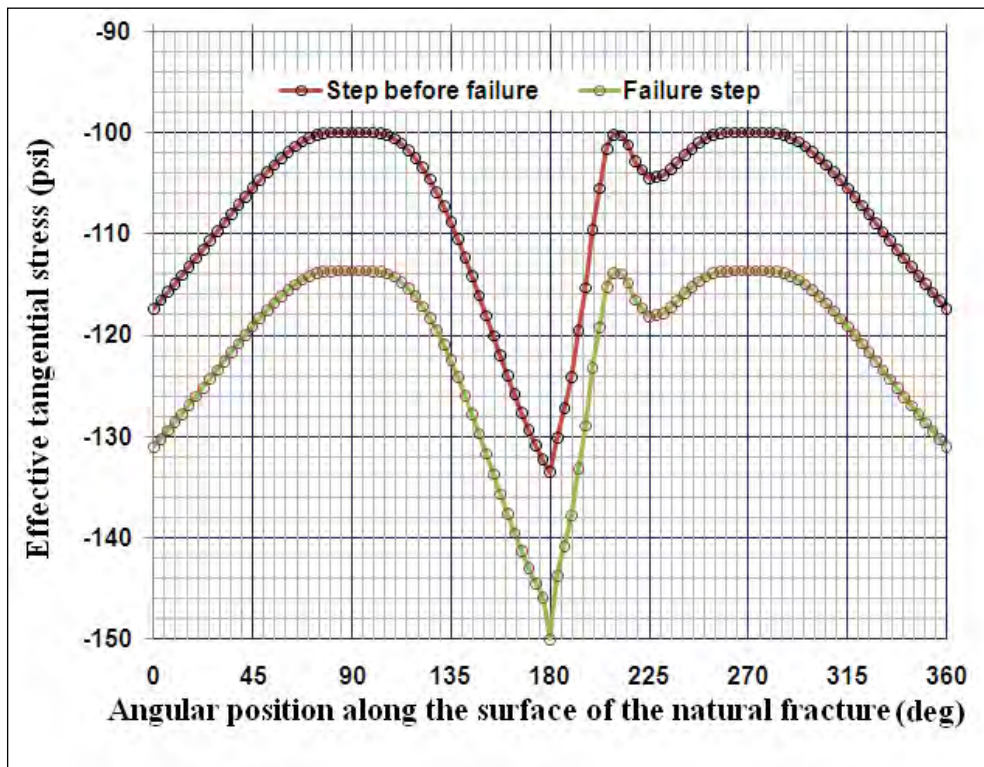


Fig. 3.44: Effective tangential stress vs. angular position at the surfaces of the natural fracture. Natural fracture length = 10 m, angle of approach = 60° , differential stress = 500 psi, injection rate 20 bbl/min.

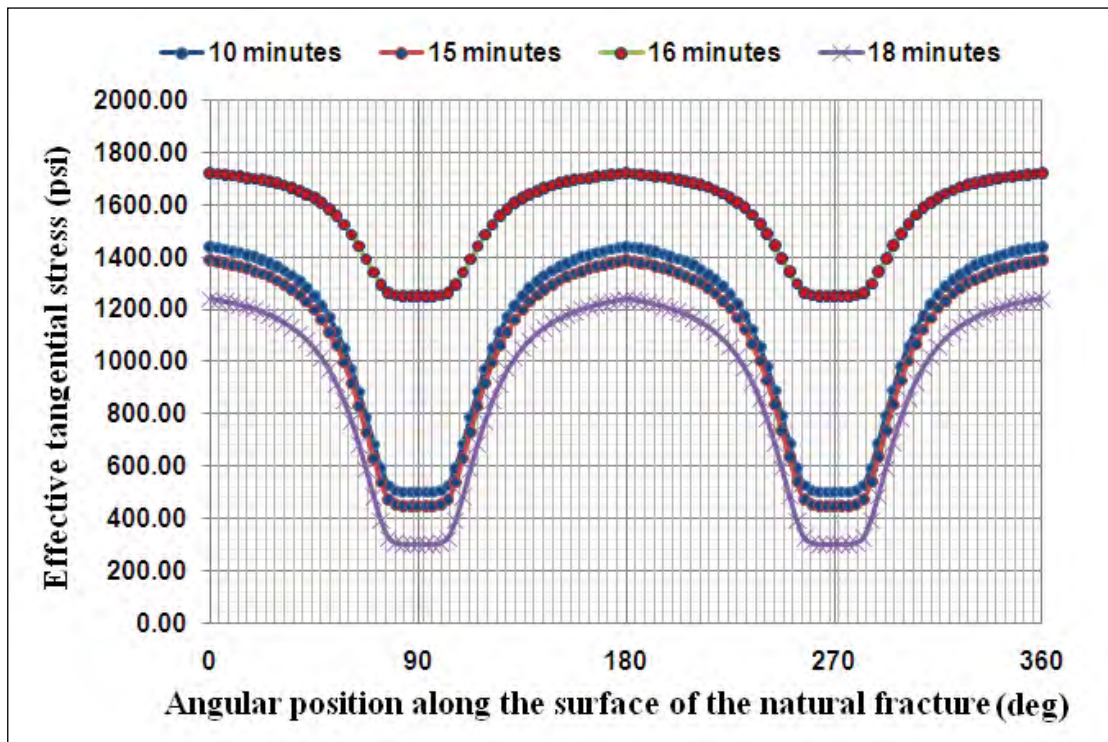


Fig. 3.45: Effective tangential stress vs. angular position at the surfaces of the natural fracture. Natural fracture length = 20 m, angle of approach = 90° , differential stress = 1000 psi, injection rate 20 bbl/min.

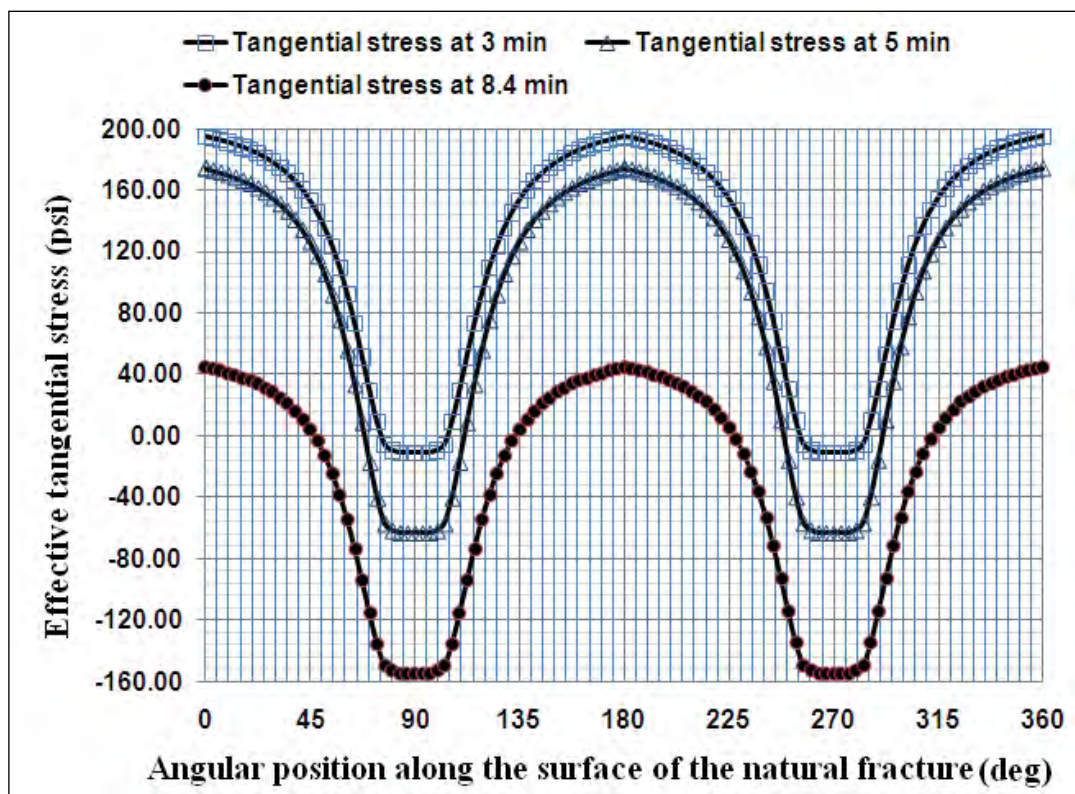


Fig. 3.46: Effective tangential stress vs. angular position at the surfaces of the natural fracture. Natural fracture length = 20 m, angle of approach = 90° , differential stress = 1000 psi, injection rate 35 bbl/min.

Chapter 4: Conclusion and Recommendation

4.1. Summary of the completed work

The main objective of this thesis is to investigate the factors responsible for hydraulic fracture propagation in presence of a natural fracture. In order to achieve this objective a finite element based poroelastic model is developed. The poroelastic model couples a wellbore, an induced fracture, an arbitrarily oriented natural fracture and poroelastic reservoir. A mesh generator is developed to generate the finite element mesh that can represent natural fracture, an induced fracture and the reservoir. The model is developed in different stages.

First an intact wellbore in a poroelastic reservoir is modeled. The model is validated against analytical solutions. Next in the poroelastic intact wellbore model an induced fracture is incorporated. This model is validated against KGD-C model and a range of sensitivity analysis is carried out by varying formation permeability, fracture toughness, injection rate and fracturing fluid viscosity. Finally an arbitrarily oriented natural fracture of variable length is introduced into the poroelastic model and parametric studies of fracture interaction are carried out.

Results of this study are presented in two parts: fracture interaction which includes fracture arrest, crossing and deviation; and a detailed description of how the induced fracture is arrested by and/or breaks out of the natural fracture.

It is observed that at high angle of approach and differential stress, it is more likely that the induced hydraulic fracture crosses the medium size natural fracture, whereas at low angle of approach and low differential stress the induced hydraulic fracture is more likely to be arrested (at least for a short time) and then reorient from the existing path and propagate along the axis of natural fracture. It is also observed that at high angle of approach and differential stress, it is more likely for the large natural fracture to stop the propagation of hydraulic fracture, while at a low angle of approach and low differential stress the induced hydraulic fracture is more likely to deviate from its existing path.

Results of this study also suggest that when a hydraulic fracture intersects a natural fracture it is initially arrested. With increased injection pressure due to continuous pumping, the induced fracture breaks out of the natural fracture. At high angle of approach and high differential stress it breaks out at the point opposite to the initial intersecting point. With decrease in angle of approach and differential stress the induced fracture is likely to break out at the far end tip of the natural fracture.

4.2 Recommendation for future works

Following further works are recommended:

- i. The current poroelastic model is a 2D model; hence it could not model the induced fracture height effect and the deep effect of the natural fracture. So further work should dictate to the modelling of fracture interaction in 3D.
- ii. This model has direct application to all the new Shale gas reservoirs around the world. One can extend this work to apply in Shale gas reservoir with appropriate field data.
- iii. In order to apply in the geothermal reservoirs, the model can be extended by incorporating heat extraction model.
- iv. In this study the induced hydraulic fracture interaction is investigated by a single natural fracture. Future work should consider hydraulic fracture propagation in the presence of multiple natural fractures.
- v. Using the appropriate field data one can study the natural and hydraulic fracture growth by interpreting treatment pressure response.

Nomenclature

A = the fracture surface (m^2)

c_t = total compressibility (psi^{-1})

c_f = fluid compressibility

c_s = solid compressibility

C_L = leak-off coefficient ($m/min^{1/2}$)

C_{nf} = natural fracture leak-off coefficient.

G = shear modulus (psi)

h_f = fracture height (ft)

k = permeability (md)

K_I = stress intensity factor for mode-I

K_{II} = stress intensity factor for mode-II

K_{IC} = Critical value of stress intensity factor

l = fracture length (ft)

l_{nf} = length of natural fracture

l_{ref} = length of the influence

p = pressure (psi)

p_r = reservoir pressure (psi)

p_w = wellbore pressure (psi)

Q_o = injection rate (bbl/min)

t = time, sec (min, hrs)

T_o = tensile strength of the rock (psi)

u_x = displacement along x axis

u_y = displacement along y axis

u_z = displacement along z axis

V_L = leak-off velocity

w = width of the natural fracture (mm)

α = Biot's coefficient

θ = angle of approach (deg)

ϕ = porosity

μ = viscosity (cp)

μ = fluid viscosity;

σ_H = maximum horizontal stress (psi)

σ_h = minimum horizontal stress (psi)

σ_t = Tangential stress (psi)

τ_o = shear strength (psi)

τ = shear stress acting on the natural fracture plane (psi)

ν = Poisson ratio

λ = drained Lamé's parameters

λ_u = undrained first Lamé's parameter.

ν = Poisson's ratio

τ = the opening time of the element of interest

ϕ = porosity

μ = fluid viscosity

ν = is the Poisson's ratio

References

- Adachi, J., Siebrits, E., Peirce, A. and Desroches, J., 2007. Computer Simulation of Hydraulic Fractures. *International Journal of Rock Mechanics and Mining Sciences*, 44(5): 739-757.
- Adachi, J.I. and Detournay, E., 2008. Plane Strain Propagation of a Hydraulic Fracture in a Permeable Rock. *Engineering Fracture Mechanics*, 75(16): 4666-4694.
- Advani, S.H., Lee, T.S., Dean, R.H., Pak, C.K. and Avasthi, J.M., 1997. Consequences of Fluid Lag in Three-Dimensional Hydraulic Fractures. *International Journal for Numerical and Analytical Methods in Engineering*, 21: 229-240.
- Advani, S.H., Lee, T.S. and Lee, J.K., 1990. Three Dimensional Modeling of Hydraulic Fractures in Layered Media: Finite Element Formulations. *J. Energy Res. Tech.*, 112: 1-18.
- Aghighi, M.A., 2007. Fully Coupled Fluid Flow and Geomechanics in the Study of Hydraulic Fracturing and Post-Fracture Production, *The University of New South Wales, Sydney*.
- Aghighi, M.A., Chen, Z. and Rahman, S.S., 2008. A Holistic Approach to the Design and Evaluation of Hydraulic Fracture Treatments in Tight Gas Reservoirs. *SPE Production and Operation*, August.
- Aghighi, M.A., Valencia, K.J., Chen, Z. and Rahman, S.S., 2006. An Integrated Approach to the Design and Evaluation of Hydraulic Fracture Treatments in Tight Gas and Coalbed Methane Reservoirs, Society of Petroleum Engineers, Annual Technical Conference and Exhibition. SPE, Paper 102880, San Antonio, Texas, U.S.A.
- Agrawal, R.G., Carter, R.D. and Pollock, C.B., 1979. Evaluation and Prediction of Performance of Low-Permeability Gas Wells Stimulated by Massive Hydraulic Fracturing. *JPT, Trans AIME*(March): 362-372.
- Ahmed, T., 2001. *Reservoir Engineering Handbook*. Elsevier.
- Ahmed, U., Schatz, J.F., Abou-Sayed, A.S. and Jones, A.H., 1982. A Step by Step Approach to Hydraulic Fracture Treatment Design, Implementation and Analysis for Tight Gas Sands, SPE/DOE Unconventional Gas Recovery Symposium of the SPE. SPE/PDE Paper 10829, Pittsburg, PA, .

- Akulich, A. and Zvyagin, A., 2008. Interaction between Hydraulic and Natural Fractures. *Fluid Dynamics*, 43(3): 428-435.
- Atkinson, B., 1987. Introduction to Fracture Mechanics and Its Geophysical Applications. *Fracture mechanics of rock*: 1–26.
- Azeemuddin, M. Ghori, S.G. and Saner S., 2002. Injection-Induced Hydraulic Fracture in a Naturally Fractured Carbonate Reservoir: A Case Study from Saudi Arabia. SPE International Symposium & Exhibition on Formation Damage Control, SPE 73784.
- Barenblatt, G., 1962a. The Mathematical Theory of Equilibrium Cracks in Brittle Fracture. *Advances in applied mechanics*, 7(2): 55-129.
- Barenblatt, G.I., 1962b. The Mechanical Theory of Equilibrium Cracks in Brittle Fracture. *Appl. Mech.*, 7(56).
- Barree, R., 1983a. A Practical Numerical Simulator for Three-Dimensional Fracture Propagation in Heterogeneous Media.
- Barree, R.D., 1983b. A Practical Numerical Simulator for Three-Dimensional Hydraulic Fracture Propagation in Heterogeneous Media, SPE Symp. Reservoir Simulation SPE Paper 12273, San Francisco.
- Barree, R.D. and Mukherjee, H., 1996. Determination of Pressure Dependent Leakoff and Its Effect on Fracture Geometry, paper SPE 36424, presented at the SPE Annual Technical Conference and Exhibition, Denver, Colorado, USA.
- Barsoum, R., 1976a. On the Use of Isoparametric Finite Elements in Linear Fracture Mechanics. *International Journal for Numerical Methods in Engineering*, 10: 25-37.
- Barsoum, R.S., 1976b. On the Use of Isoparametric Finite Elements in Linear Fracture Mechanics. *International Journal for Numerical Methods in Engineering*, 10: 25-37.
- Bear, J. and Bachmat, Y., 1991. *Theory and Application of Transport in Porous Media*, 4. Kluwer Academic Publishers, Dordrecht, Netherland.
- Ben-Naceur, K. and Economides, M.J., 1988. Production from Naturally Fissured Reservoirs Intercepted by a Vertical Hydraulic Fracture, SPE California Regional Meeting. SPE paper 17425, Long Beach, CA.
- Ben-Naceur, K. and Economides, M.J., 1989. Production from Naturally Fissured Reservoirs Intercepted by a Vertical Hydraulic Fracture. *SPE Formation Evaluation*, Dec. 1989:

550-558.

- Beugelsdijk, L.J.L., de Peter, C.J. and Sato, K., 2000. Experimental Hydraulic Fracture Propagation in a Multi-Fractured Medium, SPE Asia Pacific Conference on Integrated Modelling for Asset Management. SPE Paper 59419, Yokohama, Japan.
- Bévilion, D. and Masson, R., 2000. Stability and Convergence Analysis of Partially Coupled Schemes for Geomechanical-Reservoir Simulations, 7th European Conference on the Mathematics of Oil Recovery, ECMOR, Baveno.
- Biot, M.A., 1935. Le Probleme De La Consolidation Des Matieres Argileuses Sous Une Charge. *Ann. Soc. Sci. Bruxelles*, B55: 110-113.
- Biot, M.A., 1941. General Theory of Three-Dimensional Consolidation. *Journal of Applied Physics*, 12(2): 155-164.
- Biot, M.A., 1956. General Solutions of the Equations of Elasticity and Consolidation for a Porous Material. *Appl. Mech.*, 27: 91-96.
- Biot, M.A., Masse, L. and Medlin, W.L., 1986. A Two-Dimensional Theory of Fracture Propagation. *SPE Production Engineering*(January).
- Biot, M.A. and Willis, D.G., 1957. The Elastic Coefficient of the Theory of Consolidation. *J. Appl. Phys.*, 24: 594-601.
- Biot, M.A., Masse, L. and Medlin, W.L., 1986. A Two-Dimensional Theory of Fracture Propagation. *SPE Production Engineering*(January).
- Blair, S.C., Thorp, R.K. and Heuze, F.E., 1990. Propagation of Fluid-Driven Fractures in Jointed Rock. Part 2 – Physical Tests on Blocks with an Interface or Lens. *Int. J. Rock Mech. & Min. Sci. & Geomech. Abstr.*, 27(4): 255-268.
- Blandford, G.E., Ingraffea, A.R. and Liggett, J.A., 1981. Two-Dimensional Stress Intensity Factor Computations Using the Boundary Element Method. *International Journal for Numerical Methods in Engineering*, 17: 387-404.
- Blanton, T.L., 1982. An Experimental Study of Interaction between Hydraulically Induced and Pre-Existing Fractures, SPE/DOE Unconventional Gas Recovery Symposium. SPE Paper 10847, Pittsburg, Pennsylvania.
- Blanton, T.L., 1986. Propagation of Hydraulically and Dynamically Induced Fractures in Naturally Fractured Reservoirs, SPE Unconventional Gas Technology Symposium.

- SPE Paper 15261, Louisville, KY.
- Boone, T.J., 1989. Simulation and Visualization of Hydraulic Fracture Propagation in Poroelastic Rock, *Cornell university*, New york.
- Boone, T.J. and Detournay, E., 1990. Response of a Vertical Hydraulic Fracture Intersecting a Poroelastic Formation Bounded by Semi-Infinite Impermeable Layers. *Int. J. Rock Mech. Min. Sci and Geomech. Abs.*, 27(3): 189-197.
- Boone, T.J. and Ingraffea, A.R., 1990. A Numerical Procedure for Simulation of Hydraulically Driven Fracture Propagation in Poroelastic Media. *International Journal for Numerical Methods in geomechanics*, 14: 27-47.
- Britt, L.K. and C.J. Hager, 1994, Hydraulic fracturing in a naturally fractured reservoir, SPE 28717, presented at the SPE international petroleum conference and exhibition, Veracruz, Mexico, 10–13 October 1994.
- Burden, R.L. and Faires, J.D., 2001. *Numerical Analysis*. Brooks/Cole Publishing Company Pacific Grove, CA.
- Carmer, D., 1987. Limited Entry Extended to Massive Hydraulic Fracturing. *Oil & Gas J*, 40.
- Carslaw, H.S. and Jaeger, J.C.: *Conduction of Heat in Solids*, second edition, Clarendon Press, Oxford, UK (1959).
- Carter, B., Desroches, J., Ingraffea, A. and Wawrzynek, P., 2000. Simulating Fully 3d Hydraulic Fracturing. *Modeling in Geomechanics*: 525-557.
- Carter, B.J., Wawrzynek, P.A., Ingraffea, A.R. and Morales, H., 1994. Effect of Casing on Hydraulic Fracture from Horizontal Wellbores, 1st North American Rock Mechanics Symposium, Austin, TX, pp. 185-192.
- Carter, R.D: “Derivation of the General Equation for Estimating the Extent of the Fractured Area,” Appendix I of “Optimum Fluid Characteristics for Fracture Extension,” *Drilling and Production Practice*, G.C.Howard and C.R.Fast, American Petroleum Institute, New York, 261-269, 1957.
- Casas, L., Miskimins, J.L., Black, A. and Green, S., 2006. Laboratory Hydraulic Fracturing Test on a Rock with Artificial Discontinuities, Annual Technical Conference and Exhibition. SPE Paper 103617, San Antonio, Texas.
- Chandrupatla, T.R., *Finite Element Analysis for Engineering and Technology*, 2000,

University Press (India) Private Limited.

Charlez, P.A., 1991. *Rock Mechanics, Theoretical Fundamentals*, 1. Editions Technip, Paris.

Charlez, P.A., 1997. *Rock Mechanics - Petroleum Application*, 2. Edition Technip, Paris.

Chen, H., Teufel, L. and Lee, R., 1995a. Coupled Fluid Flow and Geomechanics in Reservoir Study-I. Theory and Governing Equations.

Chen, H.Y., Teufel, L. and Lee, R.L., 1995b. Coupled Fluid Flow and Geomechanics in Reservoir Study, I. Theory and Governing Equations, paper SPE 30752, presented at the SPE Annual Technical Conference & Exhibition, Dallas, TX.

Chen, M., Bai, M. and Roegiers, J.C., 1999. Permeability Tensors of Anisotropic Fracture Networks. *Mathematical Geology*, 31(4): 355-373.

Chen, Z., Narayan, S.P., Yang, Z. and Rahman, S.S., 2000. An Experimental Investigation of Hydraulic Behaviour of Fractures and Joints in Granitic Rock. *International Journal of Rock Mechanics and Mining Sciences*, 37(7): 1061-1071.

Cheng, A.H.D., Abousleiman, Y. and Roegiers, J.C., 1993. Review of Some Poroelastic Effects in Rock Mechanics, U.S. Rock Mechanics Symposium, Medison, Wisconsin, pp. 1119-1126.

Chin, L.Y., Raghavan, R. and Thomas, L.K., 2000. Fully Coupled Geomechanics and Fluid-Flow Analysis of Wells with Stress-Dependent Permeability. *SPE Journal*, 5(1).

Cipolla, C. and Wright, C., 2000. Diagnostic Techniques to Understand Hydraulic Fracturing: What? Why? And How?

Cleary, M.P., Crockett, A.R., Martinez, J.I. and Narendran, V.M., 1983. Surface Integral Schemes for Fluid Flow and Induced Stresses around Fractures in Underground Reservoirs, SPE/DOE Symposium on Low-Permeability Gas Reservoirs. SPE Paper 11632, Denver.

Cleary, M.P., Wright, C.A. and Wright, T.B., 1991. Experimental and Modeling Evidence for Major Changes in Hydraulic Fracturing Design and Field Procedures, SPE Paper 21494.

Clifton, R.J. and Abou-Sayed, A.S., 1979. On the Computation of the Three-Dimensional Geometry of Hydraulic Fractures, SPE 7943. Low Permeability Gas Reservoirs.

Clifton, R.J., Brown, U. and Weng, J.J., 1991. Modeling of Poroelastic Effects in Hydraulic

- Fracturing, SPE Rocky Mountain Regional Meeting nad Low-Permeability Reservoirs Symposium. SPE Paper 21871, Denver, Colorado.
- Cowper, G.R.' Gaussian quadrature formulas for triangles, *International Journal for Numerical Methods in Engineering*, Volume 7, Issue 3, pages 405–408, 1973
- Craster, R.V. and Atkinson, C., 1996. *Theoretical Aspects of Fracture in Porous Elastic Media*. In: A.P.S. Salvadurai (Editor), *Mechanics of Poroelastic Media*. Kluwer Academic Publ., Dordrecht, The Netherlands.
- Crittendon, B.C., 1959, The mechanics of design and interpretation of hydraulic fracture treatments, *Journal of Petroleum Technology*, (October), pages: 21–9.
- Crosby, D.G., Rahman, M.M., Rahman, M.K. and Rahman, S.S., 2002. Single and Multiple Transverse Fracture Initiation from Horizontal Wells. *Journal of Petroleum Science and Engineering*, 35(3-4): 191-204.
- Cui, L., Kaliakin, V.N., Abousleiman, Y. and Cheng, H.D., 1997. Finite Element Formulation and Application of Poroelastic Generalized Plane Strain Problems. *Int. J. Rock Mech. Min. Sci.*, 34(6): 953-962.
- Dahi Taleghani, A., 2009. Analysis of Hydraulic Fracture Propagation in Fractured Reservoirs: An Improved Model for the Interaction between Induced and Natural Fractures, PhD thesis, *The University of Texas at Austin*.
- Daneshy A., 1973a. A Study of Inclined Hydraulic Fractures. *Old SPE Journal*, 13(2): 61-68.
- Daneshy, A.A., 1973b. Experimental Investigation of Hydraulic Fracturing through Perforations. *JPT*, 25(10): 1201-1206.
- Daneshy, A.A., 1974. Hydraulic Fracture Propagation in the Presence of Plane of Weakness, SPE_European Spring Meeting, Amsterdam.
- Dean, R.H. and Schmidt, H., 2008. Hydraulic Fracture Predictions with a Fully Coupled Geomechanical Reservoir Simulator, SPE Annual Technical Conference and Exhibition, Denver Colorado.
- Deimbacher, F., Economides, M. and Jensen, O., 1993a. Generalized Performance of Hydraulic Fractures with Complex Geometry Intersecting Horizontal Wells.
- Deimbacher, F.X., Economides, M.J. and Jensen, O.K., 1993b. Generalized Performance of Hydraulic Fractures with Complex Geometry Intersecting Horizontal Wells, SPE.

Paper 2505.

- Desroches, J. and Carter, B.J., 1996. Three Dimensional Modeling of Hydraulic Fracture, 2nd North American Rock Mechanics Symp., Montreal, Quebec, pp. 995-1002.
- Desroches, J. et al., 1994. The Crack Tip Region in Hydraulic Fracturing. *Mathematical and Physical Sciences*, 447(192): 39-48.
- Desroches, J. and Thiercelin, M., 1993. Modelling the Propagation and Closure of Micro-Hydraulic Fractures. *International Journal of Rock Mechanics and Mining Sciences and Geomechanics Abstracts*, 30: 1231-1234.
- Detournay, E. and Cheng, A.H.D., 1988. Poroelastic Response of a Borehole in a Non-Hydrostatic Stress Field. *Int. J. of Rock Mech. Min. Sci & Geomech. Abstract*, 25(3): 171-182.
- Detournay, E. and Cheng, A.H.D., 1991. Plane Strain Analysis of a Stationary Hydraulic Fracture in a Poroelastic Medium. *International Journal of Solids and Structures*, 27: 1645-1662.
- Detournay, E. and Cheng, A.H.D., 1993. *Fundamentals of Poroelasticity*. In: Hudson (Editor), *Comprehensive Rock Engineering: Principles, Practice and Projects*. Pergamon Press, Oxford, pp. 113-171.
- Detournay, E., Cheng, A.H.D. and McLennan, J.D., 1990. A Poroelastic Pkn Hydraulic Fracture Model Based on an Explicit Moving Mesh Algorithm. *J. Energy Res. Tech. ASME*, 112: 224-230.
- Detournay, E., McLennan, J.D. and C., R.J., 1986. Poroelastic Concepts Explain Some of the Hydraulic Fracturing Mechanisms. SPE Paper 15262.
- Dong, C., 2001. Acidizing of Naturally-Fractured Carbonate Formations, *University of Texas at Austin*.
- Dong, C. and Hill, A., 2000. Modeling of the Acidizing Process in Naturally-Fractured Carbonates, SPE Annual Technical Conference and Exhibition, Dallas, Texas.
- Dong, C., Hill, A. and Zhu, D., 1999. Acid Etching Patterns in Naturally-Fractured Formations, SPE Annual Technical Conference and Exhibition.
- Dong, C., Zhu, D. and Hill, A., 2001. Acid Penetration in Natural Fracture Networks, **SPE** European Formation Damage.

- Dong, C.Y. and de Pater, C.J., 2001. Numerical Implementation of Displacement Discontinuity Method and Its Application in Hydraulic Fracturing. *Comput. Methods Appl. Mech. Engrg*, 191: 745-760.
- Dozier, G. et al., 2003. Refracturing Works. In: Schlumberger (Editor), Oilfield Review.
- Dyer, R., "Using Joint Interactions to Estimate Paleostress Ratios," *Journal of Structural Geology*, 10,7, 685-699 (April 1988).
- Economides, M.J. and Nolte, K.G., 1991. *Reservoir Stimulation*. Prentice-Hall, Inc, Englewood Cliffs New Jersey.
- Eftis, J. and Subramonian, N., 1978. The Inclined Crack under Biaxial Load. *Engineering Fracture Mechanics*, 10(1): 43-67.
- Elbel, J.L., 1986. Designing Hydraulic Fractures for Efficient Reserve Recovery, SPE Unconventional Gas Technology Symposium. SPE paper 15231, Louisville, KY.
- Elbel, J.L. and Mack, M.G., 1993. Refracturing: Observation and Theories, Paper SPE 25464, presented at the SPE Production Operation Symposium, Oklahoma City.
- Elkins, L.F. and Skov, A.M., 1960. Determination of Fracture Orientation from Pressure Interference. *Trans. AIME*, 219: 301-4.
- Erdogan, F. and Sih, G., 1963. On the Crack Extension in Plates under Plane Loading and Transverse Shear (Crack Extension in a Large Plate under Plane Loading and Transverse Shear, Studied in Terms of Local Stress and Strain Concentrations). *ASME, TRANSACTIONS, SERIES D- JOURNAL OF BASIC ENGINEERING*.
- Erdogan, F. and Biricikoglu, V., 1973. Two Bonded Half Planes with a Fracture Going through the Interface. *Int. J. Eng. Sci.*, 11: 745-766
- Finley, S.J. and Lorenz, J.C., 1989. Characterization and Significance of "Natural fractures in Mesaverde Reservoirs at the Mulli Well Experiment Site. SPE Paper 19007.
- Fleming, M.E., 1992. Successful Refracturing in the North Westbrook Unit, SPE Permian Basin Oil and Gas Recovery Conference. SPE Paper 24011, Midland, Texas, USA.
- Fung, L.S.K., Buchanan, L. and Wan, R.G., 1992. Coupled Geomechanical-Thermal Simulation for Deforming Heavy-Oil Reservoirs, CIM Annual Technical Conference, Calgary.
- Garagash, D.I. and Detournay, E., 2005. Plane-Strain Propagation of a Fluid-Driven Fracture:

- Small Toughness Solution. *ASME Journal of Applied Mechanics*, 72(November): 916-928.
- Garcia, J.C. and Teufel, L.W., 2005. Numerical Simulation of Fully Coupled Fluid-Flow/Geomechanical Deformation in Hydraulically Fractured Reservoirs, SPE Production and operation Symposium. SPE Paper 94062, Oklahoma city, OK.
- Geerstma, J. and De Klerck, F., 1969. A Rapid Method of Predicting Width and Extent of Hydraulically Induced Fracture. *JPT*(December).
- Geertsma, J. and Haafkens, R., 1979, A comparison of the theories for predicting width and extent of vertical hydraulically induced fractures, *Journal of Energy research and technology* Vol. 101, pages: 8-19.
- Ghassemi, A., 1997. Three-Dimensional Poroelastic Hydraulic Fracture Simulation Using the Displacement Discontinuity Method, *Oklahoma*, Norman.
- Ghassemi, A. and Suresh Kumar, G., 2007. Changes in Fracture Aperture and Fluid Pressure Due to Thermal Stress and Silica Dissolution/Precipitation Induced by Heat Extraction from Subsurface Rocks. *Geothermics*, 36(2): 115-140.
- Ghassemi, A., Tarasovs, S. and Cheng, A.H.D., 2007. A 3-D Study of the Effects of Thermomechanical Loads on Fracture Slip in Enhanced Geothermal Reservoirs. *International Journal of Rock Mechanics and Mining Sciences*, 44(8): 1132-1148.
- Gidely, J.L., Holditch, S.A., Nierode, D.E. and Veatch, R.W., 1989. Recent Advances in Hydraulic Fracturing, SPE Monograph Volume 12, Henry L. Doherty Series.
- Gnagi, A.F., 1978. Variation of Whole and Fractured Porous Rock Permeability with Confining Pressure. *International Journal of Rock Mechanics, Mining Sciences & Geomechanics Abstracts*, 15: 249-257.
- Griffith, A.A., 1920. The Phenomena of Rupture and Flow in Solids. *Phil. Trans. Royal Soc.*, Ser. A. 221: 163-198.
- Griffith, A.A., 1924. The Theory of Rupture, First International Congress in Applied Mechanics, Delft, pp. 55-63.
- Gringarten, A.C., Ramey, H.J. and Raghavan, R., 1974. Unsteady-State Pressure Distributions Created by a Well with a Single Infinite-Conductivity Vertical Fracture. *Spe Journal*, August: 347-360.

- Gringarten, A.C., Ramey, H.J.J. and Raghavan, R., 1975. Applied Pressure Analysis for Fractured Wells. *J. Pet. Tech. Trans., AIME* July: 887-892.
- Gu, H. and Leung, K.H., 1993. 3d Numerical Simulation of Hydraulic Fracture Closure with Application to Minifracture Analysis. *JPT*(March): 206-211.
- Gu, H., Zong, Z. and Hung, K.C., 2004. A Modified Superconvergent Patch Recovery Method and Its Application to Large Deformation Problems. *Finite Elements in Analysis and Design*, 40: 665-687.
- Gupta, A., Penuela, G. and Avila, R., 2001. An Integrated Approach to the Determination of Permeability Tensors for Naturally Fractured Reservoirs. *Journal of Canadian Petroleum Technology*, 40(12): 43-48.
- Gutierrez, M., Lewis, R.W. and Masters, I., 2001. Petroleum Reservoir Simulation Coupling Fluid Flow and Geomechanics. *SPE Res Eval Eng*(June).
- Haimson, B.C. and Fairhurst, C., 1967. Initiation and Extension of Hydraulic Fractures in Rocks. *Spe Journal*: 310-318.
- Haimson, B.C. and Fairhurst, C., 1969. Hydraulic Fracturing in Porous-Permeable Materials. *J. Pet. Tech.*(July): 811-817.
- Harrison, E., Kieschnick, W.F., McGuire, W.J., 1954, The mechanics of fracture induction and extension, *Petroleum Trans AIME*, Vol. 201 pages: 252–63.
- Hayashi, K., Willis-Richards, J., Hopkirk, R.J. and Niibori, Y., 1999. Numerical Models of Hdr Geothermal Reservoirs - a Review of Current Thinking and Progress. *Geothermics*, 28(4-5): 507-518.
- Heiland, J., 2003a. Laboratory Testing of Coupled Hydro-Mechanical Processes During Rock Deformation. *Hydrogeology Journal*, 11: 122-141.
- Heiland, J., 2003b. Laboratory Testing of Coupled Hydro-Mechanical Processes During Rock Deformation. *Hydrogeology Journal*, 11(1): 122-141.
- Helgeson, D.E. and Aydin, A., 1991. Characteristics of Joint Propagation across Layer Interfaces in Sedimentary Rocks. *J. Struct. Geol.*, 13: 897-911.
- Henshell, R.D. and Shaw, K.G., 1975. Crack Tip Finite Elements Are Unnecessary. *International Journal for Numerical Methods in Engineering*, 9: 495-507.
- Heuze, F.E., Shaffer, R.J., Ingraffea, A.R. and Nilson, R.H., 1990. Propagation of Fluid-

- Driven Fractures in Jointed Rock. Part I – Development and Validation of Methods of Analysis. *Int. J. Rock Mech. & Min. Sci. & Geomech. Abstr.*, 27(4): 243-254.
- Hidayati, D., Chen, H.-Y. and Teufel, L., 2001. Flow-Induced Stress Reorientation in a Multiple-Well Reservoir, SPE Rocky Mountain Petroleum Technology Conference. SPE 71091, Keystone, Colorado, USA.
- Holditch, S.A., 2006. Tight Gas Sands. *JPT*, June 2006.
- Holditch, S.A., Jennings, J.W. and Neuse, S.H., 1978. The Optimization of Well Spacing and Fracture Length in Low Permeability Gas Reservoirs, 53rd Annual Technical Conference and Exhibition of the SPE. SPE Paper 7496, Houston, Texas.
- Holditch, S.A. and Tschirhart, N.R., 2005. Optimal Stimulation Treatments in Tight Gas Sands, SPE Annual Technical Conference. SPE Paper 96104, Dallas, Texas.
- Horner, D.R., 1951. Pressure Build-up in Wells, Thir Pet. Cong., The Hague, pp. 503-523.
- Hossain, M.M. and Rahman, M.K., 2008. Numerical Simulation of Complex Fracture Growth During Tight Reservoir Stimulation by Hydraulic Fracturing. *Journal of Petroleum Science and Engineering*, 60(2): 86-104.
- Hossain, M.M., Rahman, M.K. and Rahman, S.S., 2000. Hydraulic Fracture Initiation and Propagation: Roles of Wellbore Trajectory, Perforation and Stress Regimes. *Journal of Petroleum Science and Engineering*, 27(3-4): 129-149.
- Hubbert, M.K., Willis, D.G., 1957, Mechanics of hydraulic fracturing, *Journal of Petroleum Technology*, 9(6), pages: 153–68.
- Ingraffea, A.R., 1977a. Discrete Fracture Propagation in Rock, *University of Colorado*, Colorado, U.S.A.
- Ingraffea, A.R., 1977b. Short Communications, Nodal Grafting for Crack Propagation Studies. *International Journal for Numerical Methods in Engineering*, 11: 1185-1187.
- ingraffea, A.R. and Manu, C., 1980. Stress-Intensity Factor Computation in Three Dimensions with Quarter Point Element. *Int. J. Numer. Meth. in Eng.*, 15: 1427-1445.
- Ingraffea, A.R. and Saouma, V., 1984. *Numerical Modeling of Discrete Fracture Propagation in Reinforced and Plain Concrete*. In: G.C. Sih and A. Ditommaso (Editors), *Application of Fracture Mechanics to Concrete Structures*. Martinus Nijhoff Publishers.

- Irwin, G., 1957. Analysis of Stress and Strain near the End of a Crack Traversing a Plane. *Journal of Applied Mechanics*, No 3: 361-364.
- Isida, M., 1971. Effect of Width and Length on Stress Intensity Factors of Internally Cracked Plates under Various Boundary Conditions. *International Journal of Fracture*, 7(3): 301-316.
- Jaeger, J.C. and Cook, N.G.W., 1969. *Fundamentals of Rock Mechanics*. Chapman and Hall, London.
- Jeffery, R.G., 1989. The Combined Effect of Fluid Lag and Fracture Toughness on Hydraulic Fracture Propagation, SPE Paper 18957.
- Jeffrey, R., 1989. The Combined Effect of Fluid Lag and Fracture Toughness on Hydraulic Fracture Propagation.
- Jeffrey, R., Vandamme, L. and Roegiers, J., 1987. Mechanical Interactions in Branched or Subparallel Hydraulic Fractures.
- Ji, L., Settari, A. and Sullivan, R.B., 2006. A New Approach to Hydraulic Fracturing Modeling - Fully Coupled with Geomechanical and Reservoir Simulation, SPE Europe/EAGE Annual Conference and Exhibition. SPE 99428, Vienna, Austria.
- Ji, L., Settari, A. and Sullivan, R.B., 2007. A Novel Hydraulic Fracturing Model Fully Coupled with Geomechanics and Reservoir Simulator, SPE Annual Technical Conference and Exhibition. SPE Paper 110845, Anaheim, California.
- Jing, Z., Willis-Richards, J., Watanabe, K. and Hashida, T., 2000. A Three-Dimensional Stochastic Rock Mechanics Model of Engineered Geothermal Systems in Fractured Crystalline Rock. *J. Geophys. Res.*, 105.
- Khristianovic, S.A. and Zheltov, Y.P., 1955. Formation of Vertical Fractures by Means of Highly Viscous Fluid, 4th World Petroleum Congress, Rome, pp. Paper 3, p. 579-586.
- Koshelev, V. and Ghassemi, A., 2003. Hydraulic Fracture Propagation Near a Natural Discontinuity. 28 Workshop on Geothermal Reservoir Engineering, Stanford University, Stanford, California, January 27-29, 2003, SGP-TR-173.
- Koutsabeloulis, N.C. and Hope, S.A., 1998. Coupled Stress/Fluid/Thermal Multi-Phase Reservoir Simulation Studies Incorporating Rock Mechanics, SPE/ISRM Eurock'98, Trondheim, Norway, pp. 449-454.

- Lam, K.Y., Cleary, M.P. and Barr, D.T., 1986. A Complete Three Dimensional Simulator for Analysis and Design of Hydraulic Fracturing, SPE paper 15266.
- Lamb, H.: *Hydrodynamics*, 6th edition, New York, Dover Publications, 1932.
- Lammont, N. and Jessen, F., 1963. The Effect of Existing Fractures in Rocks on the Extension of Hydraulic Fractures. *Journal of Petroleum Technology*, February: 203-209.
- Lecampion, B, 2008. An extended finite element method for hydraulic fracture problems. *Journal of Numerical Methods in Engineering*, Volume 25, Issue-2 , pages 121-133.
- Lee, J. and Wattenbarger, R.A., 1996. *Gas Reservoir Engineering*. Spe Textbook Series, 5. Richardson, TX.
- Lee, S.H., Lough, M.F. and Jensen, C.L., 2001. Hierarchical Modeling of Flow in Naturally Fractured Formations with Multiple Length Scales. *Water Resources Research*, 37(3): 443-455.
- Lewis, R.W. and Ghafouri, H.R., 1997. A Novel Finite Element Double Porosity Model for Multiphase Flow through Deformable Fractured Porous Media. *International Journal for Numerical and Analytical Methods in Geomechanics*, 21(11): 789-816.
- Lewis, R.W. and Schrefler, B.A., 1998. *The Finite Element Method in the Static and Dynamic Deformation and Consolidation of Porous Media*. Wiley, Newyork.
- Lewis, R.W. and Sukirman, Y., 1993. Finite Element Modelling of Three-Phase Flow in Deforming Saturated Oil Reservoirs. *International Journal for Numerical and Analytical Methods in Geomechanics*, 17(8): 577-598.
- Li, Y.C., 1999. Finite Element Analysis for a Finite Conductivity Fracture in an Infinite Poroelastic Medium. *International Journal for Numerical and Analytical Methods in Geomechanics*, 23(3): 187-215.
- Longuemare, P. et al., 2002. Geomechanics in Reservoir Simulation: Overview of Coupling Methods and Field Case Study. *Oil & Gas Science and Technology*, 57(5): 471-483.
- Mack, M.G. and Elbel, J.L., 1994. *Hydraulic Fracture Orientation and Pressure Response During Fracturing of Producing Well*. Rock Mechanics Balkema, Rotterdam.
- Mack, M.G. and Warpinski, N.R., 2000. *Mechanics of Hydraulic Fracturing*. In: M.J. Economides and K.G. Nolte (Editors), Reservoir Stimulation. John Wiley & Sons Ltd,

Chichester.

- Mahyari, A.T., 1997. Computational Modeling of Fracture and Damage in Poroelastic Media, *McGill University*, Montreal.
- Mews, H. and Kuhn, G., 1988. An Effective Numerical Stress Intensity Factor Calculation with No Crack Discretization. *International Journal of Fracture*, 38(1): 61-76.
- Morales, R.H., 1989. Microcomputer Analysis of Hydraulic Fracture Behavior with a Pseudo Three Dimensional Simulator. *SPE Formation Evaluation*(Feb.): 69-74.
- Murti, V. and Valliappan, S., 1986. A Universal Optimum Quarter Point Element. *Engineering Fracture Mechanics*, 25(2): 237-258.
- Naceur, K. and Economides, M., 1989. Production from Naturally Fissured Reservoirs Intercepted by a Vertical Hydraulic Fracture. *SPE Formation Evaluation*, 4(4): 550-558.
- Narayan, S.P., Jing, Z., Yang, Z. and Rahman, S.S., 1999. Influence of Natural Fractures and in Situ Stresses on Proppant-Free Hydraulic Stimulation of Hot Dry Rock Reservoirs. In: S.F. Simons, O.E. Morgan and M.G. Dunstall (Editors), New Zealand Geothermal Workshop. Proc. of the 21st New Zealand Geothermal Workshop, pp. 83-88.
- Nolte, K.G., 1979. Determination of Fracture Parameters from Fracturing Pressure Decline, SPE paper 8341, Las Vegas, Nevada, USA.
- Nolte, K.G., 1986. A General Analysis of Fracturing Pressure Decline Analysis with Application to Three Models. *SPE Formation Evaluation*, 1(6): 571-583.
- Nolte, K.G., 1991a. Fracturing Pressure Analysis for Non-Ideal Behavior, SPE paper 20704, New Orleans, Louisiana, USA.
- Nolte, K.G., 1991b. Fracturing Pressure Analysis for Non-Ideal Behavior. *JPT*, 43(2): 210-218.
- Nolte, K.G., 1993. A Systematic Method for Applying Fracturing Pressure Decline: Part 1, paper SPE 25845, presented at the SPE Rocky Mountain Regional Meeting and Low Permeability Reservoirs Symposium, Denver, Colorado, USA.
- Nolte, K.G. and Smith, M.B., 1981. Interpretation of Fracturing Pressures. *JPT Trans., AIME*, 271.
- Nordgren, R.P., 1972. Propagation of a Vertical Hydraulic Fracture. *Spe Journal*, Aug.: 306-

- Nouri, A., Komak Panah, A., Pak, A., Vaziri, H. and Islam, M.R., 2002. Evaluation of Hydraulic Fracturing Pressure in a Porous Medium by Using the Finite Element Method. *Energy Sources*, 24: 715-724.
- Oberwinkler, C., Ruthammer, G., Zangl, G. and Economides, M.J., 2004. New Tools for Fracture Design Optimization, SPE International Symposium and Exhibition on Formation Damage Control. SPE Paper 86467, Lafayette, Louisiana, USA.
- Olson, K.E., 1991. A Case Study of Hydraulically Refractured Wells in the Devonian Formation, Crane County, Texas, SPE Annual Technical Conference and Exhibition. SPE Paper 22834, Dallas, Texas, USA.
- Owen, D.R.J. and Fawkes, A.J., 1983. *Engineering Fracture Mechanics; Numerical Methods and Applications*. Pineridge Press Limited, Swansea, U.K.
- Pak, A., 1997. Numerical Modeling of Hydraulic Fracturing, *Alberta*, Edmonton.
- Perkins, T.K. and Kern, L.R., 1961. Widths of Hydraulic Fractures. *Journal of Petroleum Technology*, Sep.: 937-949.
- Pospisil, G., Lynch, K.W., Pearson, C.M. and Rugen, J.A., 1992. Results of a Large-Scale Refracture Stimulation Program, SPE Annual Technical Conference and Exhibition. SPE Paper 24857, Washington, DC, USA.
- Potluri, N., 2005. The Effect of Natural Fractures on Hydraulic Fracture Propagation, *The University of Texas at Austin*.
- Potluri, N., Zhu, D. and Hill, A.D., 2005. Effect of Natural Fractures on Hydraulic Fracture Propagation, SPE European Formation Damage Conference. SPE Paper 94568, Scheveningen, The Netherland.
- Prats, M., 1961. Effect of Vertical Fractures on Reservoir Behavior- Incompressible Fluid Case. *SPEJ*(June): 105-118.
- Rahman, M.K., Hossain, M.M. and Rahman, S.S., 2002a. A Shear-Dilation-Based Model for Evaluation of Hydraulically Stimulated Naturally Fractured Reservoirs. *Int. J. for Numerical and Analytical Methods in Geomech.*, 26(5).
- Rahman, M.K. and Joarder, A.H., 2006. Investigating Production-Induced Stress Change at Fracture Tip: Implications for a Novel Hydraulic Fracturing Technique. *Journal of*

- Rahman, M.K., Suarez, Y.A., Chen, Z. and Rahman, S.S., 2007. Unsuccessful Hydraulic Fracturing Cases in Australia: Investigation into Causes of Failures and Their Remedies. *Journal of Petroleum Science and Engineering*, 57(1-2): 70-81.
- Rahman, M.M., Hossain, M.M., Crosby, D.G., Rahman, M.K. and Rahman, S.S., 2002b. Analytical, Numerical and Experimental Investigations of Transverse Fracture Propagation from Horizontal Wells. *Journal of Petroleum Science and Engineering*, 35(3-4): 127-150.
- Rahman, M.M., Rahman, M.K. and Rahman, S.S., 2001a. An Integrated Model for Multi-Objective Design Optimization of Hydraulic Fracturing *J. of Petroleum Science and Engineering*, 31(41).
- Rahman, M.M., Rahman, M.K. and Rahman, S.S., 2001b. An Integrated Model for Multiobjective Design Optimization of Hydraulic Fracturing. *Journal of Petroleum Science and Engineering*, 31(1): 41-62.
- Rendulic, L., 1936. Porenwasserdruck und Porenwasserdrück in Tonen. *Der Bauingenieur*, 17: 559-564.
- Renshaw, C.E. and Pollard, D.D., 1995. An Experimentally Verified Criterion for Propagation Across Unbounded Frictional Interfaces in Brittle, Linear Elastic Materials. *Int. J. Rock Mech. & Min. Sci. & Geomech. Abstr.*, 32(3): 237-249.
- Rice, J.R. and Cleary, M.P., 1976. Some Basic Stress Diffusion Solutions for Fluid Saturated Elastic Porous Media with Compressible Constituents. *Rev. Geophys. and Space Phys.*, 14: 227-241.
- Russell, D.G. and Truitt, N.E., 1964. Transient Pressure Behaviour in Vertically Fractured Reservoirs. *Trans. AIME*, 201: 182-191.
- Sato, K., 2003. Complex Variable Boundary Element Method for Potential Flow with Thin Objects. *Computer Methods in Applied Mechanics and Engineering*, 192(11-12): 1421-1433.
- Sato, K. and Hashida, T., 2000. Development of Numerical Simulation Code for Hydraulic Fracturing Using Embedded Crack Element, World Geothermal Congress, Tohoko-Japan.

- SCR Geomechanics Group, 1993. On the Modeling of near Tip Processes in Hydraulic Fractures. *International Journal of Rock Mechanics and Mining Sciences and Geomechanics Abstracts*, 30(7): 1127-1134.
- Sepehrnoori, K., Ravi-Chandar, K., Srinivasan, S. and Laubach, S., Analysis of Hydraulic Fracture Propagation in Fractured Reservoirs: An Improved Model for the Interaction between Induced and Natural Fractures.
- Settari, A. and Price, H.S., 1984. Simulation of Hydraulic Fracturing in Low-Permeability Reservoirs. *SPEJ*, 24(2): 141-152.
- Settari, A. and Walters, D.A., 1999. Advances in Coupled Geomechanical and Reservoir Modeling with Applications to Reservoir Compaction, SPE Reservoir Simulation Symposium, Houston, Texas.
- Sih, G.C., 1974. Strain-Energy-Density Factor Applied to Mixed Mode Crack Problems. *International Journal of Fracture*, 10(3): 305-321.
- Sih, G.C. and Theocaris, P.S (Eds.), 1979. Mixed Mode Crack Propagation. Proceedings of 1st U.S.- Greece Symposium, Athenes, Greece, Sijthof and Noordhoff, Alpen aan den Rijn, The Netherlands.
- Sih, G.C., 1991. *Mechanics of Fracture initiation and Propagation*. Kluwer Academic Publisher, Dordrecht, The Netherlands.
- Smith, M.B., 1985. Stimulation Design for Short, Precise Hydraulic Fractures. *paper SPE 10313, SPEJ*, 371.
- Smith, M.B. and Shlyapobersky, J., 2000. *Basics of Hydraulic Fracturing*. In: M.J. Economides and K.G. Nolte (Editors), Reservoir Stimulation. John Wiley & Sons Ltd, Chichester.
- Smith, R.N.L. and Mason, J.C., 1982. *A Boundary Element Method for Curved Crack Problems in Two Dimensions*. Boundary Element Methods in Engineering. Springer-Verlag, Berlin.
- Sneddon, I.N., Elliot, H.A., 1946, The opening of a Griffith crack under internal pressure, *Quarterly of Applied Mathematics*, Volume 4, pages: 262–7.
- Sousa, J.L.S., Carter, B.J. and Ingraffea, A.R., 1993. Numerical Simulation of 3d Hydraulic Fracture Using Newtonian and Power-Law Fluids. *Int. J. Rock Mech. Min. Sci and*

- Geomech. Abs.*, 30: 1265-1271.
- Spence, D.A. and Sharp, P., 1985. Self-Similar Solutions for Elasto-Hydrodynamic Cavity Flow. *R. Soc.*, London, pp. 289-313.
- Stefhest, H., 1970. Numerical Inversion of Laplace Transform: a Survey and Comparison of Methods. *Commun. Ass. Comput. Mech.*, 13(624): 47-49.
- Terzaghi, K., 1923. Die Brechnung Der Durchlassigkeitsziffer Des Tones Aus Dem Verlauf Der Hydrodynamischen Spannungserscheinungen. *Sitz. Akad. Wissen., Wien Math. Naturwiss. Kl., Abt. Ila*, 132: 105-124.
- Tortike, W.S. and Farouq Ali, S.M., 1993. Reservoir Simulation Integrated with Geomechanics. *The Journal of Canadian Petroleum Technology*, 32(5): 28-37.
- Valencia, K.J., 2005. Optimizing Hydraulic Fracture Treatments in Reservoirs under Complex Conditions. Phd Dissertation, *The University of New South Wales*, Sydney.
- Valencia, K.J., Chen, Z., Hodge, M.O. and Rahman, S.S., 2005. Optimizing Stimulation of Coalbed Methane Reservoir Using Multi-Stage Hydraulic Fracturing Treatment and Integrated Fracture Modeling, *Spe Asia Pacific Oil and Gas Conference and Exhibition*. SPE Paper 93245, Jakarta, Indonesia.
- Valencia, K.J., Chen, Z., Rahman, M.K. and Rahman, S.S., 2003. An Integrated Model for the Design and Evaluation of Multiwell Hydraulic Fracture Treatments for Gas-Condensate Reservoirs, *SPE International Improved Oil Recovery Conference in Asia Pacific*. SPE Paper 84860, Kualalumpur, Malaysia.
- Valko, P. and Economides, M.J., 1993. A Continuum-Damage-Mechanics Model of Hydraulic Fracturing. *Journal of Petroleum Technology*, 45(3): 198-205.
- Valko, P. and Economides, M.J., 1995. *Hydraulic Fracture Mechanics*. John Wiley & Sons, Chichester.
- Valko, P., Oligney, R.E. and Economides, M.J., 1997. High Permeability Fracturing of Gas Wells. *Gas TIPS*, 3(3): 31-40.
- Valliappan, S. and Khalili-Naghadeh, N., 1990. Flow through Fissured Porous Media with Deformable Matrix. *International Journal for Numerical Methods in Engineering*, 29(5): 1079-1094.
- Valliappan, S., Khalili-naghadeh, N. and Murti, V., 1989. Thin Flow Element and the

- Problem of Ill-Conditioning. *International Journal for Numerical and Analytical Methods in Geomechanics*, 13(6): 611-628.
- Van As, A. and Jeffrey, R.G., 2002. Hydraulic Fracture Growth in Naturally Fractured Rock: Mine through Mapping and Analysis. In: R. Hammah, and Others, Mining and Tunnelling Innovation and Opportunity: Proceedings of the 5th North American Rock Mechanics Symposium and the 17th Tunnelling Association of Canada Conference: NARMS-TAC, Toronto, Ont. University of Toronto Press:, pp. 1461-1469.
- Vandamme, L., 1986. A Three Dimensional Displacement Discontinuity Model for the Analysis of Hydraulically Propagated Fracture, *University of Toronto*, Toronto.
- Vandamme, L., Detournay, E. and Roegiers, J.C., 1987. Poroelasticity in Hydraulic Fracturing Simulators, SPE Annual Technical Conference. Paper 16911
- Vandamme, L., Jeffrey, R.G. and Curran, J.H., 1988. Pressure Distribution in Three-Dimensional Hydraulic Fractures. *SPE Production Engineering*, 3: 181-186.
- Verruijt, A., 1969. *Elastic Storage in Aquifers*. In: R.J.M. De Wiest (Editor), Flow through Porous Media. Academic, San Diego, California, pp. 331-376.
- Vinod, P.S., Flindt, M.L., Card, R.J. and Mitchell, J.P., Dynamic Fluid-Loss Studies in Low-permeability Formations With Natural Fractures, SPE 37486, Presented at the SPE Production Operations Symposium, 9-11 March 1997, Oklahoma City, Oklahoma.
- Wang, H. F. (2000), Theory of Linear Poroelasticity with Applications to Geomechanics and Hydrogeology, Princeton University Press, Princeton, NJ, 287 pp.
- Warpinski, N., 1991a. Hydraulic Fracturing in Tight, Fissured Media. *Journal of Petroleum Technology*, 43(2): 146-151.
- Warpinski, N.R., 1988. Dual Leakoff Behavior in Hydraulic Fracturing of Tight, Lenticular Gas Sands. SPE Paper 18259.
- Warpinski, N.R., 1991b. Hydraulic Fracturing in Tight, Fissured Media. *JPT*: 146-152.
- Warpinski, N.R. and Smith, M.B., 1989. *Rock Mechanics and Fracture Geometry*. In: J.L. Gidely, S.A. Holditch, D.E. Nierode and R.W. Veatch (Editors), Recent Advance in Hydraulic Fracturing. SPE, Richardson, Texas.
- Warpinski, N.R. and Teufel, L.W., 1987. Influence of Geologic Discontinuities on Hydraulic Fracture Propagation. *Journal of Petroleum Technology*, February.

- Yamamoto, K., Shimamoto, T. and Maezumi, S., 1999. Development of a True 3d Hydraulic Fracturing Simulator, SPE Paper 54256, Jakarta, Indonesia.
- Yew, C.H., 1997. *Mechanics of Hydraulic Fracturing*. Gulf Publishing Company, Houston.
- Yew, C.H. and Liu, G.F., 1993. Fracture Tip and Critical Stress Intensity Factor of a Hydraulically Induced Fracture. *SPE Production and Facilities*, 8(3): 171-177.
- Yuan, Y., 1997. Simulation of Penny-Shaped Hydraulic Fracturing in Porous Media, *Oklahoma*, Norman.
- Zhang, X. and Jeffrey, R.G., 2006b. The Role of Friction and Secondary Flaws on Deflection and Re-Initiation of Hydraulic Fractures at Orthogonal Pre-Existing Fractures. *Geophys. J. Int.*, 166: 1454-1465.
- Zhang, X., Jeffrey, R.G. and Thiercelin, M., 2006a. Deflection and Propagation of Fluid-Driven Fractures at Frictional Bedding Interfaces: A Numerical Investigation. *Journal of Structural Geology*
- Zhou, J., Chen, M., Jin, Y. and Zhang, G.-q., 2008. Analysis of Fracture Propagation Behavior and Fracture Geometry Using a Tri-Axial Fracturing System in Naturally Fractured Reservoirs. *International Journal of Rock Mechanics and Mining Sciences*, 45(7): 1143-1152.
- Zhou, X. and Ghassemi, A., 2009. Finite Element Analysis of Coupled Chemo-Poro-Thermo-Mechanical Effects around a Wellbore in Swelling Shale. *International Journal of Rock Mechanics and Mining Sciences*, In Press, Corrected Proof.
- Zienkiewicz, O.C. and Taylor, R.L., 2000. *The Finite Element Method - Basic Formulation and Linear Problems 1*. Butterworth-Heinemann, Oxford.
- Zienkiewicz, O.C. and Zhu, J.Z., 1992a. The Superconvergence Patch Recovery and a Posteriori Error Estimates, Part I: The Recovery Techniques. *Int. J. Numer. Meth.*, 33: 1331-1364.
- Zienkiewicz, O.C. and Zhu, J.Z., 1992b. The Superconvergence Patch Recovery and a Posteriori Error Estimates, Part II: Error Estimates and Adaptivity. *Int. J. Numer. Meth.*, 33: 1365-1382.
- Zu, J.Z. and Zienkiewicz, O.C., 1988. Adaptive Techniques in the Finite Element Method. *Commun. Appl. Num. Meth.*, 4: 197-204.

Appendix-2A: Change in Bulk and Pore Volume

This appendix presents definition of basic rock properties. Solid matrix refers to the solid phase or solid skeleton of the material including all disconnected pores whereas bulk refers to the solid skeleton plus interconnected pores.

A1: Total and bulk state variables

Bulk volume is defined as the solid volume plus pore volume. So one can write:

$$V_b = V_s + V_p \quad (\text{A.1})$$

where V is volume and the subscripts b, s and p represent the bulk, solid and pores, respectively.

The total volume is the solid volume plus fluid volume:

$$V_t = V_s + V_f \quad (\text{A.2})$$

where the subscript (t) represents the total.

It is also noted that the fluid phase is contained within and completely saturates the pores. Thus, the fluid volume is the same as pore volume:

$$V_f = V_p \quad (\text{A.3})$$

So the bulk volume is the same as the total volume:

$$V_b = V_t \quad (\text{A.4})$$

Again, porosity is the ratio of interconnected pore volume to bulk volume. This can be written as:

$$\phi = \frac{V_p}{V_b} \quad (\text{A.5})$$

where (ϕ) is porosity. Now V_p can be eliminated in Eq.A.5. Using Eq.A.1 to give:

$$1 - \phi = \frac{V_s}{V_b} \quad (\text{A.6})$$

One can define all state variables over a phase, except volume, as volume averages. Thus, the total of any state variable (a) is defined as:

$$a_t V_t = a_s V_s + a_f V_f \quad (\text{A.7})$$

Using Eqs.A.3-A.6, Eq.A.7 can be rearranged as follows:

$$a_t = a_f \phi + a_s (1 - \phi) \quad (\text{A.8})$$

A2: Solid and bulk compressibility

Under certain boundary condition, compressibility of solid and bulk are determined through laboratory measurements. In all cases, the apparatus contains a jacketed rock core which is set between two caps at two ends and placed in a vessel where a confining pressure can be applied hydraulically. The caps can be designed either with drainage holes for a drained test, or solid for an undrained test. The rock sample is initially subjected to a confining pressure and a pore pressure. The change in volume is then determined by measuring the response of the rock sample to a small load increment.

Bulk compressibility is measured with a drained test in which an increment of confined pressure Δp_c leads to a bulk volume change ΔV_b , which is measured once the initial pore pressure is recovered after diminishing the early undrained response. Bulk compressibility is then calculated using the following equation (Detournay and Cheng, 1993):

$$C_b = -\frac{1}{V_b} \left[\frac{\Delta V_b}{\Delta P_c} \right]_p \quad (\text{A.9})$$

where c_b is often called drained jacketed bulk compressibility (Biot, 1935) due to the measurement method.

Solid phase compressibility, c_s can be determined through so-called unjacketed test (Biot and Willis, 1957) where an equal increment is applied for both pore pressure and confining pressure ($\Delta p = \Delta p_c$) so that the differential pressure p_d ($p_d = p_c - p$) is maintained constant. Following Detournay and Cheng (1993), this loading path is hereafter called I-loading. Under I-loading condition, it can be argued that the volumetric variation is uniform all over the material as a result of the uniform pressure everywhere. Therefore no change in shape of the pores is experienced and porosity remains constant provided the solid phase is homogenous (Biot and Willis, 1957; Geerstma, 1957). Hence it can be written:

$$\frac{\Delta V_s}{V_s} = \frac{\Delta V_p}{V_p} = \frac{\Delta V_b}{V_b} \quad (\text{A.10})$$

The measured bulk volume variation from the unjacketed test can be used to calculate c_s as follows:

$$C_s = -\frac{1}{V_b} \left[\frac{\Delta V_b}{\Delta P} \right]_{Pd} = -\frac{1}{V_s} \left[\frac{\Delta V_s}{\Delta P} \right]_{Pd} \quad (\text{A.11})$$

Hence c_s which are also called unjacketed bulk compressibility can reflect the solid phase compressibility (Chin et al., 1995; Detournay and Cheng, 1993).

A3: Total and effective stress

Total stress is defined as the total stress acting on the solid/fluid system. It can be defined using Eq.A.12 as:

$$\bar{\bar{\sigma}}_t = \bar{\bar{\sigma}}_f \phi + \bar{\bar{\sigma}}_s (1 - \phi) \quad (\text{A.12})$$

where σ_s , σ_f and σ_t are the solid, fluid and total stresses respectively.

As solid stress cannot be directly measured this relation is rarely used and in petroleum engineering it is more important for the stress on the bulk rather than the solid.

Effective stress is defined as the stress acting on the bulk. If the fluid is removed from the solid fluid system or there is no fluid stress, the total stress equals the effective stress. In general fluid is included in the system and effective stress differs from total stress. One can relate effective stress to total stress and fluid stress through superposition.

In state (b) of **Fig.A.1**, there is no external load so the stress only acts on the pores. In state (c) of Fig.A.1, the stresses are acting on the bulk. For incompressible pores, state (b) contributes no load to the bulk so the effective stress is:

$$\bar{\bar{\sigma}}' = \bar{\bar{\sigma}} \quad (\text{A.13})$$

In general both the pores and solid are compressible and the effective stress can be written as:

$$\bar{\bar{\sigma}}' = \bar{\bar{\sigma}} - \alpha \bar{\bar{\sigma}}_f \quad (\text{A.14})$$

where alpha is the Biot coefficient ($0 \leq \alpha_{ij} \leq 1$) and defined as:

$$\alpha = 1 - \frac{c_s}{c_b} \quad (\text{A.15})$$

Fluid stress comprises a deviatoric component which is zero for motionless fluid and a pressure (p). So one can write as:

$$\bar{\bar{\sigma}}_f = p \bar{\bar{\delta}} \quad (\text{A.16})$$

where (δ) is the kronecker delta. Effective stress tensor σ'_{ij} is then defined as (Nur and Byerlee, 1971):

$$\sigma'_{ij} = \sigma_{ij} - \alpha p \delta_{ij} \quad (\text{A.17})$$

A4: Changes in bulk and pore volume

In poroelastic media pore volume varies as a result of a combined effect of rock stress and fluid pressure on solid grains. In this section the study is related to the rock skeleton deformation which is basically the core problem of the poroelasticity. It provides relationships to evaluate bulk and the pore volume to be used in the derivation of linear poroelastic governing equations.

Hook's law for a poroelastic medium

The state of stress acting on an element of a porous medium can be decomposed to two components as shown in **Fig.A.2** (Cornet, 1988).

Hook's law in indicial notation is:

$$\varepsilon_{ij} = \frac{\sigma_{ij}}{2G} - \frac{V}{E} \sigma_{kk} \delta_{ij} \quad (\text{A.18})$$

where G is the shear modulus and E Young's modulus.

Subscript kk represents Einstein summation. In state (b) of the figure A.2, which corresponds to hydrostatic loading of the matrix with fluid pressure ($\sigma_1 = \sigma_2 = p$), Hook's law can be written as:

$$\varepsilon_{ij}^b = \frac{P}{3K_s} \quad (\text{A.19})$$

where b is the strain tensor corresponding to the stage b and K the bulk modulus and

the subscript “s” refers to solid or matrix ($K_s = \frac{E_s}{3(1-2\nu_s)}$).

In stage (c), a dry element of the porous media is considered. A resultant stress of σ - p is applied on the bulk. The strain tensor corresponding to this stage (ε_{ij}^c) is as follows:

$$\varepsilon_{ij}^b = \varepsilon \frac{(1+V_b)}{2E_b} (\sigma_{ij} - P\delta_{ij}) - \frac{V_b}{E_b} (\sigma_{kk} - 3p) \delta_{ij} \quad (\text{A.20})$$

The subscript “b” refers to the bulk. Adding Eqs. A.19 and A.20 gives the total strain as follows:

$$\varepsilon_{ij} = \frac{(1+V_b)}{2E_b} \sigma_{ij} - \frac{V_b}{E_b} \sigma_{kk} \delta_{ij} + \left(\frac{1}{K_b} - \frac{1}{K_s} \right) \frac{P}{3} \delta_{ij} \quad (\text{A.21})$$

Where $K_b = E_b/3(1-2V_b)$.

When solved with respect to stress, It can also be written as follows: $2G$

$$\sigma_{ij} = \left(K_b - \frac{2G}{3} \right) \varepsilon_{kk} \delta_{ij} + 2G\varepsilon_{ij} + \alpha p \delta_{ij} \quad (\text{A.22})$$

Introducing effective stresses σ'_{ij} and σ'_{kk} , one can write:

$$\varepsilon_{ij} = \frac{(1+V_b)}{2E_b} \sigma'_{ij} - \frac{V_b}{E_b} \sigma'_{kk} \delta_{ij} \quad (\text{A.23})$$

So Hook’s law for poroelastic medium can be written by introducing effective stress in place of total stress for elastic medium.

Change in bulk volume

The volumetric strain defined by $\varepsilon_V = \frac{(V_b - V)}{V_b}$ can be obtained from Eq.A.21.

$$\varepsilon_{kk} (\equiv \varepsilon_V) = \frac{(V_b - V)}{V_b} = -\frac{\Delta V_b}{V_b} = c_b \left(\frac{\sigma_{kk}}{3} - p \right) + c_s p \quad (\text{A.24})$$

or:

$$-\frac{\Delta V_b}{V_b} = \varepsilon_{kk} = c_b \sigma'_m \quad (\text{A.25})$$

where c_b is bulk compressibility, $\sigma_m = \sigma_{kk}/3$ and effective mean stress σ'_m is as follows:

$$\sigma'_m = \sigma_m - \alpha p \quad (\text{A.26})$$

Change in pore volume

Change in pore volume is only attributed to the change in normal components of stress. In order to analyse the pore volume variation, the total normal stress is first decomposed into two components: a hydrostatic part with mean stress σ_m and a deviatoric part $\sigma_{ij} - \sigma_m$:

$$\sigma_{ij} = \sigma_m + (\sigma_{ij} - \sigma_m) \quad (\text{A.27})$$

It can also be expressed that the variation in pore volume is only a function of pore pressure and mean stress (Geerstma, 1957). Hence one can write:

$$\frac{\partial V_p}{V_p} = \frac{1}{V_p} \left(\frac{\partial V_p}{\partial \sigma_m} \right)_p d\sigma_m + \frac{1}{V_p} \left(\frac{\partial V_p}{\partial p} \right) \sigma_m dp \quad (\text{A.28})$$

To evaluate the second term in the right hand side of Eq.A.28, stage (c)-loading is considered in which $\Delta \sigma_m = \Delta p$. From Eqs.A.10 and A.11 in differential form, the following equation is obtained:

$$\frac{dV_p}{V_p} = -c_s dp \quad (\text{A.29})$$

Introducing Eq.A.29 into Eq.A.28 results in:

$$-c_s = \frac{1}{V_p} \left(\frac{\partial V_p}{\partial \sigma_m} \right)_p + \frac{1}{V_p} \left(\frac{\partial V_p}{\partial p} \right) \sigma_m \quad (\text{A.30})$$

Combining Eqs.A.28 and A.30, one can write:

$$\frac{\partial V_p}{V_p} = -c_s dp + \frac{1}{V_p} \left(\frac{\partial V_p}{\partial \sigma_m} \right)_p (d\sigma_m - dp) \quad (\text{A.31})$$

In order to calculate the differentiation involved in the second term of the right hand side of Eq.A.31, Betti-Maxwell reciprocal theorem is employed. According to this theorem, the work done by the forces of the first system acting through the displacements of the second

system is equal to the work done by the forces of the second system acting through the displacements of the first system (Jaeger and Cook, 1969). Under the stage (b)-loading condition, mean stress is applied as the confining pressure which is equal to the pore pressure. In the first transformation, an increase in mean stress $d\sigma_m$ gives rise to a decrease in pore volume while the pore pressure is constant.

The second transformation involves an increase in pore pressure dp ($dp = d\sigma_m$) while the mean stress is maintained constant. This leads to an increase in bulk volume. The product of pressure-volume is identical to work, by applying the reciprocal theorem, one can write:

$$-d\sigma_m.dV_b^c = dp.dV_p^b \quad (\text{A.32})$$

where superscripts represent two transformations. Here negative sign is due to the bulk expansion which is considered negative in this work. After rearrangement:

$$\left(\frac{\partial V_p}{\partial \sigma_m}\right)_p = -\left(\frac{\partial V_b}{\partial p}\right)_{\sigma_m} \quad (\text{A.33})$$

It can be seen that the increase in bulk volume dV_b caused by dp is equal to the decrease in the pore volume dV_p caused by $d\sigma_m$ of the same magnitude. On the other hand, when $d\sigma_m = 0$, the relative bulk volume variation due to a change in pore pressure dp can be obtained from Ee.A.25 as follows:

$$\left(\frac{\partial V_b}{\partial p}\right)_{\sigma_m} = -V_b \alpha c_b \quad (\text{A.34})$$

Eliminating $\left(\frac{\partial V_b}{\partial p}\right)_{\sigma_m}$ from Eqs.A.33 and A.34, one can write:

$$\left(\frac{\partial V_p}{\partial \sigma_m}\right)_p = -V_b \alpha c_b \quad (\text{A.35})$$

By substituting Eq.A.35 into Eq.A.31 leads to:

$$\frac{\partial V_p}{V_p} = -c_s dp - \frac{1}{\phi} \alpha c_b (d\sigma_m - dp) \quad (\text{A.36})$$

Similar reasoning can be used for deviatoric component of stress so as to prove that the relative change in pore volume is zero. Therefore Eq.A.36 holds in general case.

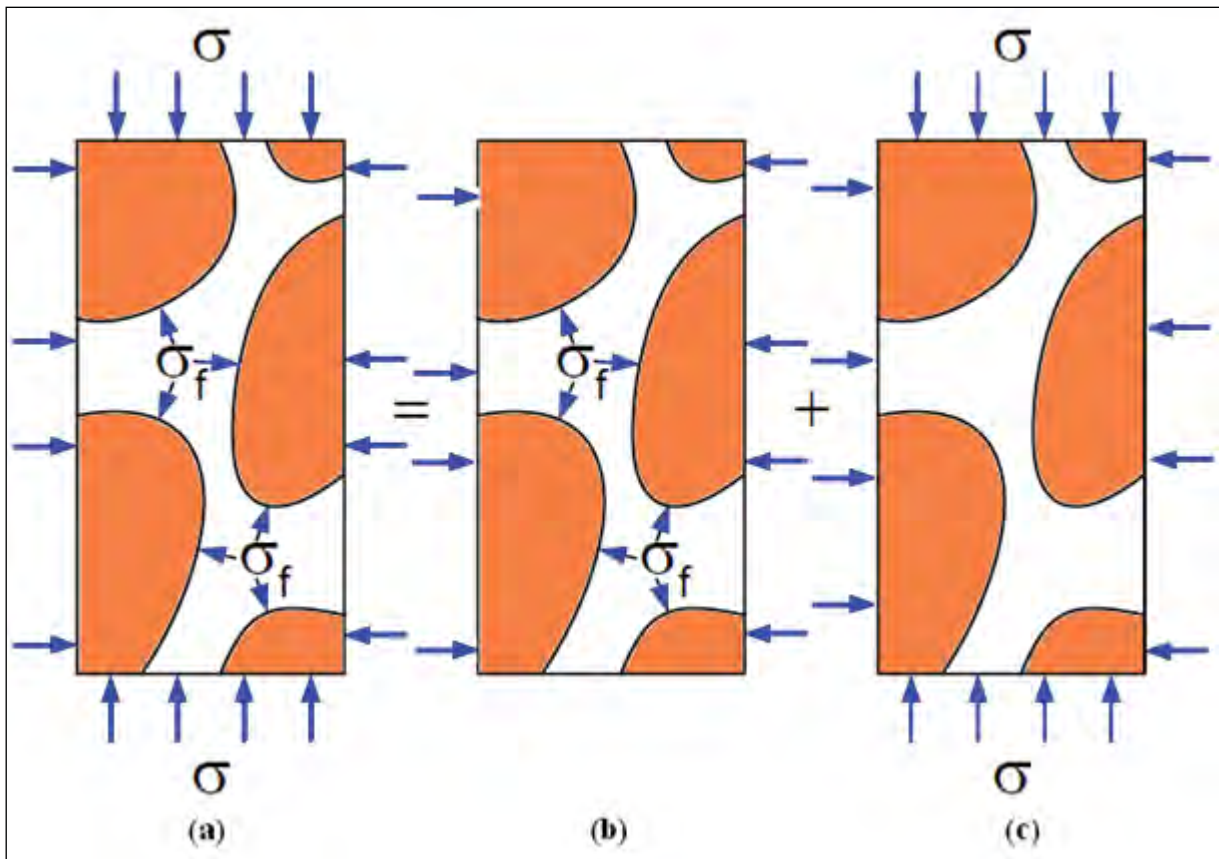


Fig. A1: Superposition to show the effect of fluid stress on bulk

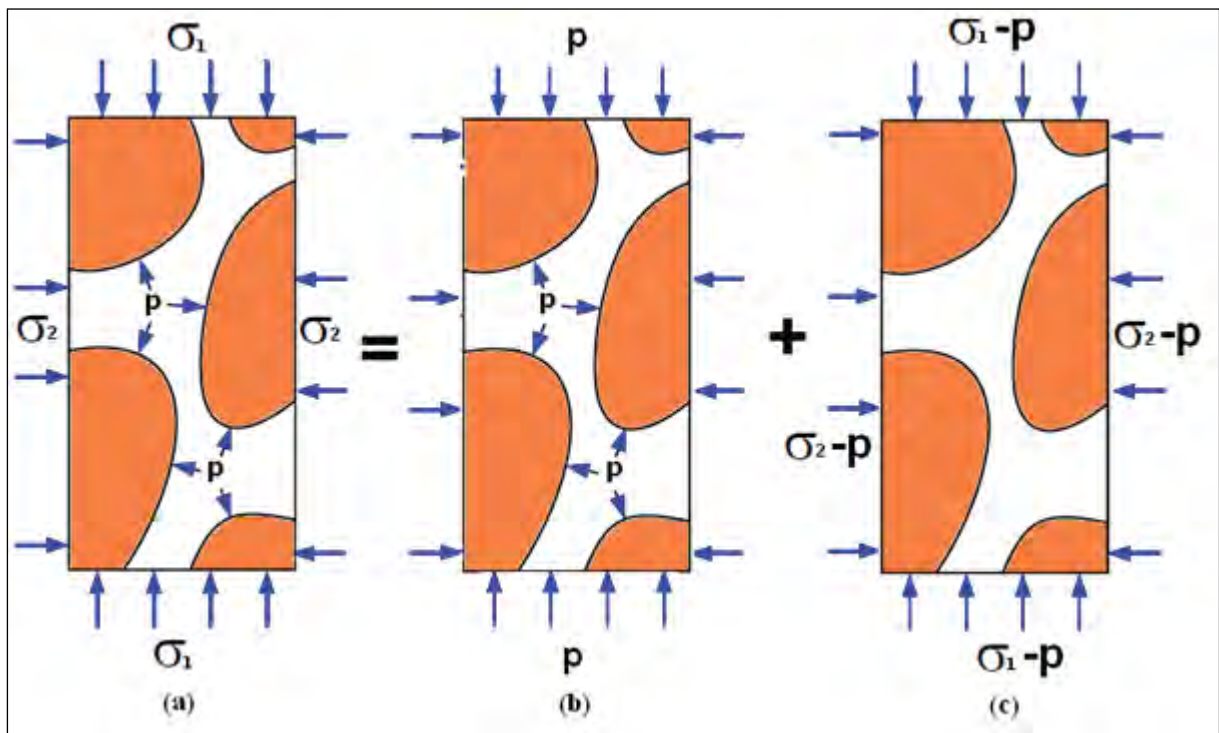


Fig. A2: Superposition of stress and fluid pressure acting on bulk

Appendix-2B: Derivation of Poroelastic Governing Equations and Analytical Equations

2.1 B Poroelastic Governing Equations

Coupled Fluid Flow Equation

In conventional reservoir simulators the diffusivity equation is used as the governing equation of pressure. This equation is derived by introducing Darcy's law into fluid continuity equation where the solid deformation (velocity of solid) is neglected.

Darcy's law in general form can be written as follows:

$$\phi(\vec{v}_f - \vec{v}_s) = -\frac{\vec{k}}{\mu}(\nabla p - \rho_f g \Delta H) \quad (\text{B.1})$$

where \vec{v}_f and \vec{v}_s are fluid and solid velocities.

Continuity equation for a fluid can be written as:

$$-\nabla \cdot (\rho_f \phi \vec{v}_f) + q = \frac{\partial(\phi \rho_f)}{\partial t} \quad (\text{B.2})$$

In the same way, Continuity equation for a solid can be written as:

$$-\nabla \cdot (\rho_s (1 - \phi) \vec{v}_s) + q = \frac{\partial((1 - \phi) \rho_s)}{\partial t} \quad (\text{B.3})$$

By combining the diffusivity equation and the continuity equation one can written:

$$\nabla \cdot \left(\rho_f \frac{\vec{k}}{\mu} (\nabla p - \rho_f g \Delta H) \right) + q = \frac{\partial(\phi \rho_f)}{\partial t} \quad (\text{B.4})$$

Where, f = fluid density, H = depth, g = gravitational acceleration

v = porosity, k = permeability tensor, μ = fluid viscosity

q = rate of mass injected/produced and p = fluid pressure.

In order to simplify the derivation of diffusivity equation with a coupled term, it is assumed that the net flow of fluid from source to sink to be zero ($q = 0$) and the effect of gravity also to be negligible i.e. $H = 0$, $q = 0$. The effect of gravitation and the source/sink term will be introduced to the final equation.

Introducing Eq.B.1 into Eq.B.2 and neglecting source sink term gives:

$$\frac{\partial(\rho_f \phi)}{\partial t} = \nabla \cdot (\rho_f \phi \vec{v}_s) + \nabla \cdot \left(\rho_f \frac{\vec{k}}{\mu} \nabla p \right) \quad (\text{B.5})$$

Expanding the right hand side of Eq.B.5 gives:

$$\frac{\partial(\rho_f \phi)}{\partial t} = \vec{v}_s \cdot \nabla(\rho_f \phi) + \rho_f \phi \cdot \nabla(\vec{v}_s) + \nabla \cdot \left(\rho_f \frac{\vec{k}}{\mu} \nabla p \right) \quad (\text{B.6})$$

Introducing the material derivative with respect to a moving solid (Chen et al., 1995),

D_s where $\frac{D_s(*)}{Dt} = \frac{\partial(*)}{\partial t} + v_s \cdot \nabla(*)$ one can write

$$\frac{D_s(\rho_f \phi)}{Dt} = \frac{\partial(\rho_f \phi)}{\partial t} + v_s \cdot \nabla(\rho_f \phi) \quad (\text{B.7})$$

Using Eq.B.7 into Eq.B.6 and after rearrangement, one can get:

$$\frac{D_s(\rho_f \phi)}{Dt} = \rho_f \phi \cdot \nabla(\vec{v}_s) + \nabla \cdot \left(\frac{\rho_f \vec{k}}{\mu} \nabla p \right) \quad (\text{B.8})$$

After differentiation of the left hand side of Eq.B.8 results in following form of the equation:

$$\rho_f \frac{D_s(\phi)}{Dt} + \phi \frac{D_s(\rho_f)}{Dt} = \rho_f \phi \cdot \nabla(\vec{v}_s) + \nabla \cdot \left(\frac{\rho_f \vec{k}}{\mu} \nabla p \right) \quad (\text{B.9})$$

Rearranging the Eq.B.9, it becomes:

$$\frac{1}{\phi} \frac{D_s(\phi)}{Dt} + \frac{1}{\rho_f} \frac{D_s(\rho_f)}{Dt} - \nabla(\vec{v}_s) = \frac{1}{\rho_f \phi} \nabla \cdot \left(\frac{\rho_f \vec{k}}{\mu} \nabla p \right) \quad (\text{B.10})$$

Expanding the solid continuity equation (Eq.B.3) and introducing the bulk density $\rho_b = (1 - \phi)\rho_s$ as well as neglecting the source/sink term the equation leads to:

$$(\nabla \cdot \rho_b) \vec{v}_s + (\nabla \cdot \rho_b) v_s + \frac{\partial(\rho_b)}{\partial t} - (\nabla \cdot \rho_b) \vec{v}_s = 0 \quad (\text{B.11})$$

After rearranging and using material derivative one can obtain:

$$\nabla \cdot v_s = \frac{1}{\rho_b} \frac{D_s(\rho_b)}{Dt} \quad (\text{B.12})$$

Substituting Eq.B.12 into Eq.B.10 results in:

$$\frac{1}{\phi} \frac{D_s(\phi)}{Dt} + \frac{1}{\rho_f} \frac{D_s(\rho_f)}{Dt} - \frac{1}{\rho_b} \frac{D_s(\rho_b)}{Dt} = \frac{1}{\rho_f \phi} \nabla \cdot \left(\frac{\rho_f \bar{k}}{\mu} \nabla p \right) \quad (\text{B.13})$$

From the definition of porosity, density and compressibility one can write:

$$\frac{\partial \phi}{\phi} = \frac{\partial V_p}{V_p} - \frac{\partial V_b}{V_b} \quad (\text{B.14})$$

$$\frac{\partial \rho_b}{\rho_b} = - \frac{\partial V_b}{V_b} \quad (\text{B.15})$$

and

$$c_f = \frac{1}{\rho_f} \frac{\partial \rho_f}{\partial p} \quad (\text{B.16})$$

where c_f is the fluid compressibility, V_p and V_s is the pore and bulk volume respectively. Substituting Eqs.B.14 and B.15 into Eq.B.13 gives:

$$\frac{1}{V_p} \frac{D_s(V_p)}{Dt} + \frac{1}{\rho_f} \frac{D_s(\rho_f)}{Dt} = \frac{1}{\rho_f \phi} \nabla \cdot \left(\frac{\rho_f \bar{k}}{\mu} \nabla p \right) \quad (\text{B.17})$$

Substituting Eqs.B.16 and A.31 (See **Appendix-2A**) into Eq.B.17, one can write:

$$(\phi c_f + \alpha c_b - \phi c_s) \frac{D_s p}{Dt} - \alpha c_b \frac{D_s \sigma_m}{Dt} = \frac{1}{\rho_f} \nabla \cdot \left(\frac{\rho_f \bar{k}}{\mu} \nabla p \right) \quad (\text{B.18})$$

where c_s and c_b are solid and bulk compressibility respectively and σ_m is the mean stress. Using the definition of the effective mean stress ($\sigma'_m = \sigma_m - \alpha p$) into Eq.B.18 leads to:

$$(\phi c_f + \alpha c_b - \phi c_s - \alpha^2 c_b) \frac{D_s p}{Dt} - \alpha c_b \frac{D_s \sigma'_m}{Dt} = \frac{1}{\rho_f} \nabla \cdot \left(\frac{\rho_f \bar{\bar{k}}}{\mu} \nabla p \right) \quad (\text{B.19})$$

Using Eq.A.15 and substituting σ'_m from Eq.A.25 into Eq.B.19 gives:

$$(\phi c_f + (\alpha - \phi) c_s - \alpha^2 c_b) \frac{D_s p}{Dt} - \alpha \frac{D_s \varepsilon_{jj}}{Dt} = \frac{1}{\rho_f} \nabla \cdot \left(\frac{\rho_f \bar{\bar{k}}}{\mu} \nabla p \right) \quad (\text{B.20})$$

where ε_{jj} is the volumetric strain defined as follows:

$$\begin{aligned} \varepsilon_{jj} &= \varepsilon_x + \varepsilon_y + \varepsilon_z \\ &= \frac{\partial u_x}{\partial x} + \frac{\partial u_y}{\partial y} + \frac{\partial u_z}{\partial z} \\ &= \nabla \cdot \vec{u} \end{aligned} \quad (\text{B.21})$$

where u_x , u_y and u_z is displacement along x, y and z axis respectively.

Expanding the right hand side of Eq.B.20 and substituting the value of ε_{jj} yields:

$$(\phi c_f + (\alpha - \phi) c_s) \frac{D_s p}{Dt} - \alpha \frac{D_s (\nabla \cdot \vec{u})}{Dt} = \nabla \cdot \left(\frac{\bar{\bar{k}}}{\mu} \nabla p \right) + c_f \nabla p \cdot \left(\frac{\bar{\bar{k}}}{\mu} \nabla p \right) \quad (\text{B.22})$$

For slightly compressible fluid one can write:

$$c_f \nabla p \cdot \left(\frac{\bar{\bar{k}}}{\mu} \nabla p \right) \ll \nabla \cdot \left(\frac{\bar{\bar{k}}}{\mu} \nabla p \right) \quad (\text{B.23})$$

Hence Eq.B.22 can be written as:

$$(\phi c_f + (\alpha - \phi) c_s) \frac{D_s p}{Dt} - \alpha \frac{D_s (\nabla \cdot \vec{u})}{Dt} = \nabla \cdot \left(\frac{\bar{\bar{k}}}{\mu} \nabla p \right) \quad (\text{B.24})$$

It is also assumed that material derivative can be approximated by normal derivative, namely $\frac{D_s}{Dt} \cong \frac{\partial}{\partial t}$. This implies that $v_s \cdot \nabla (*) \ll \frac{\partial (*)}{\partial t}$ which physically means that the medium deforms without movement. Using this assumption one can write the Eq.B.22 and B.24 as follows:

$$\left(\phi c_f + (\alpha - \phi)c_s\right) \frac{\partial p}{\partial t} - \alpha \frac{\partial(\nabla \cdot \vec{u})}{\partial t} = \nabla \cdot \left(\frac{\vec{k}}{\mu} \nabla p \right) \quad (\text{B.25})$$

$$\left(\phi c_f + (\alpha - \phi)c_s\right) \frac{\partial p}{\partial t} - \alpha \frac{\partial(\nabla \cdot \vec{u})}{\partial t} = \nabla \cdot \left(\frac{\vec{k}}{\mu} \nabla p \right) + c_f \nabla p \cdot \left(\frac{\vec{k}}{\mu} \nabla p \right) \quad (2.26)$$

The total compressibility c_t can be defined as

$$c_t = c_f + \frac{(\alpha - \phi)}{\phi} c_s \quad (\text{B.27})$$

Using the equation of total compressibility one can calculate

$$\left(\phi c_f + (\alpha - \phi)c_s\right) = \phi \left(c_f + \frac{(\alpha - \phi)c_s}{\phi} \right) = \phi c_t$$

Putting the value of $\left(\phi c_f + (\alpha - \phi)c_s\right)$ in Eq.B.26 and B.25 one can rewrite them as follows:

$$\phi c_t \frac{\partial p}{\partial t} - \alpha \frac{\partial(\nabla \cdot \vec{u})}{\partial t} = \nabla \cdot \left(\frac{\vec{k}}{\mu} \nabla p \right) + c_f \nabla p \cdot \left(\frac{\vec{k}}{\mu} \nabla p \right) \quad (\text{B.28})$$

$$\phi c_t \frac{\partial p}{\partial t} - \alpha \frac{\partial(\nabla \cdot \vec{u})}{\partial t} = \nabla \cdot \left(\frac{\vec{k}}{\mu} \nabla p \right) \quad (\text{B.29})$$

These are the coupled fluid flow equations using in the modelling of linear poroelasticity.

Displacement Equations:

The governing equation for displacement should contain the fluid pressure as the pressure is chosen as a coupling variable. The general equation of equilibrium for linear elastic materials is given as:

$$\nabla \cdot \vec{\sigma} = 0 \quad (\text{B.30})$$

By introducing effective stress in equation will result into

$$\nabla \cdot \vec{\sigma}' + \alpha p \vec{\delta} = 0 \quad (\text{B.31})$$

Where $\vec{\sigma}$ is the total stress tensor, $\vec{\sigma}'$ effective stress tensor defined as

$$\nabla \cdot \vec{\sigma}' = \nabla \cdot \vec{\sigma} - \alpha p \vec{\delta} \quad (\text{B.32})$$

and $\vec{\delta}$ is the Kronecker delta which is defined as follows:

$$\vec{\delta} = \begin{bmatrix} 1 & 0 & 0 \\ 0 & 1 & 0 \\ 0 & 0 & 1 \end{bmatrix} \quad (\text{B.33})$$

Stress strain relationship can be defined in vector form as:

$$\vec{\sigma} = \vec{D}_e \vec{\varepsilon} \quad (\text{B.34})$$

where D_e is the elastic modulus tensor (material properties matrix) defined in two dimensions is as follows:

$$\vec{D} = \begin{pmatrix} \lambda + 2G & \lambda & 0 \\ \lambda & \lambda + 2G & 0 \\ 0 & 0 & G \end{pmatrix} \quad (\text{B.35})$$

in which λ and 'G' are Lamé's parameters.

Strain which is defined as change in displacement is a function of displacement. This relationship can be represented in vector form as:

$$\varepsilon_{ij} = \frac{1}{2}(u_{i,j} + u_{j,i}) \quad (\text{B.36})$$

where u_i is solid displacement vector, $\varepsilon_{i,j}$ is solid strain tensor and $i, j=x, y, z$.

First to substitute the constitutive equations for the stress components (Eq.B.32) into Eq.B.30 and then to apply the definition of the strain components in terms of derivatives of displacement (Eq.B.36) the three constitutive equations in terms of displacement and pressure can be written as follows (Charlez, 1991):

$$G\nabla^2 u_x + (\lambda + G) \frac{(\nabla \cdot u_x)}{\partial x} - \alpha \frac{\partial p}{\partial x} = 0 \quad (\text{B.37})$$

$$G\nabla^2 u_y + (\lambda + G) \frac{(\nabla \cdot u_y)}{\partial y} - \alpha \frac{\partial p}{\partial y} = 0 \quad (\text{B.38})$$

$$G\nabla^2 u_z + (\lambda + G) \frac{(\nabla \cdot u_z)}{\partial z} - \alpha \frac{\partial p}{\partial z} = 0 \quad (\text{B.39})$$

$$\text{in which } \nabla^2 u_a = \frac{\partial^2 u_a}{\partial x^2} + \frac{\partial^2 u_a}{\partial y^2} + \frac{\partial^2 u_a}{\partial z^2}$$

Eq.B.29 associated with Eqs.B.37-B.39 are the constitutive equations of poroelasticity with four unknowns: u_x , u_y , u_z and p . Coupling occurs among these equations because pore pressure appears in the force equilibrium equations and mean stress/strain(derivative of displacement) appears in the fluid flow equation. The richness and varieties of poroelastic phenomena arise from interactions between the mechanical requirement of force equilibrium and the fluid flow requirement of continuity (H.F Wang, 2000)

Plane Strain

Due to the restriction in computing time and resources the plane strain assumption has been widely used in petroleum engineering that yield acceptable results with 2D analysis (Cui et al., 1997). This assumption has been widely used in the study of hydraulic fracturing and stress reorientation by various authors (Biot et al., 1986; Garagash and Detournay, 2005; Geerstma and De Klerck, 1969; Hidayati et al., 2001; Nouri et al., 2002; Sato and Hashida, 2000). Using the stress-displacement relationship one can reduce Eqs.B.37- B.39 into two dimensions. The stress-displacement relationship can be expressed as follows (Zienkiewicz and Taylor, 2000):

$$\vec{\sigma}' = \vec{D}_e \vec{S} \vec{u} \quad (\text{B.40})$$

$$\text{where } \vec{S} = \begin{bmatrix} \frac{\partial}{\partial x} & 0 \\ 0 & \frac{\partial}{\partial y} \\ \frac{\partial}{\partial y} & \frac{\partial}{\partial x} \end{bmatrix} \quad (\text{B.41})$$

or in incremental form:

$$\overrightarrow{\Delta \sigma'} = \vec{D}_e \vec{S} \overrightarrow{\Delta u} \quad (\text{B.42})$$

where $\overrightarrow{\Delta u}$ the change in displacement is vector and expressed as follows:

$$\overrightarrow{\Delta u} = \begin{bmatrix} \Delta u_x \\ \Delta u_y \end{bmatrix} \quad (\text{B.43})$$

Combining Esq.B.30, B.31 and B.43 yields:

$$\vec{S}^T \overrightarrow{\Delta \sigma'} + \alpha \nabla \overrightarrow{\Delta p} = \vec{0} \quad (\text{B.44})$$

or:

$$\vec{S}^T \vec{D}_e \vec{S} \overrightarrow{\Delta u} + \alpha \nabla \overrightarrow{\Delta p} = \vec{0} \quad (\text{B.45})$$

Where $\Delta \vec{\sigma} =$ Change in total stress, $= \begin{bmatrix} \Delta \sigma_x \\ \Delta \sigma_y \\ \Delta \sigma_{xy} \end{bmatrix}$

$$\Delta \vec{\sigma}' = \text{change in effective stress} = \begin{bmatrix} \Delta \sigma'_x \\ \Delta \sigma'_y \\ \Delta \sigma'_{xy} \end{bmatrix} \text{ and } \Delta \vec{p} = \text{change in pressure} = \begin{bmatrix} \Delta p \\ \Delta p \\ 0 \end{bmatrix}$$

2.2 B Analytical equations to verify the numerical results for displacement, stress and pore pressure.

The aim of this section is to present appropriate analytical solutions to be used for verification of numerical results. They include equations for displacement, pore pressure and stresses at different time and location in a horizontal reservoir intercepted by a vertical wellbore. The initial state is assumed to be drained and anisotropic stress field exists in general case. The solutions are found through superposing two cases as shown in **Fig.B.1**. In case (b), a vertical wellbore of radius r_w is located in an infinite horizontal reservoir. Reservoir fluid pressure is p_i . Wellbore pressure is considered to be equal to the reservoir pressure for superposition purpose. Solid skeleton of the rock is compressible and stress field is anisotropic. Analytical solutions for displacement, stress and pore pressure are obtained using the theory of superimposition and are given below as (Detournay and Cheng 1988; Aghighi 2007):

- **Radial displacement:**

$$u_r(r, \theta) = \frac{r}{4G} \left((\sigma_H' + \sigma_h')(1 - 2\nu + \frac{r_w^2}{r^2}) + (\sigma_H' - \sigma_h') \times \left(\frac{r_w^2}{r^2} \left(4 - 4\nu - \frac{r_w^2}{r^2} \right) + 1 \right) \cos(2\theta) \right) - \frac{p_w' r_w^2}{2G r} - \frac{\eta}{G} r_w (p_w - p_i) h(r, t) \quad (\text{B.46})$$

- **Tangential displacement:**

$$u_{\theta}(r, \theta) = -\frac{r}{4G} (\sigma_H - \sigma_h) \left(\frac{r_w^2}{r^2} \left(2 - 4\nu + \frac{r_w^2}{r^2} \right) + 1 \right) \sin(2\theta) \quad (\text{B.47})$$

- **Pore pressure:**

$$p(r, t) = p_i + (p_w - p_i) g(r, t) \quad (\text{B.48})$$

- **Radial stress:**

$$\begin{aligned} \sigma_{rr}(r, \theta) = & \frac{\sigma_H + \sigma_h}{2} \left(1 - \frac{r_w^2}{r^2} \right) + \frac{\sigma_H - \sigma_h}{2} \left(1 + 3\frac{r_w^4}{r^4} - 4\frac{r_w^2}{r^2} \right) \cos(2\theta) + \\ & p_w \frac{r_w^2}{r^2} + 2\eta(p_w - p_i) \frac{r_w}{r} h(r, t) \end{aligned} \quad (\text{B.49})$$

- **Tangential stress:**

$$\begin{aligned} \sigma_{\theta\theta}(r, \theta) = & \frac{\sigma_H + \sigma_h}{2} \left(1 + \frac{r_w^2}{r^2} \right) - \frac{\sigma_H - \sigma_h}{2} \left(1 + 3\frac{r_w^4}{r^4} \right) \cos(2\theta) - \\ & p_w \frac{r_w^2}{r^2} - 2\eta(p_w - p_i) \left(\frac{r_w}{r} h(r, t) + g(r, t) \right) \end{aligned} \quad (\text{B.50})$$

- **Shear stress:**

$$\sigma_{\theta r}(r, \theta) = -\frac{\sigma_H - \sigma_h}{2} \left(1 - 3\frac{r_w^4}{r^4} + 2\frac{r_w^2}{r^2} \right) \sin(2\theta) \quad (\text{B.51})$$

where, σ_H and σ_h are maximum and minimum horizontal stresses respectively,

p_w , p_i and p are the wellbore pressure, initial reservoir pressure and pore pressure respectively,

r_w = wellbore radius, r and θ = polar coordinates of any point, t = time.

$$g(r, t) = L^{-1}(\tilde{g}(r, s)) \quad (\text{B.52})$$

$$h(r, t) = L^{-1}(\tilde{h}(r, s)) \quad (\text{B.53})$$

L^{-1} is the Laplace inversion operator and:

$$\tilde{g}(r, s) = \frac{K_0(\xi)}{sK_0(\beta)} \quad (\text{B.54})$$

$$\tilde{h}(r, s) = \frac{1}{s} \left[\frac{K_1(\xi)}{\beta K_0(\beta)} - \frac{r_w}{r} \frac{K_1(\beta)}{\beta K_0(\beta)} \right] \quad (\text{B.55})$$

$$\eta = \alpha \frac{1-2\nu}{2(1-\nu)} \quad (\text{B.56})$$

$$\xi = r \sqrt{\frac{s}{c}} \quad (\text{B.57})$$

$$\beta = r_w \sqrt{\frac{s}{c}} \quad (\text{B.58})$$

$$c = \frac{k}{\mu} \left(\phi c_t + \frac{\alpha^2}{\lambda + 2G} \right)^{-1} \quad (\text{B.59})$$

K_0 and K_1 are the first order modified Bessel function of the first and second kind. Laplace inversion can be performed using the method presented by Stehfest (1970) which is one of the various methods of approximating Laplace inversion. The solution in time can be calculated by using the following formula:

$$f(t) \approx \frac{\ln 2}{t} \sum_{n=1}^N c_n f\left(n \frac{\ln 2}{t}\right) \quad (\text{B.60})$$

where \ln is the natural logarithm, N any positive even number between 8 and 20; and C_n can be calculated using the following equation:

$$c_n = (-1)^{n+\frac{N}{2}} \sum_{k=\text{floor}(\frac{n+1}{2})}^{\min(n, \frac{N}{2})} \frac{k^{\frac{N}{2}} (2k)!}{\left(\frac{N}{2} - k\right)! k! (k-1)! (n-k)! (2k-n)!} \quad (\text{B.61})$$

2.3 B Closed system of equations for KGD-C model

KGD-C model is chosen to compare with the current numerical model as both assume plain strain in horizontal plane. The key difference is the application of boundary condition and propagation criterion. KGD-C model assumes a constant pressure throughout the wellbore and the criterion for propagation is based on Barenblatt's (1962) hypothesis. Whereas in the proposed model, fracture fluid profile obtained from numerical calculation is used as boundary condition and the fracture propagation is based on LEFM. The KGD geometry is illustrated in **Fig.B.2**. The width, half length and net pressure obtained from the

current model and KGD-C are compared. The letter C denotes that the 2D algebraic models are combined with carter II solution (for leak off) of material balance. For constant-injection-rate/no-leak-off case the length, width and net pressure is calculated as(Geerstma and De Klerck 1969):

$$x_f = \left(\frac{16}{21\pi^3} \right)^{\frac{1}{6}} \left(\frac{\left\{ \frac{q_i}{2} \right\}^3 E'}{\mu h^3} \right)^{\frac{1}{6}} t_i^{\frac{2}{3}} = 0.593 \left(\frac{\left\{ \frac{q_i}{2} \right\}^3 E'}{\mu h^3} \right)^{\frac{1}{6}} t_i^{\frac{2}{3}} \quad (\text{B.63})$$

$$w_f = \left(\frac{5376}{\pi^3} \right)^{\frac{1}{6}} \left(\frac{\left\{ \frac{q_i}{2} \right\}^3 \mu}{E' h^3} \right)^{\frac{1}{6}} t_i^{\frac{2}{3}} = 2.36 \left(\frac{\left\{ \frac{q_i}{2} \right\}^3 \mu}{E' h^3} \right)^{\frac{1}{6}} \quad (\text{B.64})$$

$$p_{net,w} = \left(\frac{21}{16} \right)^{\frac{1}{3}} (E'^2 \mu)^{\frac{1}{3}} t^{\frac{-1}{3}} = 1.09 (E'^2 \mu)^{\frac{1}{3}} t^{\frac{-1}{3}} \quad (\text{B.65})$$

Using the carter II solution of material balance, fracture half length can be obtained from the following equation(Valko and Economides 1995):

$$X_f = \frac{(\bar{w} + 2S_p)q}{4C_L \pi h_f} \left[\exp(\beta) \operatorname{erfc}(\beta) + \frac{2\beta}{\sqrt{\pi}} - 1 \right] \quad (\text{B.67})$$

$$\beta = \frac{2C_L \sqrt{(\pi t)}}{(\bar{w} + 2S_p)} \quad (\text{B.68})$$

where, C_L = Leak-off coefficient, S_p = spurt loss coefficient, \bar{w} = Average width,

$E' = E/ (1 - \nu^2)$, μ = Fracturing fluid viscosity, q = Flow rate and h_f = height of fracture.

A closed system of equations for KGD-C model can be formed using equations B.63 to B.68. The well bore pressure, fracture half length and fracture width at the well bore can be obtained by using a numerical root finding method.

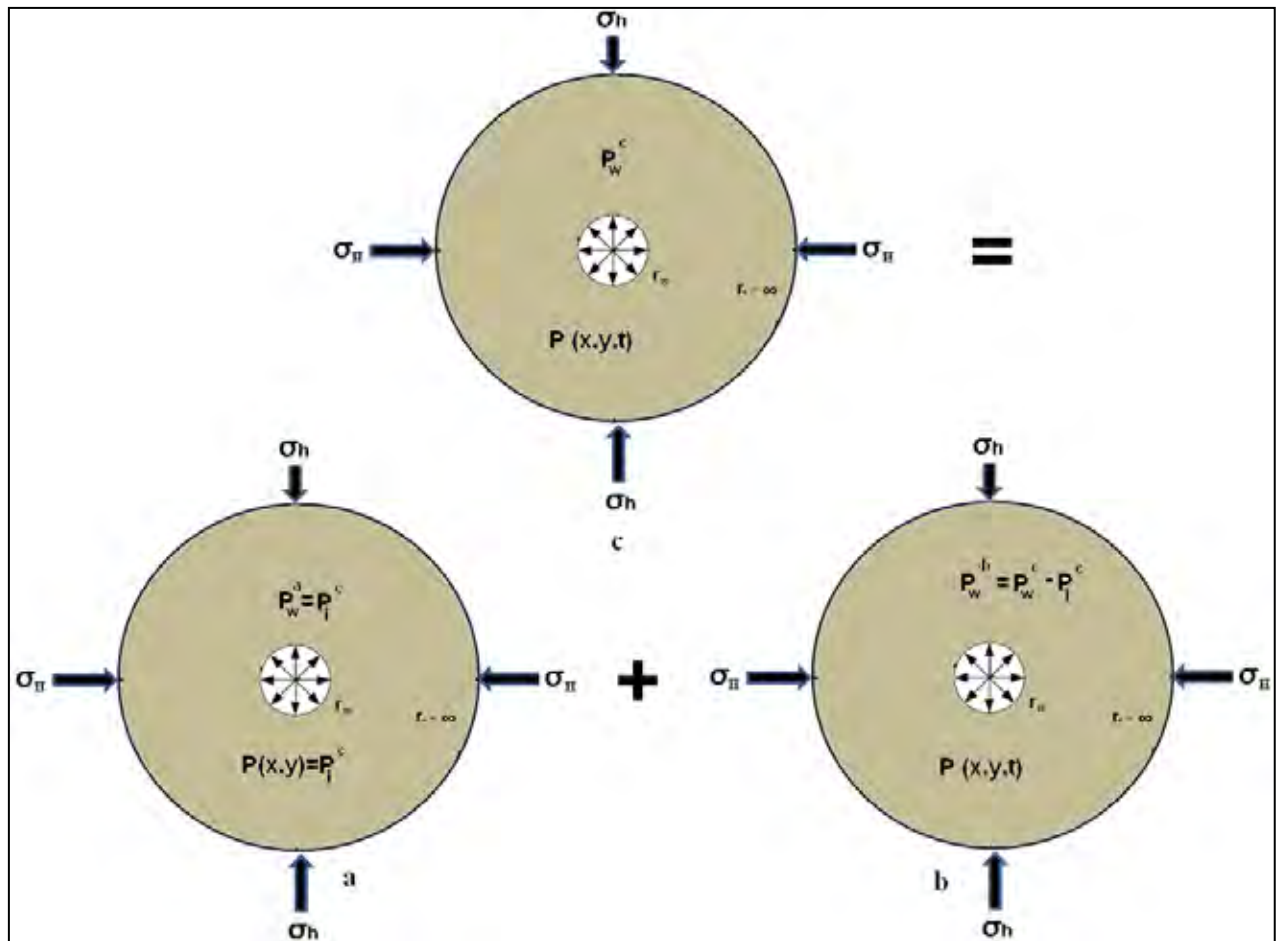


Fig. B.1: Decomposition of total problem (c) into two cases which are: (a) static state of a wellbore with balanced pressure in a drained rock subjected to anisotropic horizontal stress and (b) poroelastic response of a wellbore in an initially unstressed rock containing fluid at zero pressure (p_i = initial reservoir pressure, p_w = wellbore pressure, r_w = wellbore radius, r_e = the radius of outer boundary, Source Aghighi, 2007).

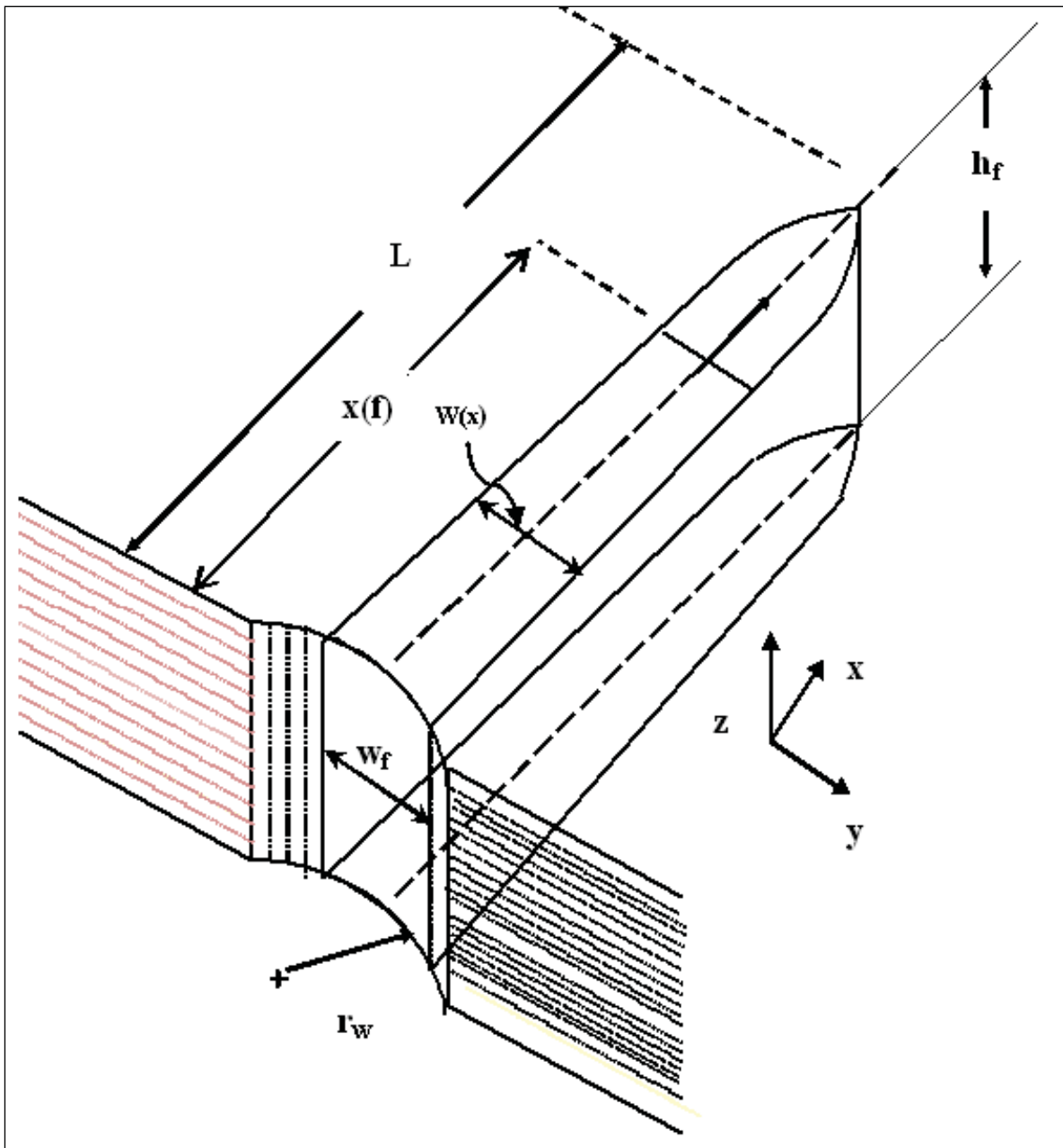


Fig. B0.2: Schematic representation of classical KGD model.

Where, w_f = Width at the well bore,

$w(x)$ = Width along the length x ,

x_f = Fracture half length and

h_f = height of the fracture

Appendix-2C: General Implementation of Finite Element Method (FEM)

Formulation of finite element equations as a result of discretization of the governing equations of poroelastic equations is discussed in **Appendix-2D**. In this section, some basics of the general implementation of FEM are presented and discussed.

C.1: Model description.

The poroelastic intact wellbore model presented here includes a reservoir which is intercepted by a vertical wellbore. Vertical stress is a principal stress and other two principal stresses (minimum and maximum horizontal in-situ stresses) are in horizontal plane and are aligned in the same direction of Cartesian coordinates of the reservoir. This can be modeled by taking a horizontal cross section of the reservoir and introducing a circular hole to represent the wellbore. The model geometry is shown in **Fig.C1**.

C.2: Quarter reservoir model and space discretization

In this study, due to the symmetrical stress field, advantage of symmetry is taken and solve on a quarter models for intact wellbore modeling. The schematic of quarter model is given in **Fig.C.2**.

To generate the finite element mesh, it is necessary to make the finest mesh near wellbore as displacement and pressure profiles are concentrated towards the wellbore. So away from the wellbore the mesh size is increases and the coarsest mesh at the outer radius. The following formula can be used:

$$r_i = c.r_{i-1} \quad (C.1)$$

where r is the radial position and c is a constant defined as follows:

$$c = \left(\frac{r_e}{r_w} \right)^{\frac{1}{m}} \quad (C.2)$$

In which r_e and r_w are the wellbore and outer radius respectively, m is the number of radial steps. To generate an accurate mesh it is necessary to use angular steps so that the

aspect ratio of the elements does not exceed 10. It is recommended to use the aspect ratio close to 1. The angular step ω is defined as.

$$\theta_i = \omega.i \quad (C.3)$$

where θ is the angular position and “i” is the number of steps.

ω and m can be adjusted according to the required density mesh. This mesh is quite efficient with fine mesh close to the wellbore and coarse mesh on the outer radius. Using Eqs.C.1 to and C.3) a regular node pattern on the quarter model can create and connect the nodes to make the mesh which is illustrated in **Fig.C.3**.

The specific mesh using the poroelastic intact wellbore modeling is given in **Fig.C.4**. Outer boundary (r_e) and wellbore radius (r_w) is 1500 m and 0.1 m. respectively. Value of angular step, ω is 15° and 42 angular steps are used.

C.3: Four noded square elements

Local coordinates are used to position the centre of an element at the origin Zienkiewicz (2000). The four noded square element are shown in **Fig.C.5** with local coordinates.

Using Lagrange polynomial one can write two linear Lagrange equations for an interval with two nodes as follows:

$$L_0^1(\xi) = \frac{\xi - \xi_1}{\xi_0 - \xi_1} \quad (C.4)$$

$$L_1^1(\xi) = \frac{\xi - \xi_0}{\xi_1 - \xi_0} \quad (C.5)$$

Using Lagrange polynomials shape functions for the square element are given by Zienkiewicz (2000) as:

$$N_{i,j}(\xi, \eta) = L_i^n(\xi) \cdot L_j^m(\eta) \quad (C.6)$$

Starting with the bottom right hand corner and working anticlockwise around the element and using the equation C.6 the four shape functions are as follows:

$$N_1(\xi, \eta) = \frac{1}{4} \cdot (1 + \xi) \cdot (1 - \eta) \quad (C.7a)$$

$$N_2(\xi, \eta) = \frac{1}{4} \cdot (1 + \xi) \cdot (1 + \eta) \quad (\text{C.7b})$$

$$N_3(\xi, \eta) = \frac{1}{4} \cdot (1 - \xi) \cdot (1 + \eta) \quad (\text{C.7c})$$

and

$$N_4(\xi, \eta) = \frac{1}{4} \cdot (1 - \xi) \cdot (1 - \eta) \quad (\text{C.7d})$$

C.4: Eight noded square elements

The eight noded square element with node numbering is shown in Fig.C.6. Node numbering starts with the bottom right hand corner and going anticlockwise around the element.

Here there is no node at the midpoint so Eq.C.6 cannot be used for making shape function for this element. The straight line equations can be use to find out the shape functions. The general straight line equation that passes through two coordinate (x_1, y_1) and (x_2, y_2) is as follows.

$$\frac{x - x_1}{x_1 - x_2} = \frac{y - y_1}{y_1 - y_2} \quad (\text{C.8})$$

Using the Eq.C.8 one can define straight lines passing through the nodes of the elements is as follows:

$$Line_{13} \equiv 1 - \xi = 0 \quad (\text{C.9a})$$

$$Line_{35} \equiv 1 - \eta = 0 \quad (\text{C.9b})$$

$$Line_{57} \equiv 1 + \xi = 0 \quad (\text{C.9c})$$

$$Line_{71} \equiv 1 + \eta = 0 \quad (\text{C.9d})$$

$$Line_{24} \equiv 1 - \xi - \eta = 0 \quad (\text{C.9e})$$

$$Line_{46} \equiv 1 + \xi - \eta = 0 \quad (\text{C.9f})$$

$$Line_{68} \equiv 1 + \xi + \eta = 0 \quad (\text{C.9g})$$

$$Line_{82} \equiv 1 - \xi + \eta = 0 \quad (\text{C.9h})$$

Now the eight shape functions can be formed using the Eq.C.9 through combinations of the lines not passing through the given node and multiplying by a constant to satisfy unity at the given node.

For the first shape function of node number 1 Line₃₅, Line₅₇ and Line₈₂ are combined with a constant $\left(-\frac{1}{4}\right)$ to give:

$$N_1(\xi, \eta) = \left(-\frac{1}{4}\right)(1+\xi)(1-\eta)(1-\xi+\eta) \quad (\text{C.10a})$$

For the second shape function of node number 2 Line₃₅, Line₅₇ and Line₇₁ are combined with a constant $\left(-\frac{1}{2}\right)$ to give:

$$N_2(\xi, \eta) = \left(\frac{1}{2}\right)(1+\eta)(1-\eta)(1+\xi) \quad (\text{C.10b})$$

Similarly the other shape functions are:

$$N_3(\xi, \eta) = \left(-\frac{1}{4}\right)(1+\xi)(1+\eta)(1-\xi-\eta) \quad (\text{C.10c})$$

$$N_4(\xi, \eta) = \left(-\frac{1}{4}\right)(1+\xi)(1-\xi)(1+\eta) \quad (\text{C.10d})$$

$$N_5(\xi, \eta) = \left(-\frac{1}{4}\right)(1-\xi)(1+\eta)(1+\xi-\eta) \quad (\text{C.10e})$$

$$N_6(\xi, \eta) = \left(\frac{1}{2}\right)(1+\eta)(1-\eta)(1-\xi) \quad (\text{C.10f})$$

$$N_7(\xi, \eta) = \left(-\frac{1}{4}\right)(1-\xi)(1-\eta)(1+\xi+\eta) \quad (\text{C.10g})$$

$$N_8(\xi, \eta) = \left(\frac{1}{2}\right)(1+\xi)(1-\xi)(1-\eta) \quad (\text{C.10h})$$

C.5: General two dimensional transformation

For an element there are four local coordinates (ξ, η) and corresponding global coordinates (x, y) . It also has shape functions in terms of local coordinates. In order to

operate on derivatives in the global coordinates, transformations from local coordinate to global coordinates are required. In this study Zienkiewicz's (2000) relationship are used and for a shape function (N_i) for this transformation is as follows:

$$\begin{pmatrix} \frac{\partial N_i}{\partial \xi} \\ \frac{\partial N_i}{\partial \eta} \end{pmatrix} = \vec{J} \cdot \begin{pmatrix} \frac{\partial N_i}{\partial x} \\ \frac{\partial N_i}{\partial y} \end{pmatrix} \quad (\text{C.11})$$

where J is Jacobian matrix and defined as

$$\vec{J} = \begin{pmatrix} \frac{\partial x}{\partial \xi} & \frac{\partial y}{\partial \xi} \\ \frac{\partial x}{\partial \eta} & \frac{\partial y}{\partial \eta} \end{pmatrix} \quad (\text{C.12})$$

To find the global derivatives of the shape functions (J) needs to invert and can be written as follows:

$$\begin{pmatrix} \frac{\partial N_i}{\partial x} \\ \frac{\partial N_i}{\partial y} \end{pmatrix} = \vec{J}^{-1} \cdot \begin{pmatrix} \frac{\partial N_i}{\partial \xi} \\ \frac{\partial N_i}{\partial \eta} \end{pmatrix} \quad (\text{C.13})$$

Again for area integrals a relationship between the area in local coordinates ($d\xi d\eta$) and the area in global coordinates ($dx dy$) are needed. Given by Zienkiewicz (2000) one can write:

$$dx dy = \begin{vmatrix} \frac{\partial x}{\partial \xi} & \frac{\partial y}{\partial \xi} \\ \frac{\partial x}{\partial \eta} & \frac{\partial y}{\partial \eta} \end{vmatrix} d\xi d\eta = \det(\vec{J}) d\xi d\eta \quad (\text{C.14})$$

In which $\det (*)$ represent the determinants of the matrix.

C.6: Four noded element transformation

For the four noded element transformation the shape functions (N_i), their derivatives with respect to global coordinates and area ($dx dy$) as functions of local coordinates (ξ, η) are needed. The shape functions as functions of local coordinates are given by Eq.C.7.

Differentiating Eq.C.7 the derivatives of shape functions with respect to local coordinates as functions of local coordinates can be written as follows:

$$\frac{\partial N_1}{\partial \xi}(\eta) = \frac{1}{4} \cdot (1 - \eta) \quad (\text{C.15a})$$

$$\frac{\partial N_2}{\partial \xi}(\eta) = \frac{1}{4} \cdot (1 + \eta) \quad (\text{C. 15b})$$

$$\frac{\partial N_3}{\partial \xi}(\eta) = -\frac{1}{4} \cdot (1 + \eta) \quad (\text{C. 15c})$$

$$\frac{\partial N_4}{\partial \xi}(\eta) = -\frac{1}{4} \cdot (1 - \eta) \quad (\text{C. 15d})$$

and

$$\frac{\partial N_1}{\partial \eta}(\xi) = -\frac{1}{4} \cdot (1 + \xi) \quad (\text{C. 16a})$$

$$\frac{\partial N_2}{\partial \eta}(\xi) = \frac{1}{4} \cdot (1 + \xi) \quad (\text{C. 16b})$$

$$\frac{\partial N_3}{\partial \eta}(\xi) = \frac{1}{4} \cdot (1 - \xi) \quad (\text{C. 16c})$$

$$\frac{\partial N_4}{\partial \eta}(\xi) = -\frac{1}{4} \cdot (1 - \xi) \quad (\text{C. 16d})$$

Using the mapping of a four noded square in local coordinates (ξ, η) onto an arbitrary four noded quadrilateral in global coordinates (x, y) leads to the following relationships for the element:

$$x = N_1 \cdot x_1 + N_2 \cdot x_2 + N_3 \cdot x_3 + N_4 \cdot x_4 \quad (\text{C.17})$$

$$y = N_1 \cdot y_1 + N_2 \cdot y_2 + N_3 \cdot y_3 + N_4 \cdot y_4 \quad (\text{C.18})$$

where the shape functions N_1 to N_4 are given by the Eq.C.7

Differentiating Eq.C.17 and using Eqs.C.15 and C.16 one can write the derivatives of the x coordinate with respect to the local coordinates as follows:

$$\frac{\partial x}{\partial \xi}(\eta) = \sum_{i=1}^4 \frac{\partial N_i}{\partial \xi} \cdot x_i = \frac{1}{4} \cdot ((1 - \eta) \cdot x_1 + (1 + \eta) \cdot x_2 - (1 + \eta) \cdot x_3 - (1 - \eta) \cdot x_4) \quad (\text{C.19})$$

$$\frac{\partial x}{\partial \eta}(\xi) = \sum_{i=1}^4 \frac{\partial N_i}{\partial \eta} \cdot x_i = \frac{1}{4} \cdot (-(1+\xi) \cdot x_1 + (1+\xi) \cdot x_2 + (1-\xi) \cdot x_3 - (1-\xi) \cdot x_4) \quad (\text{C.20})$$

Similarly differentiating Eq.C.18 and using Eqs.C.15 and C.16 one can write the derivatives of the y coordinate with respect to the local coordinates as follows:

$$\frac{\partial y}{\partial \xi}(\eta) = \sum_{i=1}^4 \frac{\partial N_i}{\partial \xi} \cdot y_i = \frac{1}{4} \cdot ((1-\eta) \cdot y_1 + (1+\eta) \cdot y_2 - (1+\eta) \cdot y_3 - (1-\eta) \cdot y_4) \quad (\text{C.21})$$

$$\frac{\partial y}{\partial \eta}(\xi) = \sum_{i=1}^4 \frac{\partial N_i}{\partial \eta} \cdot y_i = \frac{1}{4} \cdot (-(1+\xi) \cdot y_1 + (1+\xi) \cdot y_2 + (1-\xi) \cdot y_3 - (1-\xi) \cdot y_4) \quad (\text{C.22})$$

Using Eqs.C.19 to C.22 into the Eq.C.19 one can calculate Jacobian as a function of local coordinates (Gaussian point). Then using the value of Jacobian and Eqs.C.15 and C.16 with Eqs.C.13 and C.14, one can calculate the area integral as a function of local coordinates.

C.7: Eight noded element transformation

For the eight noded element transformation the shape functions (N_i), their derivatives with respect to global coordinates and area ($dx dy$) as functions of local coordinates (ξ, η) are needed. The shape functions as functions of local coordinates are given by Eq.C.10. Differentiating Eq.C.10 the derivatives of shape function with respect to local coordinates as functions of local coordinates can be written as follows:

$$\frac{\partial N_1}{\partial \xi}(\xi, \eta) = \left(\frac{1}{4}\right)(1-\eta)(2\xi + \eta) \quad (\text{C.23a})$$

$$\frac{\partial N_2}{\partial \xi}(\xi, \eta) = \frac{1}{2} \cdot (1+\eta)(1-\eta) \quad (\text{C.23b})$$

$$\frac{\partial N_3}{\partial \xi}(\xi, \eta) = \frac{1}{4} \cdot (1+\eta)(2\xi + \eta) \quad (\text{C.23c})$$

$$\frac{\partial N_4}{\partial \xi}(\xi, \eta) = -\xi \cdot (1+\eta) \quad (\text{C.23d})$$

$$\frac{\partial N_5}{\partial \xi}(\xi, \eta) = \frac{1}{4} \cdot (1+\eta)(2\xi - \eta) \quad (\text{C.23e})$$

$$\frac{\partial N_6}{\partial \xi}(\eta) = -\frac{1}{2} \cdot (1+\eta)(1-\eta) \quad (\text{C.23f})$$

$$\frac{\partial N_7}{\partial \xi}(\xi, \eta) = \frac{1}{4} \cdot (1 - \eta)(2\xi + \eta) \quad (\text{C. 23g})$$

$$\frac{\partial N_8}{\partial \xi}(\xi, \eta) = -\xi \cdot (1 - \eta) \quad (\text{C. 23h})$$

and

$$\frac{\partial N_1}{\partial \eta}(\xi, \eta) = \frac{1}{4} (1 + \xi)(2\eta - \xi) \quad (\text{C.24a})$$

$$\frac{\partial N_2}{\partial \eta}(\xi, \eta) = -\eta \cdot (1 + \xi) \quad (\text{C. 24b})$$

$$\frac{\partial N_3}{\partial \eta}(\xi, \eta) = \frac{1}{4} \cdot (1 + \xi)(2\eta + \xi) \quad (\text{C. 24c})$$

$$\frac{\partial N_4}{\partial \eta}(\xi, \eta) = \frac{1}{2} \cdot (1 + \xi)(1 - \xi) \quad (\text{C. 24d})$$

$$\frac{\partial N_5}{\partial \eta}(\xi, \eta) = \frac{1}{4} \cdot (1 - \xi)(2\eta - \xi) \quad (\text{C.24e})$$

$$\frac{\partial N_6}{\partial \eta}(\xi, \eta) = -\eta \cdot (1 + \xi) \quad (\text{C. 24f})$$

$$\frac{\partial N_7}{\partial \eta}(\xi, \eta) = \frac{1}{4} \cdot (1 - \eta)(2\xi + \eta) \quad (\text{C. 24g})$$

$$\frac{\partial N_8}{\partial \eta}(\xi) = -\frac{1}{2} \cdot (1 - \xi)(1 + \xi) \quad (\text{C. 24h})$$

Using the mapping of an eight noded square in local coordinates (ξ , η) onto an arbitrary eight noded quadrilateral in global coordinates (x, y) leads to the following relationships for the element:

$$x = \sum_{i=1}^8 N_i \cdot x_i \quad (\text{C.25})$$

$$y = \sum_{i=1}^8 N_i \cdot y_i \quad (\text{C.26})$$

where i=1 to 8 (node number of the element) and the shape functions N_1 to N_8 are given by the Eq.C.10

Differentiating Eq.C.25 and using Eqs.C.23 and C.24 one can write the derivatives of the x coordinate with respect to the local coordinates as follows:

$$\frac{\partial x}{\partial \xi}(\eta) = \sum_{i=1}^8 \frac{\partial N_i}{\partial \xi}(\xi, \eta) \cdot x_i \quad (\text{C.27})$$

$$\frac{\partial x}{\partial \eta}(\xi) = \sum_{i=1}^8 \frac{\partial N_i}{\partial \eta}(\xi, \eta) \cdot x_i \quad (\text{C.28})$$

Similarly differentiating Eq.C.26 and using Eqs.C.15 and C.16 one can write the derivatives of the y coordinate with respect to the local coordinates as follows:

$$\frac{\partial y}{\partial \xi}(\eta) = \sum_{i=1}^8 \frac{\partial N_i}{\partial \xi}(\xi, \eta) \cdot y_i \quad (\text{C.29})$$

$$\frac{\partial y}{\partial \eta}(\xi) = \sum_{i=1}^8 \frac{\partial N_i}{\partial \eta}(\xi, \eta) \cdot y_i \quad (\text{C.30})$$

Using Eqs.C.19 to C.22 into the Eq.C.19 one can calculate Jacobian as a function of local coordinates (Gaussian point). Then using the value of Jacobian and Eqs.C.23 and C.24 with Eqs.C.29 and C.30, one can calculate the area integral as a function of local coordinates.

C.8: Half reservoir model and space discretization

In this study, due to the asymmetrical nature of arbitrary oriented natural fracture quarter model cannot be used. In order to take advantage of symmetry the problem is solved on a half model with a natural fracture.

In this half model all through 4-nodded and 8-nodded square elements are used except the end point of natural fracture. In order to represent the shape of natural fracture two triangular elements are implemented at two corners (Near end tip and far end tip of the natural fracture) of natural fracture. For this purpose 3-nodded and 6-nodded triangular element transformations are used.

Starting the node numbering with the bottom right hand corner and working anticlockwise around the element and using local coordinates the three nodded triangular elements are shown in **Fig.C.7**.

The shape functions are specified in terms of local coordinates, the origin being at the centroid of the element. The shape functions in terms of the local coordinates are:

$$N_1(\xi, \eta) = \left(\frac{1}{3}\right)(1 + 2\xi) \quad (\text{C.31a})$$

$$N_2(\xi, \eta) = \left(\frac{1}{3}\right)(1 - \xi - \sqrt{3}\eta) \quad (\text{C.31b})$$

$$N_3(\xi, \eta) = \left(\frac{1}{3}\right)(1 - \xi + \sqrt{3}\eta) \quad (\text{C.31b})$$

Differentiating Eq.C.31 the derivatives of shape functions with respect to local coordinates as functions of local coordinates can be written as follows:

$$\frac{\partial N_1}{\partial \xi}(\xi, \eta) = \left(\frac{2}{3}\right) \quad (\text{C.32a})$$

$$\frac{\partial N_2}{\partial \xi}(\xi, \eta) = \frac{1}{3} \quad (\text{C.32b})$$

$$\frac{\partial N_3}{\partial \xi}(\xi, \eta) = -\frac{1}{3} \quad (\text{C.32c})$$

$$\frac{\partial N_1}{\partial \eta}(\xi, \eta) = 0 \quad (\text{C.32d})$$

$$\frac{\partial N_2}{\partial \eta}(\xi, \eta) = -\frac{1}{\sqrt{3}} \quad (\text{C.32e})$$

$$\frac{\partial N_3}{\partial \eta}(\xi, \eta) = \frac{1}{\sqrt{3}} \quad (\text{C.32f})$$

Using the mapping of a four noded square in local coordinates (ξ, η) onto an arbitrary four noded quadrilateral in global coordinates (x, y) leads to the following relationships for the element:

$$x = \sum_{i=1}^3 N_i \cdot x_i \quad (\text{C.33})$$

$$y = \sum_{i=1}^3 N_i \cdot y_i \quad (\text{C.34})$$

where the shape functions N_1 to N_3 are given by the Eq.C.31

Differentiating Eq.C.17 and using Eqs.C.31 and C.32 one can write the derivatives of the x coordinate with respect to the local coordinates as follows:

$$\frac{\partial x}{\partial \xi}(\eta) = \sum_{i=1}^3 \frac{\partial N_i}{\partial \xi} \cdot x_i \quad (\text{C.35})$$

$$\frac{\partial x}{\partial \eta}(\xi) = \sum_{i=1}^3 \frac{\partial N_i}{\partial \eta} \cdot x_i \quad (\text{C.36})$$

C.9: Super convergent patch recovery

Patch is a group of elements that belong to a corner node that is not on the boundary of the mesh. The general patch configuration is presented in the **Fig.C.8**. Using the known gradient at each super convergent point within the patch, the SPR method fits a polynomial to these points in a least squares manner. This polynomial is then used to determine the gradient at the nodes. If possible the gradients are found using interior patches. Thus, the gradient for the corner nodes is determined from one patch and for a side node the gradient is found using two patches and taking an average. In this study the gradient to be recovered are $\left(\frac{\partial u_x}{\partial x}\right)$,

$$\left(\frac{\partial u_y}{\partial x}\right), \left(\frac{\partial u_x}{\partial y}\right) \text{ and } \left(\frac{\partial u_y}{\partial y}\right).$$

Let ∂u be any one of these gradients. The procedure to calculate the gradient at a node ∂u^* from the gradient at the super convergent points is as follows.

For each super convergent point (s_{ki}, y_{ak}) one can determine the matrix, \vec{M}_k as follows:

$$\vec{M}_k = \begin{pmatrix} 1 & x_k & y_k & x_k \cdot y_k & x_k^2 & y_k^2 \end{pmatrix} \quad (\text{C.31})$$

where k is the number of super convergent point and (s_{ki}, y_{ak}) is the coordinate of these points.

Then for a patch containing “n” super convergent points one can determine the matrix, \vec{A}_k and vector \vec{X}_k as follows:

$$\vec{A}_k = \sum_{k=1}^n \left(\vec{M}_k^T \cdot \vec{M}_k \right) \quad (\text{C.32})$$

$$\vec{X}_k = \sum_{k=1}^n \left(\vec{M}_k^T \cdot \partial u_k \right) \quad (\text{C.33})$$

where (∂u_k) is the gradient at the super convergent point “k”.

Then the linear system can be solved using the following equation:

$$\vec{A}_k \cdot \vec{a} = \vec{X}_k \quad (\text{C.33})$$

Then the gradient at the node is:

$$\partial u^* = \left(1 \quad x^* \quad y^* \quad x^* \cdot y^* \quad x^{*2} \quad y^{*2} \right) \cdot \vec{a} \quad (\text{C.34})$$

where the coordinate of the node is (x^*, y^*) .

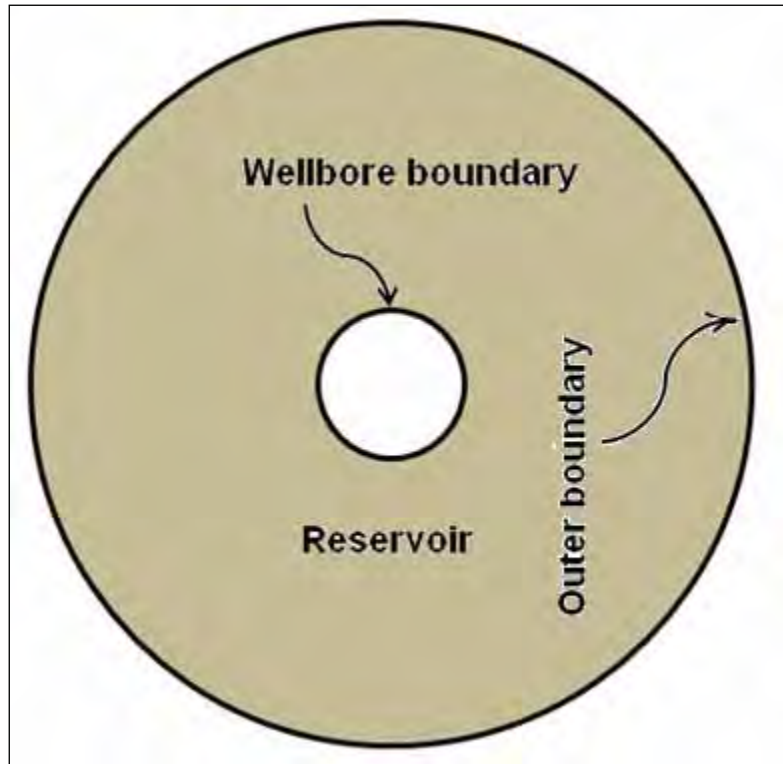


Fig.

C.1 Intact

wellbore reservoir model.

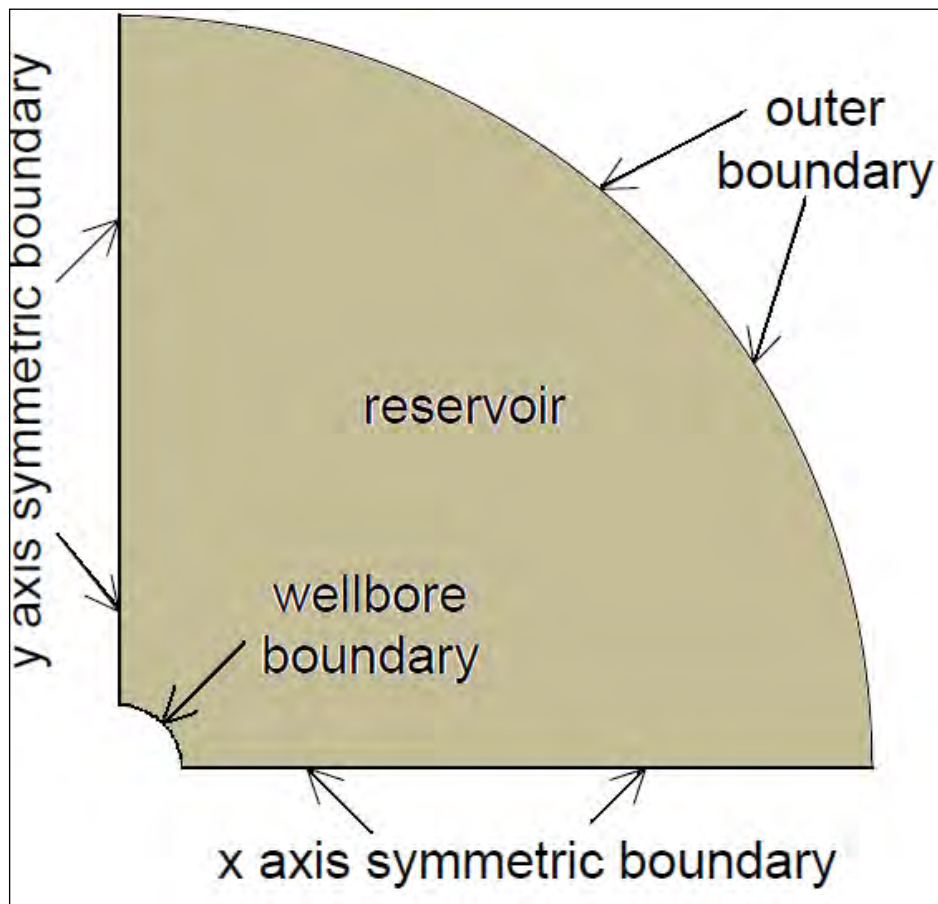


Fig.

C.2 Quarter reservoir model

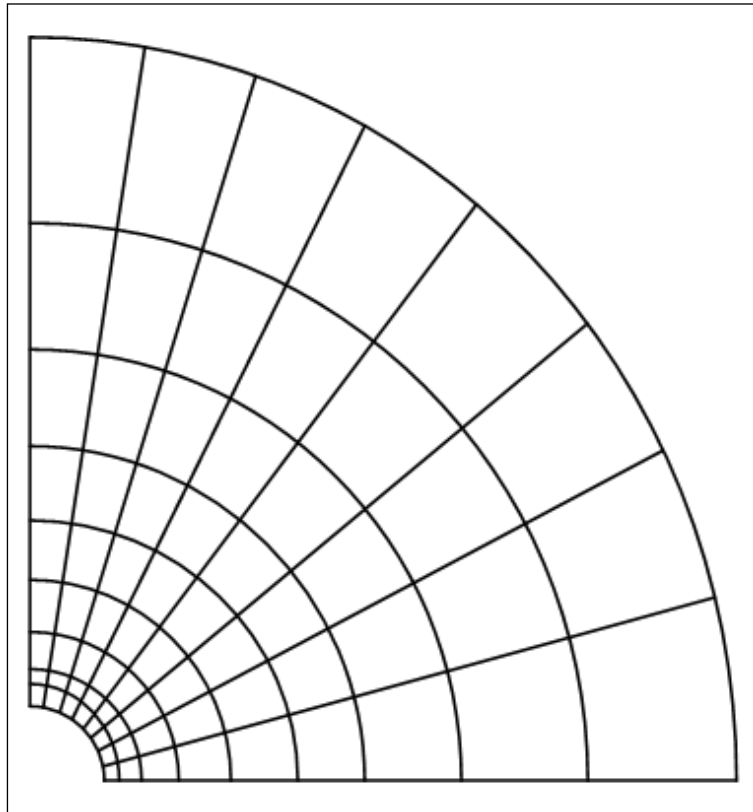


Fig. C.3 Schematic of the mesh of the Quarter model

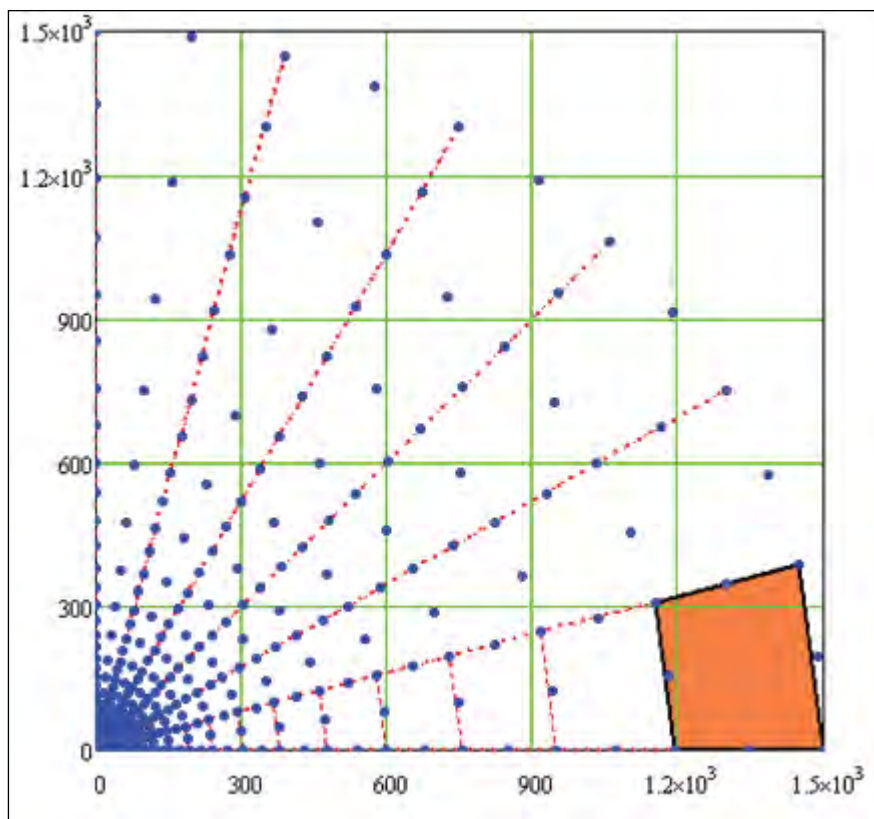
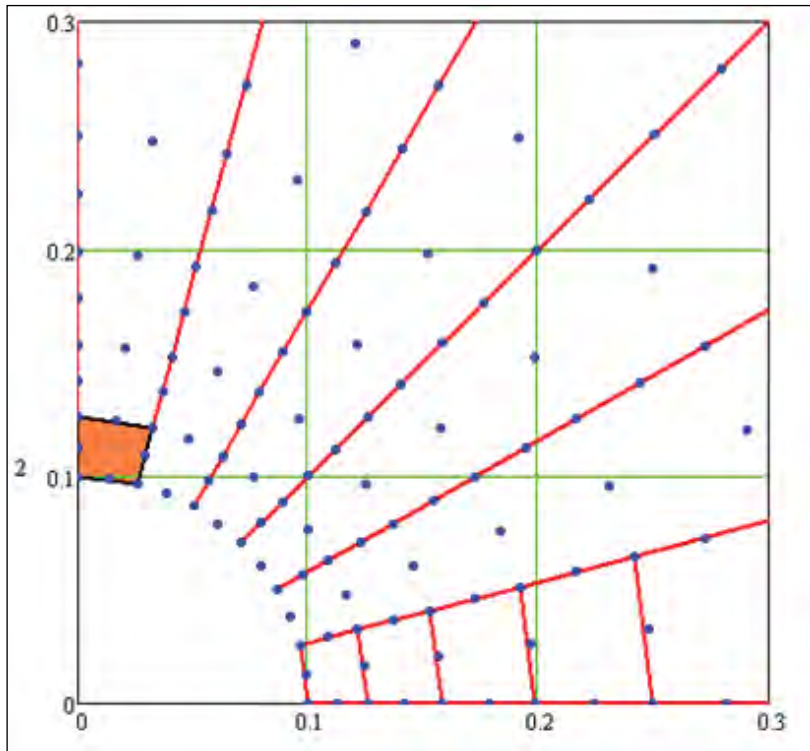


Fig. C.4 (a) Exact mesh of the Quarter model, wellbore radius is 0.1 m, outer boundary radius 1500 m, first element showing in coloured.



**Fig. C.4 (b) Exact mesh of the Quarter model zoom in from 0 meter to 0.3 meter.
Last number of element showing in coloured.**

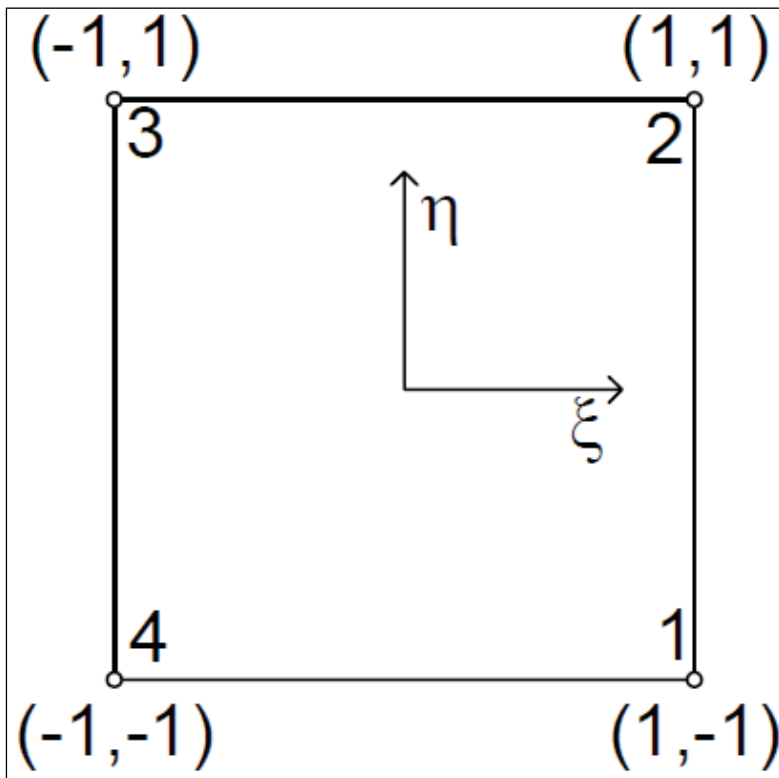


Fig. C.5 Four noded square element with local coordinates.

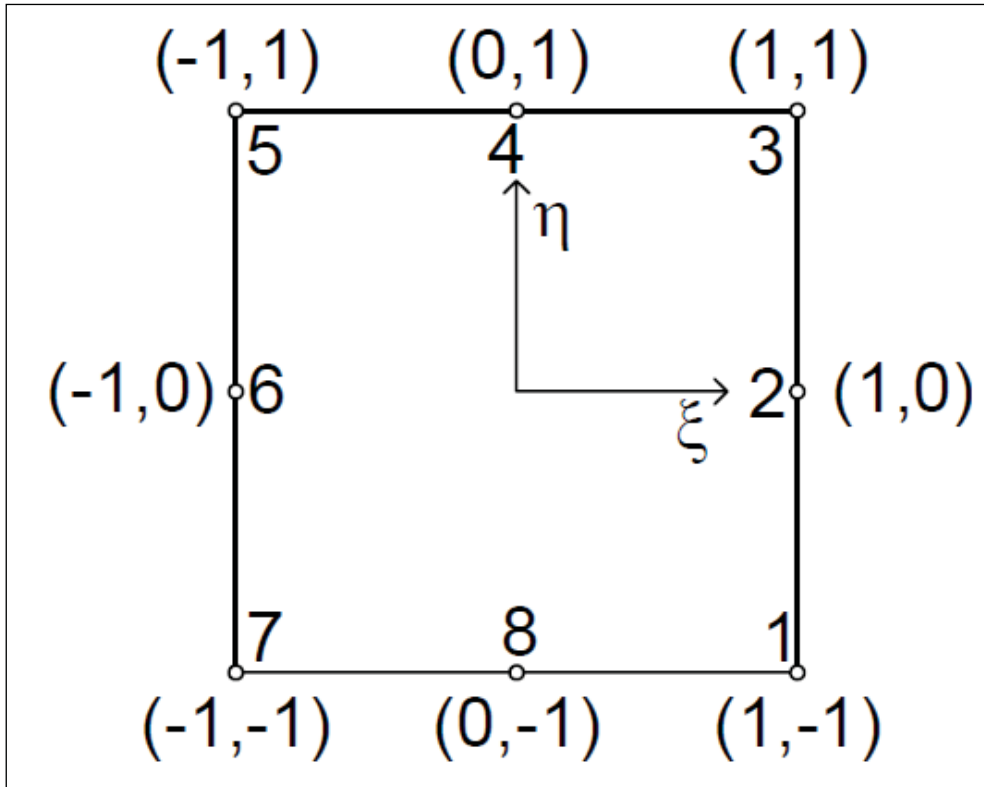


Fig. C.6 Eight noded square element with local coordinates.

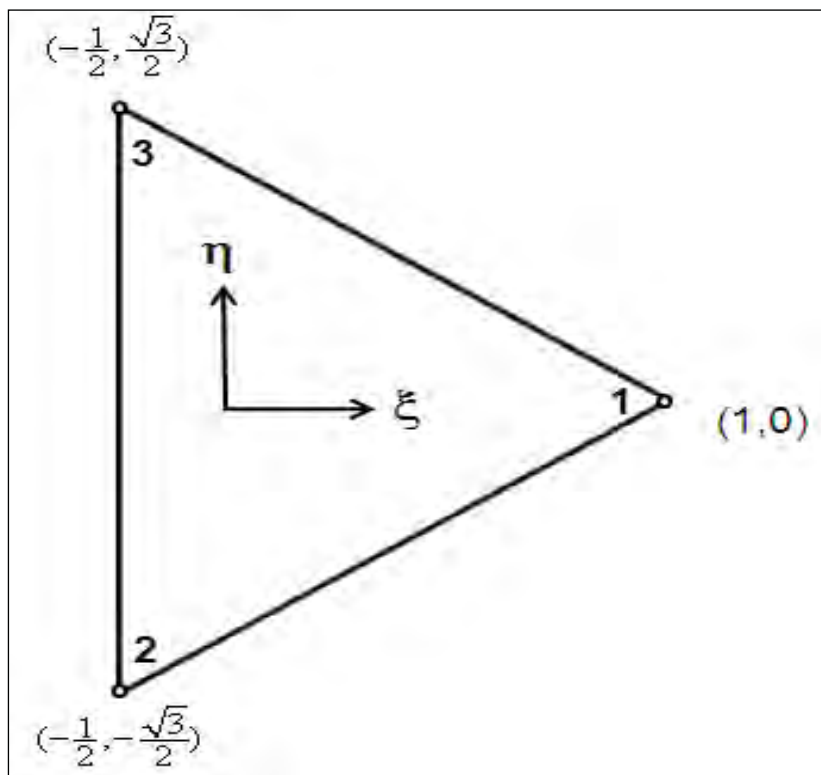


Fig. C.7 Three noded triangular element with local coordinates

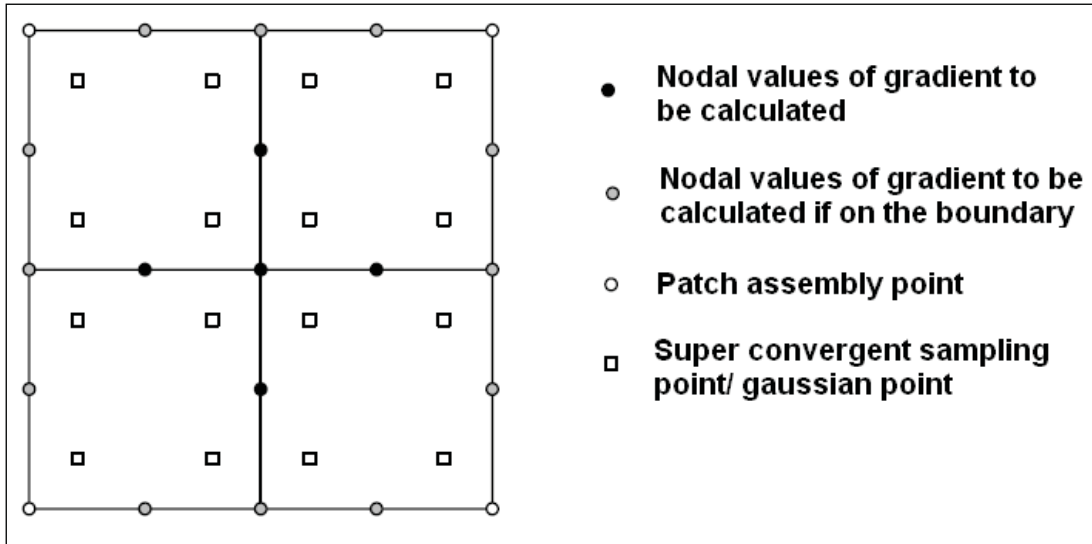


Fig. C.8 Schematic of a patch for eight noded square elements.

Appendix-2D: Implementation of Finite Element Method (FEM) for Governing Equations of Poroelasticity.

In this study, poroelastic equations are numerically solved by using the finite element formulation for space discretisation and the implicit finite difference method for time discretisation. For each time step, a system of linear equations is constructed which is solved using a standard FORTRAN routine. The finite element method used is the widely used Galerkin method, a weighted residuals approach. The essential or forced boundary conditions are applied using the method of elimination. In this section detailed formulation of the FEM is presented.

D.1: Fully Coupled Poroelastic FEM Formulation

Assuming off-diagonal components of permeability tensor are zero $\vec{k} = \begin{pmatrix} k_x & 0 \\ 0 & k_y \end{pmatrix}$,

Eq.2.2 is expanded by introducing k as:

$$\phi c_t \frac{\partial p}{\partial t} - \alpha \frac{\partial}{\partial t} \left(\frac{\partial}{\partial x} \frac{\partial}{\partial y} \right) \vec{u} = \frac{\partial}{\partial x} \left(\frac{k_x}{\mu} \frac{\partial p}{\partial x} \right) + \frac{\partial}{\partial y} \left(\frac{k_y}{\mu} \frac{\partial p}{\partial y} \right) \quad (D.1)$$

Multiplying both sides of Eq.D.1 by a trial function, w and integrating over the domain, Q yields:

$$\int_{\Omega} \left(w c_t \phi \frac{\partial p}{\partial t} \right) d\Omega - \int_{\Omega} \left[w \alpha \frac{\partial}{\partial t} \left(\frac{\partial}{\partial x} \frac{\partial}{\partial y} \right) \vec{u} \right] d\Omega = \int_{\Omega} w \left(\frac{\partial}{\partial x} \left(\frac{k_x}{\mu} \frac{\partial p}{\partial x} \right) + \left(\frac{k_y}{\mu} \frac{\partial}{\partial y} \right) \right) d\Omega \quad (D.2)$$

Using the Green formulae, Eq.D.2 becomes:

$$\int_{\Omega} \left(w c_t \phi \frac{\partial p}{\partial t} \right) d\Omega + \int_{\Omega} \frac{\partial w}{\partial x} \left(\frac{k_x}{\mu} \frac{\partial p}{\partial x} \right) d\Omega + \int_{\Omega} \frac{\partial w}{\partial y} \left(\frac{k_y}{\mu} \frac{\partial p}{\partial y} \right) d\Omega = \oint_{\Gamma} w \left(\frac{k_x}{\mu} \frac{\partial p}{\partial x} n_x + \frac{k_y}{\mu} \frac{\partial p}{\partial y} n_y \right) d\Gamma + \int_{\Omega} \left[w \alpha \frac{\partial}{\partial t} \left(\frac{\partial}{\partial x} \frac{\partial}{\partial y} \right) \vec{u} \right] d\Omega \quad (D.3)$$

where ‘ Γ ’ is the boundary and ‘n’ is the outward normal to the boundary. The boundary integral can be eliminated from the formulation for no flow boundaries and

boundaries with constant pressure. It is also assumed that porosity and permeability have no considerable change over each time step. After rearranging, Eq.D.3 becomes:

$$\begin{aligned} & \int_{\Omega} \left(w c_t^{i-1} \phi^{i-1} \frac{p^i - p^{i-1}}{\Delta t^i} \right) d\Omega + \int_{\Omega} \frac{\partial w}{\partial x} \left(\frac{k_x^{i-1}}{\mu} \frac{\partial p^i}{\partial x} \right) d\Omega + \\ & \int_{\Omega} \frac{\partial w}{\partial y} \left(\frac{k_y^{i-1}}{\mu} \frac{\partial p^i}{\partial y} \right) d\Omega = \int_{\Omega} \left[w \alpha \left(\frac{\partial}{\partial x} \frac{\partial}{\partial y} \right) \frac{\vec{u}^i - \vec{u}^{i-1}}{\Delta t^i} \right] d\Omega \end{aligned} \quad (D.4)$$

in which ‘i’ and ‘i-1’ are current and previous times respectively. Using Galerkin method (Zienkiewicz and Taylor, 2000), Eq.D.4 becomes:

$$\begin{aligned} & \left[\int_{\Omega} c_t \phi^i \vec{N}_p^T \vec{N}_p d\Omega \right] \frac{\vec{P}^i - \vec{P}^{i-1}}{\Delta t^i} + \left[\int_{\Omega} \left(\frac{k_x^{i-1}}{\mu^{i-1}} \frac{\partial \vec{N}_p^T}{\partial x} \frac{\partial \vec{N}_p}{\partial x} + \frac{k_y^{i-1}}{\mu^{i-1}} \frac{\partial \vec{N}_p^T}{\partial y} \frac{\partial \vec{N}_p}{\partial y} \right) d\Omega \right] \vec{P}^i \\ & \left(\int_{\Omega} \vec{N}_p^T \alpha \left(\frac{\partial}{\partial x} \frac{\partial}{\partial y} \right) d\Omega \right) \frac{\vec{U}^i - \vec{U}^{i-1}}{\Delta t^i} = 0 \end{aligned} \quad (D.5)$$

where:

$$\vec{P}^T = (p_1 \ p_2 \ \dots \ p_n) \quad (D.6)$$

$$\vec{N}_p^T = (N_1 \ N_2 \ \dots \ N_n) \quad (D.7)$$

$$\vec{N}_u = \begin{bmatrix} N_1 & 0 & N_2 & \dots & 0 \\ 0 & N_1 & 0 & \dots & N_n \end{bmatrix} \quad (D.8)$$

$$\vec{U}^T = (u_{x1} \ u_{y1} \ u_{x2} \ \dots \ u_{xn} \ u_{yn}) \quad (D.9)$$

and the numbered subscripts represent each node, “n” is the number of nodes and “N” is a basis/shape function. After rearrangement, Eq.D.5 can be written as:

$$\vec{M1} \left(\vec{p}^i - p^{i-1} \right) + \Delta t^i \vec{M2} \vec{p}^i - \vec{M3} \left(\vec{U}^i - U^{i-1} \right) = \vec{0} \quad (D.10)$$

where M is a mass matrix. With rearranging one can write:

$$\vec{M1} \left(\vec{p}^i - \vec{p}^{i-1} \right) + \Delta t^i \vec{M2} \left(\vec{p}^i - \vec{p}^{i-1} \right) - \vec{M3} \left(\vec{U}^i - U^{i-1} \right) = -\Delta t^i \vec{M2} \vec{p}^{i-1} \quad (D.11)$$

This can be written as:

$$\overrightarrow{\overrightarrow{M4}}\Delta P^i - \overrightarrow{\overrightarrow{M3}}\Delta U^i = \overrightarrow{f_1} \quad (\text{D.12})$$

Where

$$\Delta P^i = \overrightarrow{p}^i - \overrightarrow{p}^{i-1} \quad (\text{D.13})$$

$$\Delta U^i = \overrightarrow{U}^i - \overrightarrow{U}^{i-1} \quad (\text{D.14})$$

$$\overrightarrow{\overrightarrow{M4}} = \overrightarrow{\overrightarrow{M1}} + \Delta t^i \overrightarrow{\overrightarrow{M2}} \quad (\text{D.15})$$

$$\overrightarrow{f_1} = -\Delta t^i \overrightarrow{\overrightarrow{M2}} \overrightarrow{p}^{i-1} \quad (\text{D.16})$$

The matrix M4 can be obtained from:

$$\overrightarrow{\overrightarrow{M4}} = \sum_{e=1}^{ne} \overrightarrow{\overrightarrow{M4}}^e = \sum_{e=1}^{ne} \left(\overrightarrow{\overrightarrow{M1}}^e + \Delta t^i \overrightarrow{\overrightarrow{M2}}^e \right) \quad (\text{D.17})$$

in which ‘e’ denotes element and ‘ne’ is the number of elements and

$$\overrightarrow{\overrightarrow{M1}} = \sum_{e=1}^{ne} \overrightarrow{\overrightarrow{M1}}^e \quad (\text{D.18})$$

$$\overrightarrow{\overrightarrow{M1}}^e = \int_{\Omega} \left(c_t^{i-1} \phi^{e^{i-1}} \overrightarrow{N}_p^T \overrightarrow{N}_p \right) d\Omega \quad (\text{D.19})$$

$$\overrightarrow{\overrightarrow{M2}} = \sum_{e=1}^{ne} \overrightarrow{\overrightarrow{M2}}^e \quad (\text{D.20})$$

$$\overrightarrow{\overrightarrow{M2}}^e = \int_{\Omega} \left(\frac{k_x^{e^{i-1}}}{\mu^{e^{i-1}}} \frac{\partial \overrightarrow{N}_p^e}{\partial x} \frac{\partial \overrightarrow{N}_p^e}{\partial x} + \frac{k_y^{e^{i-1}}}{\mu^{e^{i-1}}} \frac{\partial \overrightarrow{N}_p^e}{\partial y} \frac{\partial \overrightarrow{N}_p^e}{\partial y} \right) d\Omega \quad (\text{D.21})$$

$$\overrightarrow{\overrightarrow{M3}} = \sum_{e=1}^{ne} \overrightarrow{\overrightarrow{M3}}^e \quad (\text{D.20})$$

$$\overrightarrow{\overrightarrow{M3}}^e = \alpha \int_{\Omega} \overrightarrow{N}_p^{e^T} \left(\frac{\partial N_u^e}{\partial x} + \frac{\partial N_u^e}{\partial x} \right) d\Omega \quad (\text{D.21})$$

where for an eight noded element:

$$\overrightarrow{P}^{i-1^T} = \left(p_1^{i-1} \ p_2^{i-1} \ \dots \ p_8^{i-1} \right) \quad (\text{D.22})$$

$$\vec{N}_p^e = (N_1 \ N_2 \ \dots \ N_8) \quad (\text{D.23})$$

$$\vec{N}_u^e = \begin{bmatrix} N_1 & 0 & N_2 & \dots & 0 \\ 0 & N_1 & 0 & \dots & N_8 \end{bmatrix} \quad (\text{D.24})$$

All the integrations can be carried out numerically using the Gauss-Lagrandre integration technique. Eq.D.12 is called the poroelastic balance of fluid momentum equation and needs to be solved simultaneously with coupled equilibrium equation. Also for the coupled equilibrium equation multiplying Eq.B.30 by trial function and integrating over the domain Q leads to:

$$\int_{\Omega} \left(\vec{W}^T \overleftrightarrow{S}^T \overrightarrow{\Delta\sigma} \right) d\Omega = \vec{0} \quad (\text{D.25})$$

where:

$$\vec{W} = \begin{bmatrix} W_1(x,y) \\ W_2(x,y) \end{bmatrix} \quad (\text{D.26})$$

w_1 and w_2 are trial functions. Using Green's identity one can obtains:

$$\int_{\Gamma} \left(\vec{W}^T \overleftrightarrow{M}^T \overrightarrow{\Delta\sigma} \right) d\Gamma - \int_{\Omega} \overrightarrow{\Delta\sigma}^T \left(\overleftrightarrow{S} \vec{W} \right) d\Omega = \vec{0} \quad (\text{D.27})$$

where:

$$\overleftrightarrow{M}^T = \begin{bmatrix} n_x & \mathbf{0} & n_y \\ \mathbf{0} & n_y & n_x \end{bmatrix} \quad (\text{D.28})$$

After introducing **Eq.B.45** into Eq.D.27 and rearranging, one gets:

$$\int_{\Omega} \left(\overleftrightarrow{S} \vec{W} \right)^T \overleftrightarrow{D}_e \overleftrightarrow{S} \overrightarrow{\Delta U} d\Omega + \alpha \int_{\Omega} \left(\overleftrightarrow{S} \vec{W} \right) \overrightarrow{\Delta P}^i d\Omega = \int_{\Gamma} \left(\vec{W}^T \overleftrightarrow{M}^T \overrightarrow{\Delta\sigma}^i \right) d\Gamma \quad (\text{D.29})$$

Using Galerkin method Eq.D.29 yields:

$$\left(\int_{\Omega} \left(\overleftrightarrow{S} \vec{N}_u \right)^T \overleftrightarrow{D}_e \overleftrightarrow{S} \vec{N}_u d\Omega \right) \overrightarrow{\Delta U} + \alpha \left(\int_{\Omega} \left(\left(\frac{\partial \vec{N}_u}{\partial X} \frac{\partial \vec{N}_u}{\partial X} \right) \vec{N}_p \right)^T d\Omega \right) \overrightarrow{\Delta P}^i = \int_{\Gamma} \left(\vec{N}_u^T \overleftrightarrow{M}^T \overrightarrow{\Delta\sigma}^i \right) d\Gamma \quad (\text{D.30})$$

or in compact form:

$$\overrightarrow{\overrightarrow{M5}}\Delta U^i - \overrightarrow{\overrightarrow{M6}}\Delta P^i = \overrightarrow{f_2} \quad (\text{D.31})$$

where:

$$\overrightarrow{\overrightarrow{M5}} = \sum_{e=1}^{ne} \overrightarrow{\overrightarrow{M5^e}} \quad (\text{D.32})$$

$$\overrightarrow{\overrightarrow{M5^e}} = \int_{\Omega^e} \left(\overrightarrow{\overrightarrow{SN}}_u^e \right)^T \overrightarrow{\overrightarrow{D}}_e \overrightarrow{\overrightarrow{SN}}_u^e d\Omega \quad (\text{D.33})$$

$$\overrightarrow{\overrightarrow{M6}} = \sum_{e=1}^{ne} \overrightarrow{\overrightarrow{M6^e}} \quad (\text{D.34})$$

$$\overrightarrow{\overrightarrow{M6^e}} = \int_{\Omega^e} \alpha \left(\int_{\Omega^e} \left(\left(\frac{\partial \overrightarrow{N}_u}{\partial X} \frac{\partial \overrightarrow{N}_u}{\partial X} \right) \overrightarrow{N}_p \right)^T d\Omega \right) \quad (\text{D.35})$$

$$\overrightarrow{\overrightarrow{M6^e}} = \left(\overrightarrow{\overrightarrow{M3^e}} \right)^T \quad (\text{B.36})$$

Eqs.D.12 and D.35 are the final finite element equations to be simultaneously solved as a system of linear equations which is as follows:

$$\begin{bmatrix} \overrightarrow{\overrightarrow{M5}} & \overrightarrow{\overrightarrow{M6}} \\ \overrightarrow{\overrightarrow{-M3}} & \overrightarrow{\overrightarrow{M4}} \end{bmatrix} \begin{bmatrix} \Delta \overrightarrow{U}^i \\ \Delta \overrightarrow{P}^i \end{bmatrix} = \begin{bmatrix} \overrightarrow{f_2} \\ \overrightarrow{f_1} \end{bmatrix} \quad (\text{D.37})$$

Or

$$\begin{bmatrix} \overrightarrow{\overrightarrow{M5}} & \overrightarrow{\overrightarrow{M3}}^T \\ \overrightarrow{\overrightarrow{-M3}} & \overrightarrow{\overrightarrow{M4}} \end{bmatrix} \begin{bmatrix} \Delta \overrightarrow{U}^i \\ \Delta \overrightarrow{P}^i \end{bmatrix} = \begin{bmatrix} \overrightarrow{f_2} \\ \overrightarrow{f_1} \end{bmatrix} \quad (\text{D.38})$$

D.2: Rearrangement of element mass matrix to create a Banded Structure

Solving the linear system efficiently involves giving matrix in the Eq.D.37 a banded structure and minimizing the bandwidth. This allows it to be stored in banded storage and then solved with less computation time. Rearranging the formulation of Eq.D.37 involves reordering the unknowns and load vector. The unknowns (Δu_x , Δu_y and Δp) can be reordered so that the vector of unknowns becomes:

$$X_b^T = (\Delta u_{x_1}^b \ \Delta u_{y_1}^b \ \Delta p_1^b \ \Delta u_{x_2}^b \ \Delta u_{y_2}^b \ \Delta p_2^b \ \cdots \ \Delta p_n^b) \quad (D.39)$$

In a similar fashion one can reorder the load vector to be:

$$f_b^T = (f_{2_1}^b \ f_{2_2}^b \ f_{1_1}^b \ \cdots \ f_{2_{2n}}^b \ f_{1_n}^b) \quad (D.40)$$

It follows that the equation to solve becomes:

$$\overrightarrow{\overrightarrow{M}}_b \overrightarrow{X}_b = \overrightarrow{f}_b \quad (D.41)$$

where

$$\overrightarrow{\overrightarrow{M}}_b = \sum_{e=1}^{n^e} \overrightarrow{\overrightarrow{M}}_b^e \quad (D.42)$$

and

$$\overrightarrow{\overrightarrow{M}}_b^e = \begin{bmatrix} M 5_{1,1}^e & M 5_{1,2}^e & M 6_{1,1}^e & M 5_{1,3}^e & \cdots & M 5_{1,2n}^e & M 6_{1,n}^e \\ M 5_{2,1}^e & M 5_{2,2}^e & M 6_{2,1}^e & M 5_{2,3}^e & \cdots & M 5_{2,2n}^e & M 6_{2,n}^e \\ -M 3_{1,1}^e & -M 3_{1,2}^e & M 4_{1,1}^e & -M 3_{1,3}^e & \cdots & -M 3_{1,2n}^e & M 4_{1,n}^e \\ M 5_{3,1}^e & M 5_{3,2}^e & M 6_{3,1}^e & -M 5_{3,3}^e & \cdots & M 5_{3,2n}^e & M 6_{3,n}^e \\ \vdots & \vdots & \vdots & \vdots & \ddots & \vdots & \vdots \\ M 5_{2n,1}^e & M 5_{2n,2}^e & M 6_{2n,1}^e & M 5_{2n,3}^e & \cdots & M 5_{2n,2n}^e & M 6_{2n,n}^e \\ -M 3_{n,1}^e & -M 3_{n,2}^e & M 4_{n,1}^e & -M 3_{n,3}^e & \cdots & -M 3_{n,2n}^e & M 4_{n,n}^e \end{bmatrix} \quad (D.43)$$

D.3: Rearrangement of element mass matrix for 4 and 8-noded pressure

Solving the fully couple poroelastic linear system equation involves matrix in the Eq. D.37. In general 8-noded elements are used for both displacement and pressure. But 8-noded pressure formulation is not always stable. For that reason to make the model stable and more reliable 8-noded displacement and 4-noded pressure are used in this model. So the formulation of element mass matrix is different. In this section the formulation of element mass matrix for both cases 1) 8-noded displacement and pressure $\overrightarrow{\overrightarrow{M}}_{8ND-8NP}$ and 2) 8-noded displacement and 4-noded pressure $\overrightarrow{\overrightarrow{M}}_{8ND-4NP}$ is presented.

Formulation of element mass matrix for 8-noded displacement and pressure.

The matrix M5 in the eq.D.37 represents the coefficient matrix for the deformation and the dimension of the matrix is (npE*DOF × npE*DOF) i.e. (16×16) as the degree of freedom is 2(here npE = node per element, DOF = degree of freedom is). So M5 can be written as follows:

$$\overrightarrow{\overrightarrow{M5^e}} = \begin{bmatrix} E_{1,1} & E_{1,2} & E_{1,3} & E_{1,4} & \cdots & E_{1,15} & E_{1,16} \\ E_{2,1} & E_{2,2} & E_{2,3} & E_{2,4} & \cdots & E_{2,15} & E_{2,16} \\ E_{3,1} & E_{3,2} & E_{3,3} & E_{3,4} & \cdots & E_{3,15} & E_{2,16} \\ E_{4,1} & E_{4,2} & E_{4,3} & E_{3,4} & \cdots & E_{4,15} & E_{2,16} \\ \vdots & \vdots & \vdots & \vdots & \ddots & \vdots & \vdots \\ E_{15,1} & E_{15,2} & E_{15,3} & E_{15,4} & \cdots & E_{15,15} & E_{15,16} \\ E_{16,1} & E_{16,2} & E_{16,3} & E_{16,4} & \cdots & E_{16,15} & E_{16,16} \end{bmatrix} \quad (D.44)$$

Similarly the matrix M4 in the Eq.D.37 represents the coefficient matrix for the pressure and the dimension of the matrix is (node per element x node per element) i.e. (8×8) as the degree of freedom is 1 and can be written as follows:

$$\overrightarrow{\overrightarrow{M4^e}} = \begin{bmatrix} E_{1,1} & E_{1,2} & E_{1,3} & E_{1,4} & E_{1,5} & E_{1,6} & E_{1,7} & E_{1,8} \\ E_{2,1} & E_{2,2} & E_{2,3} & E_{2,4} & E_{2,5} & E_{2,6} & E_{2,7} & E_{2,8} \\ E_{3,1} & E_{3,2} & E_{3,3} & E_{3,4} & E_{3,5} & E_{3,6} & E_{3,7} & E_{3,8} \\ E_{4,1} & E_{4,2} & E_{4,3} & E_{4,4} & E_{4,5} & E_{4,6} & E_{4,7} & E_{4,8} \\ E_{5,1} & E_{5,2} & E_{5,3} & E_{5,4} & E_{5,5} & E_{5,6} & E_{5,7} & E_{5,8} \\ E_{6,1} & E_{6,2} & E_{6,3} & E_{6,4} & E_{6,5} & E_{6,6} & E_{6,7} & E_{6,8} \\ E_{7,1} & E_{7,2} & E_{7,3} & E_{7,4} & E_{7,5} & E_{7,6} & E_{7,7} & E_{7,8} \\ E_{8,1} & E_{8,2} & E_{8,3} & E_{8,4} & E_{8,5} & E_{8,6} & E_{8,7} & E_{8,8} \end{bmatrix} \quad (D.45)$$

where $E_{i,j}$ are the component of the matrices.

Matrix M3 has the coupling term and the dimension of this matrix is (8×16). M6 is the transpose of M3 hence the dimension is (16×8) and can be written as follows:

$$\overline{\overline{M3^e}} = \begin{bmatrix} E_{1,1} & E_{1,2} & E_{1,3} & E_{1,4} & \cdots & E_{1,15} & E_{1,16} \\ E_{2,1} & E_{2,2} & E_{2,3} & E_{2,4} & \cdots & E_{2,15} & E_{2,16} \\ E_{3,1} & E_{3,2} & E_{3,3} & E_{3,4} & \cdots & E_{3,15} & E_{3,16} \\ E_{4,1} & E_{4,2} & E_{4,3} & E_{4,4} & \cdots & E_{4,15} & E_{4,16} \\ \vdots & \vdots & \vdots & \vdots & \ddots & \vdots & \vdots \\ E_{7,1} & E_{7,2} & E_{7,3} & E_{7,4} & \cdots & E_{7,15} & E_{7,16} \\ E_{8,1} & E_{8,2} & E_{8,3} & E_{8,4} & \cdots & E_{8,15} & E_{8,16} \end{bmatrix} \quad (D.46)$$

and

$$\overline{\overline{M6^e}} = \begin{bmatrix} E_{1,1} & E_{1,2} & E_{1,3} & E_{1,4} & \cdots & E_{1,7} & E_{1,8} \\ E_{2,1} & E_{2,2} & E_{2,3} & E_{2,4} & \cdots & E_{2,7} & E_{2,8} \\ E_{3,1} & E_{3,2} & E_{3,3} & E_{3,4} & \cdots & E_{3,7} & E_{2,8} \\ E_{4,1} & E_{4,2} & E_{4,3} & E_{3,4} & \cdots & E_{4,7} & E_{2,8} \\ \vdots & \vdots & \vdots & \vdots & \ddots & \vdots & \vdots \\ E_{15,1} & E_{15,2} & E_{15,3} & E_{15,4} & \cdots & E_{15,7} & E_{15,8} \\ E_{16,1} & E_{16,2} & E_{16,3} & E_{16,4} & \cdots & E_{16,7} & E_{16,8} \end{bmatrix} \quad (D.47)$$

So the dimension of the elemental mass matrix $\overline{\overline{M_{8ND-8NP}}}$ is (24×24) and can be written as:

$$\overline{\overline{M_{8ND-8NP}}} = \begin{bmatrix} M5_{1,1} & \cdots & \cdots & M5_{1,16} & M6_{1,1} & \cdots & \cdots & \cdots & M6_{1,8} \\ \vdots & \ddots & \ddots & \vdots & \vdots & \ddots & \vdots & \ddots & \vdots \\ \vdots & \ddots & \ddots & \vdots & \vdots & \vdots & \ddots & \vdots & \vdots \\ \vdots & \cdots & \cdots & \vdots & \vdots & \ddots & \vdots & \ddots & \vdots \\ M5_{16,1} & \cdots & \cdots & M5_{16,16} & M6_{16,1} & \cdots & \cdots & \cdots & M6_{16,8} \\ M3_{1,1} & \cdots & \cdots & M3_{1,16} & M4_{1,1} & \cdots & \cdots & \cdots & M4_{1,8} \\ \vdots & \ddots & \ddots & \vdots & \vdots & \ddots & \cdots & \ddots & \vdots \\ \vdots & \ddots & \ddots & \vdots & \vdots & \ddots & \cdots & \ddots & \vdots \\ M3_{8,1} & \cdots & \cdots & M3_{8,16} & M4_{8,1} & \cdots & \cdots & \cdots & M4_{8,8} \end{bmatrix} \quad (D.48)$$

Formulation of element mass matrix to create the structure for 8-noded displacement and 4-noded pressure.

In this case dimension of matrix M5 is same and can be defined as Eq.D.44. As 4-

noded pressure element is used so the dimension of the matrix M4 would be (4×4) and can be presented as:

$$\overrightarrow{\overrightarrow{M4^e}} = \begin{bmatrix} E_{1,1} & E_{1,2} & E_{1,3} & E_{1,4} \\ E_{2,1} & E_{2,2} & E_{2,3} & E_{2,4} \\ E_{3,1} & E_{3,2} & E_{2,3} & E_{3,4} \\ E_{4,1} & E_{3,2} & E_{4,3} & E_{4,4} \end{bmatrix} \quad (D.49)$$

Matrix M3 has the coupling term and the dimension of this matrix is (4×16). M6 is the transpose of M3 hence the dimension is (16×4) and can be written as follows:

$$\overrightarrow{\overrightarrow{M3^e}} = \begin{bmatrix} E_{1,1} & E_{1,2} & E_{1,3} & \cdots & \cdots & \cdots & E_{1,15} & E_{1,16} \\ E_{2,1} & E_{2,2} & E_{2,3} & \cdots & \cdots & \cdots & E_{2,15} & E_{2,16} \\ E_{3,1} & E_{3,2} & E_{3,3} & \cdots & \cdots & \cdots & E_{3,15} & E_{3,16} \\ E_{4,1} & E_{4,2} & E_{4,3} & \cdots & \cdots & \cdots & E_{4,15} & E_{4,16} \end{bmatrix} \quad (D.50)$$

and

$$\overrightarrow{\overrightarrow{M6^e}} = \begin{bmatrix} E_{1,1} & E_{1,2} & E_{1,3} & E_{1,4} \\ E_{2,1} & E_{2,2} & E_{2,3} & E_{2,4} \\ E_{3,1} & E_{3,2} & E_{3,3} & E_{3,4} \\ E_{4,1} & E_{4,2} & E_{4,3} & E_{4,4} \\ \vdots & \vdots & \vdots & \vdots \\ \vdots & \vdots & \vdots & \vdots \\ E_{15,1} & E_{15,2} & E_{15,3} & E_{15,4} \\ E_{16,1} & E_{16,2} & E_{16,3} & E_{16,4} \end{bmatrix} \quad (D.51)$$

So the dimension of the elemental mass matrix $\overrightarrow{\overrightarrow{M_{8ND-4NP}}}$ is (20×20) and can be written as:

$$\overrightarrow{\overrightarrow{M_{8ND-4NP}}} = \begin{bmatrix} M5_{1,1} & \cdots & \cdots & M5_{1,16} & M6_{1,1} & M6_{1,2} & M6_{1,3} & M6_{1,4} \\ \vdots & \ddots & \ddots & \vdots & \vdots & \vdots & \vdots & \vdots \\ \vdots & \ddots & \ddots & \vdots & \vdots & \vdots & \vdots & \vdots \\ M5_{4,16} & \cdots & \cdots & M5_{16,16} & M6_{16,1} & M6_{16,2} & M6_{16,3} & M5_{16,4} \\ M3_{1,1} & M3_{1,2} & \cdots & M3_{1,16} & M4_{1,1} & M4_{1,2} & M4_{1,3} & M4_{1,4} \\ M3_{2,1} & \cdots & \cdots & M3_{2,16} & M4_{2,1} & M4_{2,2} & M4_{2,3} & M4_{2,4} \\ M3_{3,1} & \cdots & \cdots & M3_{3,16} & M4_{3,1} & M4_{3,2} & M4_{3,3} & M4_{3,4} \\ M3_{4,1} & M3_{4,2} & \cdots & M3_{4,16} & M4_{4,1} & M4_{4,2} & M4_{4,3} & M4_{4,4} \end{bmatrix} \quad (D.52)$$

Appendix-2E: Fluid flow, Elastic and Poroelastic Analytical Solutions for Intact Wellbore

In this section various elastic and poroelastic analytical solutions for pressure, deformation and stresses are presented. These solutions are utilized to verify the accuracy of computed numerical results of poroelastic phenomenon as well as to calculate initial values for pressure, displacement and stress. These initial values are used to initialize the numerical model of poroelasticity. All the problems in this section are solved based on following assumptions:

- Rock is porous, homogenous with isotropic properties.
- The rock skeleton behaves as a linear elastic material under plane strain condition.
- Fluid is single phase and is slightly compressible.
- The rock properties are not influenced by change in pressure and displacement in both space and time increment.
- Principal stresses are oriented in the direction of Cartesian coordinates with maximum and minimum horizontal stress along X and Y axes respectively.
- Vertical wellbore intercepts the horizontal layer of reservoir wherever appropriate.
- Sign convention is same as that used in traditional rock mechanics where compressive stress, strain and pressure are positive, tensile negative.
- Outward displacement is taken as positive and inward negative.

E.1: Elastic deformation of a pressurized wellbore in a dry rock subjected to isotropic horizontal stress at finite outer boundary (Pressurized hollow cylinder)

Schematic of the problem is illustrated in **Fig.E.1** where r_w = inner/wellbore boundary radius, r_e = outer boundary radius, p_w = wellbore pressure, and p = pore pressure set to be zero as the rock is dry. Magnitudes of maximum and minimum horizontal stresses are same and equal to σ_h .

Analytical solutions for this pressurized hollow cylinder are as follows (Jaeger and Cook, 1969):

• **Radial displacement:**

$$u_r(r) = \frac{\sigma_h}{2 \cdot (\lambda + G)} \cdot r + \frac{\sigma_h - P_w}{2G} \cdot \frac{R_w^2}{r} \quad (\text{E.1})$$

The second term of the right hand side, which is often called well convergence, gives displacement due to placing a well whereas the first term of the right hand side is the displacement caused by the in situ stress before drilling.

• **Tangential displacement:**

$$u_\theta(r) = 0 \quad (\text{E.2})$$

• **Pore pressure:**

$$p = 0 \quad (\text{E.3})$$

• **Radial stress:**

$$\sigma_{rr}(r) = \frac{\sigma_h r_e^2 - P_w r_w^2}{r_e^2 - r_w^2} - (\sigma_h - P_w) \cdot \frac{r_w^2}{r^2} \cdot \frac{r_e^2}{r_e^2 - r_w^2} \quad (\text{E.4})$$

• **Tangential stress:**

$$\sigma_{\theta\theta}(r) = \sigma_{\theta\theta}(r) = \frac{\sigma_h r_e^2 - P_w r_w^2}{r_e^2 - r_w^2} + (\sigma_h - P_w) \cdot \frac{r_w^2}{r^2} \cdot \frac{r_e^2}{r_e^2 - r_w^2} \quad (\text{E.5})$$

• **Shear stress:**

$$\sigma_{r\theta}(r) = 0 \quad (\text{E.6})$$

E.2: Elastic deformation of a pressurized wellbore in an unstressed dry rock

Schematic of the problem is illustrated in **Fig.E.2** where r_w = inner/wellbore boundary radius, r_e = outer boundary radius, p_w = wellbore pressure, and p = pore pressure set to zero as the rock is dry. Magnitudes of maximum (σ_H) and minimum horizontal stresses (σ_h) are also equal to zero as the rock is unstressed.

Analytical solutions for this pressurized wellbore in unstressed rock are as follows (Jaeger and Cook, 1969):

• **Radial displacement:**

$$u_r(r) = -\frac{p_w r_w^2}{2Gr} \quad (\text{E.7})$$

• **Tangential displacement:**

$$u_\theta(r) = 0 \quad (\text{E.8})$$

• **Pore pressure:**

$$p = 0 \quad (\text{E.9})$$

• **Radial stress:**

$$\sigma_{rr}(r) = \frac{p_w r_w^2}{r^2} \quad (\text{E.10})$$

• **Tangential stress:**

$$\sigma_{\theta\theta}(r) = -\frac{p_w r_w^2}{r^2} \quad (\text{E.11})$$

• **Shear stress:**

$$\sigma_{r\theta}(r) = 0 \quad (\text{E.12})$$

E.3: Elastic deformation of an intact dry rock subjected to anisotropic in situ horizontal stress

Schematic of the problem is illustrated in **Fig.E.3** where r_e =outer boundary radius, p =pore pressure set to zero as the rock is dry; σ_H = maximum horizontal stresses and σ_h = minimum horizontal stress. For an infinite plate subjected to a biaxial compressive state of stress shown in Fig.E.3, the state of stress at all point of the solid are as follows:

$$\sigma_{xx} = \sigma_H \quad (\text{E.13})$$

$$\sigma_{yy} = \sigma_h \quad (\text{E.14})$$

$$\sigma_{xy} = 0 \quad (\text{E.15})$$

Eqs. E.13- E.15 can be written in cylindrical coordinate as given in the followings:

• **Radial stress:**

$$\sigma_{rr}(r, \theta) = \frac{\sigma_H + \sigma_h}{2} + \frac{\sigma_H - \sigma_h}{2} \cos(2\theta) \quad (\text{E.16})$$

• **Tangential stress:**

$$\sigma_{\theta\theta}(r, \theta) = \frac{\sigma_H + \sigma_h}{2} - \frac{\sigma_H - \sigma_h}{2} \cos(2\theta) \quad (\text{E.17})$$

• **Shear stress:**

$$\sigma_{r\theta}(r, \theta) = -\frac{\sigma_H - \sigma_h}{2} \sin(2\theta) \quad (\text{E.18})$$

The components of displacement can be calculated using the Hook's law and the strain-displacement relationship.

• **Radial displacement:**

$$u_r(r, \theta) = \frac{r}{4G} \left[\frac{\sigma_H + \sigma_h}{2} (2 - 4\nu) + (\sigma_H - \sigma_h) \cos(2\theta) \right] \quad (\text{E.19})$$

• **Tangential displacement:**

$$u_\theta(r, \theta) = \frac{r}{4G} (\sigma_H - \sigma_h) \sin(2\theta) \quad (\text{E.20})$$

• **Pore pressure:**

$$p = 0 \quad (\text{E.21})$$

E.4: Elastic deformation of a pressurized wellbore in a dry rock subjected to isotropic in situ horizontal stress

Schematic of the problem is illustrated in **Fig.E.4** where r_w =inner/wellbore boundary radius, r_e =outer boundary radius set as infinity, p_w =wellbore pressure, and p =pore pressure set to be zero as the rock is dry. Magnitudes of maximum and minimum horizontal stresses are same and equal to σ_h .

• **Radial displacement:**

$$u_r(r) = \frac{\sigma_h}{2 \cdot (\lambda + G)} \cdot r + \frac{\sigma_h - P_w}{2G} \cdot \frac{R_w^2}{r} \quad (\text{E.22})$$

• **Tangential displacement:**

$$u_\theta(r) = 0 \quad (\text{E.23})$$

• **Pore pressure:**

$$p = 0 \quad (\text{E.24})$$

• **Radial stress:**

$$\sigma_{rr}(r) = \sigma_h \left(1 - \frac{r_w^2}{r^2} \right) + \frac{r_w^2}{r^2} P_w \quad (\text{E.25})$$

• **Tangential stress:**

$$\sigma_{\theta\theta}(r) = \sigma_h \left(1 + \frac{r_w^2}{r^2} \right) - \frac{r_w^2}{r^2} P_w \quad (\text{E.26})$$

• **Shear stress:**

$$\sigma_{r\theta}(r) = 0 \quad (\text{E.27})$$

E.5: Elastic deformation of a pressurized wellbore in a dry rock subjected to anisotropic in situ horizontal stress (Kirsh's Problem)

Schematic of the problem is illustrated in **Fig.E.5** where r_w =inner/wellbore boundary radius, r_e =outer boundary radius set as infinity, p_w =wellbore pressure, and p =pore pressure set to be zero as the rock is dry. σ_H = maximum horizontal stresses and σ_h = minimum horizontal stress. Analytical solutions are given for zero time (initial state) when fluid is yet to flow. They are as follows (Jaeger and Cook, 1969):

• **Radial displacement:**

$$u_r(r, \theta) = \frac{r}{4G} (\sigma_H + \sigma_h) \left(1 - 2\nu + \frac{r_w^2}{r^2} \right) + \frac{r}{4G} (\sigma_H - \sigma_h) \left(\frac{r_w^2}{r^2} \left(4 - 4\nu - \frac{r_w^2}{r^2} \right) + 1 \right) \cos(2\theta) - \frac{P_w}{2G} \frac{r_w^2}{r} \quad (\text{E.28})$$

• **Tangential displacement:**

$$u_{\theta}(r, \theta) = -\frac{r}{4G}(\sigma_H - \sigma_h) \left(\frac{r_w^2}{r^2} \left[2 - 4\nu + \frac{r_w^2}{r^2} \right] + 1 \right) \sin(2\theta) \quad (\text{E.29})$$

• **Pore pressure:**

$$p = 0 \quad (\text{E.30})$$

• **Radial stress:**

$$\sigma_{rr}(r, \theta) = \frac{\sigma_H + \sigma_h}{2} \left(1 - \frac{r_w^2}{r^2} \right) + \frac{\sigma_H + \sigma_h}{2} \left(1 + 3\frac{r_w^4}{r^4} - \frac{r_w^2}{r^2} \right) \cos(2\theta) + \frac{r_w^2}{r^2} p_w \quad (\text{E.31})$$

• **Tangential stress:**

$$\sigma_{\theta\theta}(r, \theta) = \frac{\sigma_H + \sigma_h}{2} \left(1 + \frac{r_w^2}{r^2} \right) - \frac{\sigma_H - \sigma_h}{2} \left(1 + 3\frac{r_w^4}{r^4} \right) \cos(2\theta) - \frac{r_w^2}{r^2} p_w \quad (\text{E.32})$$

• **Shear stress:**

$$\sigma_{r\theta}(r, \theta) = -\frac{\sigma_H - \sigma_h}{2} \left(1 - 3\frac{r_w^4}{r^4} + 2\frac{r_w^2}{r^2} \right) \sin(2\theta) \quad (\text{E.3})$$

3)

E.6: Elastic deformation of a pressurized wellbore in a drained rock subjected to anisotropic in situ horizontal stress (Kirsh's Problem)

Schematic of the problem is illustrated in **Fig.E.6** where r_w =inner/wellbore boundary radius, r_e =outer boundary radius set as infinity, p_w =wellbore pressure, and p =pore pressure set to be initial pressure p_i . σ_H = maximum horizontal stresses and σ_h = minimum horizontal stress.

This problem is a special case of Kirsh's problem in which the concept of effective stress is introduced (Charlez, 1991). Analytical solutions can be written as follows

• **Radial displacement:**

$$u_r(r, \theta) = \frac{r}{4G} (\sigma'_H + \sigma'_h) \left(1 - 2\nu + \frac{r_w^2}{r^2} \right) + \frac{r}{4G} (\sigma'_H - \sigma'_h) \left(\frac{r_w^2}{r^2} \left(4 - 4\nu - \frac{r_w^2}{r^2} \right) + 1 \right) \cos(2\theta) - \frac{p_w^2 r_w^2}{2G r} \quad (\text{E.34})$$

where

$$\text{Pore pressure, } p = p_r \quad (\text{E.35})$$

$$\text{Effective maximum horizontal stress, } \sigma'_H = \sigma_{H-} \alpha p_r \quad (\text{E.36})$$

$$\text{Effective minimum horizontal stress, } \sigma'_h = \sigma_{h-} \alpha p_r \quad (\text{E.37})$$

$$\text{Effective wellbore pressure, } p'_w = p_{w-} \alpha p_r \quad (\text{E.38})$$

and α =Biot's coefficient

• **Tangential displacement:**

$$u_\theta(r, \theta) = -\frac{r}{4G} (\sigma_H - \sigma_h) \left(\frac{r_w^2}{r^2} \left[2 - 4\nu + \frac{r_w^2}{r^2} \right] + 1 \right) \sin(2\theta) \quad (\text{E.39})$$

• **Radial stress:**

$$\sigma_{rr}(r, \theta) = \frac{\sigma_H + \sigma_h}{2} \left(1 - \frac{r_w^2}{r^2} \right) + \frac{\sigma_H - \sigma_h}{2} \left(1 + 3 \frac{r_w^4}{r^4} - 4 \frac{r_w^2}{r^2} \right) \cos(2\theta) + \frac{r_w^2}{r^2} p_w \quad (\text{E.40})$$

• **Tangential stress:**

$$\sigma_{\theta\theta}(r, \theta) = \frac{\sigma_H + \sigma_h}{2} \left(1 + \frac{r_w^2}{r^2} \right) - \frac{\sigma_H - \sigma_h}{2} \left(1 + 3 \frac{r_w^4}{r^4} \right) \cos(2\theta) - \frac{r_w^2}{r^2} p_w \quad (\text{E.41})$$

• **Shear stress:**

$$\sigma_{r\theta}(r, \theta) = -\frac{\sigma_H - \sigma_h}{2} \left(1 - 3 \frac{r_w^4}{r^4} + 2 \frac{r_w^2}{r^2} \right) \sin(2\theta) \quad (\text{E.42})$$

E.7: Poroelastic behavior of a pressurized wellbore (p_w) in an unstressed rock containing fluid at zero pressure

Schematic of the problem is illustrated in **Fig.E.7** where r_w = inner/wellbore boundary radius, r_e = outer boundary radius set as infinity, p_w = wellbore pressure, and p = pore

pressure initially it is zero and after that pressure is a function of time and space i.e. $p = p(t, r)$. Magnitudes of maximum (σ_H) and minimum horizontal stresses (σ_h) are also equal to zero as the rock is unstressed.

This is equivalent to mode 2 of poroelastic solution given by Detournay and Cheng (1988). It should be noted that here we use the modified analytical solution given by Aghighi (2008). Analytical solutions are as follows:

• **Radial displacement:**

$$u_r(r, t) = -\frac{p_w r_w^2}{2G r} - \frac{\eta}{G} r_w p_w h(r, t) \quad (\text{E.43})$$

• **Tangential displacement:**

$$u_\theta = 0 \quad (\text{E.44})$$

• **Pore pressure:**

$$p(r, t) = p_w g(r, t) \quad (\text{E.45})$$

• **Radial stress:**

$$\sigma_{rr}(r, t) = p_w \frac{r_w^2}{r^2} + 2\eta p_w \frac{r_w}{r} h(r, t) \quad (\text{E.46})$$

• **Tangential stress:**

$$\sigma_{\theta\theta}(r, t) = -p_w \frac{r_w^2}{r^2} - 2\eta p_w \left(\frac{r_w}{r} h(r, t) + g(r, t) \right) \quad (\text{E.47})$$

• **Shear stress:**

$$\sigma_{r\theta} = 0 \quad (\text{E.48})$$

where:

$$g(r, t) = L^{-1} \left(\tilde{g}(r, s) \right) \quad (\text{E.49})$$

$$h(r, t) = L^{-1} \left(\tilde{h}(r, s) \right) \quad (\text{E.50})$$

L^{-1} is the Laplace inversion operator and

$$g(r, s) = \frac{K_0(\xi)}{sK_0(\beta)} \quad (\text{E.51})$$

$$\tilde{h}(r, s) = \frac{1}{s} \left[\frac{K_1(\xi)}{\beta K_0(\beta)} - \frac{r_w}{r} \frac{K_1(\beta)}{\beta K_0(\beta)} \right] \quad (\text{E.52})$$

$$\eta = \alpha \frac{1-2\nu}{2(1-\nu)} \quad (\text{E.53})$$

$$\xi = r \sqrt{\frac{s}{c}} \quad (\text{E.54})$$

$$\beta = r_w \sqrt{\frac{s}{c}} \quad (\text{E.55})$$

$$c = \frac{k}{\mu} \left(\phi c_t + \frac{\alpha^2}{\lambda + 2G} \right)^{-1} \quad (\text{E.56})$$

K0 and K1 are the first order modified Bessel function of the first and second kind. The solution in time is achieved by following formula:

$$f(t) \approx \frac{\ln 2}{t} \sum_{n=1}^N c_n \tilde{f} \left(n \frac{\ln 2}{t} \right) \quad (\text{E.57})$$

where (ln) is the natural logarithm, N an arbitrary integer and:

$$c_n = (-1)^{n+\frac{N}{2}} \sum_{k=\text{floor}(\frac{n+1}{2})}^{\min(n, \frac{N}{2})} \frac{k^{\frac{N}{2}} (2k)!}{\left(\frac{N}{2} - k\right)! k! (k-1)! (n-k)! (2k-n)!} \quad (\text{E.58})$$

E.8: Poroelastic behavior of a pressurized wellbore in an unstressed rock containing fluid at zero pressure

Schematic of the problem is illustrated in **Fig.E.8** where r_w = inner/wellbore boundary radius, r_e =outer boundary radius set as infinity, p_w - p_i = wellbore pressure, and p = pore pressure initially it is zero and after that pressure is a function of time and space i.e. $p = p(t, r)$. Magnitudes of maximum (σ_H) and minimum horizontal stresses (σ_h) are also equal to zero as the rock is unstressed.

Analytical solutions are as follows:

• **Radial displacement:**

$$u_r(r,t) = -\frac{p_w - p_i}{2G} \frac{r_w^2}{r} - \frac{\eta}{G} r_w (p_w - p_i) h(r,t) \quad (\text{E.59})$$

• **Tangential displacement:**

$$u_\theta = 0 \quad (\text{E.60})$$

• **Pore pressure:**

$$p(r,t) = (p_w - p_i) g(r,t) \quad (\text{E.61})$$

• **Radial stress:**

$$\sigma_{rr}(r,t) = (p_w - p_i) \frac{r_w^2}{r^2} + 2\eta (p_w - p_i) \frac{r_w}{r} h(r,t) \quad (\text{E.62})$$

• **Tangential stress:**

$$\sigma_{\theta\theta}(r,t) = -(p_w - p_i) \frac{r_w^2}{r^2} - 2\eta (p_w - p_i) \left(\frac{r_w}{r} h(r,t) + g(r,t) \right) \quad (\text{E.63})$$

• **Shear stress:**

$$\sigma_{r\theta} = 0 \quad (\text{E.64})$$

E.9: Deformation of a wellbore with balanced pressure in a drained rock subjected to anisotropic horizontal stress

Schematic of the problem is illustrated in **Fig.E.9** where r_w = inner/wellbore boundary radius, r_e = outer boundary radius set as infinity, p_w = wellbore pressure set as a constant p_i and pore also set a constant value of p_r . Magnitudes of maximum (σ_H) and minimum horizontal stresses (σ_h) are also equal to zero as the rock is unstressed.

Analytical solutions are as follows:

• **Radial displacement:**

$$u_r(r,\theta) = \frac{r}{4G} (\sigma_H' + \sigma_h') \left(1 - 2\nu + \frac{r_w^2}{r^2} \right) + \frac{r}{4G} (\sigma_H' - \sigma_h') \left(\frac{r_w^2}{r^2} \left(4 - 4\nu - \frac{r_w^2}{r^2} \right) + 1 \right) \cos(2\theta) - \frac{p_r - \alpha p_r}{2G} \frac{r_w^2}{r} \quad (\text{E.65})$$

• **Tangential displacement:**

$$u_{\theta}(r, \theta) = -\frac{r}{4G}(\sigma_H' - \sigma_h') \left(\frac{r_w^2}{r^2} \left(2 - 4\nu - \frac{r_w^2}{r^2} \right) + 1 \right) \sin(2\theta) \quad (\text{E.66})$$

• **Pore pressure:**

$$p = p_i \quad (\text{E.67})$$

• **Radial stress:**

$$\sigma_{rr}(r, \theta) = \frac{\sigma_H + \sigma_h}{2} \left(1 - \frac{r_w^2}{r^2} \right) + \frac{\sigma_H - \sigma_h}{2} \left(1 + 3\frac{r_w^4}{r^4} - 4\frac{r_w^2}{r^2} \right) \cos(2\theta) + \frac{r_w^2}{r^2} p_r \quad (\text{E.68})$$

• **Tangential stress:**

$$\sigma_{\theta\theta}(r, \theta) = \frac{\sigma_H + \sigma_h}{2} \left(1 + \frac{r_w^2}{r^2} \right) - \frac{\sigma_H - \sigma_h}{2} \left(1 - 3\frac{r_w^4}{r^4} \right) \cos(2\theta) - \frac{r_w^2}{r^2} p_r \quad (\text{E.69})$$

• **Shear stress:**

$$\sigma_{r\theta}(r, \theta) = -\frac{\sigma_H - \sigma_h}{2} \left(1 - 3\frac{r_w^4}{r^4} + 2\frac{r_w^2}{r^2} \right) \sin(2\theta) \quad (\text{E.70})$$

E.10: Drained poroelastic response of a pressurized wellbore in a drained rock subjected to anisotropic horizontal stress

Schematic of the problem is illustrated in **Fig.E.10** where r_w = inner/wellbore boundary radius, r_e = outer boundary radius set as infinity, p_w = wellbore pressure and pore pressure is a function of time and space i.e. $p = p(t, r)$. Magnitudes of maximum (σ_H) and minimum horizontal stresses (σ_h) are also equal to zero as the rock is unstressed.

Analytical solutions are as follows:

• **Radial displacement:**

$$u_r(r, \theta) = \frac{r}{4G} (\sigma_H' + \sigma_h') (1 - 2\nu + \frac{r_w^2}{r^2}) + \frac{r}{4G} (\sigma_H' - \sigma_h') \times \left(\frac{r_w^2}{r^2} \left(4 - 4\nu - \frac{r_w^2}{r^2} \right) + 1 \right) \cos(2\theta) - \frac{p_w'}{2G} \frac{r_w^2}{r} - \frac{\eta}{G} r_w (p_w - p_i) h(r, t) \quad (\text{E.71})$$

• **Tangential displacement:**

$$u_\theta(r, \theta) = -\frac{r}{4G} (\sigma_H' - \sigma_h') \left(\frac{r_w^2}{r^2} \left(2 - 4\nu + \frac{r_w^2}{r^2} \right) + 1 \right) \sin(2\theta) \quad (\text{E.72})$$

• **Pore pressure:**

$$p(r, t) = p_i + (p_w - p_i) g(r, t) \quad (\text{E.73})$$

• **Radial stress:**

$$\sigma_{rr}(r, \theta) = \frac{\sigma_H + \sigma_h}{2} \left(1 - \frac{r_w^2}{r^2} \right) + \frac{\sigma_H - \sigma_h}{2} \left(1 + 3 \frac{r_w^4}{r^4} - 4 \frac{r_w^2}{r^2} \right) \cos(2\theta) + p_w \frac{r_w^2}{r^2} + 2\eta (p_w - p_i) \frac{r_w}{r} h(r, t) \quad (\text{E.74})$$

• **Tangential stress:**

$$\sigma_{\theta\theta}(r, \theta) = \frac{\sigma_H + \sigma_h}{2} \left(1 + \frac{r_w^2}{r^2} \right) - \frac{\sigma_H - \sigma_h}{2} \left(1 + 3 \frac{r_w^4}{r^4} \right) \cos(2\theta) - p_w \frac{r_w^2}{r^2} - 2\eta (p_w - p_i) \left(\frac{r_w}{r} h(r, t) + g(r, t) \right) \quad (\text{E.75})$$

• **Shear stress:**

$$\sigma_{\theta r}(r, \theta) = -\frac{\sigma_H - \sigma_h}{2} \left(1 - 3 \frac{r_w^4}{r^4} + 2 \frac{r_w^2}{r^2} \right) \sin(2\theta) \quad (\text{E.76})$$

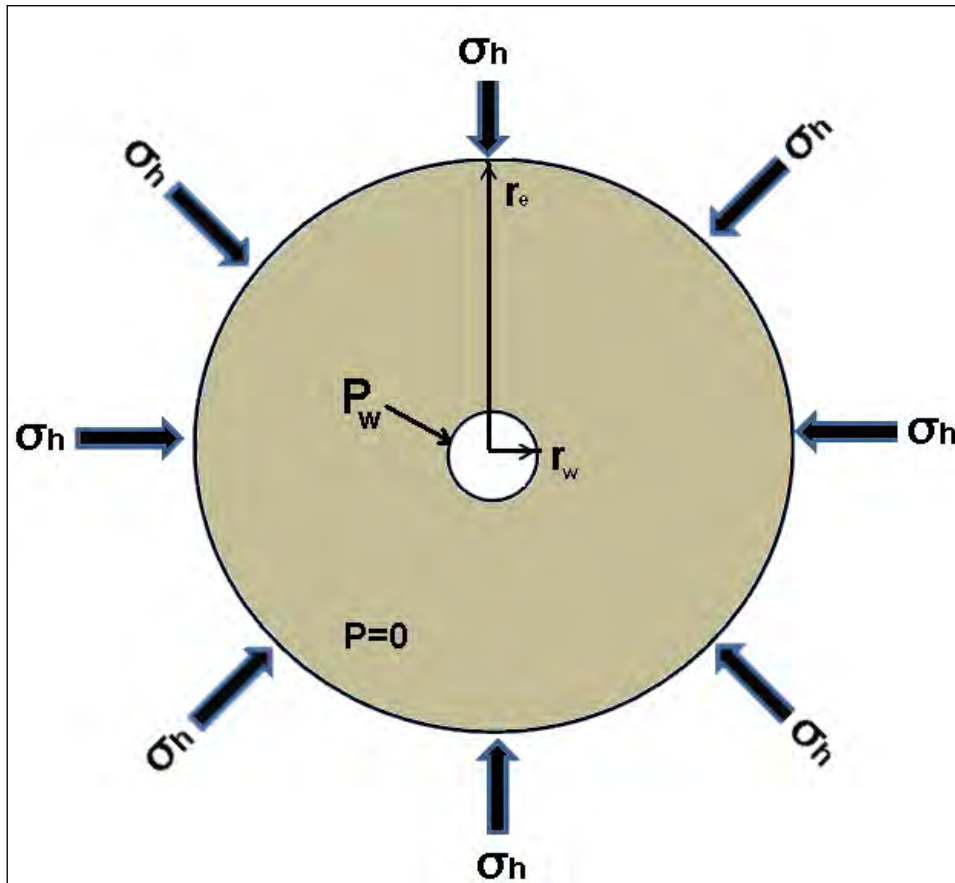


Fig. E.1: Schematic of the pressurized wellbore in a dry rock with isotropic horizontal stress and finite outer boundary.

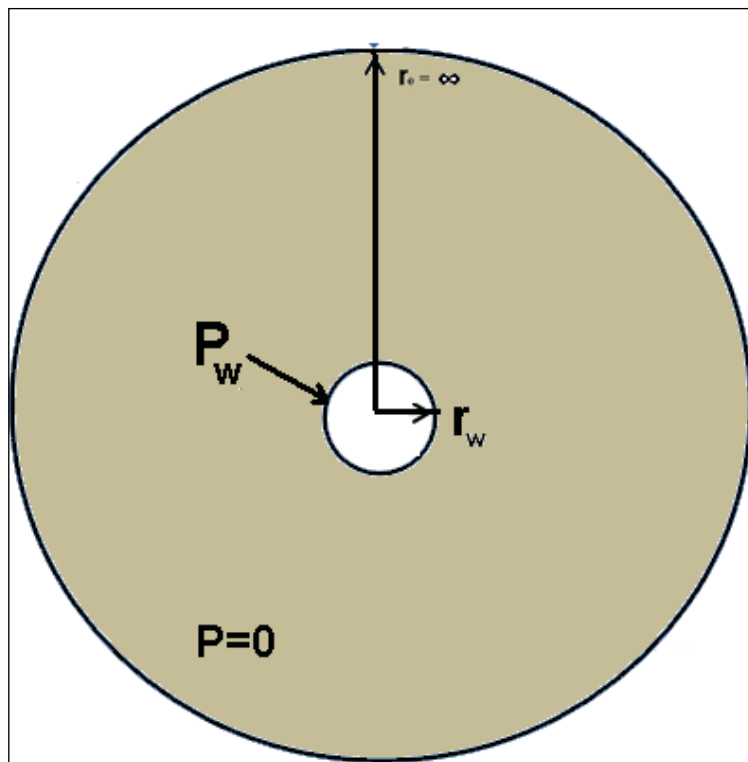


Fig. E.2: Schematic of the pressurized wellbore in an unstressed dry rock

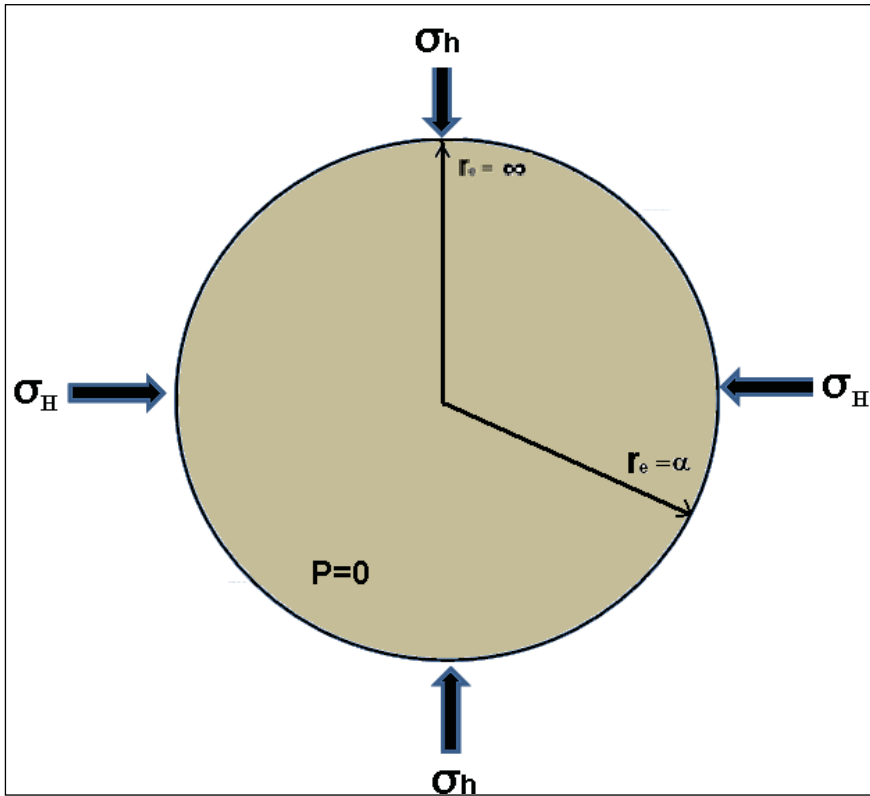


Fig. E.3: Schematic of the intact dry rock with anisotropic in situ horizontal stress.

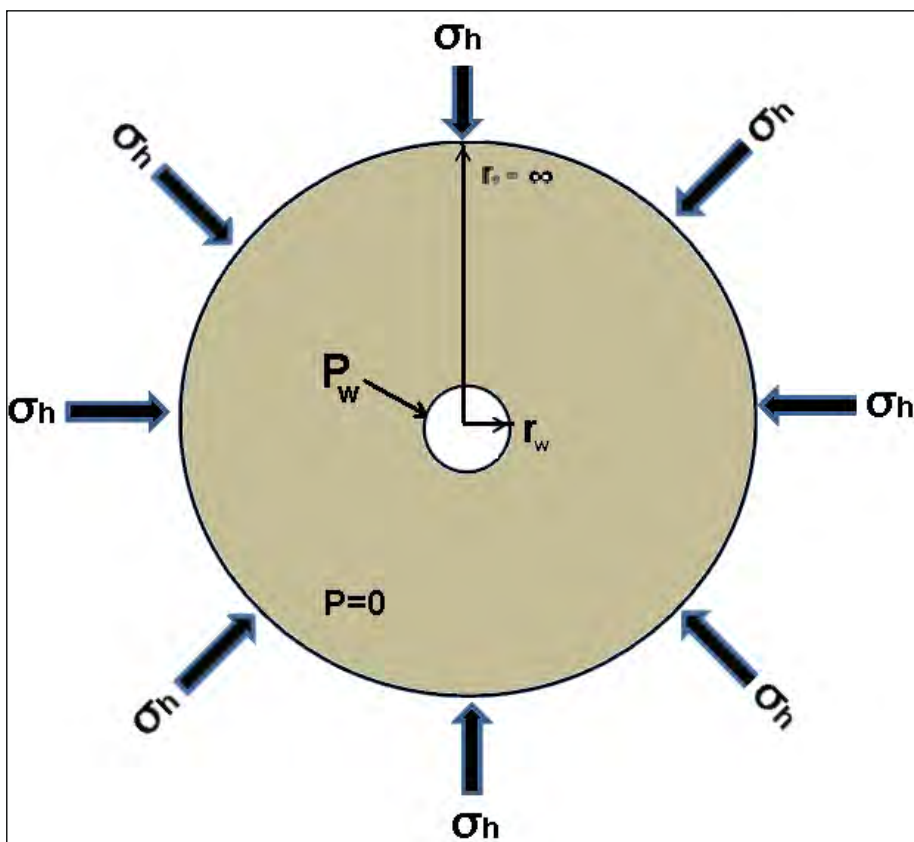


Fig. E.4: Schematic of the pressurized wellbore in a dry rock with isotropic in situ horizontal stress.

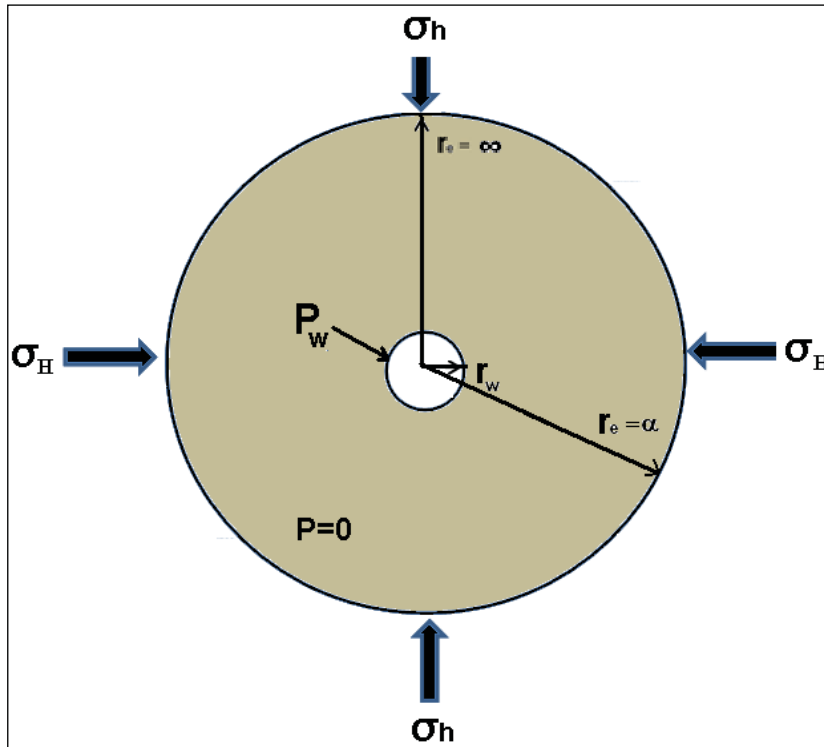


Fig. E.5: Schematic of the pressurized wellbore in a dry rock with anisotropic in situ horizontal stress.

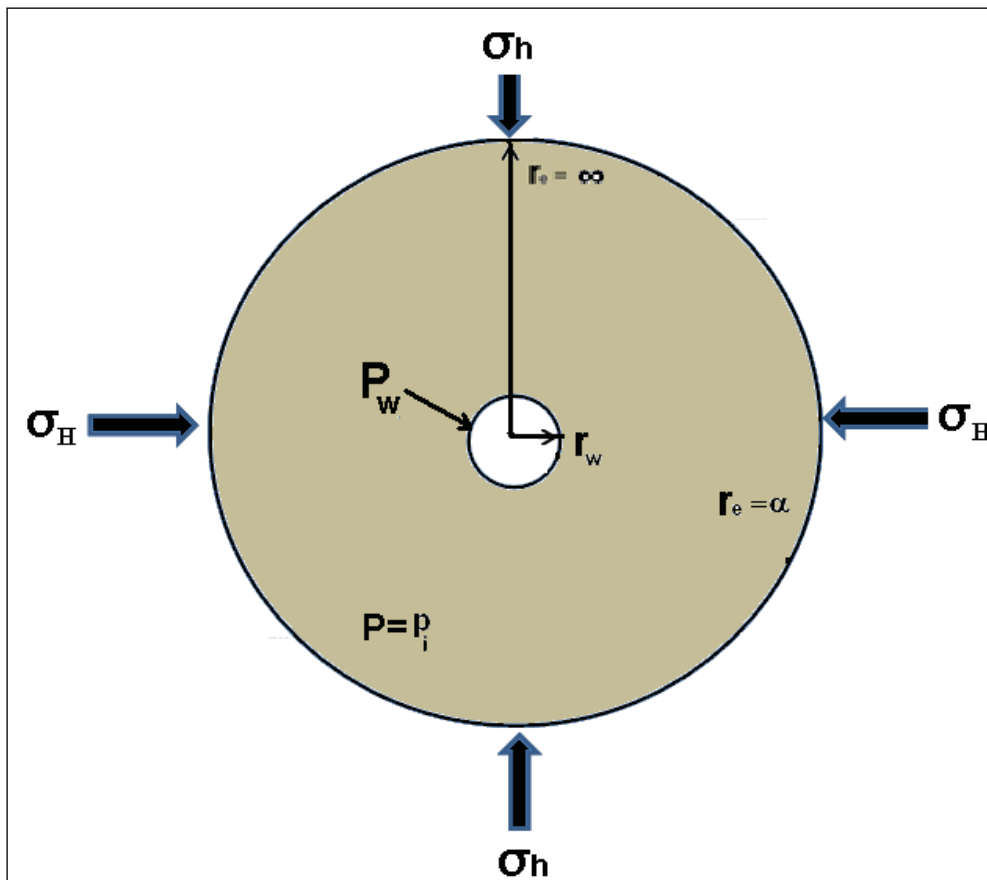


Fig. E.6: Schematic of the pressurized wellbore in a drained rock with anisotropic in situ horizontal stress.

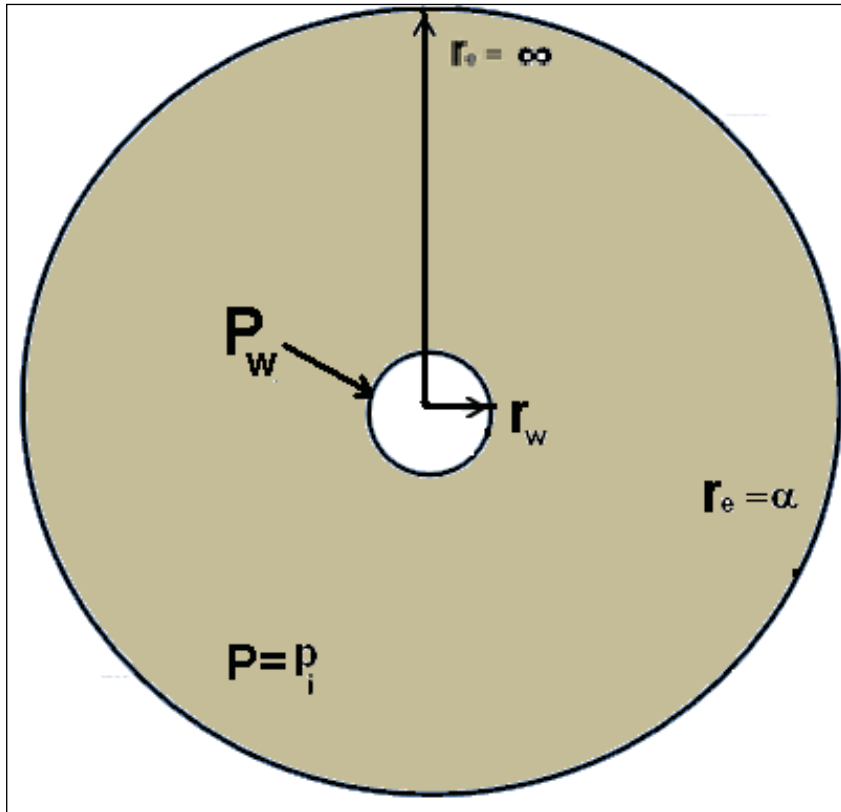


Fig. E.7: Schematic of the pressurized wellbore in an unstressed rock at zero pressure.

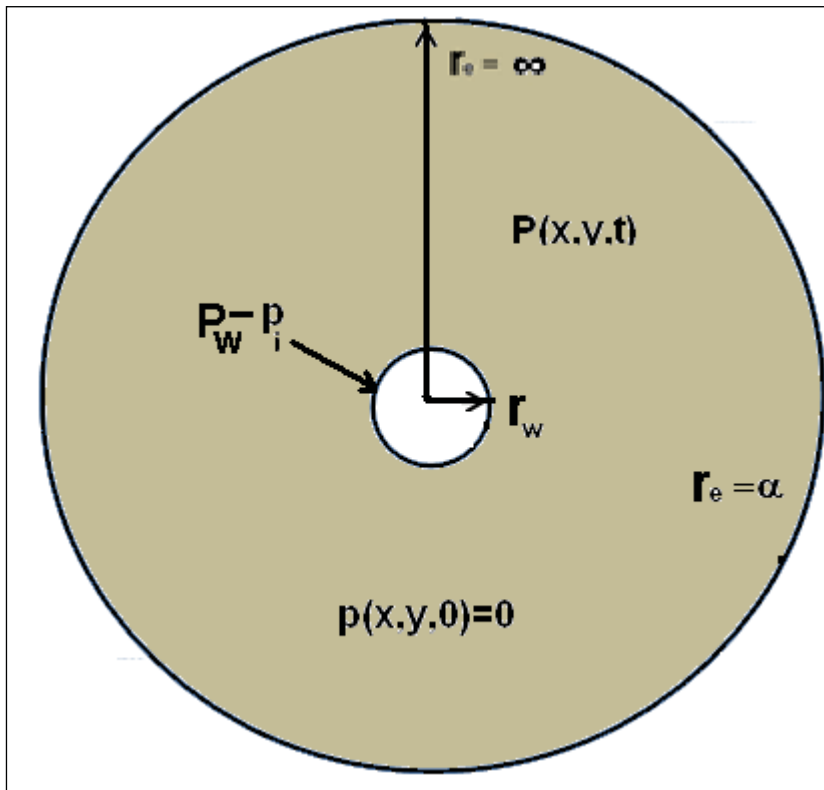


Fig. E.8: Schematic of the pressurized wellbore in an unstressed rock with zero fluid pressure.

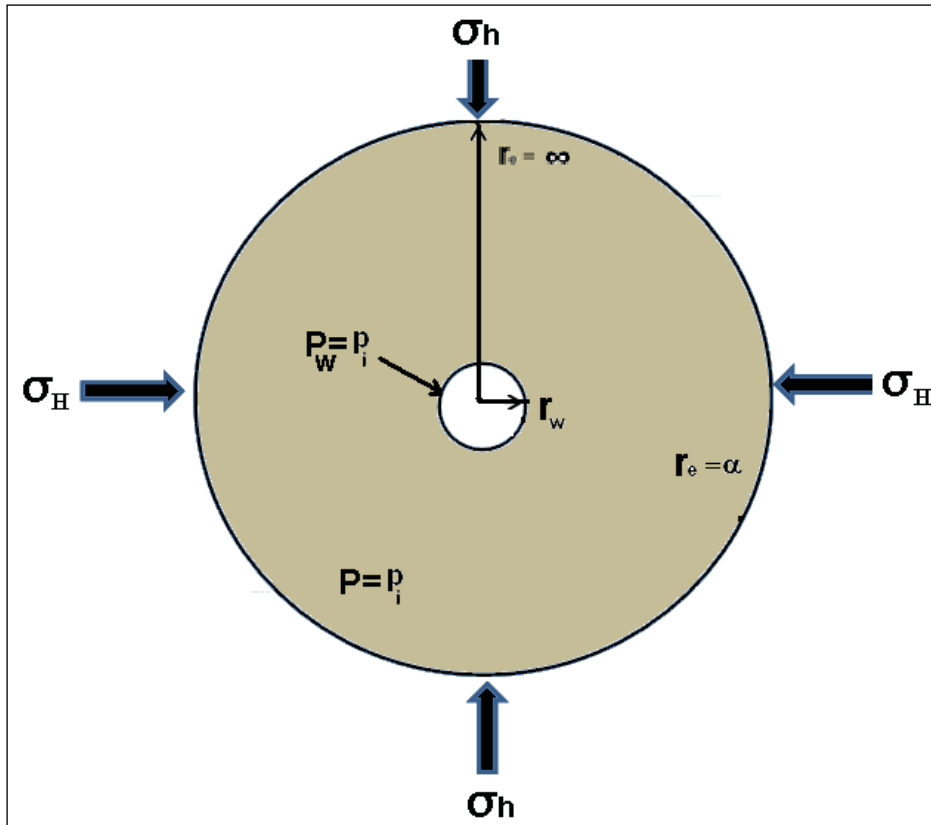


Fig. E.9: Schematic of the wellbore with balanced pressure in a drained rock with anisotropic horizontal stress.

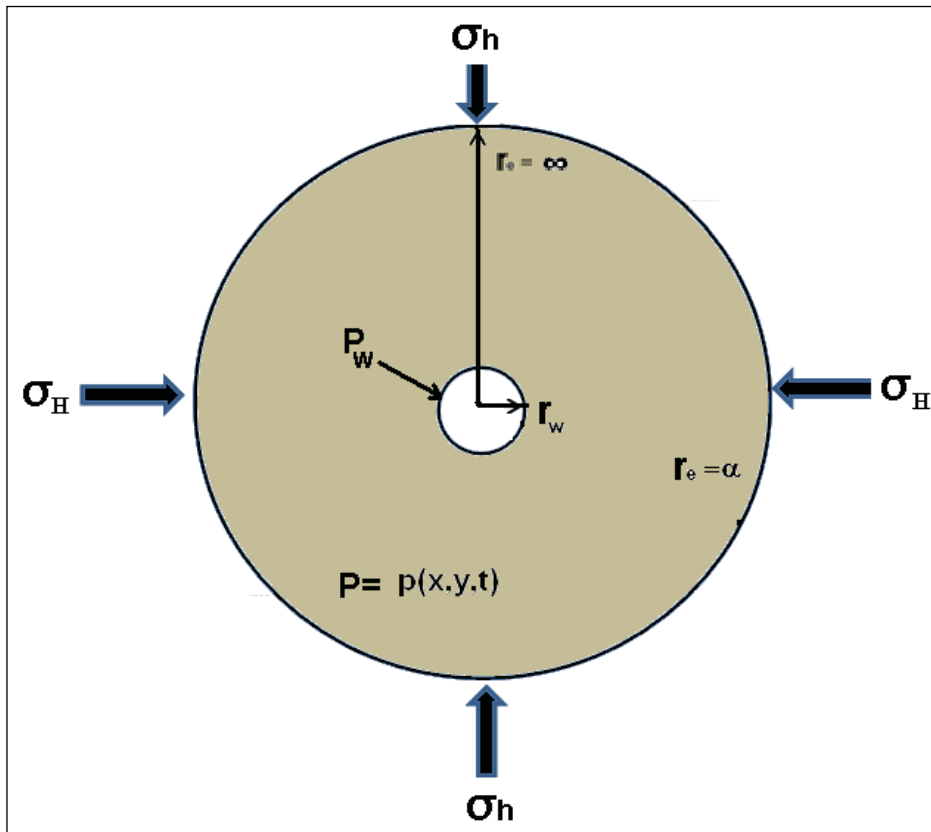


Fig. E.10: Schematic of the pressurized wellbore in a drained rock with anisotropic horizontal stress.